# Atomes froids fortement corrélés dans un réseau optique.

Tung-Lam Dao

Centre de Physique Théorique

Ecole Polytechnique

# Strongly-correlated ultracold atoms in optical lattices

*Author:*
Tung-Lam Dao

*Supervisor:*
Prof. Antoine Georges

October 2008

# Contents

# Remerciements

Pendant les trois années fantastiques au sein du groupe de physique théorique du Prof. Antoine Georges, je me suis énormément réjoui d'avoir rencontré et fait connaissance avec beaucoup de gens. Je voudrais donc consacrer cette première page à ma reconnaissance à toutes les personnes qui étaient toujours à mes cotés et qui m'ont aidé à aller jusqu'au bout. La liste des gens auxquels je voudrais adresser mes remerciements doit être infinie et j'espère que je ne vais oublier personne.

Tout d'abord, je tiens à remercier mon directeur de thèse Antoine Georges pour tout ce qu'il m'a apporté pendant ces trois années. Avoir travaillé sous sa direction n'est pas seulement un honneur, mais aussi un grand plaisir pour moi. Au delà des connaissances scientifiques que j'ai acquises à partir de ses explications très intuitives et pédagogiques basées sur des exemples simples, il m'a appris comment poursuivre des recherches. Durant les moments difficiles où le projet n'a pas avancé ou lorsque je me suis trompé dans un calcul, c'était lui qui m'a toujours fait confiance et m'a encouragé. En plus, Antoine m'a offert la possibilité de faire de la recherche dans un environnement de jeunes scientifiques. Il m'a guidé pour trouver un chemin de recherche plutôt que de me donner des tâches à finir. Il m'a encouragé à aller discuter avec d'autres chercheurs afin d'ouvrir mon esprit, au lieu de rester au bureau pour faire des calculs.

Tous mes travaux de thèse n'auraient pas pu aboutir sans mes collaborateurs. Je voudrais remercier Jean Dalibard et Christophe Salomon à l'ENS de Paris pour une belle collaboration sur mon premier projet de recherche. J'ai beaucoup appris de physique des atomes froids avec eux. Je voudrais aussi remercier mon collaborateur et aussi mon ami, Iacopo Carusotto, pour sa disponibilité. Il m'a tellement impressionné avec ses connaissances profondes et sa passion pour la science. C'est quelqu'un de très sérieux au travail, mais de très chaleureux et plein d'humour dans la vie quotidienne. Le séjour dans son groupe à Trento m'a offert une belle expérience scientifique. Je souhaite aussi remercier Massimo Capone pour une collaboration très serrée. Je lui dois beaucoup pour toutes ses explications et son aide pour apprendre les premiers programmes de calcul du champ moyen dynamique. Les trois années de thèse sont passées tellement vite que je ne suis pas arrivé à bien organiser mon temps pour travailler sur des projets envisagés. Je voudrais remercier le Prof. Thierry Giamarchi d'avoir accepté d'être mon rapporteur de thèse. C'est aussi avec lui que j'ai eu la chance de discuter sur des sujets scientifiques très intéressants. Malheureusement, suite à une mauvaise organisation de ma part, j'ai beaucoup regretté de ne pas avoir pu venir pour un stage dans son groupe comme prévu. Je voudrais remercier aussi le Prof. Wilhelm Zwerger d'avoir accepté d'être le rapporteur de ma thèse. Un grand merci à mes amis Robert David et Félix Werner avec qui je me suis beaucoup amusé à discuter après les séminaires du groupe d'atomes froids à l'ENS. Je voudrais aussi remercier mon ancien directeur de stage d'option, Grégoire Misguich, qui est toujours très enthousiaste à discuter et à répondre aux différentes questions liées à mes sujets de recherche. Je tiens à remercier Christophe Mora pour sa disponibilité et pour les discussions très intéressantes qui concernent mon dernier projet.

Je souhaite ensuite remercier toute l'équipe de la physique de la matière condensée au

CPHT. Les trois années partagées avec tous les membres de l'équipe sont inoubliables pour moi. J'ai eu la chance d'être un élément dans ce groupe "fortement corrélé". Je voudrais donc remercier tous les membres du groupe dans l'ordre de leur arrivée : Silke Biermann, Olivier Parcollet, Frank Lechermann, Sasha Poteryaev, Luca de' Medici, Jan Tomczak, Pablo Cornaglia, Daniel Rohe, Leonid Pourovskii, Michel Ferrero, Corinna Kollath, Lorenzo De Leo, Cyril Martins, Veronica Vildosola. Je ne me souviens plus combien et comment j'ai appris de choses avec eux. C'était un grand plaisir pour moi d'avoir partagé le même bureau pendant deux ans avec Pablo et Jan. Je suis sûr que je vous ai bien embêté avec des questions de toute sorte. Merci à Michel qui est toujours resté très patient pour m'aider jusqu'à la dernière minute de la rédaction de ma thèse. Pendant ma dernière année, je me suis tellement réjoui de travailler avec lui sur le dernier projet de ma thèse. Il m'a appris à la fois des techniques et de la physique. J'ai passé beaucoup de moments détendus avec lui pendant les pauses café. Merci à Corinna pour sa gentillesse et sa patience pour la correction de ma thèse. Je suis très content d'avoir travaillé avec elle et Iacopo. Merci à Silke, Sasha, Lorenzo et Olivier pour leur aide considérable. Je suis sûr que l'on trouvera la trace de tous les membres de l'équipe dans ma thèse.

Ce travail a été effectué à l'Ecole Polytechnique, au Centre de Physique Théorique (CPHT). Je voudrais remercier le Directeur Patrick Mora de m'avoir accueilli chaleureusement dans son laboratoire. Une grande partie de mon travail concernant des calculs numériques n'auraient pas pu aboutir sans l'aide de l'équipe informatique du labo. Je voudrais donc remercier tous les membres de l'équipe : Florence, Stéphane et Philippe pour leur disponibilité. Je tiens aussi à remercier l'équipe administrative du labo : Falida, Florence, Malika et Jeannine qui ne sont jamais fatigués de m'aider à régler des problèmes administratifs.

Je souhaite remercier l'Ecole Doctorale de l'Ecole Polytechnique pour son soutien financier à travers l'attribution de l'allocation internationale Gaspard Monge de l'Ecole Polytechnique. Merci à Audrey et Fabrice pour leur aide quant aux papiers administratifs et à l'organisation des activités pour les thésards à l'EDX.

Je voudrais réserver un grand remerciement au Prof. Truong Nguyen Tran qui est à la fois un grand professeur et un grand ami pour moi. J'ai reçu beaucoup de son soutien continu tout au long de mes années d'étude en France. Il m'a beaucoup aidé et donné des conseils. J'apprécie beaucoup les discussions et les expériences que nous avons partagées. Grâce à lui, j'ai bien trouvé ma direction de recherche.

La vie n'est pas faite que de science! Je voudrais remercier tous mes amis avec lesquels j'ai partagé de bons moments et qui ne m'ont jamais laissé seul lorsque j'étais en difficulté. Merci à mes chers amis D. Ha, M. Anh, Nhat Quang, Tran Phuong, Thanh Binh, Manh, Thinh, Nico, Roland, Maria Colome, Giovanni, Duong, Luca Carlevaro. Je voudrais remercier ma famille d'accueil, "ong" Loc et "ba" Mai, pour leur soutien moral et leurs encouragements.

Merci à ma femme, Huong, d'avoir suivi cette aventure avec moi jusqu'au bout. Tu m'as offert beaucoup plus que je ne peux le faire pour toi. Merci pour ton amour et d'avoir partagé tous les moments difficiles et de bonheur.

Je témoigne ma très vive reconnaissance à mes parents et à ma petite soeur, qui, de loin, n'ont jamais cessé de m'entourer de leur soutien et de leur amour. Enfin, je tiens à remercier mes beaux parents pour leur soutien et leurs encouragements.

# Introduction

The major concern of this thesis is the study of strongly-correlated ultracold atoms in optical lattices. In our study we adopt both a macroscopic and phenomenological point of view, asking questions on how to measure and observe physical quantities, and a more microscopic perspective by studying the phase diagram of specific models in different regimes of correlations.

The remarkable advances in handling ultracold atomic gases have given birth to the new field of "condensed matter physics with light and atoms". On the atomic physics side, the impressive progress in controlling such systems, particularly using Feshbach resonances, allows for the realization of interesting physical systems ranging from the weak interaction regime to strongly correlated systems, such as gases in the unitary limit. Another milestone progress is the possibility to introduce an external periodic potential to create the optical lattice with controllable parameters such as dimensionality, geometry or tunneling properties. The combination of these two aspects allows to realize and explore many interesting systems connected to condensed matter physics. Key issues in the physics of strongly correlated quantum systems can be addressed from a new perspective in this context.

There are many promising lines of research associated with ultra-cold atoms in optical lattices, of which we would like to emphasize two in particular. One attractive perspective is to use these systems as quantum simulators for outstanding problems in condensed matter physics such as the problem of high-temperature superconductivity. By allowing for a study of relevant models in a simplified and controllable setting, ultra-cold atoms may contribute to a better understanding of these complicated materials and in particular help in identifying the key physical mechanisms and in building an appropriate theoretical framework. A second direction is to study the novel physics (exotic ground-states, collective excitations...) in regimes which are not easily accessible in conventional solid-state physics. For example, one can perhaps dream of observing and manipulating the full many-body wave function of a large quantum systems, hence converting a rather abstract notion into an experimentally accessible quantity.

Motivated by these perspectives, this thesis is devoted to a study of ultra-cold fermionic atoms in optical lattices. It is organized in two parts, corresponding to two different aspects:

**I-** In the first part, consisting of two chapters, we adopt a macroscopic and phenomenological point of view. We first give a brief overview on the physics of ultracold atoms in optical lattices in Chapter 1, then we propose a novel measurement procedure of single-particle excitations of these systems in Chapter 2.

In Chapter 1, we start by establishing the theoretical framework for the description of ultracold atoms in optical lattices. We then describe some pioneering experiments in this field. We finally discuss the available experimental methods for probing and measuring physical observables of these systems.

In Chapter 2, motivated by the direct observation of single-particle excitations in condensed matter by angular resolved photoemission spectroscopy (ARPES), we propose a spectroscopic method which aims at observing the Fermi surface and the spectrum of one-particle

excitations in ultracold atomic systems. Our method is based on stimulated Raman spectroscopy. We show that, using this method, both the Fermi surface and the key physical properties of quasiparticle excitations can be accessed in a momentum and energy-resolved manner, under realistic experimental conditions in the presence of a confining potential. The end of the chapter is devoted to a discussion of the very recent experimental realization of a closely related measurement using RF spectroscopy in D. S. Jin's group at Boulder.

**II-** The second part, consisting of Chapters 3, 4, 5, is devoted to the study of the fermionic Hubbard model under different conditions and in different regions of parameters. The Hubbard model can be considered as the simplest model to describe quantum many-body systems. In some sense, we can compare it to the Ising model in magnetism. Its set of parameters is rather restricted. For a two-component system $\sigma =\uparrow,\downarrow$, the model is fully defined by the hoppings $t_\sigma$, the interaction strength $U$, the temperature $T$, the total number of particles $n = n_\uparrow + n_\downarrow$ and the polarization $p = n_\uparrow - n_\downarrow$). Nevertheless, it is still an unsolved model in two and three dimensions. Since the discovery of the high-temperature cuprate superconductors, it is believed that the Hubbard model in two dimensions is the simplest model that is able to explain the novel physics of these materials. Therefore the understanding of the ground state and phase diagram of the Hubbard model is an essential issue.

In condensed matter physics, scientists meet two major difficulties. The first one is that in order to reduce to the Hubbard model, one needs to focus on a restricted set of low-energy degrees of freedom and perform a calculation of the electronic structure in order to estimate the values of the hopping amplitude and interaction strength. Therefore, we do not really have a Hubbard model with well controllable parameters. The second one is that the interpretation of experimental measurements is further complicated by extrinsic effects such as impurities, sample quality, etc... The new field of ultracold atoms in optical lattices offers in principle the possibility to realize a pure Hubbard model whose set of parameters is very well controllable.

The second part of this thesis is devoted to theoretical studies of the Hubbard model with either mass (hopping) or population imbalance, and is organized as follows.

In Chapter 3, we introduce some theoretical tools for the study of lattice quantum many-body systems. As a many-body system contains a large number of degree of freedom, in the strongly correlated regime, no exact analytical method is available. On the other hand, despite the development of algorithms and computer power, a full numerical solution is still far from our reach. A method which combines both analytical and numerical approaches is currently the best choice for this study. In increasing order of numerical complexity, we introduce and briefly describe in Chapter 3: the usual Hartree-Fock mean field theory (HF-MFT), the slave boson mean field theory (SB-MFT) and the dynamical mean field theory (DMFT). In the following chapters, we apply these different methods to study the Hubbard model in different regimes.

In Chapter 4, we study the effect of mass imbalance on the phase diagram of a two-component fermionic mixture with attractive interactions in optical lattices. Using static and dynamical mean-field theories, we show that the pure superfluid phase is stable for all couplings when the mass imbalance is smaller than a limiting value. For larger imbalance, phase separation between a superfluid and a charge-density wave takes place when the coupling exceeds a critical strength. The harmonic trap induces a spatial segregation of the two phases, with a rapid variation of the density at the boundary.

Finally, in Chapter 5, we discuss the problem of a fermionic mixture with equal masses but population imbalance. For the continuum system in the trap, the superfluidity of this mixture has been already observed experimentally. The ground state of this kind of system has been the subject of controversial discussions. Different suggestions for the novel phase are the gapless superfluid (Sarma, or breached-pair) phase or the Fulde-Ferrell-Larkin-Ovchinnikov

state (FFLO). We discuss in this chapter the possibility to stabilize a gapless superfluid phase in the regime of strong correlations. We use for this purpose general energetic arguments, as well as analytical and numerical calculations based on static mean field theory and dynamical mean field theory.

# Chapter 1

# Ultracold atoms in optical lattices: a brief overview

*In this chapter, we first review the basic description of ultracold atoms in optical lattices by a many-body Hamiltonian. We briefly describe key experiments: the observation of the phase transition between the superfluid phase and a Mott insulator of ultracold bosonic atoms [46], as well as the possible recent observation of an incompressible Mott state of ultracold fermions [63]. In the second part of the chapter, we describe available experimental techniques for the measurement of correlation functions of physical observables.*

## 1.1 Ultracold atoms in optical lattices

In this section, we review the theoretical framework for the model of ultracold atoms in optical lattices. In the appropriate experimental conditions discussed below, we show that ultracold atoms in optical lattices can be described by the Hubbard model including the confining potential.

### 1.1.1 Many-body Hamiltonian

Here, we give a brief introduction to the Hamiltonian describing ultracold atoms in optical lattices (for more detailed references, see [42, 58, 121, 123]). For definiteness, we consider a two-component fermionic system (with hyperfine states labeled by $\sigma = \uparrow, \downarrow$), but the discussion applies in a similar way to a bosonic two-component system. The optical periodic potential

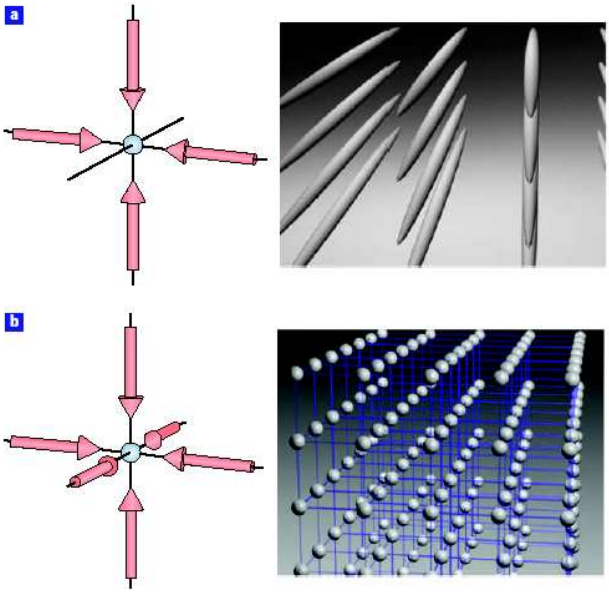


**Figure 1.1:** Controllable optical lattices: two-dimensional (top) and three-dimensional (bottom). Reprinted from [12]

is generated by the induced dipole interaction between the laser and the atoms: $V_{dip}(\mathbf{r}) = -\langle \mathbf{D}.\mathbf{E}(\mathbf{r})\rangle$. Here $\mathbf{E}(\mathbf{r})$ is the electromagnetic field and $\mathbf{D}$ is dipole operator of the atom. The atom exhibits an atomic transition from the ground state $|g\rangle$ to excited state $|e\rangle$ with a resonance frequency $\omega_{res}$. The dipole interaction can be expressed as $V_{dip} = \Omega(\mathbf{r})|e\rangle\langle g|/2+\text{h.c.}$ Here $\Omega(\mathbf{r}) = -2E(\mathbf{r})\mathbf{d}$ is the Rabi frequency with $\mathbf{d} = \langle e|\mathbf{D}|g\rangle$ the element of dipole matrix. Let $\delta$ be the detuning of the light field frequency from the atomic transition (i.e. $\delta = \omega - \omega_{res}$). For large detuning $\delta \gg \Omega(\mathbf{r})$, adiabatically eliminating the excited state $|e\rangle$ yields the interaction potential $V_{dip} = |\Omega(\mathbf{r})|^2/4\delta \propto E^2(\mathbf{r})$. The population of atoms transferred to the excited state is $|\Omega(\mathbf{r})|^2/4\delta^2$ thus the condition $\delta \gg \Omega(\mathbf{r})$ is required for the validity of the adiabatic elimination. Therefore counter-propagating laser beams can be used to generate a periodic potential (Fig. 1.1 left panels). Due to the interference between these two laser beams, a standing wave with the spatial period of $\lambda/2$ (with $\lambda$ the wavelength of the laser) is formed. By using different pairs of laser beams, different optical lattices with one, two or three dimensions can be obtained (Fig. 1.1 right panels). The periodic potential for each

species of the fermionic mixture reads

$$V_{L\sigma}(\mathbf{r}) = V_{0\sigma} \sum_{\mu} \sin^2(k_{L\mu} r_\mu), \tag{1.1}$$

where $\mu = 1, 2, 3$ corresponds to 1D, 2D or 3D cases and $k_{L\mu} = 2\pi/\lambda$ is the wave-vector of the lasers. The detuning of the laser frequency from the atomic resonance is different for the two species of atoms, therefore the induced periodic potentials for each species are different: $V_{0\sigma} = 4E_0^2 \mathbf{d}_\sigma^2/\delta_\sigma$. We note that the geometry of the optical lattice can be modified easily by changing the angle between different couple of laser beams. In addition, one can also play with the polarizations of the laser to create more interesting lattices [87]. For example, the optical lattice with geometrical frustration (triangular lattice or kagome lattice) has been proposed in Ref. [99].

An ultracold atom gas is trapped by an approximate harmonic potential. This comes from the trapping potential by a magnetic or optical trap. In addition, the gaussian profile of the laser beams used to create the optical lattice induces also a potential. More detailed discussion on the trapped potential is left for the Section 1.1.2. At this stage we neglect the harmonic potential. The non-interacting part of the Hamiltonian describing the atoms in the optical lattice reads

$$H_0 = \sum_{\sigma} \int d\mathbf{r} \Big[ -\frac{\hbar^2}{2m_\sigma} \|\nabla \psi_\sigma(\mathbf{r})\|^2 + V_{L\sigma}(\mathbf{r}) |\psi_\sigma(\mathbf{r})|^2 \Big]. \tag{1.2}$$

Here, $\psi_\sigma(\mathbf{r})$ is the many body wave function for atoms of the species $\sigma$ with mass $m_\sigma$. $V_{L\sigma}(\mathbf{r})$ is the lattice potential described above. The eigenstates of free fermions in a periodical potential are well-known in solid state physics. One obtains Bloch's wave function $|\phi_{\mathbf{k}\nu}\rangle$ corresponding to single-particle energies $\varepsilon_{\mathbf{k}\nu}$ (with $\mathbf{k}$ the quasi-momentum in the Brillouin zone of the lattice, and $\nu$ a band index)

$$H_0 |\phi_{\mathbf{k}\nu\sigma}\rangle = \varepsilon_{\mathbf{k}\nu\sigma} |\phi_{\mathbf{k}\nu\sigma}\rangle, \tag{1.3}$$

with $\phi_{k\nu\sigma}(\mathbf{r}) = e^{i\mathbf{k}.\mathbf{r}} u_{\mathbf{k}\nu\sigma}(\mathbf{r})$ and $u_{\mathbf{k}\nu\sigma}(\mathbf{r})$ a function having the periodicity of the lattice. It is

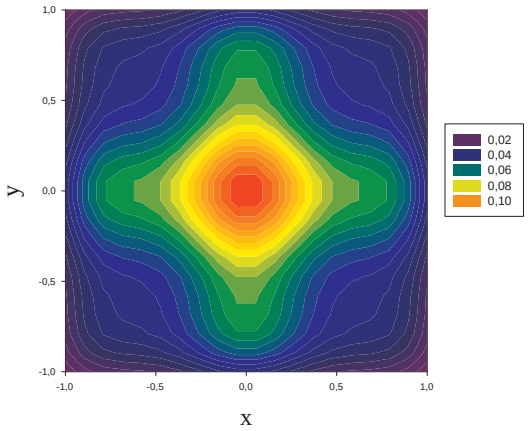


**Figure 1.2:** Contour plot of Wannier function of ultracold atom gas in two dimensional optical lattice for the first band

actually convenient to Fourier transform the Bloch wave functions in order to obtain Wannier

functions [88] which are localized around a specified lattice site $\mathbf{R}$ (at least for the lowest band). They are defined by

$$w_{\mathbf{R}\nu\sigma}(\mathbf{r}) = w_{\nu\sigma}(\mathbf{r}-\mathbf{R}) = \sum_k e^{-i\mathbf{k}.\mathbf{R}}\phi_{\mathbf{k}\nu\sigma}(\mathbf{r}) = \sum_k e^{i\mathbf{k}.(\mathbf{r}-\mathbf{R})}u_{\mathbf{k}\nu\sigma}(\mathbf{r}). \tag{1.4}$$

Fig. 1.2 displays the contour plot of the Wannier function associated with the lowest band, for a two-dimensional potential. The Fermion field operator can be decomposed on either the localized Wannier basis-set or the Bloch basis-set

$$\psi^\dagger_\sigma(\mathbf{r}) = \sum_{\mathbf{R}\nu} w^*_{\nu\sigma}(\mathbf{r}-\mathbf{R})c^\dagger_{\mathbf{R}\nu\sigma} = \sum_{\mathbf{k}\nu} \phi^*_{\mathbf{k}\nu\sigma}(\mathbf{r})c^\dagger_{\mathbf{k}\nu\sigma}, \tag{1.5}$$

in which $c^\dagger_{\mathbf{R}\nu\sigma}$ is the creation operator of an atom in the single-particle Wannier state $w_{\mathbf{R}\nu\sigma}$ on site $\mathbf{R}$ and analogously $c^\dagger_{\mathbf{k}\nu\sigma}$ the creation operator in the $\nu$-th Bloch state with quasi-momentum $\mathbf{k}$. The non-interacting Hamiltonian thus reads

$$H_0 = \sum_{\mathbf{k}\nu\sigma} \varepsilon_{\mathbf{k}\nu\sigma}c^\dagger_{\mathbf{k}\nu\sigma}c_{\mathbf{k}\nu\sigma} = -\sum_{\nu\sigma}\sum_{\mathbf{R}\mathbf{R}'} t^{\nu\sigma}_{\mathbf{R}\mathbf{R}'}c^\dagger_{\mathbf{R}\nu\sigma}c_{\mathbf{R}'\nu\sigma}. \tag{1.6}$$

In this expression, the tunneling amplitudes $t^{\nu\sigma}_{\mathbf{R}\mathbf{R}'}$ can be computed from the overlap of two Wannier functions on different sites

$$t^{\nu\sigma}_{\mathbf{R}\mathbf{R}'} = -\int d\mathbf{r} w^*_{\mathbf{R}\nu\sigma}(\mathbf{r})\Big[-\frac{\hbar^2\nabla^2}{2m_\sigma} + V_{L\sigma}(\mathbf{r})]w_{\mathbf{R}'\nu\sigma}(\mathbf{r}) = \int_{BZ} d\mathbf{k}\,\varepsilon_{\mathbf{k}\nu\sigma}\,e^{i\mathbf{k}.(\mathbf{R}-\mathbf{R}')}. \tag{1.7}$$

Let us now turn to the interaction between atoms. Under appropriate conditions [121](e.g. when the scattering length is small as compared to the spatial extension of the Wannier functions), the interactions can be described by a contact (pseudo-) potential

$$H_{int} = g\int d\mathbf{r}\psi^\dagger_\uparrow(\mathbf{r})\psi_\uparrow(\mathbf{r})\psi^\dagger_\downarrow(\mathbf{r})\psi_\downarrow(\mathbf{r}). \tag{1.8}$$

In this expression the coupling constant $g$ is related to the scattering length $a_s$ of the atomic potential by $m/4\pi a_s = 1/g + \sum_{\mathbf{k}} 1/2\epsilon_{\mathbf{k}}$ which is the kinetic energy of non-interacting gas $\epsilon_{\mathbf{k}} = \hbar^2\mathbf{k}^2/2m$. Using the decomposition of the creation operators onto the Wannier basis-set, one obtains the following expression for the interaction Hamiltonian, in second-quantized notations

$$H_{int} = \sum_{\mathbf{R}_1\mathbf{R}_2\mathbf{R}_3\mathbf{R}_4}\sum_{\nu_1\nu_2\nu_3\nu_4} U^{\nu_1\nu_2\nu_3\nu_4}_{\mathbf{R}_1\mathbf{R}_2\mathbf{R}_3\mathbf{R}_4}c^\dagger_{\mathbf{R}_1\nu_1\uparrow}c_{\mathbf{R}_2\nu_2\uparrow}c^\dagger_{\mathbf{R}_3\nu_3\downarrow}c_{\mathbf{R}_4\nu_4\downarrow}, \tag{1.9}$$

in which the coupling constants are the following matrix elements

$$U^{\nu_1\nu_2\nu_3\nu_4}_{\mathbf{R}_1\mathbf{R}_2\mathbf{R}_3\mathbf{R}_4} = g\int d\mathbf{r} w^*_{\mathbf{R}_1\nu_1\uparrow}(\mathbf{r})w_{\mathbf{R}_2\nu_2\uparrow}(\mathbf{r})w^*_{\mathbf{R}_3\nu_3\downarrow}(\mathbf{r})w_{\mathbf{R}_4\nu_4\downarrow}(\mathbf{r}). \tag{1.10}$$

The full Hamiltonian $H_0 + H_{int}$ is quite complicated and involves all the Bloch bands in the optical lattice. However, for a small enough number of particles and a deep enough lattice potential, we have well separated bands and only the first band will be populated. Hence, under appropriate conditions discussed in [121] (summarized on Fig. 1.3 left panel), we can reduce the full Hamiltonian to a one-band description

$$H = -\sum_{\langle\mathbf{R}\mathbf{R}'\rangle}\sum_\sigma (t_\sigma c^+_{\mathbf{R}\sigma}c_{\mathbf{R}'\sigma} + H.c) + U\sum_{\mathbf{R}} n_{\mathbf{R}\uparrow}n_{\mathbf{R}\downarrow}. \tag{1.11}$$

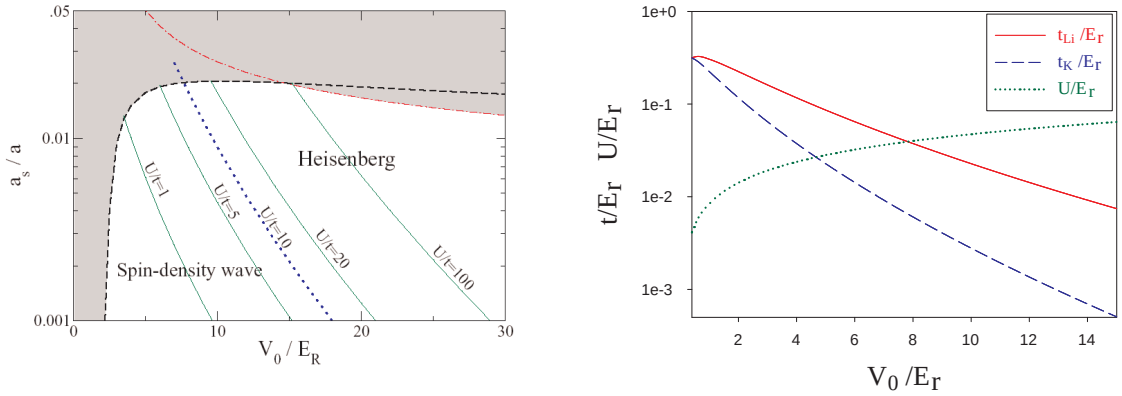


**Figure 1.3:** Left: Validity of the Hubbard model for the equal mass mixture of fermionic atoms in optical lattice. The unit of energy is chosen as the recoil energy $E_R = \hbar^2 \mathbf{k}_L^2/2m$. Reprinted from [121]. Right: Example of the hoping and interspecies interaction strength for the mixture with mass imbalance ($^6Li$ and $^{40}K$). The sketch is done with $k_F a_s = 60$.

For the first band, the estimation of the hopping and the on-site interaction are given by [123]

$$t_\sigma/E_{R\sigma} = 4\pi^{-1/2}(V_{0\sigma}/E_{R\sigma})^{3/4} e^{-2(V_{0\sigma}/E_{R\sigma})^{1/2}} \quad U/E_R = \sqrt{8/\pi} a_s \mathbf{k}_L (V_0/E_R)^{3/4}. \tag{1.12}$$

Both the interaction strength and the hopping amplitudes can be controlled by changing the intensity of the lasers beams, as displayed on Fig. 1.3 right panel. Furthermore, the interaction strength $U$ can be controlled independently using Feshbach resonances, as described below (Sec.1.1.3).

### 1.1.2 Trapping potential

In the ultracold atom experiments, we always need to trap the atoms. First, atoms are usually trapped before being cooled until low enough temperature. Until now, by mean of the usual trap such as the TOP trap or the magneto-optical trap [19], the trapping potential is approximately harmonic close to its minimum. Moreover, if we want to realize the experiment with an optical lattice, there is always an additional harmonic potential coming from the gaussian profile of the counter-propagating laser beams. In fact, the standing wave will create not only a periodical potential but also a harmonic profile. Therefore in a full description of an ultracold atom systems, we need to include the trapping potential to the Hubbard model obtained for a homogeneous case.

$$H = -\sum_{\langle \mathbf{R}\mathbf{R}' \rangle} \sum_\sigma (t_\sigma c^+_{\mathbf{R}\sigma} c_{\mathbf{R}'\sigma} + H.c) + U \sum_{\mathbf{R}} n_{\mathbf{R}\uparrow} n_{\mathbf{R}\downarrow} + \sum_{\mathbf{R},\sigma} V_{\sigma \text{trap}}(\mathbf{R}) n_{\sigma\mathbf{R}} - \sum_{\mathbf{R},\sigma} \mu_\sigma n_{\sigma\mathbf{R}}. \tag{1.13}$$

Here, the trapping potential has the following form: $V_{\sigma\text{trap}}(\mathbf{R}) = m_\sigma \omega_{ho}^2 \mathbf{R}^2/2$ in which $m$ is the mass of atoms and $\omega_{ho}$ is the trapping frequency.

In practice, the presence of this potential helps experimentalists to handle their experiments on ultracold atom gas. In the experiments described in Sec 1.2, we will see that this potential were used to perform interesting observations. By contrast, the presence of this potential raises an essential question for theorists and turns the many-body problem more complicated. Two usual approaches are a local density approximation (LDA) or numerical simulation for a finite-size system. Here, we will briefly introduce the LDA approach which will be mainly used in the next chapters of this thesis. In the LDA approach,

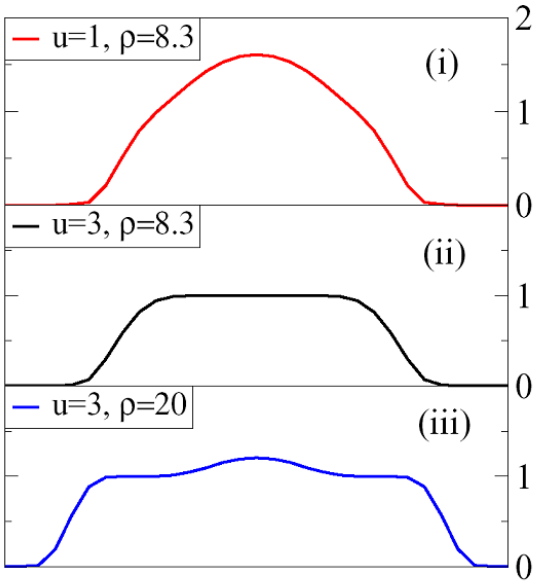


**Figure 1.4:** Density profile of 3D fermionic Hubbard model in presence of the harmonic potential obtained by DMFT with LDA [80]. (i) For small interaction ($U = 1$) or small density, the whole system is in a (Fermi-) liquid phase. The density profile displays strong variations with the trapping potential. (ii) For stronger interaction ($U = 3$), a Fermi liquid phase with a density gradually decreasing towards the boundaries, surrounds a plateau formed in the center of the trap. (iii) When the particle number is further increased the pressure exerted by the trapping potential overwhelms the incompressibility of the Mott state.

we solve the theoretical model for a homogeneous system without confining potential then extend to the non-homogeneous system by defining a spatial-dependent chemical potential $\mu_\sigma(\mathbf{r}) = \mu_\sigma - V_{\sigma\text{trap}}(\mathbf{r})$. Local physical quantities $\langle \mathbf{O}(\mathbf{r}) \rangle$ are computed via their values in the homogeneous system at this chemical potential:

$$\langle \mathbf{O}(\mathbf{r}) \rangle \approx \langle \mathbf{O}_{hom}[\mu_\sigma(\mathbf{r})] \rangle. \tag{1.14}$$

If the trapping potential is smooth enough with respect to all the variation length scales of physical quantities, we can expect that this approximation can provide a reasonable comparison with experiment. One of most obvious example is the calculation of the density profiles of the ultracold atoms (Fig. 1.4) [80, 98].

### 1.1.3 Controlling the interaction strength with Feshbach resonances

Feshbach resonances, scattering resonances, were first investigated in the context of nuclear physics [35]. The application of a Feshbach resonance for ultracold atom systems was first discussed in [115]. This resonance now becomes an indispensable tool for experimentalists to investigate the physics of cold atoms in many different contexts. Thank to this resonance, we can easily tune the interaction strength from weak interaction regime to the strongly correlated regime just by adjusting an external parameter such as the magnetic field. Detailed discussion on the Feshbach resonance can be found in [13, 19, 68].

The mechanism of the Feshbach resonance can be explained by a model with two channels (Fig. 1.5). The open channel represents scattering atoms with a continuum of states while

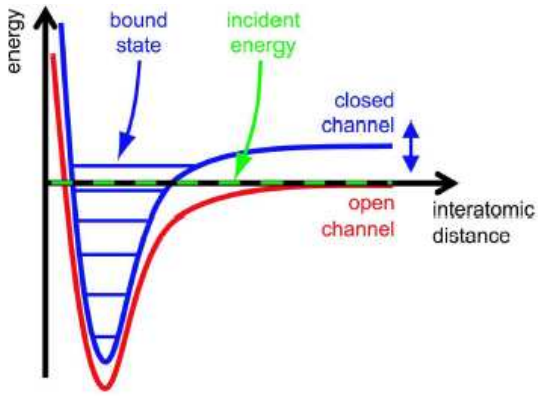


**Figure 1.5:** The two channel model for a Feshbach resonance. Atoms prepared in the open channel which corresponds to the interaction potential $V_{op}(\mathbf{r})$ (in red). They undergo a collision at low incident energy. The open channel is coupled to the closed channel $V(\mathbf{r})$ (in blue). When a bound state of the closed channel has an energy close the incident energy, a scattering resonance occurs. The position of the closed channel with respect to the open can be tuned by an external magnetic field B. Reprinted from Ref. [13]

the closed channel represents the bound state of atoms. Feshbach resonances appear when the total energy in an open channel matches the energy of a bound state in a closed channel, as illustrated in Fig. 1.5. Let $|O\rangle$ be the states of atoms in the open channel and $|C\rangle$ be the bound state of atoms in the closed channel. Atoms in the open channel interact with each other via the Hamiltonian $H_{OO}$. The two channels are coupled by the $H_{OC} = \Omega|C\rangle\langle O|$ with $\Omega = \langle O|H_{OC}|C\rangle$. Via the second-order process, two atoms in the open channel scatter into the closed channel to form a bound-state and subsequently decay to two separate atoms in the open channel. This process induces an effective interaction $H'_{OO}$ with interaction strength $\Omega^2/(E_O - E_{res})$ in the open channel. Here, $E_O$ is the energy of atoms in the open channel and $E_{res}$ is the energy of the bound state in the close channel. Therefore the scattering length in the open channel is modified to

$$\frac{4\pi\hbar^2}{m}a_s = \frac{4\pi\hbar^2}{m}a_O + \frac{\Omega^2}{E_O - E_{res}}, \tag{1.15}$$

in which $a_O$ is scattering length in the open channel without presence of closed channel. The detuning between the energy levels of open channel and closed channel $\delta = E_O - E_{res}$ can be adjusted by an external magnetic field $B$. We can rewrite the scattering length as

$$a_S = a_O(1 + \frac{\Delta B}{B - B_0}), \tag{1.16}$$

in which $\Delta B$ and $B_0$ describe the width and the location of the Feshbach resonance respectively. Fig. 1.6 shows an example of the Feshbach resonance of $^6$Li.

In practice, the Feshbach resonance works better for fermionic atoms because the life-time due to the three body recombination becomes very large at the resonance. In contrast, for the bosonic atoms this life-time becomes very small in this limit [19].

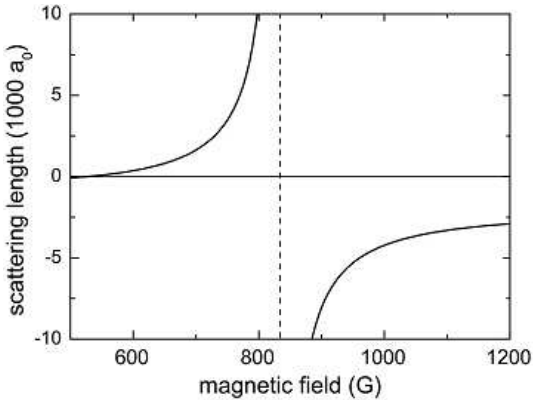


**Figure 1.6:** Magnetic field dependence of the scattering length between the two lowest hyperfine states of $^6$Li with a Feshbach resonance located at $B_0 = 834G$ and a zero crossing at $B_0 + \Delta B = 534G$. The background scattering length $a_{bg} = -1405a_B$ is exceptionally large in this case ($a_B$ being the Bohr radius). Reprinted from Ref. [13]

## 1.2 Observation of strongly correlated phases of ultracold atoms in an optical lattice

In this section, we would like to emphasize the motivations on the study of ultracold atoms in optical lattices through two of milestone experiments: the phase transition from the superfluid to Mott insulator in bosonic system and the recent evidence of the fermionic Mott insulator at high temperature.

### 1.2.1 Superfluid to Mott insulator transition of bosonic atoms

In 2002, Greiner and co-authors achieved the first experimental observation of the transition from the superfluid state to the Mott insulating state of interacting bosons, as predicted by theory [57]. In their experimental set-up, they cooled the atom $^{87}$Rb into the spin-polarized state ($F = 2, m_F = 2$) in order to create a Bose-Einstein condensate. Then, a three dimensional optical lattice was created by three optical standing waves whose crossing point was centered in the condensate. This optical lattice creates a periodic potential $V(x, y, z) = V_0(\sin^2(kx) + \sin^2(ky) + \sin^2(kz))$ where $k = 2\pi/\lambda$. The gaussian profile of the laser beams at the position of the condensate creates an additional weak isotropic harmonic confinement over the lattice.

After creating the optical lattice, the atoms are distributed over approximately 150000 lattice sites (about 65 lattice sites in each direction). In order to test whether there is still phase coherence between different lattice sites, they switched off suddenly the confining potential and let the atomic wave function expand freely. In the superfluid regime where all atoms are delocalized and coherent in phase, they observed a very high contrast three dimensional interference pattern as shown in the time of flight image (Fig. 1.7). Otherwise, in the Mott phase all atoms are well localized and there is no phase coherence. In contrast to the superfluid case, a broad background is observed. This phase transition is observed simply by tuning the intensity of the optical lattice. This observation is a fascinating example of the feasibility of the cold atoms systems for the study of the quantum phase transition.

As described above, there exists always a confining potential that in this case helps to stabilize a central region of incompressible Mott state in the trap. In the harmonic trap,

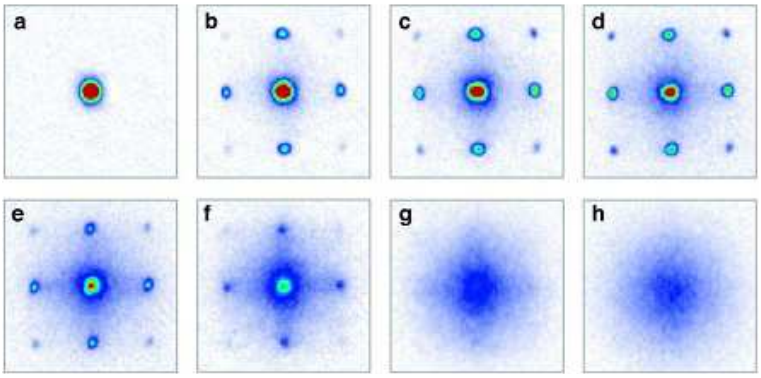


**Figure 1.7:** Superfluid to Mott insulator transition of bosons in optical lattices [46]. Absorption image of matter wave interference pattern. These were obtained after suddenly releasing atoms from optical lattice with different potential depths $V_0$ after a time of flight of 15 ms. The values of $V_0$ were: a)$0E_r$; b)$3E_r$; c) $7E_r$; d)$10E_r$; e)$13E_r$; f)$14E_r$; g)$16E_r$ and h)$20E_r$.

---

the incompressibility of the Mott phase induces the "wedding-cake" structure of the density profile. The Mott insulator has a gap $\Delta_M$ to density excitations. This is therefore an incompressible state which means that adding an extra particle will costs a finite amount of energy. It is clear from the mean-field calculation shown in [42] that if we want to vary the average density from infinitesimally below an integer value $n$ to infinitesimally above, we have to change the chemical potential across the Mott gap.

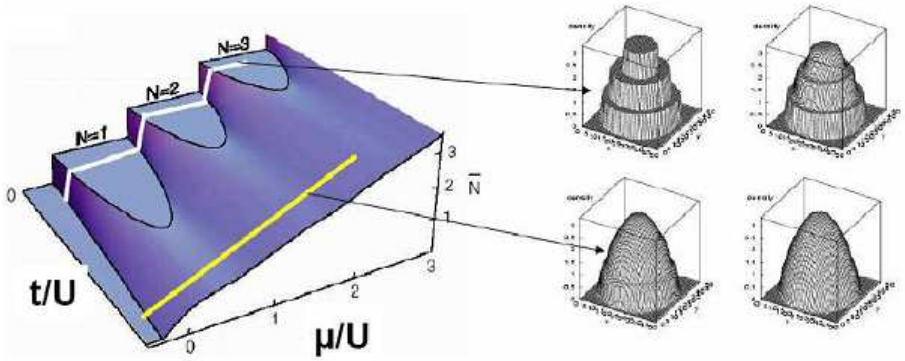


**Figure 1.8:** Left panel: phase diagram of the Bose Hubbard model as a function of chemical potential $\mu/U$ and coupling $t/U$ obtained in [36, 42, 105]. An incompressible Mott insulator is found within each lobe of integer density. Right: density profiles in a harmonic trap. The "wedding cake" structure is due to the incompressibility of the Mott insulator. Reprinted from Ref. [42].

The Mott gap is proportional to the interaction strength U in the atomic limit (large U) and vanishes at the critical coupling as $\Delta_M \propto \sqrt{U - U_c}$ (within mean-field theory). The existence of a gap means that the chemical potential can be changed within the gap without changing the density. As a result, when the system is placed in a trap, it displays density plateaus corresponding to the Mott state, leading to a wedding cake structure of the density profile (Fig. 1.8). This is easily understood in the local density approximation, in which the

local chemical potential is given by $\mu(\mathbf{r}) = \mu - m\omega_{ho}^2\mathbf{r}^2$, yielding a maximum extension of the plateau $\sqrt{2\Delta_M/m\omega_{ho}^2}$. Several authors have studied these density plateaus beyond the LDA by numerical simulation [10] and they have been recently observed experimentally [38].

### 1.2.2 Incompressible Mott state of ultracold fermions

Another important experiment is the observation of quantum phase transition from Mott insulator to Fermi liquid phase in a mixture of fermionic atoms in optical lattice [63]. We describe briefly here how they observe the Mott state. In the experiment, the equal fermionic mixture is prepared in strongly correlated regime with two hyperfine states $|9/2, -9/2$ and $9/2, -5/2$ of $^{40}$K. The degenerate gas is loaded into an optical lattice. The s-wave scattering length between two species of atoms is tuned from $a_s = 240 \pm 4a_0$ to $a_s = 810 \pm 40a_0$ by the Feshbach resonance located at $B = 224.21$ Gauss. The idea of the experiment is to observe the Mott phase via the double occupation number. For a fermionic system, the Mott phase is characteristic by the regular filling of one particle per site with small particle fluctuation. Therefore, this state is interpreted by a low double occupation $\langle D \rangle = \langle n_\uparrow n_\downarrow \rangle$.

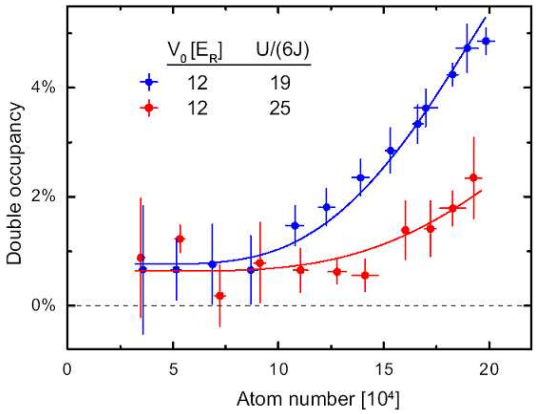


**Figure 1.9:** Appearance of double occupancy in the strongly interacting regime. The double occupancy for low atom numbers is nearly constant and starts to increase only for large atom numbers. The blue and red lines represent the theoretical expectation for D in the atomic limit. Reprinted from Ref. [63].

In order to measure this quantity in experiment, they first increased the lattice depth. The state of atoms which is frozen and the filling number at each site is exactly determined (no particle fluctuation). For a general configuration, we can have lattice sites with zero particle, one particle or two particles. By tuning the interaction to the BEC-side of Feshbach resonance , they formed molecules in the sites with double occupation. The number of molecules were then measured by the RF spectroscopy technique (discussed in Section 1.3.2). The experiment is repeated for different total number of atoms. In the Fig. 1.9, we see how the double occupation varies when the total number of atoms increased. The symbols are the experimental values while the continue curves are theoretical prediction at atomic limit. We see that for a small number of atom, there is a plateau of small double occupation (less than 1%). As far as the particle number greater than a critical value $n_c$ ($\approx 8 \times 10^4$ for $U/6J = 19$ and $\approx 14 \times 10^4$ for $U/6J = 25$), the double occupation increases. The presence of this plateau has been interpreted as evidence for a Mott insulator region. We note that in this experiment the temperature is undetermined.

## 1.3 Measuring physical observables in ultracold atomic systems: available methods

In this section, we summarize some of the measurement techniques that have been implemented experimentally in order to probe these systems. It is convenient to distinguish two kinds of measurements: those probing the *single-particle* response functions, and those probing the *two-particle* response. Among the latter are the measurement of the density-density correlation function $\langle \rho(\mathbf{r},t)\rho(\mathbf{r}',t')\rangle$ or the spin-spin correlation function $\langle S(\mathbf{r},t)S'(\mathbf{r}',t')\rangle$. In solid-state physics, these can be probed by X-ray or neutron scattering. In contrast, the correlation function associated with a single-particle operator (such as the operator creating or destroying a single atom in the system) involves transitions between the ground-state and an excited state of the many-body system with one atom added to it or one atom removed from it. In solid-state physics, this can be probed by photoemission (or inverse photoemission) experiments. Since one of the main work in this thesis has been to propose a new measurement method for the one-particle response function, I will mainly summarize in this chapter the probes of two-particle correlation functions. One-particle correlation functions will be addressed in detail in the next chapter.

### 1.3.1 General consideration on response functions

In general terms, measurements which involve a weak perturbation of the system coupling to a physical observable $\hat{O}$ (such as, e.g. the density or the spin-density) will probe the correlation function associated with this observable, namely

$$C_O(\mathbf{r},\mathbf{r}';t,t') = -i\langle T_t \hat{O}(\mathbf{r},t)\hat{O}^+(\mathbf{r}',t')\rangle. \tag{1.17}$$

Here, $T_t$ is the time order product. This is true when linear response theory applies, which assumes that the system is not disturbed too far out of equilibrium. In this expression, the operators evolve in the Heisenberg representation, and the brackets denote either an average in the ground-state (many-body) wave function (for a measurement at $T = 0$) or, at finite temperature, a thermally weighted average with the equilibrium Boltzmann weight.

The behavior of this correlation function is controlled (at $T = 0$) by the excited states which are coupled to the ground-state upon application of $\hat{O}$. In order to see this, we insert a complete set of states in the above expression and obtain the following spectral representation for $t > t'$(given here at $T = 0$ for simplicity)

$$C_O(\mathbf{r},\mathbf{r}';t-t') = \sum_n e^{-i(E_n-E_0)(t-t')/\hbar}\langle\Phi_0|\hat{O}(\mathbf{r})|\Phi_n\rangle\langle\Phi_n|\hat{O}^+(\mathbf{r}')|\Phi_0\rangle. \tag{1.18}$$

In this expression,$|\Phi_0\rangle$ is the ground-state (many-body) wave function, and the summation is over all admissible many-body excited states (i.e. having non-zero matrix elements). We can introduce a spectral function, which measures how many such excited states contribute to this correlation function in a given energy interval. It is defined for $\omega > 0$

$$A_O(\mathbf{r},\mathbf{r}';\omega) = \sum_n \langle\Phi_0|\hat{O}(\mathbf{r})|\Phi_n\rangle\langle\Phi_n|\hat{O}^+(\mathbf{r}')|\Phi_0\rangle\, \delta\left[\omega - (E_n - E_0)/\hbar\right]. \tag{1.19}$$

This spectral function obeys the sum-rule

$$\int_{-\infty}^{+\infty} d\omega A_O(\mathbf{r},\mathbf{r}';\omega) = \langle\Phi_0|\left[\hat{O}(\mathbf{r}),\hat{O}(\mathbf{r}')\right]_{\pm}|\Phi_0\rangle \tag{1.20}$$

where the commutator (resp. anticommutator) applies to bosonic (resp. fermionic) observables $\hat{O}$. In a translationally invariant system (which is not the case if a trapping potential is present), the spatial Fourier components of the spectral function can be considered instead. For $\omega > 0$ the spectral function reads

$$A_O(\mathbf{k},\omega) = \sum_n |\langle\Phi_0|\hat{O}_\mathbf{k}|\Phi_n\rangle|^2\, \delta\left[\omega - (E_n - E_0)/\hbar\right]. \tag{1.21}$$

In the following, we discuss how to measure such correlation functions and spectral functions, focusing mainly on two-particle observables. In the next chapter we will consider in more details the measurement of the single-particle spectral function in an energy- and momentum-resolved way.

### 1.3.2 Partial information on one-particle correlations from time-of-flight and RF spectroscopy

Single-particle correlation functions probe excited states of the many-body system with one atom added to it, or one atom removed, i.e. coupled to the ground-state via a single particle process. This is described by the creation or annihilation operator of a single atom. Specializing the above formulas to $\hat{O} = \psi(\mathbf{r},t)$, we have to consider the correlation function

$$\langle \mathrm{T}_t \psi(\mathbf{r},t)\psi(\mathbf{r}',t')\rangle = iG_1(\mathbf{r},\mathbf{r}';t,t'), \tag{1.22}$$

which is usually called the single-particle Green's function $G_1$ ($\mathrm{T}_t$ denotes time ordering). The corresponding spectral decomposition involves the one-particle spectral function (written here, for simplicity, for a homogeneous system so that crystal momentum is a good quantum number and at $T = 0$)

$$A(\mathbf{k},\omega) = \sum_n |\langle\Phi_n^{N-1}|c_k|\Phi_0^N\rangle|^2 \delta(\omega + \mu + E_{N-1} - E_0)(\omega < 0) \tag{1.23}$$

$$A(\mathbf{k},\omega) = \sum_n |\langle\Phi_n^{N+1}|c_k^+|\Phi_0^N\rangle|^2 \delta(\omega + \mu + E_0 - E_{N+1})(\omega > 0). \tag{1.24}$$

The spectral function is normalized to unity for each momentum, due to the anti-commutation of fermionic operators

$$\int_{-\infty}^{+\infty} d\omega A(\mathbf{k},\omega) = 1. \tag{1.25}$$

The momentum and frequency dependence of this quantity contains key information about the important low-energy excitations of fermionic systems (hole-like, i,e corresponding to the removal of one atom, for $\omega < 0$, and particle- like for $\omega > 0$). Let us note that information on one-particle correlators of a Bose system can be obtained from two-particle ones, when the system is made to interfere with either another identical system [94] or with a reference condensate [89]. By contrast, in Fermi systems the distinction between one- and two-particle correlators is essential.

#### Time of flight measurement

As we now explain, time of flight measurements probe the single-particle Green's function *at equal times* $\langle\psi^+(\mathbf{r},t)\psi(\mathbf{r}',t)\rangle$, i.e. the one-body density matrix. Its Fourier transform is the momentum distribution at finite temperature

$$N(\mathbf{k}) = \langle c_\mathbf{k}^+ c_\mathbf{k}\rangle = \int_{-\infty}^{0} n_F(\omega) A(\mathbf{k},\omega) d\omega, \tag{1.26}$$

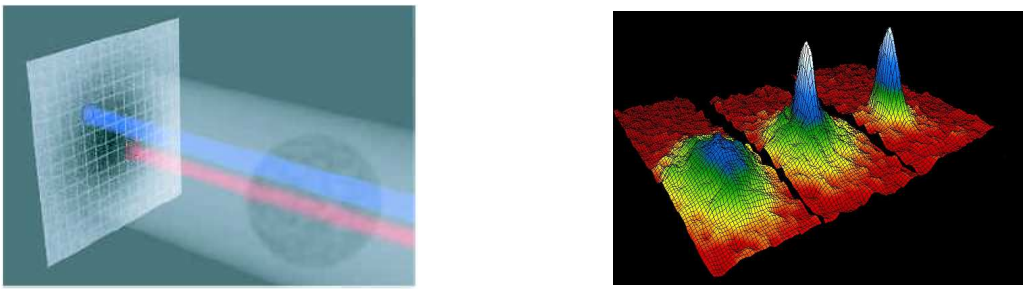

**Figure 1.10:** Time of flight imaging technique. Left panel: Schema of the TOF experiment [12]. Right panel: First observation of the BEC in ultracold atoms. Figure shows the momentum distribution of Bose Einstein condensation at temperatures 400 nK, 200 nK and 50 nK of $^{87}$Rb [4].

in which $n_F(\omega)$ is the Fermi-Dirac distribution. In an experiment of time-of-flight imaging, the cloud of ultracold atoms is first released from the harmonic trap. The interaction between atoms is tuned to weak interacting regime in order to make a ballistic expansion. After a time of flight $\Delta t$, the position of the atoms is proportional to the momentum of the atoms in the initial cloud $\mathbf{r} \sim h\mathbf{k}\Delta t/m$. Finally, an absorption image of the expanding cloud of atoms is taken by a probing laser (Fig. 1.10 left panel). The resulting image provides directly the distribution of the momentum space $N(\mathbf{k})$ (Fig. 1.10 right panel).

The time of flight imaging is a very powerful technique to probe the quantum gases. From the beginning of the ultracold atom field, it permitted to observe the Bose Einstein condensation [4]. The right panel of Fig. 1.10 shows how one can observe the BEC by time of flight technique. At high temperature $T = 400nK$, the thermal gas is characterized by the broad particle distribution in momentum space. When the temperature is smaller than a critical temperature $T_c$, a sharp peak of density emerging at zero momentum is an evidence of BEC. Otherwise, it can be combined with other techniques such as RF spectroscopy, Raman spectroscopy etc (discussed later in Chapter 2) in order to perform more sophisticated measurement.

### Measurement of Fermi surfaces by time-of-flight for weakly interacting cold fermions in an optical lattice

Another interesting observation by this technique is the imaging of the Fermi surface in a fermionic system. This experiment was realized in the Zürich group [67]. It is one of the milestones which fills the gap between ultracold atoms physics and condensed matter physics.

In this experiment, the mixture of bosonic $^{87}$Rb and fermionic $^{40}$K atoms was in a magneto-optical trap. For the magnetic trapping, they used the optical pumping to obtain the potassium in the $|F = 9/2, m_F = 9/2\rangle$ state and the rubidium in the $|F = 2, m_F = 2\rangle$ state. Applying the sympathetic cooling for the mixture, they obtained the potassium at a temperature of $T/T_F = 0.32$ ($T_F = 260nK$ is the Fermi temperature of non-interacting gas). After removing the rubidium atoms, they prepared a spin mixture with $(50\% \pm 4)$ in each of the $|F = 9/2, m_F = -9/2\rangle$ and $|F = 9/2, m_F = -7/2\rangle$ spin states by using two radio-frequency pulses. In order to reach a lower temperature, they performed an evaporative cooling. Finally, the mixture is brought to the temperature $T/T_F = 0.2$.

The lattice was switched off in a adiabatic way such that atoms still stay in the lowest band and the quasi-momenta are conserved. Then they took the time of flight absorption image. This image reflects the quasi-momentum distribution of atoms in the k-space divided in different Brillouin zones. As the density profile of atoms in the lattice depends on the harmonic

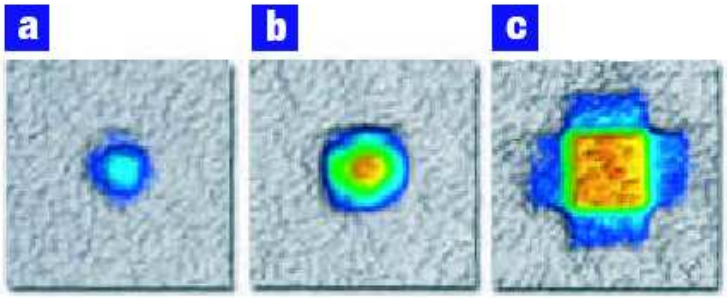


**Figure 1.11:** Imaging of non-interacting Fermi surfaces. Figures from left to right show the Fermi surface of the system with low filling (a), mediate filling (b) and high filling (c). The density of atom is simply controlled by the confining potential. Reprinted from Ref. [67]

---

confinement potential, the atom distribution is characterized by a the length $\zeta_\alpha = \sqrt{2t/m\omega_\alpha^2}$. Here, $\omega_\alpha$ is the harmonic confinement frequency in the direction $\alpha = x, y, z$. If the confinement is weak, the atoms are distributed in a broad region with low filling (Fig. 1.11a). In contrast, while the confinement is strong, the atoms are entirely filled the centered sites of the lattice with high density (Fig. 1.11 b and c). Therefore, the confinement potential helps to change the a normal state configuration to a band insulator configuration as shown in the Fig. 1.11.

### RF spectroscopy

The RF method was first introduced in 2003 by the JILA group for $^{40}$K [97, 112] and by the MIT group for $^{6}$Li [49]. The idea of the RF spectroscopy is illustrated in the Fig. 1.12 for

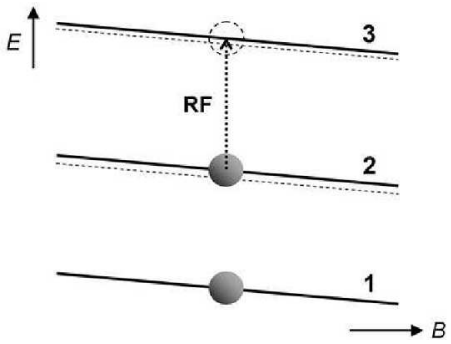


**Figure 1.12:** Illustration of RF spectroscopy for $^{6}$ Li. Atoms are prepared initially in the two hyperfine states $|1\rangle$ and $|2\rangle$. The RF pulse couples the two hyperfine states $|2\rangle$ and $|3\rangle$, therefore it probes only the atoms in the state $|2\rangle$. Fig is Reprinted from Ref. [48]

the Lithium 6. Initially, the mixture is prepared in two hyperfine states $|1\rangle$ and $|2\rangle$ and the third state $|3\rangle$ is empty. The RF pulse induces the transfer of atoms from state $|2\rangle$ to state $|3\rangle$. The transfer rate can be measured in experiment by the number of atoms appearing in the state $|3\rangle$ or the loss of atoms in the state $|2\rangle$. Remark that the third state has a short life-time because of the rapid decay due to the three body collision with state $|1\rangle$ and $|2\rangle$ [48]. Therefore, in the experiment of the Innsbruck group they measured the loss of atoms in the state $|2\rangle$ instead of atoms appearing in state $|3\rangle$.

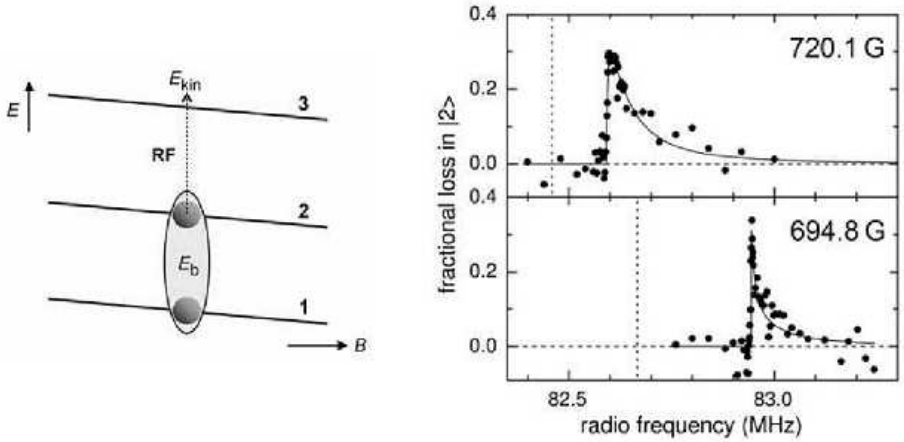


**Figure 1.13:** RF spectroscopy for weakly bound molecules in the fermionic mixture of $^6$ Li atoms. Left panel: Schema of the RF spectroscopy. Right panel: Experimental data of the RF spectrum for BCS phase. Reprinted from Ref. [48]

As an example, we present the experiment of RF spectroscopy on weakly bound molecules (Fig. 1.13) which is performed in the Innsbruck group [23]. In this experiment, in order to dissociate the pairing state the RF photon needs to provide an extra energy from the bare atomic transition frequency. As mentioned in [125], the RF spectroscopy makes a vertical transition in the momentum-space (with zero transfer momentum) of atoms in the state $|2\rangle$ to the state $|3\rangle$. If one supposes that the interaction between the third state $|3\rangle$ and the two initial states is negligible, the shift in the RF spectrum can be explained in basing on the a BCS description: $\omega - \omega_0 = \Delta^2/2\mu$ corresponding to the displacement of the lowest point in the energy dispersion. Hence, this RF shift does not directly measure the superfluid order [52, 66]. For the real experimental condition, the this interaction is not negligible. It was demonstrated that even taking in account the interaction effect, the RF shift is still proportional to the square of the gap $\omega - \omega_0 \propto \Delta^2$ [13].

Here, we have presented the usual form of the RF spectroscopy which conversely to the TOF technique gives some access to the frequency dependence of the one-particle spectral function, but not to its momentum dependence. We note that a novel RF spectroscopy recently realized in Jin's group with momentum-resolution. We postpone the detail discussion on this method in Chapter 2.

### 1.3.3 Two-particle correlation measurement

#### Bragg spectroscopy in BEC

The Bragg spectroscopic techniques are quite similar in spirit to what is done in condensed matter physics to probe the correlation function of local observables such as the local density or the local spin-density. The Bragg spectroscopy method was first realized by the MIT group [110, 111] in order to measure the density-density dynamical correlation function $\langle \rho(\mathbf{r}, t)\rho(\mathbf{r}', t')\rangle$ of a bosonic system. Later, theoretical studies in Ref. [16, 21] have shown that polarized light can also allow us to probe the spin-spin response $\langle S(\mathbf{r}, t)S'(\mathbf{r}', t')\rangle$ for fermionic systems. In condensed matter physics, analogous measurements can be done by light or neutron scattering.

In order to show the main idea of this spectroscopy method, we propose to analyze the experiment realized by the MIT group [111]. The scheme of the experiment is presented in

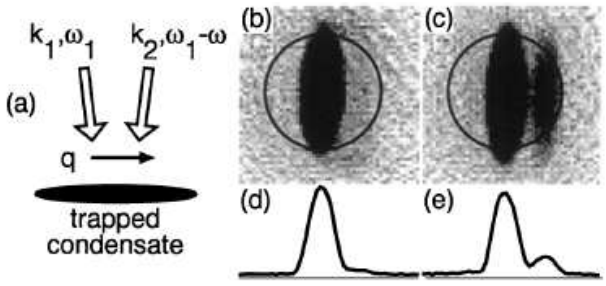


**Figure 1.14:** Bragg scattering scheme for measuring the density-density correlation function (experiment in MIT group [110]). The figure (a) shows the schema of the experiment. By using two laser beams with a transfer momentum $\mathbf{q} = \mathbf{k}_1 - \mathbf{k}_2$, they were able to excite a part of the condensate to the excited phonon modes. The figure (b) and (c) show the the absorption image and the column density of the initial condensate respectively. The figure (d) and (e) show the situation after the Bragg spectroscopy. In the absorption image (d), we find a picture with two parts in which the excited part is shifted to the right by the transfer momentum during the time-of-flight.

---

Fig. 1.14. Two laser beams of a transfer momentum $\mathbf{q} = \mathbf{k}_1 - \mathbf{k}_2$ and of a frequency difference $\omega = \omega_1 - \omega_2$ were used to focus on a Bose Einstein condensate. This frequency difference was chosen such that $\omega \ll \Delta$ with $\Delta$ the detuning from the atomic resonance. These two laser beams create a modulated potential $V_{mod} \propto \cos(\mathbf{q}.\mathbf{r} - \omega t)$ coupling to the atoms via the dipole interaction. In the second-quantized notation, this interaction is expressed by the Hamiltonian:

$$\hat{V}_{mod} = \frac{V}{2}[\hat{\rho}^\dagger(\mathbf{q})e^{-i\omega t} + \hat{\rho}^\dagger(-\mathbf{q})e^{i\omega t}]. \tag{1.27}$$

Here, $\hat{\rho}^\dagger(\mathbf{q}) = \sum_k \hat{a}^\dagger_{\mathbf{k}+\mathbf{q}}\hat{a}_{\mathbf{k}}$ is the Fourier transform of the atomic density operator at wave vector $\mathbf{q}$ and $V$ depends on the experimental parameters. The linear response of the many-body system can be estimated by the Fermi golden rule. For the ground-state $|g\rangle$ with energy $E_g$ the excitation rate is given by:

$$\frac{2\pi}{N\hbar}\sum_f |\langle f|\hat{\rho}^\dagger(\mathbf{q})|g\rangle|^2\delta(\hbar\omega - E_f + E_g) = 2\pi\omega_R^2 S(\mathbf{q},\omega), \tag{1.28}$$

where the excited states $|f\rangle$ have energy $E_f$ and $\omega_R = V/2\hbar$. The integration over all the frequency gives directly the static structure factor (Fourier transform of the density-density correlation function).

$$S(\mathbf{q}) = \langle g|\hat{\rho}(\mathbf{q})\hat{\rho}^\dagger(\mathbf{q})|g\rangle. \tag{1.29}$$

The right panel of Fig. 1.14 shows the time of flight image of a condensate undergone a Bragg scattering. After a long enough time of flight $\approx 70ms$, we see a part of condensate is transferred by a momentum given by Bragg scattering. This transfer momentum splits this excited part from the initial condensate. By integrating over the intensity of TOF image of the excited cloud, we obtain the total number of the transfer rate corresponding to the transfer momentum $\mathbf{q}$. This value is in fact proportional to the imaginary part of the two-particle response function or particularly the structure factor at zero temperature.

### Shot noise correlations

Shot noise correlation measurement for ultracold atoms has been proposed by Altman et al. [3] in inspiring the idea of the experiment of Hanbury Brown-Twiss [15]. Later different groups have realized measurements for various systems such as the Mott insulator state [37], the superfluid state [47] or tested the quantum properties like the bunching or anti-bunching for Bose gases and Fermion gases [60].

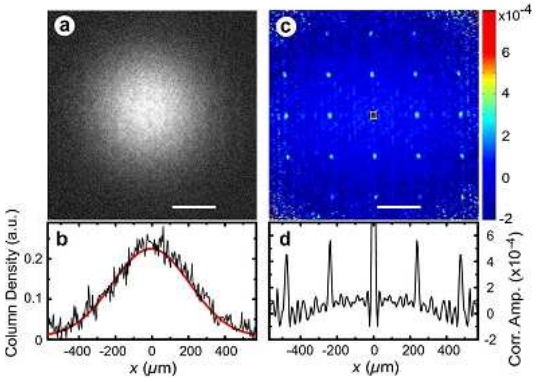


**Figure 1.15:** Single shot absorption image and the associated spatial correlation function. (a) Two-dimensional column density distribution of a Mott insulating phase. (b) Horizontal section (black line) through the center of the image in (a) and gaussian fit (red line) to the average over a set of 43 independent images. (c) Spatial noise correlation function obtained by analyzing the same set of images, which shows a regular pattern revealing the lattice order of the particles in the trap. (d) Horizontal profile through the center of the pattern, containing the peaks separated by integer multiples of lattice spacing. Reprinted from [37].

In a time of flight absorption image, one measures only the spatial distribution after a certain expansion time $t$. This distribution reflects the momentum distribution of the initial cloud of atoms $\langle n(\mathbf{r})\rangle_t \approx (2\pi m/\hbar t)\langle \hat{n}_{\mathbf{k}(\mathbf{r})}\rangle$ where the momentum $\mathbf{k}$ is related to the position $\mathbf{r}$ after time of flight $t$ by $\mathbf{k}(\mathbf{r}) = m\mathbf{r}/\hbar t$. However, in the absorption image (Fig. 1.15 a), we found that the density always fluctuates around some average value. To see that, we compare the density distribution of a single shot absorption image to the average density taken on a set of many picture (Fig. 1.15 b). These density fluctuations relate to a higher order correlation function which characterized by

$$\mathcal{G}(\mathbf{r},\mathbf{r}') = \langle \hat{n}(\mathbf{r})\hat{n}(\mathbf{r}')\rangle_t - \langle \hat{n}(\mathbf{r})\rangle_t\langle \hat{n}(\mathbf{r}')\rangle_t. \tag{1.30}$$

We can relate this correlation to the correlation function of the ground state before ballistic expansion in momentum space: $\mathcal{G}(\mathbf{r},\mathbf{r}') \propto \langle \hat{n}_{\mathbf{k}(\mathbf{r})}\hat{n}_{\mathbf{k}(\mathbf{r}')}\rangle - \langle \hat{n}_{\mathbf{k}(\mathbf{r})}\rangle\langle \hat{n}_{\mathbf{k}(\mathbf{r}')}\rangle$.

To analyze the fluctuation in experiments, the spatially averaged normalized density-density correlation function is defined as following

$$\mathcal{C}(\mathbf{d}) = \frac{\int d\mathbf{R}\langle \hat{n}(\mathbf{R}+\mathbf{d}/2)\hat{n}(\mathbf{R}-\mathbf{d}/2)\rangle_t}{\int d\mathbf{R}\langle \hat{n}(\mathbf{R}+\mathbf{d}/2)\rangle_t\langle \hat{n}(\mathbf{R}-\mathbf{d}/2)\rangle_t}, \tag{1.31}$$

in which $\hat{n}(\mathbf{r})$ is the column density obtained from a single absorption image. In fact, this two particles correlation measures the conditional probability of finding two particles at two positions separated by the vector $\mathbf{d} = \mathbf{r} - \mathbf{r}'$ over all the positions $\mathbf{R} = (\mathbf{r} + \mathbf{r}')/2$. To

compute the average value $\langle . \rangle$, a statistic average has been taken in a set of independently acquired images. For the Mott phase where the repulsive interaction sets the atomic density to exactly an integer number of atoms per lattice site, the direct absorption image gives no interference pattern because of lack of coherence ( Fig. 1.15 a,b). However, an analysis of the noise correlation gives a very well contrast regular pattern revealing the lattice order of particles in the trap (Fig. 1.15 c,d).

# Chapter 2

# Spectroscopy of one-particle excitations

*In this chapter, we address one of the aspects discussed in Chapter 1, namely the probes and the measurements of physical quantities in ultracold atom systems. We propose and demonstrate the possibility to use a Raman spectroscopy in order to probe the one particle Green's function. Different features of quasiparticles can be revealed from this method. Via some practical examples, we show also that the imaging of the Fermi surface can be obtained simply by measuring the Raman spectroscopy rate. The following Fig. 2.1 is an example of the simulated Fermi surface image for both non-interacting and strongly correlated systems. In the first part*

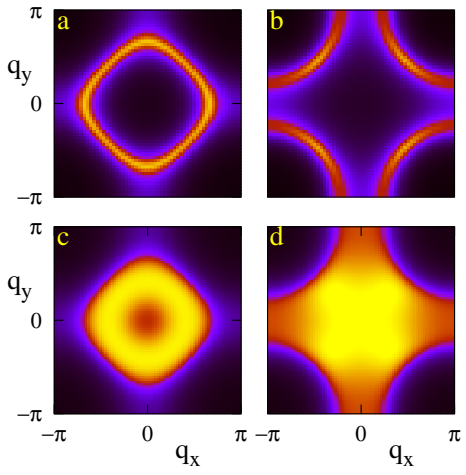


**Figure 2.1:** *Imaging the Fermi surface of ultracold atoms by Raman spectroscopy. The left panels are images of the Fermi surface for a homogeneous systems without interaction (up) or with strongly correlated (down). The right panels are images of the Fermi surface in the presence of confined trap.*

*of the chapter, we discuss the general formalism of the Raman spectroscopy in ultracold atom system. Next, we exploit different possibilities to measure the Fermi surface and the properties of one-particle excitations. We further analyze experimental aspects for commonly used atoms such as Lithium ($^6Li$) and Potassium ($^{40}K$). At the end, we summarize the first experimental realization of this spectroscopy by D. S. Jin's group and compared experimental results with numerical simulations taking account the trap potential.*

## 2.1 Single particle excitations

We will briefly recall in this section some fundamental conceptions of many-body physics. The concept of a quasiparticle excitation and the spectral function are essential for a description of the physics at low energy scale [1, 6, 83]. An indispensable experimental method, angular resolved photoemission spectroscopy (ARPES), for probing these quantities will be also discussed.

### 2.1.1 Low energies: Quasiparticle excitations

Most interacting fermion systems have low-energy excitations which are well-described by "Fermi liquid theory". In this description, the low-energy excitations are built out of quasiparticles, long-lived (coherent) entities carrying the same quantum numbers than the original particles. There are three key quantities characterizing the quasiparticle excitations:

- Their dispersion relation, i.e. the energy $\xi_{\mathbf{k}}$ (measured from the ground-state energy) necessary to create such an excitation with (quasi-) momentum $\mathbf{k}$. The interacting system possesses a Fermi surface (FS) defined by the location in momentum space on which the excitation energy vanishes: $\xi_{\mathbf{k}_F} = 0$. Close to a given point on the FS, the quasiparticle energy vanishes linearly as: $\xi_{\mathbf{k}} \sim \mathbf{v}_F(\mathbf{k}_F) \cdot (\mathbf{k} - \mathbf{k}_F) + \dots$. Here $\mathbf{v}_F$ is the local Fermi velocity at that given point of the Fermi surface.

- The spectral weight $Z_{\mathbf{k}} \leq 1$ carried by these quasiparticle excitations, in comparison to the total spectral weight ($= 1$, see above) of all one-particle excited states of arbitrary energy and fixed momentum.

- Their lifetime $\Gamma_{\mathbf{k}}^{-1}$. It is finite away from the Fermi surface, as well as at finite temperature. The quasiparticle lifetime diverges however at $T = 0$ as $\mathbf{k}$ gets close to the Fermi surface. Within Fermi liquid theory, this happens in a specific manner (for phase-space reasons), as $\Gamma_{\mathbf{k}}^{-1} \sim \xi_{\mathbf{k}}^2$. This insures the overall coherence of the description in terms of quasiparticles, since their inverse lifetime vanishes faster than their energy.

For a non-interacting system, the notion of quasiparticle excitations coincides exactly with the particle excitation. In this case, the spectral weight of the quasiparticle is 1 and the lifetime is infinite. By contrast, in the presence of strong correlations, some of these key quantities can be very different from the non-interacting system. Typical signatures of strong correlations are the following effects (not necessarily occurring simultaneously in a given system): i) strongly renormalized Fermi velocities, as compared to the non interacting (band) value, corresponding e.g. to a large interaction induced enhancement of the effective mass of the quasiparticles, ii) a strongly suppressed quasiparticle spectral weight $Z_{\mathbf{k}} \ll 1$, possibly non-uniform along the Fermi surface, iii) short quasiparticle lifetimes. These strong deviations from the non-interacting system can sometimes be considerable: the "heavy fermion" materials for example (rare-earth compounds) have quasiparticle effective masses which are several hundred times bigger than the mass from band theory, and in spite of this are mostly well described by Fermi liquid theory.

### 2.1.2 Green's function and spectral function

The Green's function is defined as the response function to the one-particle excitation while the spectral function is a function characterizing the decomposition of one single-particle excitation into the spectrum of all excited states. The coherent part in this decomposition characterizes the nature of quasiparticle excitations discussed above. For simplification, we

define these quantities at zero temperature. Assuming that at $T = 0$, the many-body system is in the ground state $|\phi_0^N\rangle$ of N particles, the Green's function is defined as

$$G(\mathbf{r}, t; \mathbf{r}', t') \equiv -i\langle\phi_0^N|Tc(\mathbf{r}, t)c^\dagger(\mathbf{r}', t')|\phi_0^N\rangle, \tag{2.1}$$

in which the $T$-product is the time order product[1]. For a time-independent Hamiltonian, the Green's function depends on the time difference $t - t'$ only. Remark that when $t - t' = 0$ the Green's function is simply the single particle density matrix. Assuming the translation invariance, the Green's function depends only on the relative distance $\mathbf{r} - \mathbf{r}'$. Therefore the Green function can be reduced to simple form $G(\mathbf{r}, t; \vec{0}, 0) = G(\mathbf{r}, t)$.

The physical interpretation of the Green's function is related directly to the concept of quasiparticles. Let us consider an initial system of N particles in the ground state $|\phi_0^N\rangle$ with energy $E_N^0$. The number of particles is controlled by the chemical potential $\mu$. At the instant $t = 0$, we extract a particle with momentum $\mathbf{k}$ from the initial system. The new wave function describing the N-1 particles system is $|\phi(t = 0)\rangle = c_\mathbf{k}|\phi_0\rangle$. In general, this wave function is not an eigenstate of the Hamiltonian. At time $t$, this state evolves to $|\phi(t)\rangle = e^{-i\hat{H}t}c_\mathbf{k}|\phi_0\rangle$ which is a linear combination of the whole excitation spectrum of N-1 particles. In order to observe the correlation of the single excitation with the initial N particles, we compare this wave function to the one describing N-1 particles in the ground state after having removed one particle at time $t$: $|\phi_e\rangle = c_\mathbf{k}e^{-i\hat{H}t}|\phi_0\rangle = e^{-i(E_N^0-\mu N)t}c_\mathbf{k}|\phi_0\rangle$. A natural way to compare these two wave functions is to compute their scalar product (the overlap of these waves functions). The overlap is nothing else than the Green's function defined above at time $t > 0$

$$\langle\phi_e|\phi(t)\rangle = \langle\phi_0^N|e^{i\hat{H}t}c_\mathbf{k}^\dagger e^{-i\hat{H}t}c_\mathbf{k}|\phi_0^N\rangle = iG(\mathbf{k}, -t). \tag{2.2}$$

For a non-interacting system, the state with a less particle is also an eigenstate of the total Hamiltonian with energy $E_{N-1}^*$. The corresponding wave function evolves coherently into the same state and only changes its phase with time $|\phi(t)\rangle = e^{-i[E_{N-1}^*-\mu(N-1)]t}c_\mathbf{k}|\phi_0^N\rangle$ and does not decay to any other excited states. The Green's function is thus a simple phase $e^{-i(E_{N-1}^*-E_N^0+\mu)t}$.

For a system with interaction, the wave function of the $N-1$ particles after a time $t$ is a decomposition on all the eigenstates $|\phi_\alpha^{N-1}\rangle$ of the $N-1$ particles. In order to evaluate the expression for the Green's function, we take a decomposition of the initial state $c_\mathbf{k}|\phi_0^N\rangle$ onto the basis of system (N-1)-particles with all the eigenstate $|\phi_\alpha^{N-1}\rangle$. The probability to find the system at the excited state $|\phi_\alpha^{N-1}\rangle$ of energy $E_{N-1}^\alpha - (N-1)\mu$ is $|\langle\phi_0|c_\mathbf{k}^\dagger|\phi_\alpha^{N-1}\rangle|^2$. We define then the spectral function as a measurement of this weight over the whole range of energy

$$A(\mathbf{k}, \omega) = \sum_\alpha |\langle\phi_0^N|c_\mathbf{k}^\dagger|\phi_\alpha^{N-1}\rangle|^2\delta(\omega + \mu + E_{N-1}^\alpha - E_N^0). \tag{2.3}$$

The frequency contributions are given by $\omega = E_N^0 - E_{N-1}^\alpha - \mu$ which is negative. Remark that in the opposite case where we inject one particle, the new state has a decomposition on the basis $\{|\phi_\beta^{N+1}\rangle\}$ of system with N+1 particles leading to the frequency $\omega = E_{N+1}^\alpha - E_N^0 - \mu > 0$ (the energy of the excitation measured from the ground state of $N$ particle). Our state $|\phi(t)\rangle$ can be now written in this spectral decomposition

$$|\phi(t)\rangle = \sum_\alpha \langle\phi_\alpha^{N-1}|c_\mathbf{k}|\phi_0^N\rangle\ \rangle \times e^{-i[E_{N-1}^\alpha-\mu(N-1)]t}|\phi_\alpha^{N-1}. \tag{2.4}$$

Therefore, the overlap of two wave functions now is $\sum_\alpha e^{-i(E_{N-1}^\alpha-E_N^0+\mu)t}|\langle\phi_0^N|c_\mathbf{k}^\dagger|\phi_\alpha^{N-1}\rangle|^2$. This quantity is no longer a simple phase and decreases in time. At $t = 0$, there is no phase

[1]The time order product is defined as $Tc(\mathbf{r}, t)c^\dagger(\mathbf{r}', t') \equiv \theta(t - t')c(\mathbf{r}, t)c^\dagger(\mathbf{r}', t') - \theta(t' - t)c^\dagger(\mathbf{r}', t')c(\mathbf{r}, t)$.

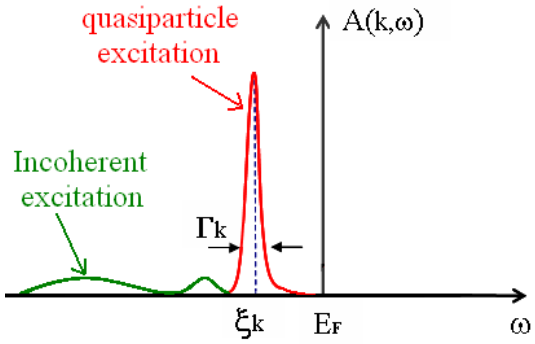


**Figure 2.2:** Spectral function of an interacting system that measures the weight in a decomposition on a basis of "N-1" particles. Here, the peak centered at energy $\xi_{\mathbf{k}}$ represents the quasiparticle coherent excitation with the lifetime $\Gamma_{\mathbf{k}}^{-1}$ while the broad part represents the incoherent excitation part. The Fermi energy $E_F$ is the last level up to what the fermions are filled.

difference between the contributed terms in the sum, then the overlap is 1. When $t$ is small, the difference of phase between the terms is small and the amplitude of the overlap decreases. At long time, all the phases can become incoherent and the sum can tend to zero. The rate at which phase coherence is lost depends on the distribution of the spectral weight $A(\mathbf{k}, \omega)$. If the spectral weight is very localized around one excitation level with a width $\Gamma_{\mathbf{k}}$, so the typical time after which we loose the coherence (or the particle character) is $\tau = \Gamma_{\mathbf{k}}^{-1}$. This characteristic time scale is called the time of life of the excitation[2]. Below this time scale, this excitation is well-defined as a quasiparticle excitation.

The quasiparticle description applies only at low energy, below some characteristic energy (and temperature) scale $T_F^*$ , the quasiparticle coherence scale. Close to the Fermi surface, the one-particle spectral function displays a clear separation of energy scales, with a sharp coherent peak carrying spectral weight $Z_{\mathbf{k}}$ corresponding to quasiparticles (a peak well-resolved in energy means long-lived excitations), and an "incoherent" background carrying spectral weight $1 - Z_{\mathbf{k}}$. A convenient form to have in mind (Fig. 2.2) is

$$A(\mathbf{k}, \omega) \simeq Z_{\mathbf{k}} \frac{\Gamma_{\mathbf{k}}}{\pi[(\omega - \xi_{\mathbf{k}})^2 + \Gamma_k^2]} + A_{\text{inc}}(\mathbf{k}, \omega). \tag{2.5}$$

Hence, measuring the spectral function, and most notably the evolution of the quasiparticle peak as the momentum is swept through the Fermi surface, allows one to probe the key properties of the quasiparticle excitations: their dispersion (position of the peak), lifetime (width of the peak) and spectral weight (normalized to the incoherent background, when possible), as well of course as the location of the Fermi surface of the interacting system in the Brillouin zone.

### 2.1.3 Measuring spectral function by photoemission in solid state physics

In condensed matter physics, angle-resolved photoemission spectroscopy (ARPES) provides a direct probe of the one-particle spectral function (for a pedagogical introduction, see [27]). This technique has played a key role in revealing the highly unconventional nature of single-particle excitations in cuprate superconductors [28]. It consists in measuring the energy and

[2]The spectral function is a $\delta$-function, so $\Gamma_{\mathbf{k}} = 0$ and the time of life of particle is infinite. At long time, there is no lost of coherence and the Green's function has no decay.

momentum of electrons emitted from the solid exposing to an incident photon beam (Fig. 2.3). In the simplest approximation, the emitted intensity is directly proportional to the single-electron spectral function (multiplied by the Fermi function and by some matrix elements). We can describe the system at the initial state and the final state as follows:

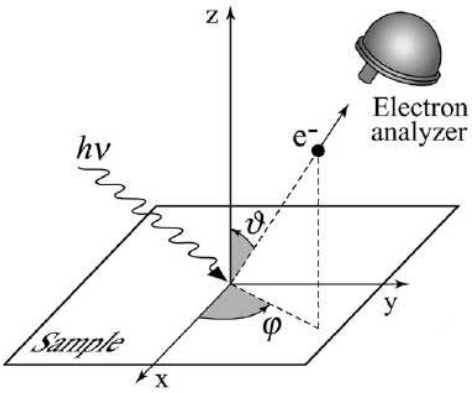


**Figure 2.3:** Scheme of the photoemission process in which a photon $h\nu$ is sent to the sample. The photon excites the system and extract an electron out off the system. The out-going electron is detected with angle resolved $(\varphi, \vartheta)$ by the electron analyzer. Reprinted from Ref. [27].

- Initial state made of photon with energy $\hbar\omega_p$, momentum $\mathbf{p}$ and the solid system with energy $E_i^N$, total momentum $\vec{0}$
- Final state made of photoelectron with energy $E_{\text{kin}}$, momentum $\mathbf{K}$ and the solid system with energy $E_f^{N-1}$ and total momentum $-\mathbf{k}$. In order to kick the electron out of the system, the incident photon needs to provide an energy to overcome the work of the surface $\phi$.

The conservation of energy is equivalent to the resonance condition of the photoemission process

$$E_i^N + \hbar\omega_p = E_{kin} + \phi + E_f^{N-1}, \tag{2.6}$$

which means that in the spectral function we measure the energy defined by

$$\hbar\omega = E_i^N - E_f^{N-1} = E_{\text{kin}} + \phi - \hbar\omega_p. \tag{2.7}$$

For the conservation law in momentum, only the momentum in the direction parallel to the surface of the sample is conserved: $\mathbf{K}_{\parallel} = \mathbf{k}_{\parallel} = \hbar^{-1}\sqrt{2mE_{\text{kin}}}\sin\theta$. The perpendicular component is derived by the energy conservation: $\mathbf{k}_{\perp} = \hbar^{-1}\sqrt{2m(E_{\text{kin}}\cos^2\theta + V_0)}$

### Non-interacting electron gases

The ARPES spectrum measures all the excitations of negative energy because the out-going electron was initially lying below the Fermi level. For the simple case of a non-interacting gas, Fig. 2.4 (left side) shows the region in the plan $(\mathbf{k}, E)$ with non-zero signal. All the single particle excitations are eigenstate of the free Hamiltonian. Therefore the spectral function $A(\mathbf{k}, E)$ is a $\delta$-peak (Fig. 2.4 right side).

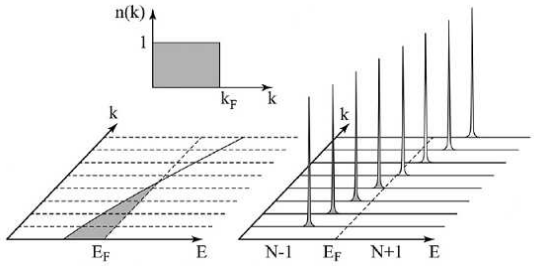


**Figure 2.4:** Example of a non-interacting gas. Left panel (down) shows the intensity of emitted ARPES signal in the plane of $(E, \mathbf{k})$ near the Fermi surface while in the upper panel, we see a sharp jump with amplitude $Z = 1$ in the density distribution. Right panel represents the spectral functions of quasiparticle excitations of different energies. They consist of a well-defined delta-peak with infinite lifetime. Reprinted from Ref. [27].

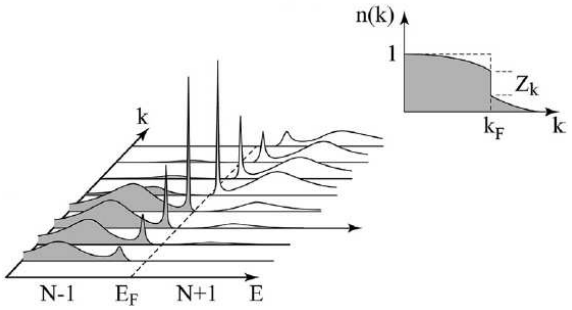


**Figure 2.5:** Same as Fig. 2.4 for a Fermi liquid. The left panel shows the spectral function in which the coherent part is the quasiparticle excitation with the renormalization of spectral weigh $Z_{\mathbf{k}} < 1$ . The jump present in the momentum distribution is no longer 1 (upper panel on the right). The lower panel on the right shows the experimental data of the photoemission. The intensity of out-going atoms measured by the electron analyzer is plotted versus the their kinetic energy in the selected direction $0 - 0$. Reprinted from Ref. [27].

---

**Interacting gases: Fermi liquid quasiparticles**

The Fig. 2.5 shows another system which is described by the Fermi liquid theory. As discussed in the last section, in the spectral function we find a coherent part at low energy which looks like an one-particle excitation in the non-interacting gas but with a smaller weight. The remaining part of the spectral weight is transferred to the incoherent part at high energy. The closer we approach the Fermi level (Fermi surface) the better the quasiparticle is defined.

## 2.2 Measurement of one particle excitation by Raman spectroscopy in ultracold atoms

Similarly to the ARPES measurement described above, we propose here to use stimulated Raman spectroscopy [30] as a probe of one-particle excitations in a two-component mixture of ultracold fermionic atoms. By this measurement, the frequency and momentum dependence of the spectral function can be observed.

### 2.2.1 Raman spectroscopy

Stimulated Raman spectroscopy has been considered previously in the context of cold atomic gases, both as an out-coupling technique to produce an atom laser [51] and as a measurement technique for bosons [59, 81, 84] and fermions [31, 118]. In the Raman process of Fig. 2.6, atoms are transferred from $\alpha$ into another internal state $\beta \neq \alpha, \alpha'$, through an intermediate excited state, using two laser beams of wave-vectors $\mathbf{k}_1, \mathbf{k}_2$ and frequencies $\omega_{1,2}$. If $\omega_{1,2}$ is sufficiently far from single photon resonance to the excited state (i.e. $\omega_1$, $\omega_2$ not close to $\varepsilon_\beta - \varepsilon_\alpha$), we can neglect spontaneous emission. The atom-laser interaction is described by

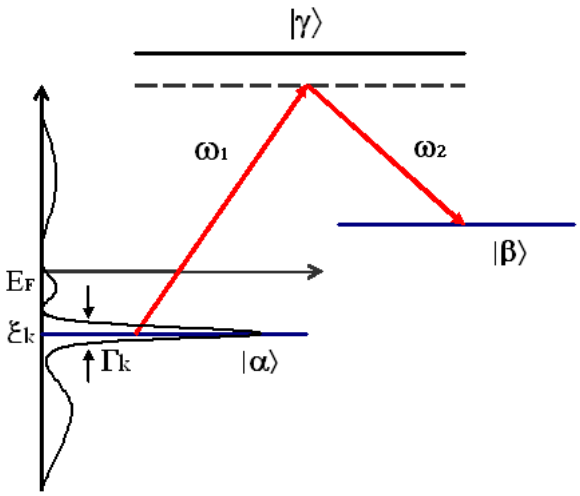


**Figure 2.6:** Raman process: transfer from an internal state $\alpha$ to another internal state $\beta$ through an excited state $\gamma$. The momentum-resolved spectral function is schematized, consisting of a quasiparticle peak and an incoherent background.

the interaction between the dipole moment of atoms and the electromagnetic field of laser beams: $V_{\text{dip}} = -\mathbf{D}.\mathbf{E}(\mathbf{r})$. The dipole moment matrix and the laser field are defined as

$$\mathbf{D} = \mathbf{d}_{\alpha\gamma}|\gamma\rangle\langle\alpha| + \mathbf{d}_{\beta\gamma}|\gamma\rangle\langle\beta| + \text{h.c}, \quad \mathbf{E}(\mathbf{r}) = i\sum_\lambda \sqrt{\hbar\omega_\lambda/2\epsilon_0 L^3}\ \epsilon\ (a_\lambda e^{i\mathbf{k}_\lambda \mathbf{r}} - a_\lambda^\dagger e^{-i\mathbf{k}_\lambda \mathbf{r}}).$$

Here, the laser field couple these two hyperfine states $|\alpha\rangle$, $|\beta\rangle$ of the mixture to the continuum of state $|\gamma\rangle$ by the matrix element $\mathbf{d}_{\alpha\gamma}$, $\mathbf{d}_{\beta\gamma}$. $a_\lambda^\dagger$ is the creation operator of the photon mode $\lambda$ ($\lambda = 1, 2$) with momentum $\mathbf{k}$. In this description, $L^3$ is just a mathematical object chosen as the volume of the quantized box in the real space. The continuum limit is obtained by taking the limit $L \to \infty$. Later, we'll show that the only important quantity is the density of photon $n_i = N_i/L^3$. $\epsilon_0$ is the dielectric constant of the vacuum. Using the rotating field approximation and eliminating the intermediate state $|\gamma\rangle$, thus we obtain a simple form of the interaction potential

$$V = \frac{C}{L^3}|\alpha\rangle\langle\beta|a_1^\dagger a_2 e^{i(\mathbf{k}_1 - \mathbf{k}_2).\vec{r}} + \text{h.c.} \tag{2.8}$$

Here, $C$ is a constant depending on the dipole matrix elements $\mathbf{d}^*_{\gamma\alpha}$, $\mathbf{d}_{\beta\gamma}$ and the mode $\omega_\lambda$. In the second quantization, this potential can be expressed as a summation over the real space of the field operator of creation and annihilation of an atom $\psi^\dagger_{\alpha,\beta}$, $\psi_{\alpha,\beta}$. Therefore, the coupling between these two modes $\omega_1$, $\omega_2$ with the atoms fields $\psi_{\alpha,\beta}$ is described by the potential

$$\hat{V} = \frac{C}{L^3}\int \mathbf{d}^3\mathbf{r}\psi^\dagger_\alpha(\mathbf{r})\psi_\beta(\mathbf{r})e^{i(\mathbf{k}_2 - \mathbf{k}_1).\mathbf{r}}a_1^\dagger a_2 + \text{h.c.} \tag{2.9}$$

Let us now consider a system of interacting cold atoms initially prepared in the internal state $|\alpha\rangle, |\alpha'\rangle$. The interaction strength is controlled by the two-body s-wave scattering length via the Feshbach resonance. The Raman scattering transfers a fraction of the initial atoms into the third internal state $|\beta\rangle$ conserving the momentum and energy of the whole system "atom+light". The total transfer rate to state $\beta$ can be calculated [11, 59, 81] using the Fermi golden rule

$$\mathbf{R} = \frac{2\pi}{\hbar}\sum_f |\langle f|\hat{V}|i\rangle|^2\delta(E_f - E_i) = \frac{1}{\hbar}\int_{-\infty}^{\infty}\langle i|\tilde{V}(t)\tilde{V}(0)|i\rangle dt,$$

where $\tilde{V}(t) = e^{i\hat{\mathbf{H}}t/\hbar}\hat{V}e^{-i\hat{\mathbf{H}}t/\hbar}$ is the time-dependent Heisenberg representation of the interaction. $H$ is the total Hamiltonian. In order to decouple the correlation between the two states $\alpha$ and $\beta$, we assume that no atoms are initially present in $\beta$ and that the scattered atoms in $\beta$ do not interact with the atoms in the initial $\alpha, \alpha'$ states. We discuss later on the appropriate experimental conditions. Under this assumption the general Hamiltonian reads

$$\hat{\mathbf{H}} = \hat{H}_\alpha + \hat{H}_\beta \tag{2.10}$$

Here $\hat{H}_\alpha$ is the one which describes the interacting system of two component fermionic mixture in the initial states $|\alpha\rangle, |\alpha'\rangle$. The time-evolution operator can be decoupled as $e^{i\hat{\mathbf{H}}t/\hbar} = e^{i\hat{H}_\alpha t/\hbar} \times e^{i\hat{H}_\beta t/\hbar}$. The Hamiltonian $\hat{H}_\beta$ describes the atoms in the internal state $|\beta\rangle$ which undergo an external potential reads

$$\hat{H}_\beta = \int \mathbf{d}^3\mathbf{r}\varepsilon_\beta\hat{n}_\beta(\mathbf{r}) + \frac{\hbar^2}{2M}\int \mathbf{d}^3\mathbf{r}|\nabla\psi_\beta|^2 + \int \mathbf{d}^3\mathbf{r}V_\beta(\mathbf{r})\hat{n}_\beta(\mathbf{r}). \tag{2.11}$$

Here, $\varepsilon_\beta$ is the internal energy of the internal $\beta$-state. The potential $V_\beta(\mathbf{r})$ consist of two part: i) $V_{\text{trap}}$ the confined trap potential (magnetic or optic trap), ii) $V_{\text{lat}}$ the potential of optical lattice. By convention, the energy of the hyperfine state$|\alpha\rangle$ is fixed to zero ($\varepsilon_\alpha = 0$).

Let us calculate the term $\langle i|\tilde{V}(t)\tilde{V}(0)|i\rangle$ which appears in the transferred rate as given by Fermi's golden rule. Under the initial conditions, we start with a "atom+light" state with $N_\alpha$ atom in the internal state $\alpha$, no atom in the state $\beta$ and the laser lights populated in two mode $\omega_1, \omega_2$ with the populations $N_1, N_2$: $|i\rangle = |N_\alpha, 0_\beta, N_1, N_2\rangle$. This quantity can be calculated by applying the different operators for atoms and light to respected parts of the initial state $|i\rangle = |N_\alpha, 0_\beta, N_1, N_2\rangle$

$$\langle i|\tilde{V}(t)\tilde{V}(0)|i\rangle = \frac{|C|^2}{L^6}N_1(N_2+1)\int \mathbf{d}^3\mathbf{r}\mathbf{d}^3\mathbf{r}'e^{i(\Omega t - \mathbf{q}.\Delta\mathbf{r})}g(\mathbf{r},\mathbf{r}';t)\langle N_\alpha|\psi_\alpha^\dagger(\mathbf{r},t)\psi_\alpha(\mathbf{r}',0)|N_\alpha\rangle. \tag{2.12}$$

Here, we set $\Delta\mathbf{r} = \mathbf{r} - \mathbf{r}'$, $\mathbf{q} = \mathbf{k}_1 - \mathbf{k}_2$ the momentum difference of the two laser modes. The free propagator for $\beta$-state atoms in vacuum is to be taken: $g_\beta(\mathbf{r},\mathbf{r}';t) \equiv \langle 0_\beta|\,\psi_\beta(\mathbf{r},t)\psi_\beta^\dagger(\mathbf{r}',0)|0_\beta\rangle$. We define the frequency $\Omega$ as

$$\Omega = \omega_1 - \omega_2 + \mu, \tag{2.13}$$

with $\mu$ is the chemical potential used to fix initial total number of the mixture in $\alpha$ and $\alpha'$ states. In this notation, we absorb $\mu$ into the definition of frequency in Raman rate. Defining the density of photons in two modes $n_i = N_i/L^3$ and taking the continue limit, the expression of the Raman transfer rate finally reads

$$\mathbf{R}(\mathbf{q},\Omega) = \frac{|C|^2 n_1 n_2}{\hbar}\int_{-\infty}^{\infty}dt\int \mathbf{d}^3\mathbf{r}d^3\mathbf{r}'e^{i(\Omega t - \mathbf{q}.\Delta\mathbf{r})}g(\mathbf{r},\mathbf{r}';t)\langle N_\alpha|\psi_\alpha^\dagger(\mathbf{r},t)\psi_\alpha(\mathbf{r}',0)|N_\alpha\rangle. \tag{2.14}$$

The correlation function entering (Eq. 2.14) is proportional to the one-particle Green's function $\langle N_\alpha|\psi^\dagger_\alpha(\mathbf{r},t)\psi_\alpha(\mathbf{r}',0)|N_\alpha\rangle = -iG^<_\alpha(\mathbf{r}',\mathbf{r},-t)$ of the strongly interacting Fermi system. The superscript $<$ indicates that $\psi^\dagger$ is always to the left of $\psi$. Operators are evolved in the grand-canonical ensemble [1, 83]. The formalism obtained for Raman spectroscopy until now is general and applicable for any system. The Raman transfer rate contains information about the one-particle Green's function of the interacting atoms in $\alpha$-states. However, it is a complicate expression which concerns a convolution of the free propagator $g(\mathbf{r},\mathbf{r}';t)$ of atoms in the $\beta$-state with the Green's function. From Eq. 2.14, it is clear that a full determination of the one-particle Green's function requires measuring the rate $R(\mathbf{q},\Omega)$ for a large enough set of wavevectors $\mathbf{q}$ and frequency shifts $\Omega$ such that an inverse Fourier transform can be performed. Division by the known expression of $g_\beta$ would then yield the Green's function. This seems an ambitious task however. We rather examine whether useful information can be extracted directly from the measured Raman intensity $R(\mathbf{q},\Omega)$. In the next sections, we discuss two possibilities to probe directly the properties of one-particle excitations from Raman rate.

Ultracold atomic systems are always obtained within a confined potential (magnetic or optical trap). Moreover, if we have an optical lattice, the gaussian profile of the laser beams will induce also an additional harmonic potential. We propose to study first the two possibilities of measurement in the context of the homogeneous system then address the case with presence of the confined potential by the local density approximation (LDA).

### 2.2.2 Measurement principles for homogeneous system

In a homogeneous system, we can exploit the translation invariance in order to simplify the expression of Raman transfer rate. In this homogeneous case, the translation invariance is conserved thus we can effectuate Fourier transform into the momentum space. The expression 2.14 can be written as

$$\begin{aligned}\mathbf{R}(\mathbf{q},\Omega) &= i\frac{|C|^2 n_1 n_2}{\hbar}\int dt\int \mathbf{d}^3\mathbf{r}\mathbf{d}^3\mathbf{r}' e^{i[\Omega t-\mathbf{q}.(\mathbf{r}-\mathbf{r}')]}g(\mathbf{r}-\mathbf{r}',t)G^<_\alpha(\mathbf{r}',\mathbf{r},-t)\\ &= \frac{|C|^2 n_1 n_2}{(2\pi)^3\hbar}\int \mathbf{d}^3\mathbf{k}\; n_F(\varepsilon_{\beta\mathbf{k}}-\Omega)A(\varepsilon_{\beta\mathbf{k}}-\Omega,\mathbf{k}-\mathbf{q}).\end{aligned}$$

For the atoms in the $\alpha$-state, the Green's function has been expressed in terms of the spectral function and the Fermi factor $n_F$ as [1, 83]: $G^<_\alpha(\mathbf{k},\omega) = i\,n_F(\omega)\,A(\mathbf{k},\omega)$. As usual in the solid state literature, single-particle energies $\xi^0_\mathbf{k} = \varepsilon_{\mathbf{k}\alpha} - \mu$ for the $\alpha$ state (as well as the frequency $\omega$) are here measured from the chemical potential, i.e. the Fermi energy, at $T = 0$. As atoms in the $\beta$-state do not interact with the rest of the system, their non-interaction Green's function reads: $G_\beta(\mathbf{k},t) = -i[\theta(\varepsilon_{\beta\mathbf{k}})\theta(t)e^{-i\varepsilon_{\beta\mathbf{k}}t} - \theta(-\varepsilon_{\beta\mathbf{k}})\theta(-t)e^{i\varepsilon_{\beta\mathbf{k}}t}]$ thus the propagator $g(\mathbf{r},t)$ in (Eq. 2.14) reads

$$g(\mathbf{r},t) = \int \frac{\mathbf{d}^3\mathbf{k}}{(2\pi)^3}e^{i(\mathbf{k}.\mathbf{r}-\varepsilon_{\beta\mathbf{k}}t)}. \tag{2.15}$$

Hence, the Raman spectroscopy gives access to the spectral function $A(\omega,\mathbf{p})$ in which the energy of single particle excitation and the momentum are measured by $\omega = \varepsilon_{\beta\mathbf{k}}-\Omega$, $\mathbf{p} = \mathbf{k}-\mathbf{q}$. Moreover, this expression the appearance of the Fermi-Dirac factor fixes a cut-off in energy or a threshold of measurable signal as we discuss later in more detail. In the later of this section, we will discuss two possible measurements which help to access directly to the one particle correlation function.

### Conservation laws and spectral function

Let us now discuss the conservation laws present the Raman scattering process. In this measurement, our system is prepared in the initial state with two lasers fields $\omega_1$ and $\omega_2$ and a mixture of ultracold atoms prepared in two hyperfine states $\alpha\rangle$ and $\alpha'\rangle$. In the final state, the system has one less $\alpha$-atom and one more atom in the third hyperfine state $|\beta\rangle$.

- Initial state made of : i) an ensemble of $N_\alpha$ atoms with energy $E_i^{N_\alpha}$, total momentum $\vec{0}$, ii) $N_1$ photons of frequency $\omega_1$ and momentum $\mathbf{k}_1$, ii) $N_2$ photons of frequency $\omega_2$ with momentum $\mathbf{k}_2$.

- Final state made of: i) an ensemble of $N_\alpha - 1$ atoms with energy $E_f^{N_\alpha - 1}$, total momentum $-\mathbf{p}$, ii) one atom in the internal state $\beta$ with energy $\varepsilon_{\beta\mathbf{k}}$, momentum $\mathbf{k}$, iii) $N_1 - 1$ photons $\omega_1$, $\mathbf{k}_1$, iv)$N_2 + 1$ photon $\omega_2$, $\mathbf{k}_2$.

The conservation of energy gives us the relation

$$E_i^{N_\alpha} + N_1\hbar\omega_1 + N_2\hbar\omega_2 = E_f^{N_\alpha - 1} + \varepsilon_{\beta\mathbf{k}} + (N_1 - 1)\hbar\omega_1 + (N_2 + 1)\hbar\omega_2. \tag{2.16}$$

The energy measured in the spectral function is then defined by

$$\hbar\omega = E_i^{N_\alpha} - E_f^{N_\alpha - 1} - \mu = \varepsilon_{\beta\mathbf{k}} - \Omega, \tag{2.17}$$

where $\Omega = \omega_1 - \omega_2 + \mu$ is introduced in order to shift the energy reference to the Fermi level.

For the conservation law of momentum, we have the total momentum is conserved

$$\vec{0} = -\mathbf{p} + \mathbf{k} + \mathbf{k}_2 - \mathbf{k}_1. \tag{2.18}$$

Let us define $\mathbf{q} = \mathbf{k}_1 - \mathbf{k}_2$, so the momentum measured in the spectral function is: $\mathbf{p} = \mathbf{k} - \mathbf{q}$. The present situation is more favorable than the photoemission case because we do not have the surface effect, which in ARPES prevents momentum conservation in the perpendicular direction.

### Measurement of total Raman rate by varying q

Let us now consider the first experimental scheme which allows to probe the physical properties of low energy excitations near the Fermi surface. Assuming that the out-going atoms stay in the lattice, therefore the energy dispersion reads $\varepsilon_{\beta\mathbf{k}} = \varepsilon_\beta - 2t_\beta \sum_\mu \cos \mathbf{k}_\mu$.

Here, we briefly show that it is possible to exploit directly the image of the Fermi surface and the information about the quasiparticle excitation near the Fermi surface from the measurement of Raman transfers rate near the threshold of extinction of signal. In the next sections 2.3 and 2.4, we discuss in more detailed this measurement via concrete examples. As shown in the Fig. 2.7, when the frequency difference $\omega_1 - \omega_2$ is small than the distance $\varepsilon_\beta - \mu$ from the lowest level in the $\beta$-branch to the Fermi level of the many-body system in $\alpha$-state, there is no measurable Raman signal. As far as the frequency difference becomes greater than this threshold, we start to have the first signal which measures the excitation around the Fermi surface. Fixing the probed frequency around this threshold $\Omega \approx \Omega_T = \varepsilon_\beta$ and making a $\mathbf{q}$-resolved measurement, the topography of the Fermi surface can be observed. We can vary the module $|\mathbf{q}|$ in the interval $[0, 2|\mathbf{k}_0|]$ by controlling the direction of the two laser beams. The difference of the frequency can be changed in the order of the band width of the spectral density of the system expected to be measured.

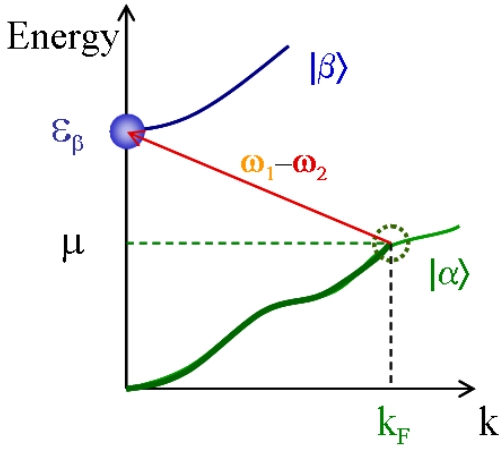


**Figure 2.7:** Measurement at the threshold frequency of extinction. Atoms initially prepared in the $\alpha$-states are filled up to Fermi momentum $\mathbf{k}_F$ corresponding to the Fermi level $E_F = \mu$. We perform the Raman spectroscopy with resolved transfer momentum $\mathbf{q}$ and a fixed Raman frequency near the threshold of extinction $\omega_1 - \omega_2 + \mu \approx \varepsilon_\beta$. This process brings atoms close to the Fermi level of the $\alpha$-branch to the lowest level of the $\beta$-branch.

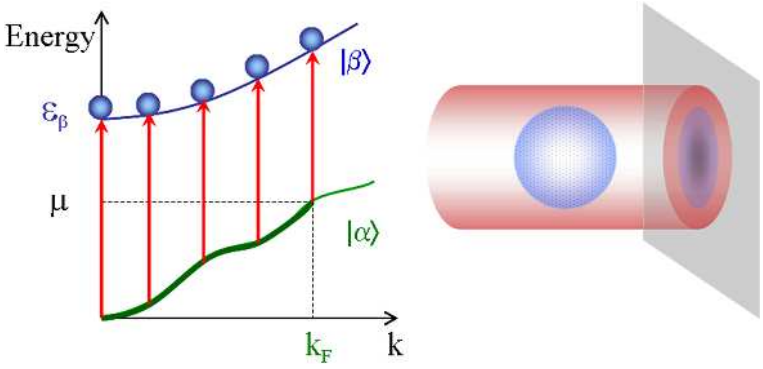


**Figure 2.8:** Example of selective time of fight imaging for the $\beta$-state. In this experiment, we first apply a vertical Raman transition with $\mathbf{q} = 0$ (left panel) then take the selective time of flight absorption image of the expanding cloud of $\beta$-atoms (right panel).

---

### Measurement at fixed laser momentum by time of flight imaging

In experiment, we can envisage to measure the momentum distribution of the out-going atoms by taking a selective time of flight image (TOF). The scheme of the experiment is illustrated in the Fig. 2.8. We propose to do a Raman spectroscopy with a fixed momentum difference of the probed lasers $\mathbf{q}$ =const and to take a TOF picture of the expanding atoms in the $\beta$-state. Repeating the experiment for different frequencies, we are able to make a scan in frequency. From the TOF momentum distribution, we can extract the Raman rate as a function of the momentum $\mathbf{k}$ of the scattered atoms. The Raman rate measured in each direction is proportional to the intensity of the TOF image. If the particles in $\beta$-state are free, their energy is determined by their momentum, $\varepsilon_{\beta\mathbf{k}} = \varepsilon_\beta + \hbar^2\mathbf{k}^2/2M$ (i.e they do not see the trap or optical lattice). In this case, the rate of transition to internal state $|\beta\rangle$ is measured

selectively in the momentum $|\mathbf{k}\beta\rangle$ (i.e. this is the momentum of the atoms in the $\beta$-state). With a fixed value of $\mathbf{q}$, we obtain the Raman rate in the direction of the momentum $\mathbf{k}$ of out-going atoms

$$\mathbf{R}_{\mathbf{q}}(\mathbf{k},\Omega) = \frac{|C|^2 n_1 n_2}{\hbar}\, n_F(\varepsilon_{\beta\mathbf{k}} - \Omega) A(\varepsilon_{\beta\mathbf{k}} - \Omega, \mathbf{k} - \mathbf{q}). \tag{2.19}$$

Here, we remind that the Raman frequency is defined as $\Omega = \omega_1 - \omega_2 + \mu$. The described measurement is very similar to ARPES. In addition, we do not encounter some well-known problem in ARPES like non-conservation of total momentum and the surface effect.

Another way to realize this time of flight measurement is RF spectroscopy. This spectroscopy method is equivalent with fixed momentum $\mathbf{q} = 0$ Raman spectroscopy. In order to make the transition to the third internal state, we can apply a RF pulse which couples directly the $\alpha$-state to the $\beta$-state. The RF field has a very long wave length so the momentum transfer is negligible. The RF field is essentially constant over the size of the sample, thus the entire system is simultaneously addressed by the same coupling.

**Summary**

Finally, we would like to summarize in Table 2.1 the three described methods for measuring the one-particle excitations in the following table. By exploring directly the experimental data of Raman spectroscopy, we can have access to the properties of quasiparticle excitations at low energy and also the image of the Fermi surface. In comparing to ARPES used in solid state physics, the Raman spectroscopy has some more advantages. It permits first to probe precisely excitations in different regions. The threshold measurement for excitation near Fermi surface while the TOF measures all excitation deep inside the Fermi sea. Secondly, the cold atoms system is more proper then we do not encounter any surface problem as in ARPES. We demonstrated also that there is different possibilities to effectuate the TOF measurement such as Raman spectroscopy or RF spectroscopy.

| ARPES (photoemission) | Raman spectroscopy at threshold of extinction | TOF measurement (Raman at fixed $\mathbf{q}$ or RF) |
|---|---|---|
| One photon process | Two photons process | 2 photon (Raman), 1 photon(RF) |
| Photon: $\omega, \mathbf{p}$ | Two photons: $\omega_1 - \omega_2$, $\mathbf{q} = \mathbf{p}_1 - \mathbf{p}_2$ | One or two photons: $\omega$, $\mathbf{q}(\mathbf{q} = 0)$ |
| Surface work $\phi$ | Zeeman shift $\varepsilon_\beta$ | Zeeman shift $\varepsilon_\beta$ |
| Scattered electron: $\mathbf{k}, \varepsilon_{\mathbf{k}}$ | Scattered atom: $\mathbf{k} \approx 0, \varepsilon_{\beta\mathbf{k}} \approx 0$ | Scattered atom: $\mathbf{k}, \varepsilon_{\beta\mathbf{k}}$ |
| $\mathbf{k}$ momentum resolved | $\mathbf{q}$ momentum resolved | $\mathbf{k}$ momentum resolved |
| Angular resolved signal | Total signal | Angular resolved signal |

**Table 2.1:** Summary of the different methods for measuring the single particle excitations.

## 2.3 Illustration on non-interacting systems

We have discussed so far different possibilities to probe a many-body system by the Raman spectroscopy. Let us now demonstrate the feasibility of the proposed measurement via some examples. The first case we would like to discuss is the system of non-interacting ultracold fermions in optical lattices. If we have the translation invariance, then momentum $\mathbf{k}$ is a good

quantum number. At zero temperature $T = 0$, the Fermi function $n_F(\omega)$ becomes a $\theta(-\omega)$ function. Due to the Pauli principle, the fermionic particles fill all the one-particle states in the momentum space up to the Fermi energy $E_F$. The filling up to the last energy level $E_F$ form a Fermi surface.

We now discuss in this section the measurement at the extinction threshold with the **q**-resolved method. The second method by time of flight imaging will be addressed later more in detail within the section 2.7. The spectral function of a non-interacting system is simply a Dirac distribution $A(\mathbf{k}, \omega) = \delta(\omega - \xi_{\mathbf{k}})$ ($\hbar$ is considered as unit). Let us insert this expression into the Raman transferred rate (Eq. 2.14) and change the variable $\mathbf{k} \to \mathbf{k} + \mathbf{q}$, we have

$$\mathbf{R}(\mathbf{q}, \Omega) = \frac{|C|^2 n_1 n_2}{(2\pi)^3 \hbar} \int \mathbf{d}^3\mathbf{k}\; n_F(\varepsilon_{\beta\mathbf{k}+\mathbf{q}} - \Omega)\delta(\varepsilon_{\beta\mathbf{k}+\mathbf{q}} - \Omega - \xi_{\mathbf{k}}). \tag{2.20}$$

In this expression, we see that the total Raman rate is the sum over the one-particle excitation state of energy $\xi_{\mathbf{k}} = \varepsilon_{\beta\mathbf{k}+\mathbf{q}} - \Omega$ which is inside the Fermi surface $\varepsilon_{\beta\mathbf{k}+\mathbf{q}} - \Omega < 0$ (included in the Fermi-Dirac factor). In order to evaluate an integral of the Dirac function, we need to solve the following equation to get its poles $\mathbf{k}_i(\mathbf{q}, \Omega)$

$$f(\mathbf{k}) = \varepsilon_\beta(\mathbf{k} + \mathbf{q}) - \Omega - \xi(\mathbf{k}) = 0. \tag{2.21}$$

We use the following property of the Dirac function: $\delta(g(x)) = \sum_i \delta(x - x_i)/|g'(x_i)|$. Thus the Raman rate has an analytical form

$$\mathbf{R}(\mathbf{q}, \Omega) = \frac{|C|^2 n_1 n_2}{(2\pi)^3 \hbar} \sum_i \frac{\theta(\Omega - \varepsilon_\beta(\mathbf{k}_i + \mathbf{q}))}{f'(\mathbf{k}_i)}. \tag{2.22}$$

From this equation, we can conclude that when we look at the intensity of $\mathbf{R}(\mathbf{q}, \Omega)$ there is some region in the $(\mathbf{q}, \Omega)$-plane where no signal can be measured. In fact, the curve which limit this zone gives us the direct access to the Fermi surface. We find that the zone without signal given by zero point of the argument in the Heaviside function $\Omega - \varepsilon_\beta(\mathbf{k}_i + \mathbf{q}) = 0$ where $k_i$ is the solution of Eq. 2.21. These two conditions give the wave-vector are: i)$\xi(\mathbf{k}) = 0$ and ii) $\Omega - \varepsilon_\beta(\mathbf{k} + \mathbf{q}) = 0$. The first equation gives us the solution $\mathbf{k}_F$. Replacing it into the second one, we have the following relation which determine the vanishing of the signal in the measurement of $\mathbf{R}(\mathbf{q}, \Omega)$.

$$\Omega - \varepsilon_\beta(\mathbf{k}_F + \mathbf{q}) = 0. \tag{2.23}$$

We illustrate the behavior in a 1D or 2D systems assuming all hyperfine states to be trapped in an optical lattice.

### 1D system in a optical lattice

In a one dimensional system, the Fermi surface consists of just two value $\pm\mathbf{k}_F$. Let us take $\varepsilon_\beta(\mathbf{k}) = \varepsilon_\beta - 2t_\beta \cos k$ be the energy dispersion for the $\beta$-atoms in the optical lattice and $\xi(\mathbf{k}) = -2t \cos k - \mu$ be the one for $\alpha$-atoms. The condition for vanishing of the signal Eq. 2.23 becomes

$$\Omega + 2t_\beta \cos(\pm\mathbf{k}_F + \mathbf{q}) = 0. \tag{2.24}$$

Therefore, the signal vanishes for $\mathbf{q} = \pm k_F$ and $\Omega = \varepsilon_\beta - 2t_\beta$. This measurement gives direct access to the Fermi points of a one dimension system.

### 2D gas in an optical lattice

In a 2D system, the Fermi surface which is determines by $\mathbf{k}_F$ is supposed in the form of curve in a two dimensional plot. The out-going atom is trapped in the optical lattice. In this case, we have $\epsilon_\beta(\mathbf{k}) = -2t_\beta(\cos\mathbf{k}_x + \cos\mathbf{k}_y)$ and $\xi(\mathbf{k}) = -2t(\cos\mathbf{k}_x + \cos\mathbf{k}_y) - \mu$. Therefore, the condition of vanishing of the signal Eq. 2.23 becomes

$$\Omega + 2t_\beta\Big(\cos(\mathbf{k}_{Fx} + \mathbf{q}_x) + \cos(\mathbf{k}_{Fy} + \mathbf{q}_y)\Big) = 0. \tag{2.25}$$

When $\Omega = 0$ we have $\mathbf{q} = -\mathbf{k}_F$, so the measurement of the signal with respect to $\mathbf{q}$ give us the information of the Fermi surface.

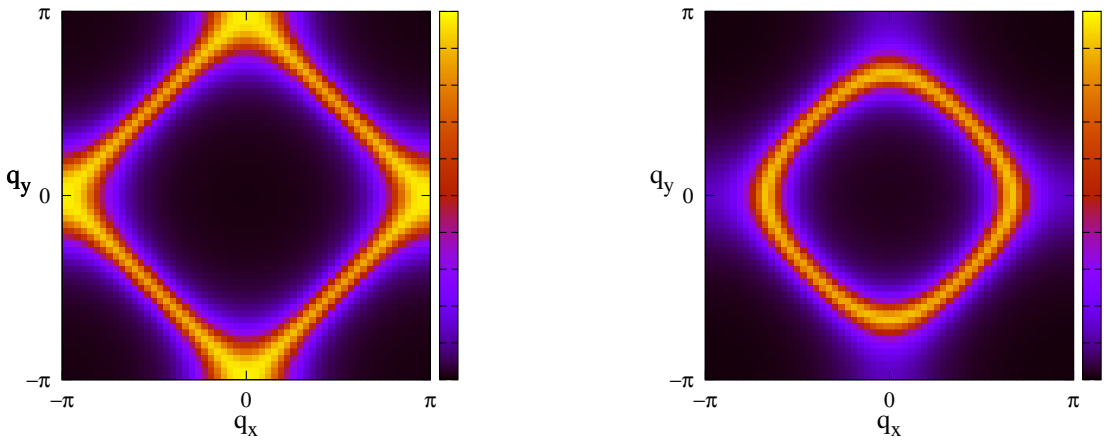


**Figure 2.9:** Intensity plots of the Raman signal on the plane $(q_x, q_y)$ for 2D non-interacting fermions in optical lattice. Left panel is for the case with half-filling. Right panel is for the system with density $n_\alpha = 0.22$. The non-vanishing zone gives the form of the Fermi surface with the width of the order $\sqrt{2m\Delta\Omega}$. Here $\Delta\Omega$ is chosen close to the threshold $\Delta\Omega \approx 0.01t$.

- 2D half-filling Fermi surface
  Let us consider the case where atoms in the internal state $|\beta\rangle$ are free, and the system of atoms in the internal state $|\alpha\rangle$ is trapped in 2D optical lattice. The system of cold atoms has the average filling of one particle per site. In this example, we take a measurement with $\Delta\Omega$ fixed at value 0.01t close to the threshold of extinction. The width of the quasiparticle peak is homogeneous $\Gamma = 0.4t$. The right panel on Fig. 2.9 shows the measurable Raman signal whose maximal value is located at the Fermi surface. As the the system at half-filling has no interaction, then the Fermi surface has the square form and coincides to the half Brillouin zone.

- 2D hole-doped Fermi surface
  The second case that we would like to check is the Fermi surface of the system of cold atom in 2D optical lattice with hole-doped (less than one atom per site). The result presented in Fig. 2.9 left panel is calculated with $\Delta\Omega = 0.01t$ and a homogeneous width of the quasiparticle peak $\Gamma = 0.4t$. The chemical potential is about $\mu = -1.0t$. The non-zero Raman signal form a Fermi surface inside the half Brillouin zone.

**Conclusion** In the experience, we expect to observe the image of the Fermi surface by measuring the Raman rate resolvedly in transfer momentum for a fixed frequency close to

the threshold of extinction. This measurement requires to be repeated for many value of $\mathbf{q}$, therefore it is more convenient to realize the experiment in a chosen direction.

## 2.4 More exotic many-body states: towards the feature of cuprates

We consider now some more sophisticated models in solid state physics where the strong correlation introduces many new effects. In the case with moderate interaction ($U$ is smaller than the kinetic energy scale) the Fermi liquid description of quasiparticle is still valid. In contrast, when the interaction becomes comparable to the kinetic energy scale, many fascinating effects occur such as the Mott insulator-metal transition, or high $T_c$ superconductivity. In the following, we discuss the two possible measurements described above in the context of a system in a normal phase with a pseudogap. Very interesting structures of Fermi surface such as the arc form or the formation of pockets can be also observed within this spectroscopy.

### 2.4.1 Spectroscopy for strong interacting systems

As described in the section 2.1, for an interacting system the Green's function or spectral function can be separated in two parts. The first one consists of a quasiparticle peak (coherent part) with the life-time $\Gamma_k^{-1}$ and a spectral weight $Z_{\mathbf{k}} < 1$. The second part consists of the broaden part of the spectral describing the incoherent excitations. Therefore, the spectral function and the Green function's function have the following representations

$$A(\mathbf{k},\omega) = \frac{Z_{\mathbf{k}}}{\pi}\frac{\Gamma_{\mathbf{k}}}{(\omega-\xi_{\mathbf{k}})^2+\Gamma_{\mathbf{k}}^2} + A_{inc}(\mathbf{k},\omega). \tag{2.26}$$

$$G(\mathbf{k},\omega) = \frac{Z_{\mathbf{k}}}{\omega-\xi_{\mathbf{k}}+i\Gamma_{\mathbf{k}}} + G_{\mathrm{inc}}(\vec{\mathbf{k}},\omega). \tag{2.27}$$

Here, $A_{\mathrm{inc}}(\mathbf{k},\omega)$ ($G_{\mathrm{inc}}(\mathbf{k},\omega)$) is the incoherent part of the spectral function (Green's function). Other quantities like $Z_{\mathbf{k}}$, $\xi_{\mathbf{k}}$ and $\Gamma_{\mathbf{k}}$ can be obtained by the self-energy $\Sigma(\mathbf{k},\omega)$

$$Z_{\mathbf{k}} = (1-\partial\Sigma'/\partial\omega)^{-1} \quad \xi_{\mathbf{k}} = Z_{\mathbf{k}}(\varepsilon_{\mathbf{k}}-\mu) \quad \Gamma_{\mathbf{k}} = Z_{\mathbf{k}}|\Sigma''|.$$

For the simplification of calculation, we consider the case where $Z_{\mathbf{k}} = 1$, so we have a quasiparticle with the life-time $\Gamma_{\mathbf{k}}^{-1}$. Let us study now the case of a system in two dimension (generalization for 3D case is straight forward). As we see in the last simple cases, the frequency $\Delta\omega$ useful to probe the Fermi surface is the one close to the minimum energy of the out-going atom. So we propose to measure $\mathbf{R}(\mathbf{q},\Omega)$ with $\Omega \approx \min\varepsilon_\beta(\mathbf{k})$. The general formulation for $\mathbf{R}_{\mathbf{q}}(\mathbf{k},\Omega)$ is

$$\mathbf{R}_{\mathbf{q}}(\mathbf{k},\Omega) = \frac{2|C|^2 n_1 n_2}{(2\pi)^{d+1}\hbar} n_F(\varepsilon_\beta(\mathbf{k})-\Omega)\frac{\Gamma_{\mathbf{k}-\mathbf{q}}}{[\varepsilon_\beta(\mathbf{k})-\Omega-\xi(\mathbf{k}-\mathbf{q})]^2+\Gamma_{\mathbf{k}-\mathbf{q}}^2}. \tag{2.28}$$

#### Threshold of extinction measurement

We can develop the energy of the atom in the internal state $\beta$ around its minimum point $\mathbf{k} = \vec{0}$. The energy dispersion for atoms in $\beta$-state read $\varepsilon_\beta(\mathbf{k}) = \varepsilon_{\min} + \mathbf{k}^2/2M$ in which $\varepsilon_{\min}$ is the lowest energy level corresponding to momentum $\mathbf{k} = \vec{0}$ and $M$ is the effective mass of $\beta$-atoms in near the lowest energy. At zero temperature the Fermi-Dirac distribution becomes a cut-off for the momentum in the $\mathbf{k}$-integral. In evaluating the non-zero domain of

this function, we obtain the boundary for the integral. The integral will be taken over the disk $\|\mathbf{k}\| \leq \sqrt{2M(\Omega - \varepsilon_{\min})} = \sqrt{2M\Delta\Omega}$

$$\mathbf{R}(\mathbf{q},\Omega) = \frac{2|C|^2 n_1 n_2}{(2\pi)^{d+1}\hbar} \int_{\|\mathbf{k}\|\leq\sqrt{2M\Delta\Omega}} \mathbf{d}^d\mathbf{k}\ \frac{\Gamma_{\mathbf{k}-\mathbf{q}}}{[\varepsilon_\beta(\mathbf{k}) - \Omega - \xi(\mathbf{k}-\mathbf{q})]^2 + \Gamma^2_{\mathbf{k}-\mathbf{q}}}. \tag{2.29}$$

From the boundary of the integral, we see that whenever $\Omega < \Omega_T = \min_{\mathbf{k}} \varepsilon_{\beta\mathbf{k}}$, there is no Raman signal. This can be explained that in order to obtain the Raman signal, we need to probe the system with a frequency larger than the gap from the Fermi level to the lowest energy of the $\beta$-state. We propose to turn the Raman frequency around this threshold ($\Delta\Omega = \Omega - \Omega_T$ small enough) and measure the signal. In this case we can evaluate the integral simply by the value of the spectral function at the point $\mathbf{k} = \vec{0}$. Then we have

$$\mathbf{R}(\mathbf{q},\Omega) = \frac{|C|^2 n_1 n_2}{(2\pi)^d\hbar} \frac{2M\Delta\Omega\Gamma_{-\mathbf{q}}}{[\Delta\Omega + \xi(-\mathbf{q})]^2 + \Gamma^2_{-\mathbf{q}}}. \tag{2.30}$$

The intensity of the signal measured is a Lorentz peak, which is situated at $\Delta\Omega + \xi(\mathbf{q}) = 0$. Measuring $\Delta\Omega$ really small, this peak determines the Fermi surface. Let us do an approximation for $\xi(\mathbf{q})$ near Fermi level: $\xi(\mathbf{q}) = \mathbf{V}_F.(\mathbf{q} - \mathbf{q}_F)$. Here $\mathbf{V}_F$ is the Fermi velocity which is in the normal direction of the Fermi surface. If we look at the distribution of intensity one direction $\mathbf{k}_F$ (which means $\mathbf{q} \parallel \mathbf{k}_F$), thus the width of the intensity peak $\Gamma_s$ can be obtained like: $\Gamma_s = \Gamma_{\mathbf{q}}/\|\mathbf{V}_F\|\cos\vartheta$ where $\vartheta$ is the angle between $\mathbf{V}_F$ and $\mathbf{k}_F$. Otherwise, if we consider the distribution of intensity with $\delta\mathbf{q} = \mathbf{q} - \mathbf{k}_F$ in the direction of $\mathbf{V}_F$ (the normal direction of the Fermi surface), then we have the width of the intensity peak in k-space $\Gamma_s = \Gamma_{\mathbf{q}}/\mathbf{V}_F$.

In the case where we can not reach the region where $\Delta\Omega$ is small enough (because of the limit of the experimental resolution or two small number of atom excited to the $\beta$-state), we must evaluate the integral over a small disk $\|\mathbf{k}\| < \sqrt{2M\Delta\Omega}$. In order to evaluate the broadness comes this effect, we suppose that $\Gamma_{\mathbf{k}}$ is uniform $\Gamma_{\mathbf{k}} = \Gamma$ and develop $\xi(\mathbf{q} - \mathbf{k})$ around $\mathbf{k}_F$

$$\xi(\mathbf{q} - \mathbf{k}) = \mathbf{V}_F.(\mathbf{q} - \mathbf{k} - \mathbf{k}_F). \tag{2.31}$$

Let us change this integral to the one over energy scale. We pose $E = \mathbf{k}^2/2M + \mathbf{V}_F.\mathbf{k} - \Delta\Omega$, and define the density of state (DOS) with respect to this energy dispersion

$$D(E) = \frac{1}{(2\pi)^d} \int_{\|\mathbf{k}\|<\sqrt{2M\Delta\Omega}} \mathbf{d}^d\mathbf{k}\ \delta(E - \frac{\mathbf{k}^2}{2M} - \mathbf{V}_F.\mathbf{k} + \Delta\Omega). \tag{2.32}$$

In the energy variable representation, the Raman spectroscopy rate reads

$$\mathbf{R}(-\mathbf{q},\Omega) = \frac{|C|^2 n_1 n_2}{\pi\hbar} \int dE \frac{D(E)\Gamma}{[E - \mathbf{V}_F.(\mathbf{q} - \mathbf{k}_F)]^2 + \Gamma^2}. \tag{2.33}$$

Let us estimate the region where we can measure non-zero signal of Raman spectroscopy. The boundary of the domain where $D(E)$ is non-zero is determined by the equation

$$E - \frac{\mathbf{k}^2}{2M} + \mathbf{V}_F.\mathbf{k} + \Delta\Omega = 0.$$

Thus for all value $\mathbf{k}$ belong to the disk $\|\mathbf{k}\| < \sqrt{2M\Delta\Omega}$, the function $D(E)$ is non-zero

$$MV_F - \sqrt{2M\Delta\Omega} < \sqrt{2M(E + \Delta\Omega) + (MV_F)^2} < MV_F + \sqrt{2M\Delta\Omega}, \tag{2.34}$$

which gives us the boundary of integral: $-V_F\sqrt{2M\Delta\Omega} < E < V_F\sqrt{2M\Delta\Omega}$.

In combining with the broadness of the Raman signal due to the quasiparticle life-time, we can determine the whole condition for region where the signal vanishes

$$\|\mathbf{V}_F.(\mathbf{q}-\mathbf{k}_F)\| \;>\; V_F\sqrt{2M\Delta\Omega}+\Gamma_{\mathbf{k}_F}. \tag{2.35}$$

For one dimensional system in optical lattice, this result leads to the estimation of the size of the measurable signal zone located at the two Fermi points $\pm k_F$: $\Delta\mathbf{q}=\mathbf{q}-\mathbf{k}_F=\Gamma/V_F+\sqrt{2M\Delta\Omega}$. For systems with higher dimension (2D,3D), this condition defines the boundary of the sizable signal. Therefore, in experiment measuring the width of the Fermi shell will provide the properties of the quasiparticles excitations near the Fermi surface ($\Gamma_{\mathbf{k}_F},\ \mathbf{V}_F$). We will discuss in more detail later how to extract these information.

**Measurement by time of flight imaging**

We propose here the second measurement which permits to see the Fermi surface of the strongly correlated cold atoms. We apply the Raman spectroscopy for a fixed transferred momentum $\mathbf{q}$ or the RF spectroscopy accompanying by the TOF imaging. After transferring atoms in the internal state $|\alpha\rangle$ to an other internal state $|\beta\rangle$, we turn off the optical lattice and take the image of the atoms in the internal state $|\beta\rangle$. We obtain a distribution of atoms in the momentum space where the intensity of the image is proportional to the Raman transfer rate

$$\mathbf{R}_{\mathbf{q}}(\mathbf{k},\Omega)=\frac{|C|^2n_1n_2}{\hbar}n_F(\varepsilon_\beta(\mathbf{k})-\Omega)A(\varepsilon_\beta(\mathbf{k})-\Omega,\mathbf{k}-\mathbf{q}). \tag{2.36}$$

Here, the momentum $\mathbf{q}$ and the frequency $\Omega$ are fixed. In order to reconstruct the Fermi surface, we fix the momentum $\mathbf{q}$ to a convenient value and take different image with many frequencies $\Omega_n$. Superposition of these images gives us the picture of the Fermi surface. According to the appropriate choice of the momentum $\mathbf{q}$, we have the following cases.

If the two hyperfine states $|\alpha\rangle$ and $|\beta\rangle$ do not see the same optical lattice (i.e. they have different effective mass or see trapped by different optical lattices). The convenient value of transferred momentum for this measurement is $\mathbf{q}=(2n\pi/a,2m\pi/a,2p\pi/a)$. Let us take $\mathbf{q}=(0,0,0)$ and make the superposition of images measured with different frequencies. We obtain the total intensity of the Raman rate as a function of the momentum $\mathbf{k}$. Let us consider the case in which the incoherent part of the spectral function is negligible. With the lorentzian form of $A(\omega,\mathbf{k})$, then we have

$$\mathbf{R}(\mathbf{k},\mathbf{q})=\frac{|C|^2n_1n_2}{\hbar}\sum_n n_F(\varepsilon_\beta(\mathbf{k})-\Omega_n)\frac{\Gamma_{\mathbf{k}}^2}{[\varepsilon_\beta(\mathbf{k})-\Omega_n-\xi(\mathbf{k})]^2+\Gamma_{\mathbf{k}}^2}. \tag{2.37}$$

The borders of the non-signal zone make a contour of the Fermi-Surface. At zero temperature, the vanishing of signal is determined by the Fermi-Dirac factor $n_F$ which reads $\varepsilon_\beta(\mathbf{k})-\Omega_n>0$. In addition, the maximal intensity is found on the lines $\varepsilon_\beta(\mathbf{k})-\Omega_n-\xi(\mathbf{k})=0$. So the intersection of the two ensembles of curves gives us the points which belong to the Fermi-surface $\xi(\mathbf{k}_n)=0$. Here, $\mathbf{k}_n$ are the points satisfied both conditions for a measurement with Raman frequency $\Omega_n$.

The spectral density with negative energy $A(\omega)$ can be obtained by making the sum of the measured signal over the $\mathbf{k}$-space for many time of flight measurement. The discussion on the quasiparticle excitations properties will presented later in the section 2.7 concerning the recent experiment in Jin's group.

### 2.4.2 Phenomenological model of d-wave pseudogap

In this section, we study whether this Raman spectroscopy technique can be used to probe more exotic states, such as the unconventional metallic state of high-temperature superconductors. This is currently one of the most outstanding problems in condensed matter physics. Angular-resolved photoemission spectroscopy (ARPES) has played a particularly important role in revealing important physical aspects of these materials. Apart from the property of

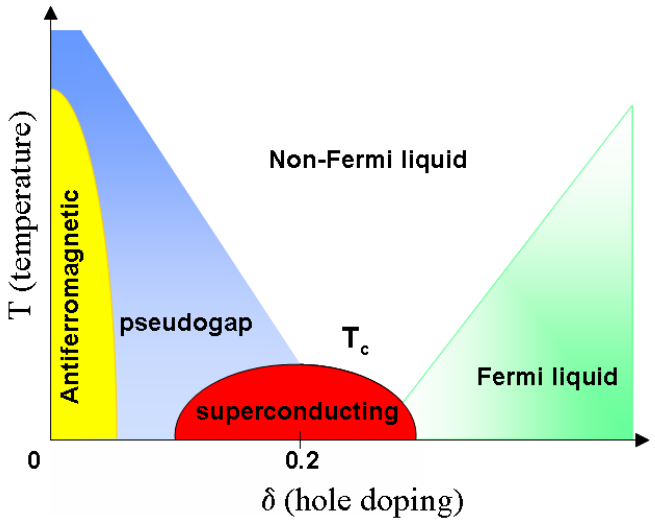


**Figure 2.10:** Generic phase diagram of high temperature superconductivity on the $(\delta - T)$ hole doping-temperature plane.

the superconductivity at high temperature, the phase diagram of cuprates is very rich, as illustrated by the generic phase diagram in Fig. 2.10. This phase diagram is presented versus temperature $T$ and hole-doping $\delta$. Doping measures the deviation from half-filling (one electron per site) and corresponds to the introduction of charge careers in the copper-oxygen plane, usually achieved in these materials by chemical substitution.

The following regions are apparent on this generic phase diagram. At zero doping, we have a Mott insulator which orders antiferromagnetically below the Néel temperature $T_N$. Upon doping, the Néel temperature is quickly suppressed and a superconducting phase appears upon further doping. The superconducting transition temperature $T_c$ displays a dome-like shape, and is highest at some "optimal" doping (close to 15%). It is established that the superconducting order parameter has d-wave symmetry.

The non-superconducting (metallic, or "normal") phase is actually particularly interesting. At high doping levels (above optimal doping), the properties of a conventional Fermi-liquid are gradually recovered. In contrast, at low doping (below optimal doping, corresponding to the so-called "underdoped" regime), the "normal" state is far from having the properties of a normal metal ! A distinctive property of this phase is that it displays a suppression of low-energy excitations, which shows up in many experimental probes (for example, the magnetic susceptibility is not Pauli-like but decreases at low temperature). This suppression corresponds to the appearance of a "pseudogap", which opens up below some characteristic temperature $T^*$, and has a similar momentum-dependence as the superconducting gap. This is most clearly revealed by ARPES. In Fig. 2.11, the photoemission intensity of three samples with different doping levels is displayed. In the underdoped samples, it is seen that the Fermi surface is only visible near the diagonal directions of the Brillouin zone (the diagonal

direction is usually called the "nodal" direction since it is the direction along which the d-wave gap $\propto \cos k_- \cos k_y$ vanishes). Near the "antinodes" $(\pi, 0)$ and $(0, \pi)$, the photoemission intensity is suppressed, so that the Fermi surface appears to consists in disconnected "arcs".

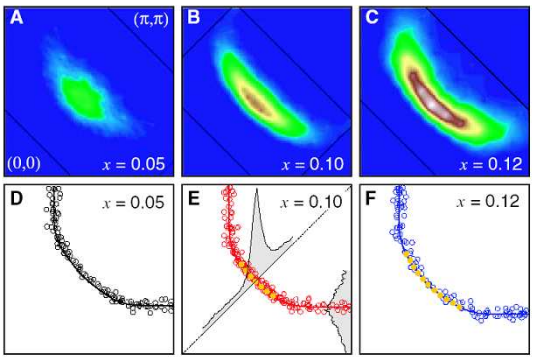


**Figure 2.11:** A quarter of the Fermi surface in the d-wave pseudogap phase observed by the photoemission. The upper panels (A-C) show the intensity plot of the signal measured in ARPES experiment for different hole-doping concentrations ($\delta = 0.05,\ 0.1,\ 0.12$ from left to right).The lower panels (D-F) show the form of the Fermi surface determined by the maximal signal of measured intensity. Reprinted from Ref. [72].

Until now, there exists no widely accepted microscopic theory which is able to understand completely the physics of this pseudogap phase. There are two main classes of explanations for this phase. The first one assumes that the physics of this phase is a precursor of the superconducting phase at low temperature, i.e that it is physically connected to the SC region, and associated with preformed pairs without any phase coherence. The second class of explanations argues that the pseudogap is associated with a different physical phenomenon than superconductivity itself. For example, in some theories, the pseudogap is associated with the Mott gap, which may survive near the antinodes upon doping and truncates the Fermi surface into arcs (Fig. 2.11 A-C).

Here, we do not address the microscopic origin of the pseudogap formation, but we want to understand whether the single-particle spectroscopy technique that we have proposed is able to detect its formation in the context of ultracold fermionic atoms. It is important in this respect to mention that theoretical studies of the two-dimensional Hubbard model [24, 34, 56, 64, 103] have unambiguously revealed that the truncation of the Fermi surface into arcs is indeed a characteristic feature of this model.

For our purpose, it is therefore sufficient to adopt a phenomenological form of the spectral function appropriate to the pseudogap phase. It has been shown in the context of cuprates[90] that the ARPES experimental results can be reasonably well described by the following form of the one-particle Green's function:

$$G(\mathbf{k}, i\omega) = \frac{1}{i\omega - \xi_{0\mathbf{k}} + i\Gamma_1 - \Delta_{\mathbf{k}}^2/(i\omega + \xi_{0\mathbf{k}} + i\Gamma_0)}. \tag{2.38}$$

In this expression, $\Delta_{\mathbf{k}} = \Delta_0(\cos \mathbf{k}_x - \cos \mathbf{k}_y)$ describes the pseudogap with d-wave symmetry and $\xi_{0\mathbf{k}}$ is the bare energy dispersion of the non-interacting system. In order to be able to compare with a realistic situation, we have introduced the damping parameters: $\Gamma_0$ for the self-energy and $\Gamma_1$ for the Green's function. The spectral function reads

$$A(\mathbf{k}, \omega) = \frac{1}{\pi} \frac{\Gamma_{\mathbf{k}}}{(\omega - \xi_{0\mathbf{k}} - \Sigma'_{\mathbf{k}})^2 + \Gamma_{\mathbf{k}}^2}. \tag{2.39}$$

Here, $\Gamma_{\mathbf{k}}^{-1}$ is the life time of the quasiparticle excitations and $\Sigma_{\mathbf{k}}$ is the self-energy. This spectral function has the form of a Lorentz peak around the energy for quasiparticle $\xi_{\mathbf{k}} = \xi_{0\mathbf{k}} + \Sigma'_{\mathbf{k}}$. Here, $\Sigma'_{\mathbf{k}}$ is the real part of self-energy (used to renormalize the quasiparticle dispersion) reads

$$\Sigma'_{\mathbf{k}} = \frac{\Delta_{\mathbf{k}}^2(\omega + \xi_{0\mathbf{k}})}{(\omega + \xi_{0\mathbf{k}})^2 + \Gamma_0^2}. \tag{2.40}$$

The life time of the quasiparticle for the d-wave pseudogap phase depends on the momentum

$$\Gamma_{\mathbf{k}} = \Gamma_1 + \frac{\Gamma_0 \Delta_{\mathbf{k}}^2}{(\omega + \xi_{0\mathbf{k}})^2 + \Gamma_0^2}.$$

As the d-wave gap vanishes on the nodal direction and is important on the antinodal direction, the quasiparticle is very well-defined at the nodal point and very broaden at the antinodal point (Fig. 2.11E). This form of the spectral function also provides a reasonable qualitative description of recent theoretical results for the two-dimensional Hubbard model.

### Measurement at threshold of extinction

In the Fig. 2.12, we present the numerical result which simulated the measurable Raman signal for a d-wave pseudogap phase in the momentum space. The region without intensity corresponding to the vanishing of Raman signal while the maximal intensity shows the image of the Fermi surface. The Raman spectroscopy shows a clear image of the arc structure with a high intensity in the nodal point where the pseudogap vanishes and a low intensity in the antinodal point at which the value of the pseudogap is optimal. Performing an experiment

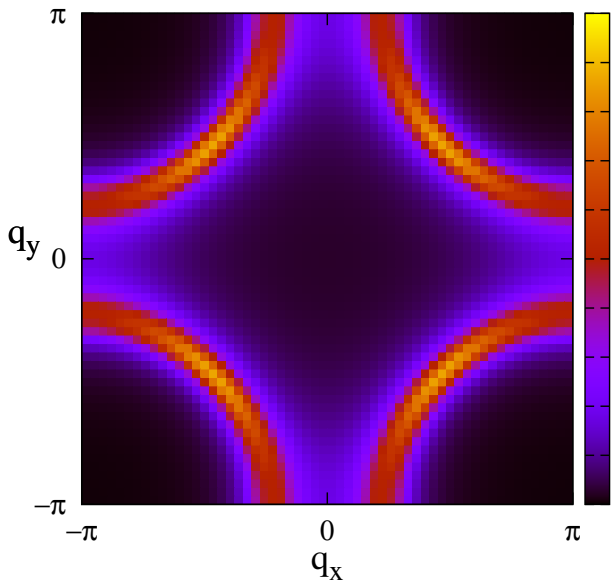


**Figure 2.12:** Model *d*-wave pseudogap state (see text), with $\Delta_0 = 0.1\,t_\alpha$, $\Gamma_0 = 0.05\,t_\alpha, \Gamma_1 = 0.4\,t_\alpha$. The plot is for a hole-doped system ($n_\alpha = 0.45$) with a nearest ($t_\alpha$) and next-nearest neighbor ($t'_\alpha$) hopping, with $t'_\alpha/t_\alpha = -0.3$ (typical for cuprates, but similar effects are expected also for smaller $|t'_\alpha/t_\alpha|$).

near the threshold of extinction can help to observe the Fermi velocity $\mathbf{V}_F$. The value of $\Delta\Omega$ ($\Delta\Omega = \Omega - \varepsilon_{\min}$) will be chosen small enough, so a rough approximation for the integral in

the Raman rate is acceptable. For the convenience of calculation, we consider the Raman transfer rate with transferred momentum $-\mathbf{q}$

$$\mathbf{R}(-\mathbf{q},\Omega) = \frac{|C|^2 n_1 n_2}{(2\pi)^d \hbar} \frac{2M\Delta\Omega\Gamma_{\mathbf{q}}}{\left[\Delta\Omega + \xi_{\mathbf{q}}\right]^2 + \Gamma_{\mathbf{q}}^2}. \tag{2.41}$$

The maximal signal of Raman rate is located at $\Delta\Omega + \xi_{\mathbf{q}} = 0$. In the case of a d-wave pseudogap phase, this relation becomes

$$\Delta\Omega + \xi_{0\mathbf{q}} + \Sigma'_{\mathbf{q}} = 0. \tag{2.42}$$

If we are exactly at the threshold $\Delta\Omega = 0$, this equation indicates the location of the Fermi surface. For a measurement near the threshold, the location of the maximal Raman signal no longer coincides with the Fermi surface. Let us define position of maximal signal be $\mathbf{q}_{\max}$ which is moved from the $\mathbf{k}_F$. Develop $\xi_{\mathbf{q}}$ near the Fermi surface as $\xi_{\mathbf{q}} = \mathbf{v}_F.(\mathbf{q} - \mathbf{k}_F)$. Therefore, the position of the maximal Raman intensity is determined by

$$\Delta\Omega = \mathbf{v}_F.(\mathbf{k}_F - \mathbf{q}_{\max}). \tag{2.43}$$

By performing the experiment for many frequencies $\Delta\Omega$ (Fig. 2.43) and measuring the positions of the peak of intensity $\mathbf{q}_{\max}$, then the Fermi velocity $\mathbf{V}_F$ can be extracted directly from the relation 2.43.

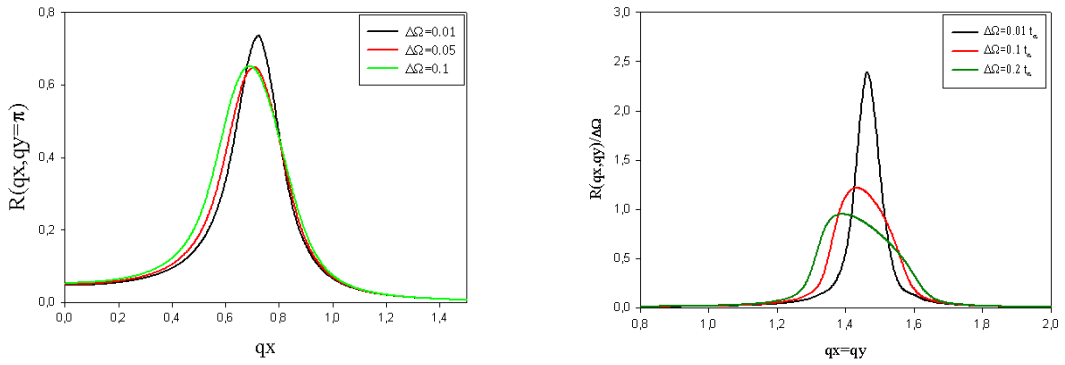


**Figure 2.13:** The Raman rate at the antinodal and nodal direction. Different curves of the Raman rate for different $\Delta\Omega$ shows the displacement of the peak

Once we obtained the Fermi velocity $bV_F$, we can measure the lifetime of quasiparticle excitation $\Gamma_{\mathbf{k}}^{-1}$. In the discussion on the measurement at the threshold of extinction, we have shown that the width of the intensity peak is related to the inverse of the quasiparticle lifetime as

$$\Delta q = \sqrt{2m\Delta\Omega} + \frac{\Gamma}{\mathbf{v}_F}. \tag{2.44}$$

In this paragraph, we would like to show how the Raman rate is similar to the spectral function if we perform the Raman spectroscopy with many value of frequencies (not necessary closed to the threshold of extinction) for a fixed transferred momentum. For the convenience of the order of magnitude in the comparison, we compare the Raman rate renormalized by the factor $1/\Delta\Omega$ because the Raman signal is an integral over the disk of radius $\sqrt{2m\Delta\Omega}$. For the d-wave pseudogap model, we're interested in the two main points: the nodal point and the antinodal point of the Fermi surface. For the nodal direction, from the model we

know that the quasiparticle is well defined (Fig. 2.14) because there is no pseudogap $\Delta = 0$. For the Raman scattering rate, it is the average value of the spectral function in the disk $\varepsilon_{\beta\mathbf{k}} - \varepsilon_{\min} < \Delta\Omega$ thus this peak becomes to be broader and lower than the one in spectral function.

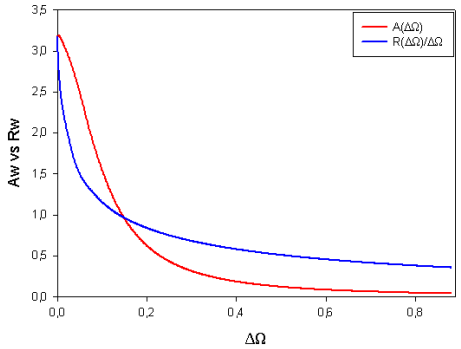


**Figure 2.14:** Comparison between the spectral function and the Raman scattering rate $\mathbf{R}(\Delta\Omega)$ renormalized by factor $1/\Delta\Omega$ at the nodal point of the Fermi surface

For antinodal direction, the quasiparticle peak in the spectral function becomes very broad because the pseudogap is maximal. In fact, the appearance of the pseudogap has split the quasiparticle peak. The numerical calculation (Fig. 2.15) shows that one can find the same structure in $A(\omega)$ and $R(\omega)/\omega$. The same effect of enlargement happens in the Raman scattering rate as the previous case.

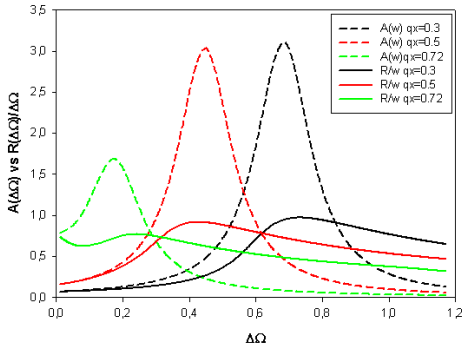


**Figure 2.15:** Comparison between the spectral function and the Raman scattering rate $\mathbf{R}(\Delta\Omega)$ renormalized by factor $1/\Delta\Omega$ at the same points in k-space. Dash line refers to spectral function, solid line refers to Raman scattering rate

### Time of flight measurement

The discussion so far has assumed that it is possible to repeat the measurement of the total rate $R$ for many different values of $\mathbf{q}$. In some cases, a different scheme with a momentum-selective detection of the scattered $\beta$ atoms may be instead favorable, in which a single value of $\mathbf{q}$ is used, and a time of flight expansion of the $\beta$ atoms cloud is performed (after

suddenly turning off the trap and the lattice potential) in order to reconstruct the momentum distribution of the atoms. This scheme most closely resembles ARPES experiments in solids. As shown in Fig. 2.16a, the Raman resonance condition allows for a selective addressing of the different regions in $\mathbf{k}$ by tuning the frequency $\Omega$. The number of Raman-scattered atoms with final momentum $\mathbf{k}$ is proportional to the integrand $n_F(\varepsilon_{\mathbf{k}\beta} - \Omega)\, A(\mathbf{k} - \mathbf{q}, \varepsilon_{\mathbf{k}\beta} - \Omega)$ of Eq. 2.15.

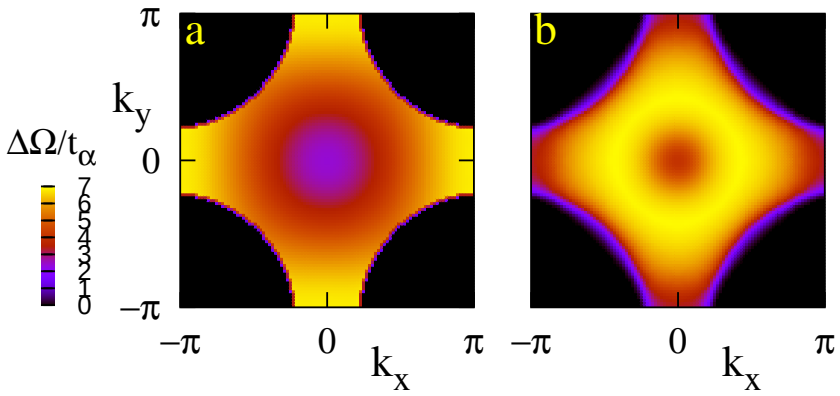


**Figure 2.16:** (a) Color plot illustrating the selective addressing of $\beta k$-space by a proper choice of $\Omega$. (b) Time of flight $\beta k$-map obtained by integrating the Raman intensity for $\Delta\Omega$ varied in the range $[2.4t_\alpha, 6.8t_\alpha]$. The dispersion relation of the $\beta$-atoms is taken as $\varepsilon_{\mathbf{k}\beta} = \varepsilon_\beta - 2t_\beta(2 + \cos k_x + \cos k_y)$ with $t_\beta = 1.5t_\alpha$ (note that interactions will renormalize downwards the effective $t_\alpha$ even if bare values are equal). Parameters are as in the last measurement and $\mathbf{q} = 0$.

In right panel of the Fig. 2.16, we present the superposition of the time selective TOF image of out-going $\beta$-atoms for many Raman frequency satisfied $\Omega - \Omega_T \in [2.4t_\alpha, 6.8t_\alpha]$. The transfer momentum is chosen as $\mathbf{q} = 0$. In this simulation, we assume that both atoms in $\alpha$-state and $\beta$-state are confined by two different optical lattices. Fig. 2.16 shows that the resulting $\mathbf{k}$-map of the intensity also reveals the pseudogap physics.

## 2.5 Harmonic trap

During an experiment the quantum gas is confined by a harmonic potential due to the magnetic trap, optical trap or the gaussian profile of the laser beam. This additional potential, a priori, modifies the measurement of the system in comparison to the homogeneous one. In particular, the harmonic potential breaks the translation invariance, so the k-momentum is no longer a good quantum number. In presence of the trap, the Fermi surface is not well-defined even in the non-interacting case. For the interacting case, the sharpness of Fermi surface is modified by two contributions. The first one is the interaction which makes the life-time of quasiparticle become finite. The second one is the contribution of the harmonic trap potential. In this section we discuss how this additional potential modify the Fermi surface.

One way to treat the cold atoms in presence of the harmonic potential is using the local density approximation (LDA). The idea of this approximation is to consider the a spatially varying chemical potential for the atoms in $\alpha$-state $\mu^\alpha_{\mathbf{R}} = \mu_0 - V_\alpha(\mathbf{R})$ with $\mu_0$ is the chemical potential at the center of the trap. Observables of the system are then calculated by using

locally the solution for the homogeneous system at corresponding chemical potential. For example, the Green's function of the inhomogeneous system is approximated by the homogeneous Green function with local chemical potential $\mu_{\mathbf{R}}$.

$$G(\mathbf{k},\omega,\mathbf{R}) \approx G_{\text{hom}}(\mathbf{k},\omega;\mu_{\mathbf{R}}) \tag{2.45}$$

this leads directly to the approximation of the spectral function

$$A(\mathbf{k},\omega,\mathbf{R}) \approx A_{\text{hom}}(\mathbf{k},\omega;\mu_{\mathbf{R}}). \tag{2.46}$$

This approximation is the same as the semi-classical description in [Stringari and Pitaevskii] which supposes to write the Fermi-Dirac distribution for a particle in the phase-space $(\vec{R},\mathbf{k})$ as $n(R,\mathbf{k}) = 1/(e^{\beta[\epsilon_{\mathbf{k}}-\mu_{\mathbf{R}}]}+1)$. In fact, this density distribution can be obtained within the LDA approximation of the spectral function by using the expression of spectral function for the free fermions gas $A(\mathbf{k},\omega;\mu_{\mathbf{R}}) = \delta(\omega-\varepsilon_{\mathbf{k}}+\mu_{\mathbf{R}})$. The local density distribution in momentum space reads

$$n(R,\mathbf{k}) = \int d\omega n_F(\omega) A(\mathbf{k},\omega;\mu_{\mathbf{R}}). \tag{2.47}$$

For general case including the strong correlation effect, the spatial dependent spectral function reads

$$A(\mathbf{k},\omega;\mu_{\mathbf{R}}) = \frac{1}{\pi}\frac{\Gamma_{\mathbf{k}}}{(\omega-\xi_{\mathbf{Rk}})^2+\Gamma_{\mathbf{k}}^2},$$

where $\xi_{\mathbf{Rk}} = \varepsilon_{\mathbf{k}} - \mu_{\mathbf{R}}$ is the quasiparticle dispersion energy with energy reference determined by the Fermi level. The LDA is good approximation if the trap potential is smooth with respect to all the macroscopic length scales of the system. Both Raman spectroscopy and RF spectroscopy discussed above are local processes. They consist of changing locally the internal state of atom. Therefore, we expect the LDA to give a good description of the system.

### 2.5.1 Untrapped out-going atoms

Let us apply this approximation for estimating the Raman transfer rate in a harmonic trap. We assume in the first case that only the atoms in the $\alpha$-state are trapped. The scattered atoms in the $\beta$-state are free particles. That the harmonic trap for the atoms in $\alpha$-state can be written in the cylindrical coordination $(\mathbf{R},\theta,z)$ as

$$V_\alpha(\mathbf{R},z) = \frac{1}{2}m\omega_R^2 R^2 + \frac{1}{2}m\omega_z^2 z^2. \tag{2.48}$$

Considering the case of 2D system, the system is strongly confined in the z direction $\omega_z \gg \omega_{\mathbf{R}}$, then the gases are confined in 2D, with the Thomas-Fermi radius $R_{TF}$ in the plan. Taking the energy reference to be $\mu_0$ (the same choice with the homogeneous analysis), the amplitude of Raman scattering reads

$$\mathbf{R}(\mathbf{q},\Omega) = \frac{|C|^2 n_1 n_2}{(2\pi)^d\hbar}\int \mathbf{d}^d\mathbf{k}\int \mathbf{d}^d\mathbf{R}\; n_F(\frac{\hbar^2\mathbf{k}^2}{2M}+\varepsilon_\beta^0-\Omega)A(\mathbf{k}-\mathbf{q},\frac{\hbar^2\mathbf{k}^2}{2M}+\varepsilon_\beta^0-\Omega;\mu_{\mathbf{R}}), \tag{2.49}$$

in which $\Omega = \omega_1-\omega_2+\mu_0$ is the difference of frequencies including the energy reference of the $\beta$-state. The resonance condition of this equation can be translated directly to the energy conservation

$$\varepsilon_{\mathbf{k}-\mathbf{q}} - \mu_{\mathbf{R}} = \frac{\hbar^2\mathbf{k}^2}{2M} + \varepsilon_\beta^0 - \Omega. \tag{2.50}$$

It shows an explicit dependence on the the distance from the center of the trap (Fig. 2.17). The threshold condition determined by the Fermi factor in Eq. 2.49 reads $(\hbar^2\mathbf{k}^2/2M+\varepsilon_\beta^0-\Omega) \leq 0$.

This condition leads to the threshold frequency of Raman process $\Omega_T = \varepsilon^0_\beta$. The Fig. 2.17 shows the Raman process for two different positions $\mathbf{R}_1 > \mathbf{R}_2$ (i.e. $\mathbf{R}_2$ is closer to the center than $\mathbf{R}_2$) in the harmonic trap. For $\alpha$-atoms seeing a harmonic potential, the energy dispersion of the position $\mathbf{R}_1$ is higher than the position $\mathbf{R}_2$. The true chemical potential is the same for the whole system, therefore the position $\mathbf{R}_2$ has a higher filling than $\mathbf{R}_1$. Within the hypothesis of no trap potential for $\beta$-atoms, the threshold frequency $\Omega_T$ for non vanishing signal (distance from the Fermi level to the lowest energy level of the $\beta$-states) is the same for all the positions in the trap. Assume that we are at zero temperature $T = 0$, the Fermi-Dirac

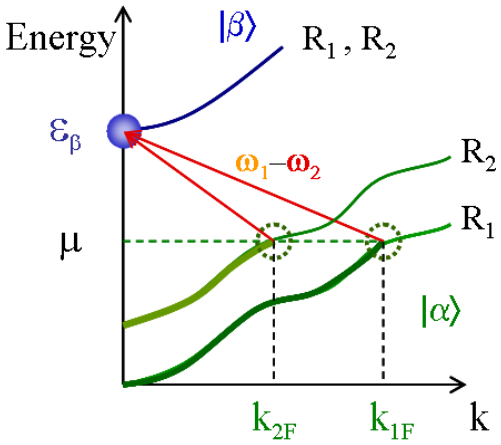


**Figure 2.17:** The upper band is the $\beta$-state dispersion without any trap effect (same dispersion for two positions $R_1 > R_2$. The lower bands are $\alpha$-state dispersions for two position $R_1 > R_2$ which are shifted by the trap effect. For different position, we always find the same threshold energy)

distribution becomes $\Theta(\Omega + \mu_{\mathbf{R}} - \hbar^2\mathbf{k}^2/2M - \varepsilon^0_\beta)$. Let us consider a measurement close to the threshold of the extinction ($\Delta\Omega = \Omega - \Omega_T \approx 0$). The Raman spectrum will be related directly to the spectral function of one-particle excitation via an integration over the radius of the trap

$$\mathbf{R}(\mathbf{q}, \Omega) = \frac{|C|^2 n_1 n_2 M \Delta\Omega}{(2\pi)^{d-2}\hbar^2 m\omega^2_{\mathbf{R}}} \int dV \; A(-\mathbf{q}, -\Delta\Omega; \mu_0 - V). \tag{2.51}$$

In this expression, we have performed a change of variable $R \to V = m\omega^2_R R^2/2$. Evaluating this formula numerically, we obtain a superposition of many Fermi surfaces at different fillings as shown in the right panels of Fig. 2.18. The up panel is for the non-interacting system while the down panel is for the system with d-wave pseudogap. Although the presence of the trap breaks the homogeneity of the system, the Raman scattering map still gives useful information of the Fermi surface of the center of the trap. In particular, the d-symmetry observed explains the feature of the d-wave pseudogap phase.

We can event extract the Fermi surface for the density of the center of the trap by performing two measurements with fixed chemical potentials $\mu$ and $\mu' = \mu + \Delta\mu$. Then the difference of these two maps contains the information about the Fermi surface of the center part of the trap

$$\mathbf{R}(\mu') - \mathbf{R}(\mu) \propto \int_0^{\mu'} dV \; A(\mathbf{q}, \Omega; \mu' - V) - \int_0^{\mu} dV \; A(\mathbf{q}, \Omega; \mu - V) = \Delta\mu A(\mathbf{q}, \Delta\Omega; \mu).$$

This is shown in the left panels of Fig. 2.18 for a non-interacting system (upper panel) and a system with d-wave pseudogap (lower panel).

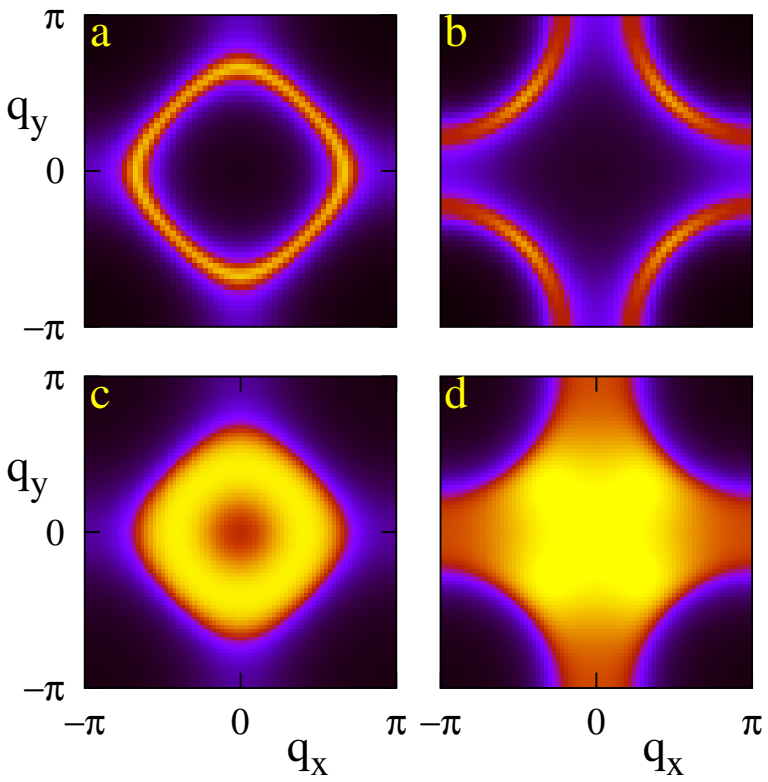


**Figure 2.18:** The right panel shows the Fermi in a harmonic trap with LDA calculation. The left panel shows the image by taking the difference of maps which gives the Fermi surface image of the center of the trap

### 2.5.2 Trapped out-going atoms

The second situation is that atoms in both internal states $\alpha$ and $\beta$ are confined the the trap potentials. The energy dispersion of the scattered atoms in the $\beta$-state becomes $\varepsilon_{\beta\mathbf{k}}(\mathbf{R}) = \hbar^2\mathbf{k}^2/2m + \varepsilon^0_\beta - V_\beta(\mathbf{R})$. With same energy reference as $\mu_0$, the amplitude of Raman scattering reads

$$\mathbf{R}(\mathbf{q},\Omega) = \frac{|C|^2 n_1 n_2}{(2\pi)^d \hbar} \int \mathbf{d}^d\mathbf{k} \int \mathbf{d}^d\mathbf{R}\; n_F(\varepsilon_{\beta\mathbf{k}}(\mathbf{R}) - \Omega) A(\mathbf{k}-\mathbf{q}, \varepsilon_{\beta\mathbf{k}}(\mathbf{R}) - \Omega; \mu_{\mathbf{R}}), \tag{2.52}$$

in which $\Omega = \omega_1 - \omega_2 + \mu_0$. The resonance condition of the spectroscopy now becomes

$$\varepsilon_{\mathbf{k}-\mathbf{q}} - \mu + V_\alpha(\mathbf{R}) = \frac{\hbar^2\mathbf{k}^2}{2M} + \varepsilon^0_\beta + V_\beta(\mathbf{R}) - \Omega. \tag{2.53}$$

The threshold condition determined by the Fermi factor now depends explicitly on the position in the trap

$$\hbar^2\mathbf{k}^2/2M + \varepsilon^0_\beta + V_\beta(\mathbf{R})) - \Omega \leq 0. \tag{2.54}$$

The Raman process is illustrated by Fig. 2.19. For two different positions in the trap $\mathbf{R}_1 > \mathbf{R}_2$, the Fermi level is always fixed by the bare chemical potential $\mu_0$. As the $\beta$-atoms now see also the confined potential, the lowest energy level for $\beta$-atoms at $\mathbf{R}_1$ and $\mathbf{R}_2$ are different ($\varepsilon_{\min}(\mathbf{R}_1) \neq \varepsilon_{\min}(\mathbf{R}_2)$). Therefore, the threshold frequency $\Omega_T$ for sizable Raman signal is different for $\mathbf{R}_1$ and $\mathbf{R}_2$.

We remark that the form of the trap decides whether we obtain the threshold corresponding to the center of the trap or the boundary of the trap. Assume that the trap potential for

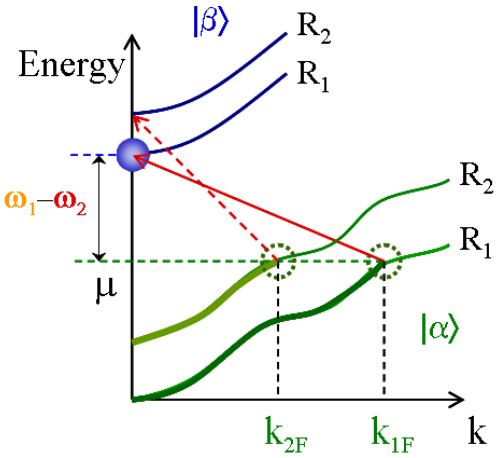


**Figure 2.19:** The upper bands is the $\beta$-state dispersions for two positions $R_1$ and $R_2$. The lower bands are $\alpha$-state dispersions for two position $R_1$ and $R_2$. For both $\alpha$ and $\beta$ states, the bands are shifted by the trap effect. For different position, we find now threshold frequency)

---

both $\alpha$ and $\beta$ states are the same form (with the minimal potential in the center of the trap) as shown in the Fig. 2.19, the first signal will correspond to the probe of the center with the threshold of extinction $\Omega_T = \varepsilon^0_\beta$. The Raman transfer rate now reads

$$\mathbf{R}(\mathbf{q}, \Omega) \propto A(-\mathbf{q}, \Omega_T - \Omega; \mu_0). \tag{2.55}$$

Considering an ideal case where the traps for $\alpha$ and $\beta$ states are exactly the same. For a Raman frequency $\Omega > \Omega_T$, it corresponds to the threshold frequency of the position $\mathbf{R}$ in the trap satisfied $\Omega - V_\beta(\mathbf{R}) = \Omega_T$. The intensity image of the measured Raman signal now again is a superposition of different signals obtained from the center of the trap to the position $\mathbf{R}$. Performing two Raman measurement two different frequencies $\Omega$ and $\Omega + \Delta$ for systems with the same number of atoms, therefore we are able to image the Fermi surface at of the shell at position $\mathbf{R}$ in the trap by making the difference between these two measured images.

## 2.6 Experimental conditions for the measurement

We discuss in this section the possibility to realize the proposed measurements. The main approximation we used in our discussion is that the initial $|\alpha\rangle$ and final $|\beta\rangle$ states do not interact. We show how to choose the states $|\alpha\rangle$ and $|\beta\rangle$ for a gas of Potassium $K^{40}$ or Lithium $Li^6$ atoms.

### 2.6.1 Experimental conditions for Lithium

According to the measurement of scattering length of $Li^6$ in [2, 114], we have the two typical scattering lengths for singlet and triplet channels at zero magnetic field

$$\text{singlet channel:} \quad a_s = 45a_0 \qquad \text{triplet channel:} \quad a_t = -2160a_0. \tag{2.56}$$

So the two atoms in the same spin state (triplet channel) interact much more than two atoms in different spin state (singlet channel). The natural choice for our problem is that the two hyperfine states for the mixture $|\alpha\rangle$ and $|\alpha'\rangle$ are the two lowest energy state

$$|\alpha\rangle = |-1/2, 1\rangle \qquad |\alpha'\rangle = |-1/2, 0\rangle, \tag{2.57}$$

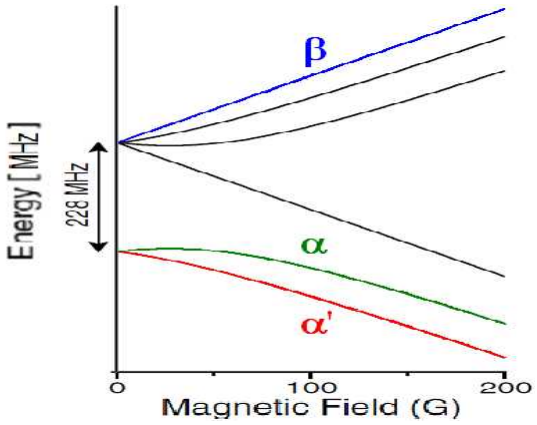


**Figure 2.20:** Hyperfine states of $Li^6$. Reprinted from Ref. [50]

and the internal state $|\beta\rangle$ is the one with the spin state $1/2$. One take the following state because of its well-known properties in atomic physics $\beta\rangle = |1/2, 1\rangle$. The Raman diffusion makes the transition from $|\alpha\rangle$ to $|\beta\rangle$. In order to control the interaction between two internal states $|\alpha\rangle$ and $|\alpha'\rangle$, we introduce a magnetic field near the Feshbach resonance located at $B = 850G$.
In addition, the collision between these two states $|\alpha\rangle$ and $|\alpha'\rangle$ can make the transition to these other hyperfine state. Let us consider the one from $|\alpha\rangle \rightarrow |\beta\rangle$. The main interaction term which causes this transition is the center term $V^c$ (spin exchange). In the [2], we have this decay rate is of the order of $10^{-12}\text{cm}^3/s$ which means the life-time is of the order of a few second ($\gg$ time of experience).

We present here some detail estimations for the realizability of the experiment. One considers the Lithium atom with the Feshbach resonance is about $B \approx 850G$. With the choice of the three state as above, one can do some following estimations.

- Energy shift in the final state $|\beta\rangle$ (Hartree mean field energy)

$$\langle H_{\alpha\beta}\rangle \simeq \frac{4\pi\hbar^2 a_{62}}{m} n_2, \tag{2.58}$$

  where $n_2$ is the density of atom in the state $|\alpha\rangle$. If we have one atom per site then $n_2 = (2/\lambda)^3$ ($\lambda$ is the wave length of the laser which constructs the optical lattice).

$$\langle H_{\alpha\beta}\rangle = \frac{4\pi\hbar^2 a_{62}}{m}\left(\frac{2}{\lambda}\right)^3 = \frac{\hbar^2}{2m}\left(\frac{2\pi}{\lambda}\right)^2 \frac{16 a_{62}}{\pi\lambda} = \frac{16 a_{62}}{\pi\lambda}\varepsilon_{rec}$$

  Let's take $a_{62} = 45a_0 = 25nm$ and $\lambda = 800nm$, then we have: $\Delta\varepsilon = 1.6\ 10^{-2}\varepsilon_{rec}$

- Cross section of the elastic collision in the singlet channel is $\sigma_{62} = 4\pi a_{62}^2$ thus the collision rate is $\gamma_c = n_2\sigma_{62}v_{rec}$ in which $v_{rec}$ is recoil velocity $h/(M\lambda)$. Numerical estimation of the collision rate gives

$$\gamma_c = \left(\frac{2}{\lambda}\right)^3 4\pi a_{62}^2 v_{rec} \approx 10^2 \text{s}^{-1}. \tag{2.59}$$

- Inelastic collision from $|\alpha\rangle$ state to $\beta\rangle$ state
  According to the data in [2, 114] we have $G_{62} = 10^{-12}\text{cm}^3\text{s}^{-1}$, thus the rate of inelastic transition reads

$$\Gamma = n_2.G_{62} = \left(\frac{2}{\lambda}\right)^3 G_{62} \approx 15\text{s}^{-1}. \tag{2.60}$$

The typical time for atom to stay in the lattice is

$$\tau = \frac{L}{v_{rec}} = \frac{Lm}{2\hbar k_{rec}} = 6\ 10^{-5}\text{s}. \tag{2.61}$$

So the loss by inelastic collision is about: $\Gamma\tau \approx 9\ 10^{-4}$ which does not cause any problem for the experiment.

### 2.6.2 Experimental conditions for Potassium

Another candidate of fermionic atom for the choice of the three proposed states in our Raman spectroscopy measurement is potassium 40 ($^{40}$K). In the experimental point of view, this is a well-known atom with the presence of different Feshbach resonances. In a series of experiments

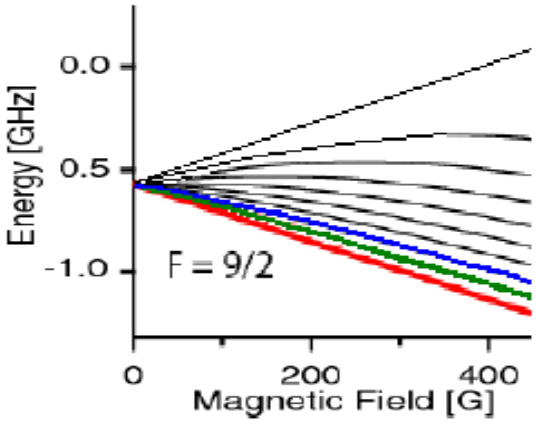


**Figure 2.21:** Hyperfine structure of Potassium $^{40}$K. Reprinted from Ref. [125]

on the BEC-BCS crossover [82, 113], D. S. Jin's group has used the mixture of potassium atoms in two hyperfine states:

$$|\alpha\rangle = |f, m_f\rangle = |9/2, -7/2\rangle \quad \text{and} \quad |\alpha\rangle = |f, m_f\rangle = |9/2, -9/2\rangle.$$

The Feshbach resonance between these two state is located at $B = 202.10 \pm 0.07G$ [96].

For the choice of the $\beta$-state, the hyperfine state $|9/2, -5/2\rangle$ is a very good candidate. In fact, its interaction with the two others states is very small. At zero magnetic field, the two-body scattering length between $|9/2, -5/2\rangle$ and $|9/2, -7/2\rangle$ ($|\alpha\rangle$ and $|\beta\rangle$) is about $a_{1s} = 130a_O \approx 78nm$ while the one between $|9/2, -5/2\rangle$ and $|9/2, -9/2\rangle$ ($|\alpha'\rangle$ and $|\beta\rangle$) is about $a_{2s} = 250a_0 \approx 134nm$ ($a_0$ is the Bohr radius). The interaction between the two hyperfine states $\alpha$ and $\alpha'$ are controlled by the Feshbach resonance, therefore can be tuned to be very large in comparison to the other interactions. In the $^{40}$K this resonance is out of the region in which we have the Feshbach resonance between $\beta$ and $\alpha$, $\alpha'$.

Let us now estimate the energy of the interaction between $\beta$-atoms with $\alpha$ and $\alpha'$ atoms and the lost of elastic collision. The spectroscopy will excite a small number of atoms from $\alpha$-state to $\beta$-state but enough to be counted or observed by TOF image.

- Within the Hartree approximation, we obtain the interaction energy for gases in continuum (discussed in next section)

$$\langle H_{\alpha\beta}\rangle \propto a_{\alpha\beta} k_F E_F, \tag{2.62}$$

in which $k_F$ is the Fermi wave vector and $E_F$ is the energy at the Fermi level. Using the experimental conditions in D. S. Jin's group, we have $k_F \approx 8.6\mu\text{m}^{-1}$, then we have $\langle H_{\alpha\beta}\rangle \sim 0.007E_F$ and $\langle H_{\alpha'\beta}\rangle \sim 0.014E_F$.

- The rate of elastic collision is estimated by $\gamma_c = n_\alpha \sigma v_F$. For the experiment with $n_\alpha \approx 10^{15}m^{-3}$, $\sigma = 4\pi a_{\alpha\beta}^2 \simeq 10^{-13}m^{-2}$ and the Fermi velocity $v_F \approx 2.4 \times 10^{-3}m/s$ [3], the collision rate reads: $\gamma_c \approx 0.24s^{-1}$.

## 2.7 Experiment in D. S. Jin's group

Recently, the first observation of the one-particle excitation with momentum resolution in a two component fermionic gases has been realized in D. S. Jin's group [112]. They have used this technique to follow the BEC-BCS crossover in order to exploit different features like excitation dispersion, the pairing gap and to compare to some phenomenological models.

### 2.7.1 Experimental measurement

In their experimental setup, they have used the quasi-equal mixture of potassium in two hyperfine states $|9/2, -7/2\rangle$, $|9/2, -9/2\rangle$ as discussed above. The Fermi gas mixture consists of $3 \times 10^5$ potassium atoms. By using the RF (radio-frequency) technique with $\omega_{rf} \approx 47$ MHz, they transferred atoms in the initial state $|9/2, -7/2\rangle$ to the final state $|9/2, -5/2\rangle$. Immediately after the RF pulse, they switched off the optical trap and let the atoms expand ballistically during 3 to 6.5 ms before taking a selective resonant absorption image (TOF). The time of flight image gives a direct access to the momentum distribution of the out-going atoms in the $\beta$-state. The idea is essentially the same used in our proposition of direct measurement by time of flight in the last section. This experiment corresponds to the case where we do the Raman spectroscopy with zero transferred momentum ($\mathbf{q} = 0$) and the RF frequency is the difference of frequency of two lasers $\omega = \omega_1 - \omega_2$. This experiment has shown very nice results of the one-particle excitation spectrum for different interaction strength Fig. 2.22. The energy conservation in this case is given by

$$\varepsilon_{\alpha\mathbf{k}} = \frac{\hbar^2\mathbf{k}^2}{2m} + \varepsilon_\beta - \omega_{rf}. \tag{2.63}$$

In experiment, by using the information of the momentum distribution near the resonance (maximum of the RF signal), one can reconstruct the energy dispersion of single atom in the initial $\alpha$-state $E_s = \hbar^2\mathbf{k}^2/2m + \varepsilon_\beta - \omega_{rf}$. Performing this measurement for both the non-interacting gases and over the BEC-BCS crossover, D. S. Jin has shown that this kind probe on one-particle excitation can give direct access to the physics quantity like the energy dispersion, the pairing-gap, or different kind of excitations (single fermionic excitation, pair destroyed excitation ...).

### 2.7.2 Explanation of experimental spectra

We now analyze the experimental data and make some comparison between our proposed measurement applied in the case of zero transferred momentum with the experiment realized by D. S. Jin's group. As shown in the section 2.1.4, the rate of transferred atoms in the $\beta$-state is

$$\mathbf{R}(\mathbf{k}, \Omega) = \frac{|C|^2 n_1 n_2}{\hbar}\, n_F(\varepsilon_\beta + \hbar\mathbf{k}^2/2M - \Omega) A(\varepsilon_\beta + \hbar\mathbf{k}^2/2M - \Omega, \mathbf{k}), \tag{2.64}$$

[3] This velocity corresponds to the Fermi wave vector $k_F \approx 8.6 \pm 0.3\mu m^{-1}$ in the experiment of Jin's group

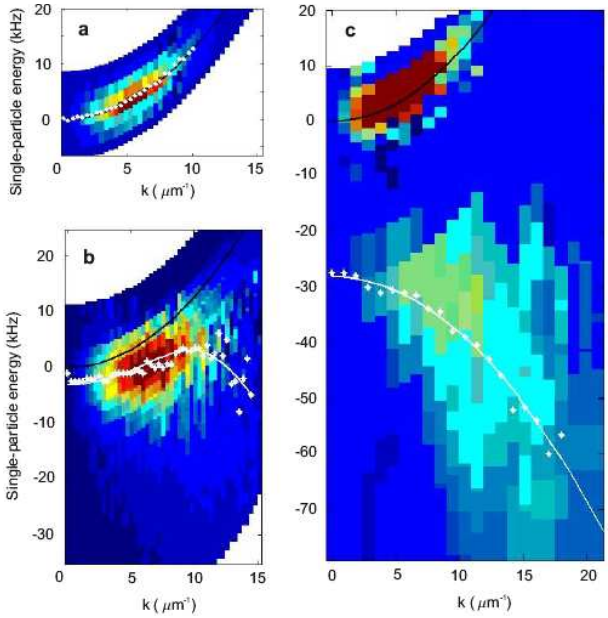


**Figure 2.22:** Single-particle excitation spectra obtained using RF spectroscopy for ultracold atoms. Plotted are intensity maps (independently scaled for each plot) of the number of atoms out coupled to a weakly interacting spin state as a function of the single-particle energy $E_s$ and wave vector k. The black lines are the expected dispersion curve for an ideal Fermi gas. The white points (*) mark the center of each fixed energy distribution curve. a) Data for a very weakly-interacting Fermi gas. The Fermi wave vector $k_F$ is $8.6 \pm 0.3$ $\mu$m$^{-1}$. b) Data for a strongly interacting Fermi gas $1/k_F a = 0$ and $T \approx T_c$. The white line is a fit of the centers to a BCS-like dispersion. c) Data for a gas on the BEC side of the resonance where $1/k_F a \approx 1$ and the measured two-body binding energy is $h \cdot (25 \pm 2)$ kHz. The upper feature is attributed to unpaired atoms and the lower feature is attributed to molecules. The white line is a fit to the centers using a quadratic dispersion. Reprinted from Ref. [112].

---

where $\Omega = \omega_{rf} + \mu$. Here the energy origin is taken as the Fermi level of the system in the $\alpha$-state. For a fixed momentum, the maximal peak of the RF signal corresponds to the RF resonance in which the following condition is satisfied: $\xi_{\alpha\mathbf{k}} = \varepsilon_\beta + \hbar\mathbf{k}^2/2M - \Omega$ where $\xi_{\alpha\mathbf{k}}$ is measured from the Fermi level. In this relation, we remark that $\xi_{\alpha\mathbf{k}} < 0$ which means that by using this spectroscopy technique, we have the same access as ARPES to the negative frequency part of the spectral function.

### Non-interacting Fermi gases BCS-side

The first experiment has been performed at the limit of weakly interacting gases in which the experimental temperature is higher than the BCS-critical temperature. In this case, the system is in the normal phase and the atoms in the $\alpha$-state and the $\beta$-state have the same energy dispersion which is $\hbar^2k^2/2m$. Thus the RF resonance occurs when $\omega_{RF} = \varepsilon_\beta$. In the intensity plot, we see clearly the resulting dispersion $E_s = \hbar^2k^2/2m$.

### Preformed molecular BCS-like behavior at Feshbach resonance

Another measurement is on the BCS side but with a temperature higher than $T_c$. In this case, we do not expect any property of superfluidity. However, as proposed by theory, we expect to see a pseudogap of preformed BCS-molecular. This phase has a similar spectral function

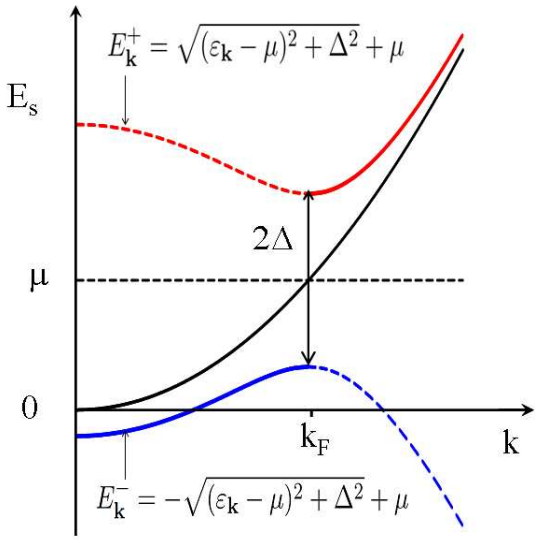


**Figure 2.23:** The pseudogap model for the gas at unitary limit. The black line is the free dispersion while the blue and red curves are two branches of quasiparticle dispersion separated by $2\Delta$ at the Fermi level. The pseudogap comes from the presence of preformed pairs of fermions.

with BCS phase but without any superfluid order $\langle c^{\dagger}_{\mathbf{k}\uparrow} c^{\dagger}_{-\mathbf{k}\downarrow} \rangle = 0$. The energy dispersion of this phase can be obtained in replacing the superfluid gap $\Delta_{SF} = 0$ by the pseudogap $\Delta_{ps}$ (see Fig. 2.23).

$$A(\mathbf{k}, \omega) = u^2_{\mathbf{k}} \delta(\omega - E^{-}_{\mathbf{k}}) + v^2_{\mathbf{k}} \delta(\omega - E^{+}_{\mathbf{k}}) \tag{2.65}$$

in which $E^{\pm}_{\mathbf{k}} = \pm\sqrt{(\varepsilon_{\mathbf{k}} - \mu)^2 + \Delta^2_{ps}}$ are the quasiparticle excitation energies and $u^2_{\mathbf{k}}$, $v^2_{\mathbf{k}}$ are the spectral weights. Similar to the ARPES technique, this measurement probes only the negative energy part with the dispersion $\xi_{\mathbf{k}} = E^{-}_{\mathbf{k}}$. Replacing this dispersion in the resonance condition, we obtain

$$E^{-}_{\mathbf{k}} = \hbar^2 \mathbf{k}^2 / 2m + \varepsilon_{\beta} - \omega_{RF} - \mu. \tag{2.66}$$

Thus the quantity defined in the experiment $E_s = \hbar^2 \mathbf{k}^2 / 2m + \varepsilon_{\beta} - \omega_{RF}$ can be now fitted with the dispersion $\mu + E^{-}_{\mathbf{k}}$.

### BEC side with double branches

In the BEC side, we have a phase where fermionic atoms of different hyperfine states start to pair up to form molecules under the effect of strong interaction. The one-particle spectrum consists then of one part single unpaired atoms and another part from the breaking up of molecules. The first part is the excitation at low energy while the second part concerns high energy excitation (Fig. 2.24).

In order to figure out the energy dispersion of the second excitation, we use an energy conservation argument at resonance as shown in Fig. 2.25. In the initial state, we have a system of N atoms with energy $E^N_i$ which can be decomposed in the sum of N-2 atoms $E^{N-2}_i$

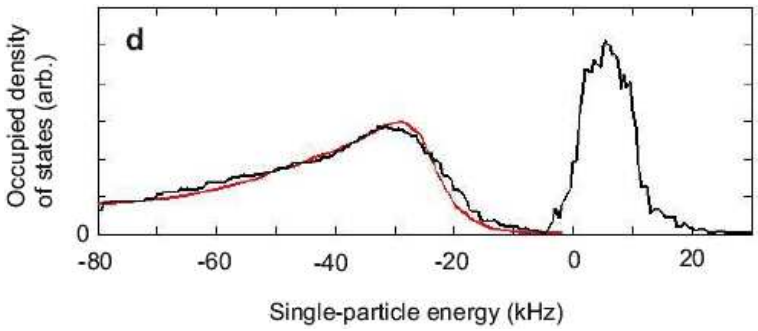


**Figure 2.24:** RF spectrum of the Fermi gases on the BEC-side. The spectrum presents two energy scales: (i) low energy scale characterizes the single unpaired atom excitation, (ii) high energy scale characterizes the excitations of breaking up of molecules. Reprinted from Ref. [112].

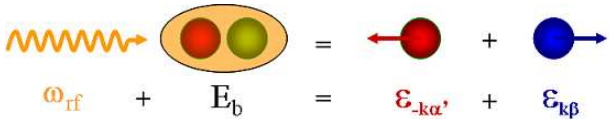


**Figure 2.25:** Energy conservation for the RF spectroscopy in BEC limit.

---

and one molecule $E_b$ (binding energy). We suppose that the molecule in the condensed state at zero-momentum. In the final state after applying the RF pulse, the molecule is destroyed and breaks into two singles atoms of momentum $\mathbf{k}$ and $-\mathbf{k}$ (one in $\mathbf{k}\beta$-state other in $-\mathbf{k}\alpha'$-state). Thus we obtain a system of N-1 particles $E_f^{N-1} = E_i^{N-2} + \varepsilon_{-\mathbf{k}\alpha'}$ and an out-going atom in the $\beta$-state with energy $\hbar^2\mathbf{k}^2/2m + \varepsilon_\beta$. The energy conservation law reads

$$E_i^{N-2} + E_b + \omega_{rf} = E_i^{N-2} + \varepsilon_{-\mathbf{k}\alpha'} + \hbar^2\mathbf{k}^2/2m + \varepsilon_\beta. \tag{2.67}$$

Thus the single particle excitation energy $E_s$ which can determined from RF experiment reads

$$E_s = \hbar^2\mathbf{k}^2/2m + \varepsilon_\beta - \omega_{rf} = E_b - \varepsilon_{-\mathbf{k}\alpha'}. \tag{2.68}$$

In the experimental data on the BEC side, we observe the structure of two branches. The first one is quite similar to the free fermion dispersion which is the unpaired particle excitation while the second one with an negative effective mass corresponds to $E_b - \varepsilon_{-\mathbf{k}\alpha'} = E_b - \hbar^2\mathbf{k}^2/2m^*$ dispersion with $m^*$ is the effective mass of the $\alpha'$ atoms (see Fig. 2.22 right panel).

### 2.7.3 Effect of the harmonic trap on the RF experiment

All the analysis above has been done in the homogeneous case. In the following, we would like now to study the effect of the optical trap (harmonic trap) on the obtained data obtained in D. S. Jin's experiment. So during the spectroscopy, the whole system is trapped by the harmonic potential. In particular as well the out-going atom is trapped. The initial atoms and the out-going atoms see respectively the trap potentials $V_\alpha(\mathbf{r})$, $V_\beta(\mathbf{r})$. The transfer rate is estimated within local density approximation

$$\mathbf{R}(\mathbf{k}, \omega_{rf}) = \frac{|C|^2 n_1 n_2}{\hbar} \int \mathbf{dr}^d n_F(\varepsilon_{\beta\mathbf{k}}(\mathbf{r}) - \Omega) A(\varepsilon_{\beta\mathbf{k}}(\mathbf{r}) - \Omega, \mathbf{k}; \mu_\mathbf{r}), \tag{2.69}$$

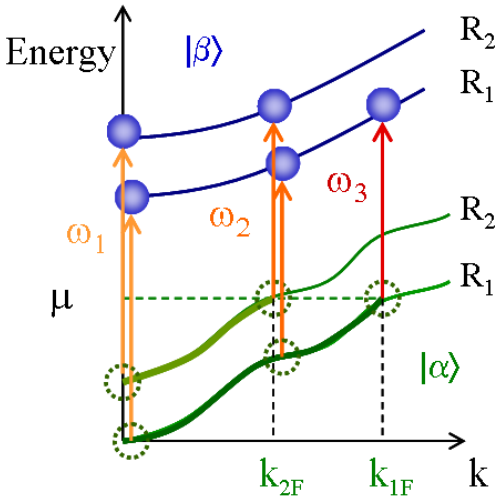


**Figure 2.26:** The upper bands is the $\beta$-state dispersions for two positions $R_1$ and $R_2$. The lower bands are $\alpha$-state dispersions for two position $R_1$ and $R_2$. For both $\alpha$ and $\beta$ states, the bands are shifted by the trap effect. For different positions, we find different threshold frequencies)

---

where $\Omega = \omega_{RF} - \mu_0$ with $\mu_0$ the energy reference and $\varepsilon_{\beta\mathbf{k}}(\mathbf{r}) = \varepsilon_\beta + \hbar\mathbf{k}^2/2M + V_\beta(\mathbf{r})$. The energy conservation relation now reads

$$\xi_{\alpha\mathbf{k}}(\mathbf{r}) = \varepsilon_\beta + \hbar\mathbf{k}^2/2M + V_\beta(\mathbf{r}) - \omega_{RF} - \mu_0. \tag{2.70}$$

In the free Fermi gases, $\xi_{\alpha\mathbf{k}}(\mathbf{r}) = \varepsilon_{\alpha\mathbf{k}} - \mu_\mathbf{r}$ with $\mu_\mathbf{r} = \mu_0 - V_\alpha(\mathbf{r})$. Therefore, this resonance condition becomes $\varepsilon_{\alpha\mathbf{k}} = \varepsilon_\beta + \hbar\mathbf{k}^2/2M + V_\beta(\mathbf{r}) - V_\alpha(\mathbf{r}) - \omega_{RF}$. For the pseudogap case, we have $\xi_{\alpha\mathbf{k}}(\mathbf{r}) = E^-_\mathbf{k}(\mathbf{r}) = -\sqrt{(\varepsilon_{\alpha\mathbf{k}} - \mu_\mathbf{r})^2 + \Delta^2_{\rm ps}}$ and resonance condition becomes

$$\mu_\mathbf{r} + E^-_\mathbf{k}(\mathbf{r}) - V_\beta(\mathbf{r}) = \varepsilon_\beta + \hbar\mathbf{k}^2/2M - \omega_{RF}, \tag{2.71}$$

We now take two situations:

- Let us first assume that the harmonic trap is the same for the initial atom and the out-going atom, i.e. $V_\alpha(\mathbf{r}) = V_\beta(\mathbf{r}) = V_{\rm trap}(\mathbf{r})$. Thus the signal intensity in the case with the trap is

$$\mathbf{R}(\mathbf{k}, \omega_{rf}) = \frac{|C|^2 n_1 n_2}{\hbar} \int \mathbf{dr}^d n_F(\varepsilon_{\beta\mathbf{k}} - \omega_{rf} - \mu_\mathbf{r}) \delta(\varepsilon_{\beta\mathbf{k}} - \omega_{rf} - \xi_{\alpha\mathbf{k}}(\mathbf{r}) - \mu_\mathbf{r}), \tag{2.72}$$

- Assuming that the $\beta$-state do not see any trap potential, we obtain

$$\mathbf{R}(\mathbf{k}, \omega_{rf}) = \frac{|C|^2 n_1 n_2}{\hbar} \int \mathbf{dr}^d n_F(\varepsilon_{\beta\mathbf{k}} - \omega_{rf} - \mu_0) \delta(\varepsilon_{\beta\mathbf{k}} - \omega_{rf} - \xi_{\alpha\mathbf{k}}(\mathbf{r}) - \mu_0). \tag{2.73}$$

### 2.7.4 Numerical simulation including the trap compared to experimental data

We now simulate the RF transfer rate within the local density approximation for a ultracold fermionic gas confined in an isotropic optical trap. Different physics that occur along the BEC-BCS crossover under the effect of the trapping potential can be observed. Our theoretical results obtained by phenomenological models along the BCS-BEC crossover agree quite well with the experimental data obtained by Jin's group.

### Free Fermi gases (BCS-side)

In the first example, we consider the experiment on weakly interacting gases. The set of parameters in the experiment on the free Fermi gases is

- Fermi energy $E_F = h.(9.4 \pm 0.5)$kHz
- The Fermi wave vector $k_F = 8.6 \pm 0.3\ \mu\text{m}^{-1}$
- Temperature $T/T_F = 0.18$ where $T_F = E_F/k_B$

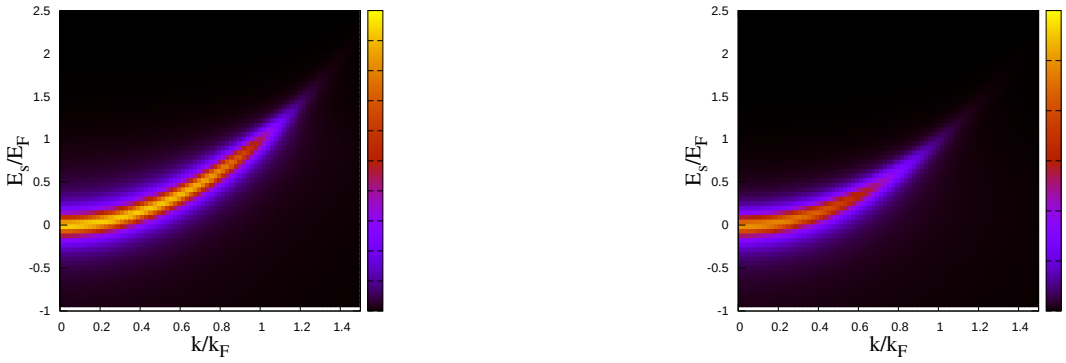


**Figure 2.27:** Contour plot of the RF intensity in the plane of $(E_s, \mathbf{k})$ for free Fermi gases. The left panel is for the homogeneous system while the right one is for experimentally realizable conditions with a harmonic trap. The curve of maximum signal corresponds to the resonance condition which gives a parabolic form of the single-particle excitation.

We simulated the model for different configurations discussed above in the trap with the choice in which the trap potential acts more and less in the same way for atoms in both the $\alpha$ and $\beta$ states. In order to see the trap effect on the measurement, we compare the signal obtained in the trap to the homogeneous case (see Fig. 2.27) for a system with the same Fermi wavevector $\mathbf{k}_F$. The comparison is shown in the Fig. 2.28 in which the left panel is the simulation for a homogeneous system while the right panel is for the system in a harmonic trap. We remark that for the homogeneous system the intensity of system along the resonant curve is uniform till the Fermi level. We do not observe a clear jump at the Fermi level because of the finite temperature. In contrast, for the non-homogeneous system, the signal density is maximal for small momentum and very weak for high momentum near the Fermi level. In fact, the small momentum state is filled every in the trap while the high momentum close to the Fermi level is essentially filled only in the center of the trap. That explains why the obtained signal is very weak near $\mathbf{k}_F$. By integrating the RF intensity over the $\mathbf{k}$-space, we obtain the density distribution in frequency. Fig. 2.28 left panel shows the density distribution in the trap for the free Fermi gases. It is very good agreement with the experimental result obtained in Fig. 2.28 right panel.

### BCS-like behavior at Feshbach resonance

The second experiment is realized at the Feshbach resonance. At this special point, there's no typical energy scale and the scattering parameter $a_s$ is divergent. This limit is situated in the middle of the BCS limit and the molecular BEC limit. Under a critical temperature $T_c$, we have a super fluid formed by pairs of Fermi gas while at higher temperature the superfluid order disappears but the gap still remains in the spectral function. The appearance of this

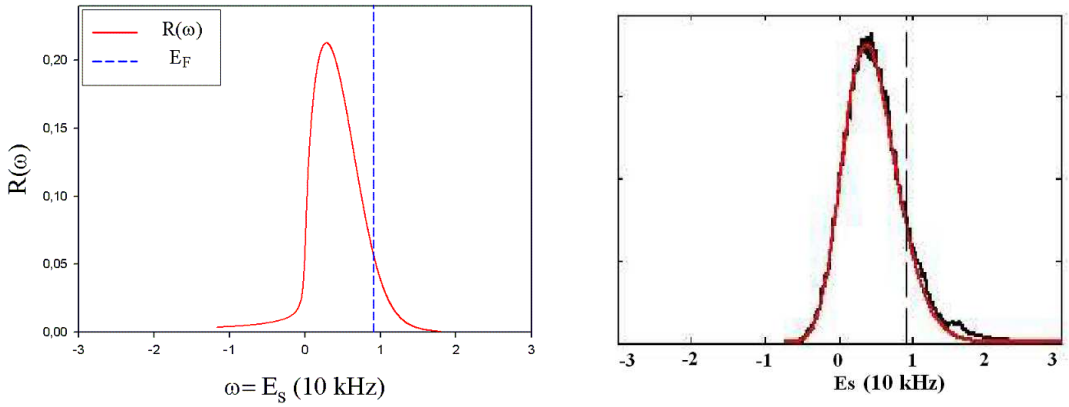


**Figure 2.28:** RF spectral function after integrating over the momentum. This distribution is calculated in the presence of the trap potential (left panel). The main form agrees to the one measured from Jin's experiment (right panel).

pseudogap can be interpreted as the signature of the preformed pairs even in the normal state of the mixture. In the simulation, we supposed it has the same behavior as the BCS gap. The parameters of the experiment on the interacting Fermi gases at this resonant point are:

- Temperature $T/T_c = 0.9 \pm 0.1$ or $T = 0.18T_F$ (other measurement for non-interacting initial gas at temperature $T_{\text{int}}/T_F = 0.1$ which leads to $T < T_c$ at unitary limit).
- Before ramping the magnetic field to tune the interaction, the Fermi energy is $E_F = h.(9.4 \pm 0.5)$kHz and the Fermi wave vector is $k_F = 8.6 \pm 0.3\ \mu\text{m}^{-1}$.

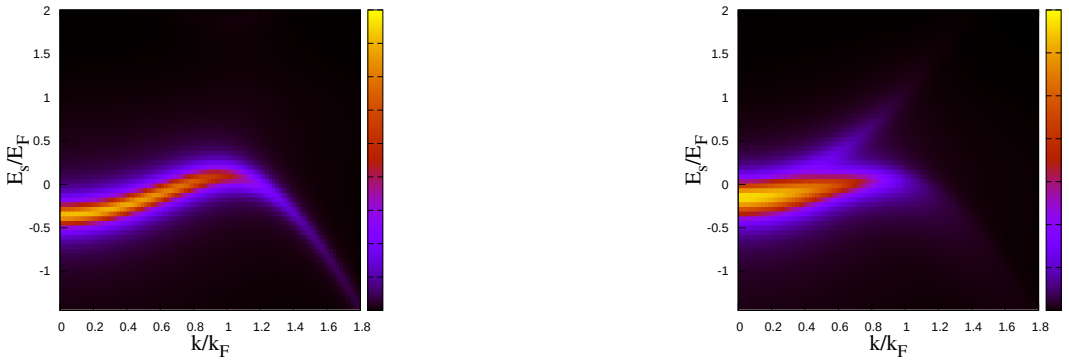


**Figure 2.29:** Contour plot of the RF intensity in the plane of $(E_s, \mathbf{k})$ for Fermi gases at Feshbach resonance $(1/k_F a_s = 0)$. The left panel is for the homogeneous system while the right one is the experimentally realizable conditions with an isotropic harmonic trap. The curve of maximum signal for fixed momentum corresponds to the resonance condition which gives the energy dispersion the single-particle excitation.

In the Fig. 2.29, we present the comparison of the intensity plot of the RF signal of a homogeneous system (left panel) to the system confined in an optical trap. We remark that in this case the trap effect deforms a lot the energy dispersion of quasiparticle excitations. Two main effects happened with the presence of the trap. The first one is the enhancement at low momentum as above. The second one is that the RF distribution in frequency for fixed momentum is more broad than the homogeneous case. This effect comes from the fact that

the pseudogap is different for different fillings (maximal in the center of the trap and minimal on the boundary).

The lowest energy level (corresponding to $\mathbf{k} = 0$)of the energy dispersion of the phenomenological model for pseudogap phase $E_s(\mathbf{k}) = \mu_\mathbf{r} - \sqrt{(\varepsilon_{\alpha\mathbf{k}} - \mu_\mathbf{r})^2 + \Delta_\mathbf{r}^2}$ is shifted by $\mu_\mathbf{r} - \sqrt{\mu_\mathbf{r}^2 + \Delta_\mathbf{r}^2}$. Therefore the lowest level for the energy dispersion corresponding to the shifted in the center of the trap $\mu_0 - \sqrt{\mu_0^2 + \Delta^2}$. In order to compare the LDA approximation result to the experimental data, we need to fit with three variables: chemical potential $\mu$, the pseudogap $\Delta$ and temperature $T$ in the center of the trap. In the fit, we fixed the shift from zero origin $\mu_0 - \sqrt{\mu_0^2 + \Delta^2}$ by the experimental value. The most difficult thing is to determine the dependence of the pseudogap at unitary limit on the temperature[4] and the spatial dependence chemical potential $\Delta_\mathbf{r} = \Delta(T, \mu_\mathbf{r})$ within LDA. In trying to interpret qualitatively the experimental data, we accept that the pseudogap respects the behavior of the BCS-gap[5].

The integrating image over the $\mathbf{k}$-space of the RF spectral gives the direct access to the density distribution in frequency. In this RF spectrum we recognize the pseudogap which shifts the whole spectrum to the left in comparison with the non-interacting gases.

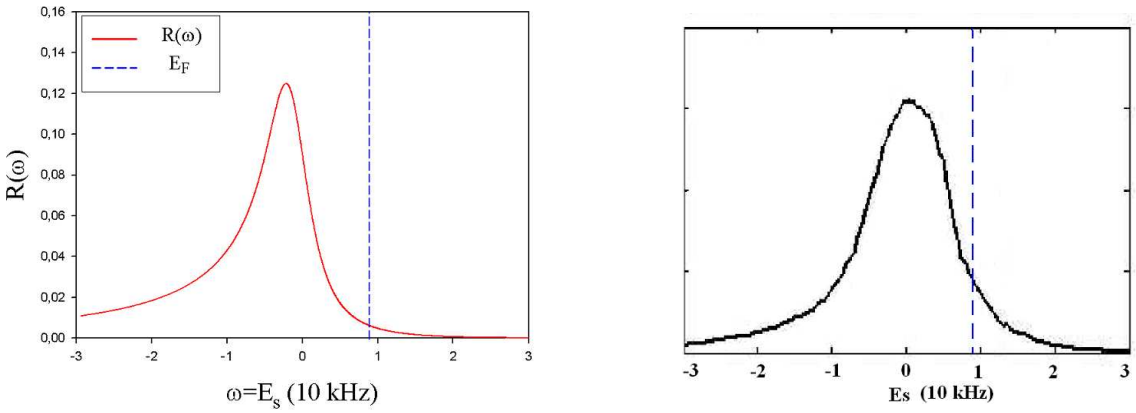


**Figure 2.30:** RF spectral function after integrating over the momentum. This distribution is calculated in the presence of the trap potential (left Fig). This measurement shows clearly the existence of a pseudogap which is different from the non-interacting case Fig. 2.28.

### Molecular limit (BEC-side)

We turn now to the opposite side of the Feshbach resonance (the BEC limit), the set of experimental parameters is:

- Molecular binding energy $E_b = h.(25 \pm 2)$Hz.
- Temperature of non-interacting gas $T = 0.18T_F$.
- Scattering length $1/k_F a = 1$.

In order to understand the double branch structure obtained in the experiment at the temperature $T = 0.18T_F$, we used the most simple model explaining the physics of the BEC-BCS

[4]The temperature of the interacting system at unitary limit is unknown parameter. The only controlled temperature is the one of the initial non-interacting gases before tuning to the Feshbach resonance.

[5]The BCS-gap is quite correct even in the limit of strong interaction.

crossover in Ref. [32]. The simulation was performed for different configurations discussed above with the same choice for the trapping potential. Within this theory, below the critical temperature $T_c$, the effects of fluctuations are small even for strong coupling. Therefore the quasiparticle dispersions in a homogeneous system can be obtained by BCS mean-field theory:

$$E_{\mathbf{k}}^{\pm} = \mu \pm \sqrt{(\varepsilon_{\mathbf{k}} - \mu)^2 + \Delta^2} \tag{2.74}$$

in which $\mu$ and $\Delta$ are solutions of the self-consistency equations. At zero temperature, we have $\mu = -E_b/2 + 2\varepsilon_F(k_F a_s)/3\pi$ and $\Delta = (16/\pi)^{1/2}\varepsilon_F/\sqrt{k_F a_s}$. Here, $E_b$ is the pair binding energy $E_b = 1/ma_s^2$. On Fig. 2.31, we obtained two branches of quasiparticles. The upper

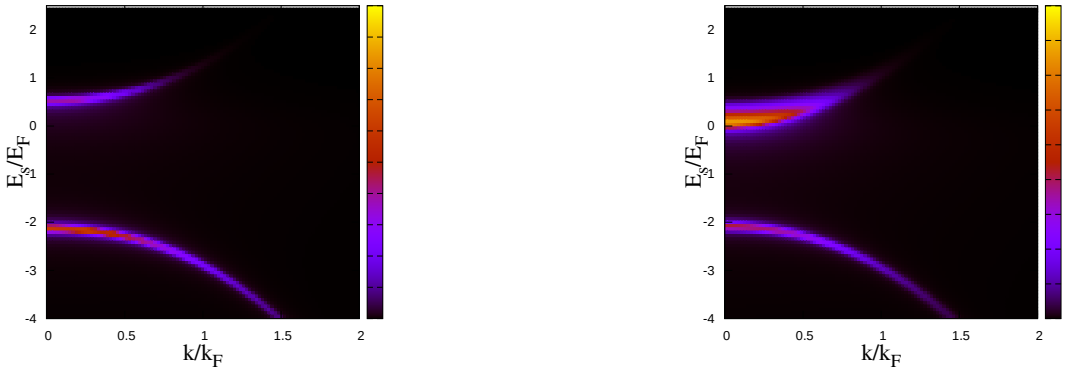


**Figure 2.31:** Contour plot of the RF intensity in the plane of $(E_s, \mathbf{k})$ for Fermi gases on the BEC-side $(1/k_F a_s = 1)$. The left panel is for the homogeneous system while the right one is the experimentally realizable conditions with an isotropic harmonic trap. The curve of maximum signal for fixed momentum corresponds to the resonance condition which gives the energy dispersion the single-particle excitation.

branch corresponds to the thermal excitations of single particle while the lower branch reflects the excitation of molecules. The integrated RF signal over the momentum space is presented in Fig 2.32.

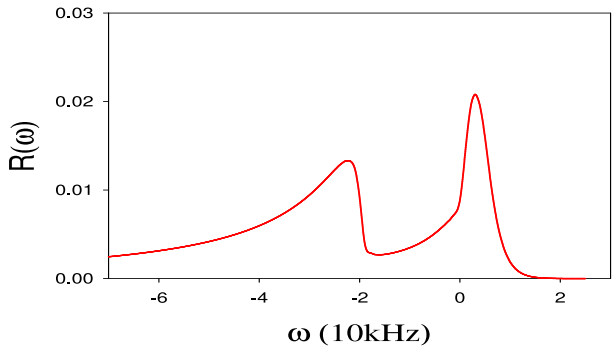


**Figure 2.32:** RF spectral function after integrating over the momentum. This distribution is calculated in the presence of the trap potential. This measurement shows clearly the existence of two energy scales corresponding to the two branches obtained in Fig. 2.31.

## 2.8 Conclusions and perspectives

In conclusion, we have proposed a Raman spectroscopy technique which, analogously to ARPES in solid-state physics, is able to probe the one-body Green's function. Via various illustrations from simple systems without interaction to strongly correlated systems, we have shown that within Raman spectroscopy we can perform two possibles measurements. The first one consists of measuring the Raman spectrum near the extinction threshold both in energy resolved and momentum resolved. This measurement gives access to the quasiparticles just near inside the Fermi surface thus provides directly the image of the Fermi surface. The second measurement consists of performing the energy resolved Raman spectroscopy with a fixed transfer momentum (or RF spectroscopy with zero transfer momentum). The time of flight imaging of the excited cloud can help to reconstruct the Fermi surface of the interacting system and understand the single particle excitations in all energy scale.

The problem of a harmonic trap which is encountered frequently in an ultracold atom experiment is also discussed. We have shown that, the measured Raman signal in this condition will be much more different from a homogeneous system. However, some main properties of the quasiparticle excitations are still preserved. For example, the d-wave symmetry of the pseudogap can be observed even with the presence of the harmonic trap. Within the reasonable experimental condition, the experimental can be interpreted by the local density approximation.

With the success of the first experiment of momentum resolved RF spectroscopy realized in Jin's group, we believe that this technique will play an important role in the experimental characterization of the novel quantum states of matter that can be obtained with ultracold atoms both in continuum and optical lattices such as the d-wave pseudogap phase, the phase with preformed pairs or the phase with long-range order (the gapless superfluid in a polarized fluid).

**First article:**

Measuring the One-Particle Excitations of Ultracold Fermionic Atoms by Stimulated Raman Spectroscopy

*Physical Review Letters* 98, 240402 (2007)

Eprint: cond-mat/0611206

# Measuring the One-Particle Excitations of Ultracold Fermionic Atoms by Stimulated Raman Spectroscopy

Tung-Lam Dao,[1] Antoine Georges,[1] Jean Dalibard,[2] Christophe Salomon,[2] and Iacopo Carusotto[3]
[1]*Centre de Physique Théorique, CNRS, Ecole Polytechnique, Route de Saclay, 91128 Palaiseau Cedex, France*
[2]*Laboratoire Kastler-Brossel, CNRS, Ecole Normale Supérieure, 24, rue Lhomond, 75231 Paris Cedex 05, France*
[3]*CNR-INFM BEC Center and Università di Trento, 38050 Povo, Italy*
(Received 8 November 2006; published 14 June 2007)

We propose a Raman spectroscopy technique which is able to probe the one-particle Green function, the Fermi surface, and the quasiparticles of a gas of strongly interacting ultracold atoms. We give quantitative examples of experimentally accessible spectra. The efficiency of the method is validated by means of simulated images for the case of a usual Fermi liquid as well as for more exotic states: specific signatures of, e.g., a $d$-wave pseudogap are clearly visible.

DOI: 10.1103/PhysRevLett.98.240402 PACS numbers: 03.75.Lm, 32.80.Pj, 71.10.Fd, 71.30.+h

The remarkable advances in handling ultracold atomic gases have given birth to the new field of "condensed matter physics with light and atoms." Key issues in the physics of strongly correlated quantum systems can be addressed from a new perspective in this context. The observation of the Mott transition of bosons in optical lattices [1], the superfluidity of fermionic gases [2], and the recent imaging of Fermi surfaces [3] have been important milestones in this respect. Ultimately fermionic atoms in optical lattices [4,5] could help in understanding some outstanding problems of condensed matter physics, such as high-temperature superconductivity. In this context, a key issue is the nature of the low-energy excitations of low-dimensional strongly interacting Fermi systems. There is abundant experimental evidence that those are highly unconventional, departing from standard Fermi-liquid theory.

In this Letter, we study how to probe the one-particle excitations of interacting ultracold fermionic atoms using stimulated Raman spectroscopy. This technique has been considered previously in the context of cold atomic gases, as an outcoupling technique to produce an atom laser [6], and also as a measurement technique for bosons [7–10] and fermions [11,12]. Here, we demonstrate that this technique provides, for strongly interacting fermion gases, a momentum-resolved access to key properties of the quasiparticle excitations, such as their dispersion relation and lifetime. It also allows for a determination of the Fermi surface itself in strongly interacting regimes, whereas previously demonstrated methods [3] apply to the noninteracting case. Furthermore, it is shown that the suppression of quasiparticles due to a pseudogap in the excitation spectrum can also be detected by this method.

In a conventional Fermi liquid, low-energy excitations are built out of quasiparticles [13]. Those are characterized by their dispersion relation, i.e., the energy $\xi_{\mathbf{k}}$ (measured from the ground-state energy) necessary to create such an excitation with (quasi)momentum $\mathbf{k}$. The interacting system possesses a Fermi surface (FS) defined by the location in momentum space on which the excitation energy vanishes: $\xi_{\mathbf{k}_F} = 0$. Close to a given point on the FS, the quasiparticle energy vanishes as: $\xi_{\mathbf{k}} \sim \mathbf{v}_F(\mathbf{k}_F) \cdot (\mathbf{k} - \mathbf{k}_F) + \cdots$, with $\mathbf{v}_F$ the local Fermi velocity (inversely related to the effective mass). Quasiparticle excitations have a finite lifetime $\Gamma_{\mathbf{k}}^{-1}$ and are well defined provided $\Gamma_{\mathbf{k}}$ vanishes faster than $\xi_{\mathbf{k}}$ as the FS is approached ($\Gamma_{\mathbf{k}} \sim \xi_{\mathbf{k}}^2$ in Fermi-liquid theory). In contrast, one-particle excitations in the "normal" (i.e., nonsuperconducting) state of the cuprate superconductors (SC) reveal strong deviations from this behavior [14]. Reasonably well-defined quasiparticle excitations only exist close to the diagonal direction of the Brillouin zone (the "nodal" direction along which the $d$-wave gap vanishes in the SC phase), and even there $\Gamma_{\mathbf{k}}$ is rather large. Away from this direction (in the "antinodal" region), excitations appear to be short-lived and gapped already above the SC critical temperature (the so-called pseudogap phenomenon). This momentum-space differentiation is a key to the physics of cuprates.

Experiments probing directly nondiagonal one-particle correlators $\langle \psi^\dagger(\mathbf{r}, t)\psi(\mathbf{r}', t')\rangle$ of a many-body system are therefore highly desirable but also relatively scarce. Most physical measurements indeed provide information on two-particle correlators of the form $\langle \psi^\dagger(\mathbf{r}, t)\psi(\mathbf{r}, t)\times \psi^\dagger(\mathbf{r}', t')\psi(\mathbf{r}', t')\rangle$ [15]. Examples are neutron scattering or transport measurements in the solid-state context [13] and Bragg scattering [18] or noise correlations measurements [19] in the cold atom context. For Bose systems with a finite condensate density $n_0$, the two-particle correlator is closely related to the one-particle correlator via terms such as $n_0\langle \psi^\dagger(\mathbf{r}, t)\psi(\mathbf{r}', t')\rangle$. By contrast, in Fermi systems, the distinction between one- and two-particle correlators is essential and specific measurement techniques of the former are requested.

In solids, angle-resolved photoemission spectroscopy (ARPES) provides a direct probe of the one-particle spectrum [20], and has played a key role in revealing momentum-space differentiation in cuprates [14]. It consists in measuring the energy and momentum of electrons emitted out of the solid exposed to an incident photon

 

beam. In the simplest approximation, the emitted intensity can be related to the single-electron spectral function, defined at $T = 0$ and for $\omega < 0$, i.e., for holelike excitations by $A(\mathbf{k}, \omega) = \sum_n |\langle \Psi_n^{N-1} | \psi_{\mathbf{k}} | \Psi_0^N \rangle|^2 \delta(\omega + \mu + E_n - E_0)$. In this expression, $\psi_{\mathbf{k}}$ is a destruction operator for an electron with momentum $\mathbf{k}$, $\Psi_0^N$ is the ground state of the $N$-particle system, and $\Psi_n^{N-1}$ are the eigenstates of the system with one less particle. In a conventional Fermi liquid, and for momenta close to the FS, the spectral function can be separated [13] into a coherent quasiparticle contribution and an incoherent contribution: $A = A_{\mathrm{QP}} + A_{\mathrm{inc}}$, with $\pi A_{\mathrm{QP}}(\mathbf{k}, \omega) \simeq Z_{\mathbf{k}} \Gamma_{\mathbf{k}} / [(\omega - \xi_{\mathbf{k}})^2 + \Gamma_{\mathbf{k}}^2]$ and $A_{\mathrm{inc}}$ widely spread in frequency. Only a finite fraction $Z_{\mathbf{k}} < 1$ of the total spectral weight corresponds to long-lived quasiparticle excitations.

In this Letter, we consider stimulated Raman spectroscopy on a two-component mixture of ultracold fermionic atoms in two internal states $\alpha$ and $\alpha'$. Atoms are transferred from $\alpha$ into another internal state $\beta \neq \alpha, \alpha'$, through an intermediate excited state $\gamma$, using two laser beams of wave vectors $\mathbf{k}_{1,2}$ and frequencies $\omega_{1,2}$. If $\omega_1$ is sufficiently far from single photon resonance to the excited $\gamma$ state, we can neglect spontaneous emission. Eliminating the excited state, we write an effective Hamiltonian, $\hat{V} = C \int d\mathbf{r} \psi_\alpha^\dagger(\mathbf{r}) \psi_\beta(\mathbf{r}) e^{i(\mathbf{k}_1 - \mathbf{k}_2)\cdot\mathbf{r}} a_1^\dagger a_2 + \mathrm{H.c.}$, in which $a_1^\dagger$ ($a_2$) denotes the creation (destruction) operator of a photon, respectively, in mode 1 (2) and the constant $C$ is proportional to the product of the dipole matrix elements $d_{\alpha\gamma}$ and $d_{\beta\gamma}$ of the optical transitions and inversely proportional to the detuning from the excited state.

The total transfer rate to state $\beta$ can be calculated [7–9] using the Fermi golden rule:

$$R(\mathbf{q}, \Omega) = |C|^2 n_1 (n_2 + 1) \int_{-\infty}^{\infty} dt \int d\mathbf{r} d\mathbf{r}' e^{i[\Omega t - \mathbf{q}\cdot(\mathbf{r} - \mathbf{r}')]} \times g_\beta(\mathbf{r}, \mathbf{r}'; t) \langle \psi_\alpha^+(\mathbf{r}, t) \psi_\alpha(\mathbf{r}', 0) \rangle. \quad (1)$$

Here $\mathbf{q} = \mathbf{k}_1 - \mathbf{k}_2$ and $\Omega = \omega_1 - \omega_2 + \mu$ with $\mu$ the chemical potential of the interacting gas and $n_{1,2}$ the photon numbers present in the laser beams. Assuming that no atoms are initially present in $\beta$ and that the scattered atoms in $\beta$ do not interact with the atoms in the initial $\alpha$, $\alpha'$ states, the free propagator for $\beta$-state atoms in vacuum is to be taken: $g_\beta(\mathbf{r}, \mathbf{r}'; t) \equiv \langle 0_\beta | \psi_\beta(\mathbf{r}, t) \psi_\beta^\dagger(\mathbf{r}', 0) | 0_\beta \rangle$. The correlation function entering (1) is proportional to the one-particle Green function [21] $\langle \psi_\alpha^+(\mathbf{r}, t) \psi_\alpha(\mathbf{r}', 0) \rangle = -i G_\alpha^<(\mathbf{r}', \mathbf{r}, -t)$ of the strongly interacting Fermi system. For a uniform system, the rate (1) can be related to the spectral function $A(\mathbf{k}, \omega)$ of atoms in the internal state $\alpha$ by [8]

$$R(\mathbf{q}, \Omega) \propto \int d\mathbf{k} n_F(\varepsilon_{\mathbf{k}\beta} - \Omega) A(\mathbf{k} - \mathbf{q}, \varepsilon_{\mathbf{k}\beta} - \Omega), \quad (2)$$

in which the Green function has been expressed in terms of the spectral function and the Fermi factor $n_F$ as [13] $G_\alpha^<(\mathbf{k}, \omega) = i n_F(\omega) A(\mathbf{k}, \omega)$, and $\varepsilon_{\mathbf{k}\beta}$ is the band dispersion of $\beta$-state atoms.

In order to physically understand which information can be extracted from a measurement of the rate (2), let us first approximate the spectral function by $A(\mathbf{k}, \omega) = \delta(\omega - \xi_{\mathbf{k}})$, i.e., neglect the incoherent part and consider quasiparticles with an infinite lifetime. The Raman rate then reads at $T = 0$: $R = \int_{\xi_{\mathbf{k}} < 0} d\mathbf{k} \delta(\varepsilon_{\mathbf{k}+\mathbf{q},\beta} - \xi_{\mathbf{k}} - \Omega)$. Contributions to this integral come from momenta inside the FS ($\xi_{\mathbf{k}} < 0$) which satisfy the Raman resonance condition $\varepsilon_{\mathbf{k}+\mathbf{q},\beta} - \xi_{\mathbf{k}} = \Omega$. When the frequency shift $\Omega$ is small, $R$ vanishes since there is no available phase space satisfying these constraints. The smallest frequency at which a signal starts to be observed is $\Omega_T = \min_{\mathbf{k}} \varepsilon_{\mathbf{k}\beta} \equiv \varepsilon_\beta^0$ [22]. This corresponds to a momentum transfer $\mathbf{q} = -\mathbf{k}_F$ which lies itself on the FS (i.e., $\xi_{\mathbf{k}_F} = 0$) [23]. For $\Omega$ very close to the extinction threshold ($\Delta\Omega = \Omega - \Omega_T \gtrsim 0$), the region in momentum space inside which a sizable transfer rate $R$ is measured consists of a shell surrounding the FS, centered at a momentum $\mathbf{q}$ such that $\Delta\Omega = -\xi_{-\mathbf{q}} \sim \mathbf{v}_F(\mathbf{k}_F) \cdot (\mathbf{q} + \mathbf{k}_F)$, and of width $\Delta q_\parallel \sim \sqrt{2M\Delta\Omega}$. In these expressions, $M$ is the effective mass at the bottom of the $\beta$ band and $\mathbf{v}_F$ is the Fermi velocity.

This analysis remains unchanged when considering quasiparticles with a finite lifetime $\Gamma^{-1}$ (uniform along the FS), the width of the momentum shell being simply replaced by $\Delta q_\parallel \sim \sqrt{2M\Delta\Omega} + \Gamma / v_F$. Hence, measuring the Raman signal for $\Omega$ close to the extinction threshold $\Omega_T$ and sweeping over $\mathbf{q}$ provides a determination of the FS in an interacting system (while the method of [3] applies to noninteracting fermions). It also gives access to the velocity of quasiparticles (from the displacement of the measured signal as a function of $\Omega$) and to their lifetime (from the width of the momentum shell).

Examples of numerically simulated spectra for uniform interacting systems are given in Figs. 1(a) and 1(b), where a color intensity plot of the Raman rate (2) is shown for a fixed value of the frequency shift close to threshold. In 1(a), we consider the case of a Lorentzian spectral function centered around the free dispersion relation of a two-dimensional square lattice: $\xi_{\mathbf{k}} = -2t_\alpha(\cos k_x + \cos k_y) - \mu$. In 1(b) a phenomenological form [24] of the spectral function is used, which captures the main aspects of the ARPES data in the non-SC (normal) state of high-temperature superconductors. The key feature entering this phenomenological form is a *pseudogap* with $d$-wave symmetry $\Delta_{\mathbf{k}} = \Delta_0(\cos k_x - \cos k_y)$, corresponding to a depletion of low-energy excitations even when no long-range SC order is present. $\Delta_{\mathbf{k}}$ vanishes along the zone diagonal (nodes) and is maximum along $(0, 0) - (\pi, 0)$ (antinodes). A self-energy $\Delta_{\mathbf{k}}^2 / (\omega + \xi_{\mathbf{k}})$ is a convenient modelization of this effect. In addition, finite lifetime effects are introduced, resulting in the form $\pi A(\mathbf{k}, \omega) = -\mathrm{Im}[\omega - \xi_{\mathbf{k}} + i\Gamma_1 - \Delta_{\mathbf{k}}^2 / (\omega + \xi_{\mathbf{k}} + i\Gamma_0)]^{-1}$. This corresponds to a quasiparticle dispersion which is gapped out except at the nodes. The width $\Gamma_{\mathbf{k}} = \Gamma_1 + \Delta_{\mathbf{k}}^2 \Gamma_0 / [(\omega + \xi_{\mathbf{k}})^2 + \Gamma_0^2]$ is largest near the antinodes. This form of

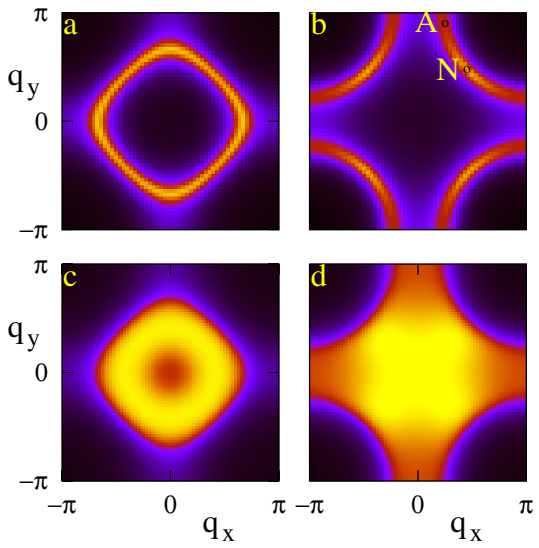


FIG. 1 (color online). Intensity plots of the Raman rate $R(\mathbf{q}, \Omega)$, for $\Omega$ close to threshold $\Omega_T$ ($\Delta\Omega = 0.01t_\alpha$). (a) Noninteracting fermions on the homogeneous 2D square lattice with density $n_\alpha = 0.22$ and a Lorentzian broadening of the spectral function $\Gamma = 0.4t_\alpha$ uniform in $\mathbf{k}$ space. (b) Model $d$-wave pseudogap state (see text), with $\Delta_0 = 0.1t_\alpha$, $\Gamma_0 = 0.05t_\alpha$, $\Gamma_1 = 0.4t_\alpha$. The plot is for a hole-doped system ($n_\alpha = 0.45$) with a nearest ($t_\alpha$) and next-nearest neighbor ($t'_\alpha$) hopping, with $t'_\alpha/t_\alpha = -0.3$ (typical for cuprates, but similar effects are expected also for smaller $|t'_\alpha/t_\alpha|$). (c),(d) Same as (a) and (b) in the presence of a harmonic trap ($\omega_0 = 0.02t_\alpha$). The pseudogap and nodal-antinodal differentiation are clearly visible in both (b) and (d).

$A(\mathbf{k}, \omega)$ also provides a reasonable qualitative description of recent theoretical results for the two-dimensional Hubbard model [25]. The momentum-space differentiation encoded in the model spectral function is clearly visible in Fig. 1(b), with nodal regions displaying quasiparticles while antinodal ones are gapped out and short-lived. This illustrates how the Raman spectroscopy method can be used to determine the FS not only of a Fermi liquid but also of a strongly interacting system with suppressed quasiparticles. In Fig. 2 we further show that the line shape of the Raman signal for a fixed value of $\mathbf{q}$ does reveal the essential features of the spectral function, namely, quasiparticles at the nodes and a pseudogap at the antinodes.

Since most cold atom experiments are performed in a trap, it is important to verify that the spatial inhomogeneity does not spoil the predicted signatures. Within the local density approximation, and assuming that the trap potential only acts on the $\alpha$, $\alpha'$ states, the observed signal is the sum of the contributions of the different points $\mathbf{R}$ of the trap, with a local chemical potential $\mu_\mathbf{R} = \mu - M\omega_0^2\mathbf{R}^2/2$. The results are summarized in Figs. 1(c) and 1(d) for physical situations such that the value of the chemical potential at the trap center coincides with that of the homogeneous system in Figs. 1(a) and 1(b). As expected, the intensity map is now a superposition of the Fermi surfaces corresponding to all the densities realized in the trap. The outer shell delimited by the extinction of the signal still gives a direct access to the FS corresponding to the highest densities at the center of the trap. The typical signatures of an unconventional state remain clearly visible in the trap as well: in Fig. 1(d), the nodal-antinodal differentiation is apparent in the outer shell of this plot, as seen from the suppressed intensity along the antinodal direction. A possible way of revealing the region around the Fermi surface is to measure the intensity maps for two, slightly different values of the frequency and/or the total atom number, and then take their difference: the resulting differential images for the trapped system (not shown) recover the same qualitative features of the homogeneous system shown in Figs. 1(a) and 1(b).

The discussion so far has assumed that it is possible to repeat the measurement of the total rate $R$ for several different values of $\mathbf{q}$. In some cases, a different scheme with a momentum-selective detection of the scattered $\beta$ atoms may be instead favorable, quite similar to ARPES in solids. A single value of $\mathbf{q}$ is used, and a time of flight expansion of the $\beta$ atoms cloud is performed (after suddenly turning off the trap and the lattice potential) in order to reconstruct the momentum distribution of the atoms. As shown in Fig. 3(a), the Raman resonance condition allows for a selective addressing of the different regions in $\mathbf{k}$ by tuning the frequency $\Omega$. The number of Raman-scattered atoms with final momentum $\mathbf{k}$ is proportional to the integrand $n_F(\varepsilon_{\mathbf{k}\beta} - \Omega)A(\mathbf{k} - \mathbf{q}, \varepsilon_{\mathbf{k}\beta} - \Omega)$ of (2). Figure 3(b) shows that the resulting $\mathbf{k}$-space intensity map is able to reveal the details of the pseudogap physics, in particular, its $\mathbf{k}$ dependence. By varying both $\Omega$ and $\mathbf{q}$, Raman scattering offers more possibilities for probing the system in a momentum-selective way than microwave spectroscopy techniques [26].

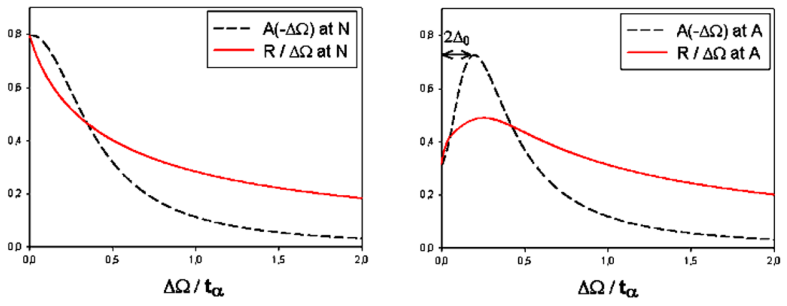


FIG. 2 (color online). Comparison between the spectral function $A$ and the Raman rate $R/\Delta\Omega$ for two points in momentum space indicated in Fig. 1. In the nodal direction ($N$, left), the spectrum displays a quasiparticle peak, while in the antinodal direction ($A$, right) a depletion of the signal is observed at low energy, corresponding to the pseudogap.

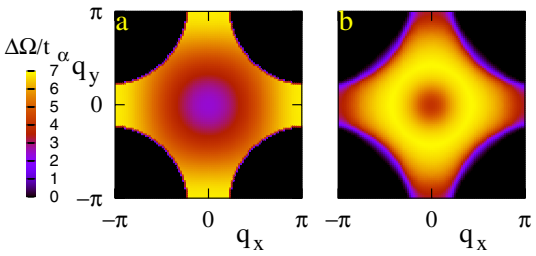


FIG. 3 (color online). (a) Color plot illustrating the selective addressing of $\mathbf{k}$ space by a proper choice of $\Omega$ (cf. color scale on the left). (b) Time of flight $\mathbf{k}$ map obtained by integrating the Raman intensity for $\Delta\Omega = \Omega - \Omega_T$ varied in the range $[2.4t_\alpha, 6.8t_\alpha]$. The dispersion relation of the $\beta$ atoms is taken as $\varepsilon_{\mathbf{k}\beta} = \varepsilon^0_\beta - 2t_\beta(2 + \cos k_x + \cos k_y)$ with $t_\beta = 1.5t_\alpha$ (note that interactions will renormalize downwards the effective $t_\alpha$ even if bare values are equal). Parameters are as in Fig. 1(c) and $\mathbf{q} = 0$.

As a final point, we discuss some orders of magnitude which are important for the actual feasibility of the experiments proposed in this Letter. Specifically, we consider $^6$Li atoms (see also Ref. [12]) in the two lowest hyperfine states $|\alpha\rangle = |I_z = 1, m = -1/2\rangle$ and $|\alpha'\rangle = |0, -1/2\rangle$. The coupling between these two states can be made very large thanks to the Feshbach resonance at 834 G. On the other hand, if we choose the final state of the Raman process to be $|\beta\rangle = |1, 1/2\rangle$ with the same nuclear spin component as $\alpha$, the interaction of $|\beta\rangle$ with both $|\alpha\rangle$ and $|\alpha'\rangle$ is nonresonant, corresponding to a low value of the scattering length $a_{\alpha,\beta} \simeq a_{\alpha',\beta} \simeq 2.5$ nm [27]. This yields a typical scale for the interaction energy between an atom in $\beta$ and the background in $\alpha, \alpha'$ which is smaller than the typical bandwidth, and hence negligible. Furthermore, taking typical values for the lattice wavelength $\lambda \sim 800$ nm, the atomic density $\rho \sim (2/\lambda)^3$, and the recoil velocity $v \sim h/(M\lambda)$ of atoms in state $\beta$, we evaluate the collision rate to be $\gamma_c = \rho\sigma v \sim 10^2$ s$^{-1}$. The Raman detection sequence can therefore be performed in a time scale of the order of a few milliseconds, yielding an energy resolution in the 100 Hz range. Losses due to inelastic transitions from state $\beta$ have a rate $\sim 10^{-12}$ cm$^3$ s$^{-1}$ and can be neglected on this time scale.

In summary, we have proposed a Raman spectroscopy technique which, analogously to ARPES in solid-state physics, is able to probe the one-body Green function. This technique can be used to obtain information on the Fermi surface, and on the quasiparticles (or absence thereof) of a gas of fermionic atoms, even in strongly correlated states. In the near future, this technique may play an important role in the experimental characterization of the novel quantum states of matter that can be obtained with ultracold atoms in optical lattices.

We are grateful to T. Esslinger for an interesting discussion. We acknowledge support from the ANR under contract "GASCOR," IFRAF, and CNRS and Ecole Polytechnique. Laboratoire Kastler-Brossel is a research unit of Ecole normale supérieure and Université Paris 6, associated to CNRS.

[1] M. Greiner *et al.*, Nature (London) **415**, 39 (2002).
[2] See, for example, M. Greiner *et al.*, Nature (London) **426**, 537 (2003); S. Jochim *et al.*, Science **302**, 2101 (2003); M. W. Zwierlein *et al.*, Phys. Rev. Lett. **91**, 250401 (2003); J. Kinast *et al.*, Phys. Rev. Lett. **92**, 150402 (2004); T. Bourdel *et al.*, Phys. Rev. Lett. **93**, 050401 (2004).
[3] M. Köhl *et al.*, Phys. Rev. Lett. **94**, 080403 (2005).
[4] For a review, see I. Bloch, Nature Phys. **1**, 23 (2005).
[5] J. K. Chin *et al.*, Nature (London) **443**, 961 (2006).
[6] E. W. Hagley *et al.*, Science **283**, 1706 (1999).
[7] Y. Japha *et al.*, Phys. Rev. Lett. **82**, 1079 (1999).
[8] D. L. Luxat and A. Griffin, Phys. Rev. A **65**, 043618 (2002).
[9] P. Blair Blakie, New J. Phys. **8**, 157 (2006).
[10] I. E. Mazets, G. Kurizki, N. Katz, and N. Davidson, Phys. Rev. Lett. **94**, 190403 (2005).
[11] P. Törmä and P. Zoller, Phys. Rev. Lett. **85**, 487 (2000).
[12] W. Yi and L. Duan, Phys. Rev. Lett. **97**, 120401 (2006).
[13] A. A. Abrikosov *et al.*, *Methods of Quantum Field Theory in Statistical Physics* (Dover, New York, 1963); G. D. Mahan, *Many Particle Physics* (Plenum, New York, 1981).
[14] A. Damascelli *et al.*, Rev. Mod. Phys. **75**, 473 (2003).
[15] Information on one-particle correlators of a Bose system can be obtained from two-particle ones, when the system is made to interfere with either another identical system [16] or with a reference condensate [17].
[16] A. Polkovnikov, E. Altman, and E. Demler, Proc. Natl. Acad. Sci. U.S.A. **103**, 6125 (2006).
[17] Q. Niu, I. Carusotto, and A. B. Kuklov, Phys. Rev. A **73**, 053604 (2006).
[18] D. M. Stamper-Kurn *et al.*, Phys. Rev. Lett. **83**, 2876 (1999); I. Carusotto, J. Phys. B **39**, S211 (2006).
[19] S. Fölling *et al.*, Nature (London) **434**, 481 (2005); M. Greiner, C. A. Regal, J. T. Stewart, and D. S. Jin, Phys. Rev. Lett. **94**, 110401 (2005); E. Altman *et al.*, Phys. Rev. A **70**, 013603 (2004).
[20] A. Damascelli, Phys. Scr. **T109**, 61 (2004).
[21] The superscript $<$ indicates that $\psi^\dagger$ is always to the left of $\psi$. Operators are evolved in the grand-canonical ensemble [13].
[22] The threshold corresponds to $(\omega_1 - \omega_2)_T = \varepsilon^0_\beta - \mu$. This is of order $\varepsilon^0_\beta - \varepsilon^0_\alpha$ at weak coupling, while interactions can lead to a shift comparable to the Hubbard coupling.
[23] The accessible range of $\mathbf{q}$ is $0 \leq c|\mathbf{q}|/2 \leq \omega_1 \simeq \omega_2$. In a red-detuned lattice with respect to $\omega_{1,2}$, all values of $\mathbf{q}$ in the first Brillouin zone are therefore accessible.
[24] M. R. Norman *et al.*, Phys. Rev. B **57**, R11 093 (1998).
[25] C. Honerkamp *et al.*, Phys. Rev. B **63**, 035109 (2001); A. A. Katanin and A. P. Kampf, Phys. Rev. Lett. **93**, 106406 (2004); D. Sénéchal and A.-M. S. Tremblay, Phys. Rev. Lett. **92**, 126401 (2004); M. Civelli *et al.*, Phys. Rev. Lett. **95**, 106402 (2005).
[26] C. Chin *et al.*, Science **305**, 1128 (2004).
[27] F. A. van Abeelen *et al.*, Phys. Rev. A **55**, 4377 (1997).

# Chapter 3

# Many-body methods for models of two-component fermionic mixtures

*We describe the various mean-field techniques that will be used in the following to analyze the properties of two-component fermionic mixtures confined in optical lattices. We begin by discussing the Hubbard model and the possible phases that may occur. We then show that for the weak-coupling regime of the model, a usual Hartree-Fock mean-field theory can be applied by neglecting particle fluctuations. In the opposite limit of a very strong coupling, we map the initial model to an effective spin model, which can be treated by classical mean-field theory. At intermediate couplings, correlations cannot be neglected and the competition between the kinetic and the interaction energy induces many fascinating effects. In this regime, a simple description by static mean-field theory is not sufficient. More sophisticate methods that fully treat quantum fluctuations are required for solving the many-body problem. We present the slave-boson and the dynamical mean-field theory that are better suited to describe this intermediate-coupling regime.*

## 3.1 Hubbard model

### 3.1.1 Hubbard model for mixtures of ultracold fermionic atoms

Recent progress in experiments on fermionic mixtures has allowed to have a direct access to many interesting properties of strongly correlated fermions. Thanks to the Feshbach resonance, one can tune the s-wave interaction from the BCS to the BEC side, and even study the universality of the unitary limit. With the introduction of an optical lattice, phenomena related to solid state physics are observed as, for example, the BCS superfluid, the Mott insulator, etc. Mixtures of two-component atoms with different masses (e.g. $^6$Li, $^{40}$K) introduce an additional parameter, namely the difference between the hopping amplitudes associated with each species in the optical lattice. As we have shown in Chapter 1, such a mixture of two fermionic components can be expressed by an extended Hubbard model. In order to avoid working directly in canonical ensemble with fixed atom number, we propose to study of the ground state in the grand canonical ensemble then come back to the canonical system by the Legendre transform (see Section 3.2.1).

$$H = -\sum_{\langle i,j,\sigma\rangle} (t_\sigma c^\dagger_{i\sigma} c_{j\sigma} + H.c) + U\sum_i n_{i\uparrow} n_{i\downarrow} - \sum_{i\sigma} \mu_\sigma n_{i\sigma}. \tag{3.1}$$

Here, the spin index $\sigma$ refers to the two different species. The first term of the model represents the tunneling of the atoms on the lattice (the kinetic term), while the second represents the local interaction when two atoms of different species meet on an identical site. $\mu_\sigma$ is the chemical potential used to fix the atom number for the species $\sigma$. We introduce the new variables $\mu = (\mu_\uparrow + \mu_\downarrow)/2, h = (\mu_\uparrow - \mu_\downarrow)/2$ which are the chemical potential and the effective magnetic field, respectively. They are used to fix the total atom number for both species $n = n_\uparrow + n_\downarrow$ and the polarization $p = n_\uparrow - n_\downarrow$ (population imbalance).

In experiments on ultracold atoms, the parameters of this model are very well controlled. One can change the geometry or the dimensionality of the optical lattice by changing the orientation of the laser beams. The hopping (tunneling parameter) for each species $t_\sigma/E_{R\sigma} = 4\pi^{-1/2}(V_{0\sigma}/E_{R\sigma})^{3/4} e^{-2(V_{0\sigma}/E_{R\sigma})^{1/2}}$ can also be controlled by the depth of the optical lattice or by the intensity of the laser beams. The interaction strength is related to the scattering length $a_s$ by $U/E_R = \sqrt{8/\pi} a_s \mathbf{k}_L (V_0/E_R)^{3/4}$. Thus, it depends both on the scattering length and on the depth of the lattice. In Fig. 3.1, we plot the hopping of the different species ($^6$Li and $^{40}$K) $t_\sigma$ and the interaction coupling $U$ as a function of $V_0/E_R$. Defining the hopping imbalance parameter as $z = (t_\uparrow - t_\downarrow)/(t_\uparrow + t_\downarrow)$, we can vary this quantity from $z = 0$ to $z = 1$ by changing the intensity of the optical lattice as shown in the right panel of Fig. 3.1.

The number of atoms of each species is fixed in the experiment and can be controlled by various methods, for example by applying a radio-frequency (RF) pulse to add or extract atoms of one species. Therefore, we can decide to study the problem as a function of the filling. Two classes of mixture that one can consider are: (i) Mixtures with an equal number of particles for both species ($n_\uparrow = n_\downarrow$); (ii) Mixtures with a density imbalance ($p = n_\uparrow - n_\downarrow > 0$).

### 3.1.2 Particle-hole transformation

Let us introduce here a particle-hole transformation of the Hubbard model that will turn out to be very useful in the following in order to formulate different mean-field theories. As we will see, the particle-hole transformation maps the model with attractive interactions ($U < 0$) to a model with repulsive interactions ($U > 0$). In this section, we establish a dictionary for this mapping. Assuming that the Hubbard model is defined on a bipartite lattice which consists

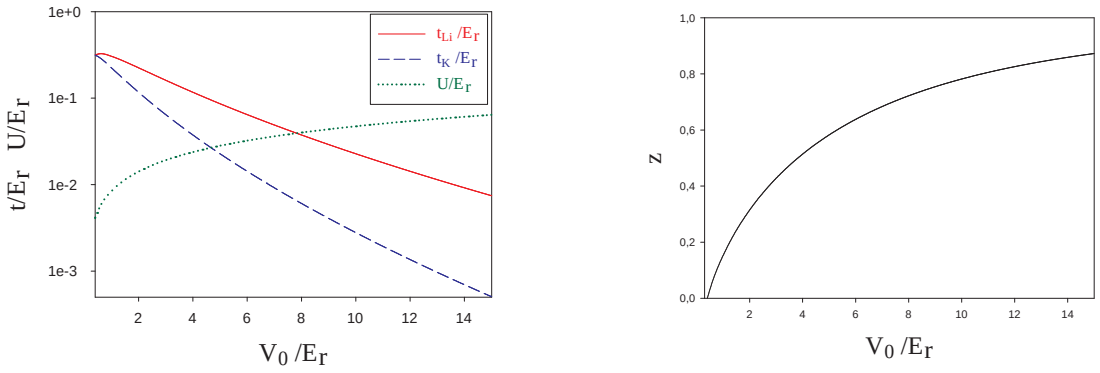


**Figure 3.1:** Left panel: Hopping $t_\sigma$ and interspecies interaction strength $U$ for the mixture of $^6Li$ and $^{40}K$ as a function of the depth of the optical lattice $V_0/E_R$. Right panel: Hopping imbalance parameter $z$ as a function of $V_0/E_R$.

of two sublattices A and B, the particle-hole transformation is defined as follows

$$\begin{cases} c^\dagger_{i\uparrow} & \rightarrow & d^\dagger_{i\uparrow} \\ c^\dagger_{i\downarrow} & \rightarrow & (-1)^i d_{i\downarrow} \end{cases}$$

where $(-1)^i = 1$ when $i \in A$ and $(-1)^i = -1$ when $i \in B$. Hence, the number operator of each species and the kinetic terms are transformed according to $n_{c\uparrow} \rightarrow n_{d\uparrow}$; $n_{c\downarrow} \rightarrow 1 - n_{d\downarrow}$ and $c^\dagger_{i\downarrow} c_{j\downarrow} \rightarrow (-1)^{i+j} d_{i\downarrow} d^\dagger_{j\downarrow} = d^\dagger_{j\downarrow} d_{i\downarrow}$. Let us start with the attractive model in the grand canonical ensemble

$$H = -\sum_{\langle i,j,\sigma\rangle} (t_\sigma c^\dagger_{i\sigma} c_{j\sigma} + H.c) - |U| \sum_i n_{i\uparrow} n_{i\downarrow} - \sum_i \mu(n_i - n) - \sum_i h(p_i - p). \tag{3.2}$$

In this Hamiltonian, the chemical potential $\mu$ is used to fix the total number of atoms and the effective magnetic field $h$ is used to set the polarization. Applying the particle-hole transformation described above, one obtains a new Hamiltonian with a repulsive interaction

$$H = -\sum_{\langle i,j,\sigma\rangle} (t_\sigma d^\dagger_{i\sigma} d_{j\sigma} + H.c) + |U| \sum_i n_{di\uparrow} n_{di\downarrow} - h' \sum_i (n_{di} - n_d) - \mu' \sum_i (p_{di} - p_d), \tag{3.3}$$

where $h' = h + |U|/2$, $n_d = 1 + p$, $\mu' = \mu + |U|/2$ and $p_d = n - 1$. We can summarize this transformation in a dictionary that expresses the correspondence of two models.

For example, let us focus on the negative-$U$ model with $n_\uparrow = n_\downarrow$ away from half-filling ($n_\uparrow + n_\downarrow = 1 + \delta$). We see that after the particle-hole transformation, this model is mapped to a positive $U$ model at half-filling in a magnetic field with a polarization $p = \delta$.

### 3.1.3 Possible phases of the Hubbard model

In the following chapters, we will be interested in establishing the phase diagram of the Hubbard model for different kind of mixtures of fermionic atoms. As we will show in this chapter, the tools we use are all based on different mean-field theories and it is important to know the phases that one might expect in order to formulate the mean-field equations for each of them. The competition between the phases can then be addressed by comparing their energy. Let us enumerate here the phases that we will consider. Note that phases breaking a symmetry have a different interpretation in the original $U < 0$ model and after the particle-hole transformation, therefore, we will discuss their realization in both frameworks.

| Model | -\|U\| | \|U\| |
|---|---|---|
| Creation operator ↑ | $c^{\dagger}_{i\uparrow}$ | $d^{\dagger}_{i\uparrow}$ |
| Creation operator ↓ | $c^{\dagger}_{i\downarrow}$ | $(-1)^{i} d^{\dagger}_{i\downarrow}$ |
| Number of particle ↑ | $n_{c\uparrow}$ | $n_{d\uparrow}$ |
| Number of particle ↓ | $n_{c\downarrow}$ | $1 - n_{d\downarrow}$ |
| Doping | $n_c - 1 = \delta$ | $p_d$ |
| Polarization | $p_c$ | $n_d - 1 = \delta_d$ |
| Chemical potential | $\mu$ | $\mu^{'} = h + \|U\|/2$ |
| External magnetic field | $h$ | $h^{'} = \mu + \|U\|/2$ |
| Paring operator | $c^{\dagger}_{i\uparrow} c^{\dagger}_{i\downarrow}$ | $(-1)^{i+1} d^{\dagger}_{i\downarrow} d_{i\uparrow} = (-1)^{i+1} S^{-}_{di}$ |
| Charge density | $c^{\dagger}_{i\uparrow} c_{i\uparrow} + c^{\dagger}_{i\downarrow} c_{i\downarrow}$ | $1 - (d^{\dagger}_{i\uparrow} d_{i\uparrow} - d^{\dagger}_{i\downarrow} d_{i\downarrow}) \propto -S^{z}_{di}$ |

**Table 3.1:** Particle-hole transformation mapping the $U < 0$ model onto the $U > 0$ model.

### Normal phase

The normal phase is a phase that does not spontaneously break any symmetry. It has the same interpretation for $U < 0$ and $U > 0$. Even though it might look trivial, this phase is already very rich in the Hubbard model. For example, let us consider the Hubbard model at half-filling with positive coupling and no spin or hopping imbalance. It is now well-known that in the weak-coupling regime the normal phase is a Fermi liquid while in the strong-interaction regime (the atomic limit) we obtain an insulator. The origin of the insulator is an effect driven by the strong correlations: When the on-site interaction $U$ is big enough, the many-body system tries to avoid configurations with double occupancies. As a consequence, it becomes very difficult for a particle to move to a neighboring site, with energy cost of order $U$ (which is the gap in the spectral function). The competition between the kinetic and the interaction energy generates a critical value of $U$ where one finds a phase transition (the Mott metal-insulator transition). Whenever we change the other parameters of the system such as the temperature, the doping or the hopping imbalance, the physics driven from this Mott transition becomes more and more interesting.

### Charge-density wave (CDW) / Antiferromagnetism (AF)

*Charge-density wave ($U < 0$):* When the interaction is attractive, the CDW phase has a ground state with a density modulation for both species. This phase is stabilized when it is favorable to gain interaction energy by having ↑-atoms and ↓-atoms on the same sites (Fig. 3.3). In the sketch 3.3, we see a the possible configuration of this phase with density modulation of wave vector $\mathbf{q} = (\pi/a, \ldots \pi/a)$.

*Antiferromagnetism ($U > 0$):* When the interaction is repulsive, the phase that corresponds to the commensurate CDW is the antiferromagnetic phase. In this phase, the many-body system stabilizes a state, where the densities of both species are modified in order to gain interaction energy. The Fig. 3.4 shows a classical image of the antiferromagnetic state in a cubic lattice which is stabilized by the positive spin exchange coupling.

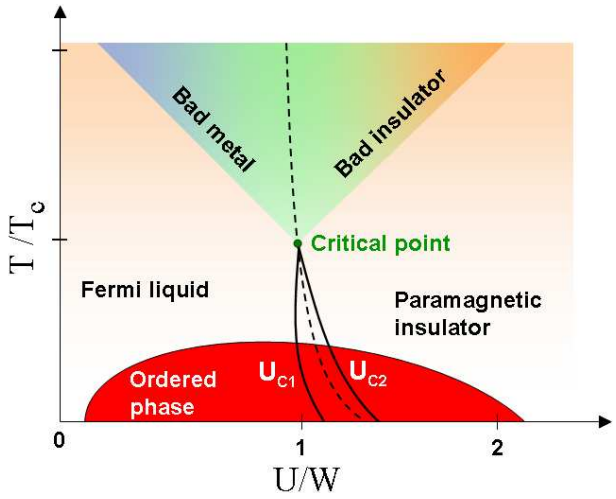


**Figure 3.2:** Phase diagram of half-filling Hubbard model in the plane (T,U) obtained by DMFT. Above the red region (ordered phase at low temperature), there is a first order phase transition from a Fermi liquid regime (weak coupling) to a paramagnetic insulator (Mott insulator) below some critical temperature $T_c$. Above this $T_c$, the phase transition becomes a crossover from a bad metal to a bad insulator. Reprinted from Ref. [42]

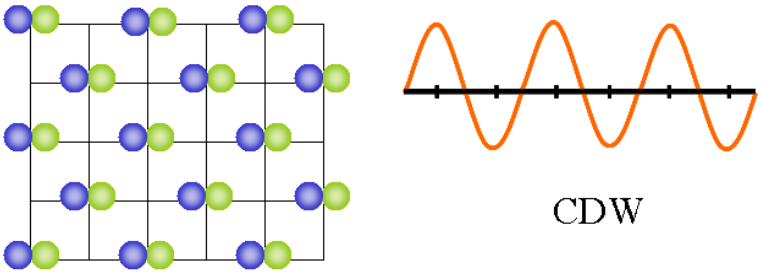


**Figure 3.3:** Commensurate charge density wave. The left panel shows a configuration of charge density wave with two particles every two lattice sites. The right panel shows the density modulation in one direction.

---

### Superfluid (SF) / In-plane spin-density wave (SDW$_{xy}$)

*Superfluid ($U < 0$):* In the attractive model, one can also expect to stabilize a ground state with superfluid long-rang order. In weak coupling, this phase (called the BCS phase) can be explained by the formation of Cooper pairs with zero total momentum $\mathbf{q} = \mathbf{k}_1 + \mathbf{k}_2 = 0$. At low temperature, the pairs of fermions condensate in order to gain potential energy. In the strong coupling limit instead, the particles of different species form local bosons which become a Bose-Einstein condensate (BEC) at low temperatures. These states have a phase coherence and are at the origin of the superfluidity.

*In-plane spin-density wave ($U > 0$):* The equivalent of the superfluid phase in the positive-$U$ language is the in-plane spin-density wave (SDW$_x y$). In this phase there is an ordering of the spins within the $x - y$ plane [54]. We can write the spin ordering of this phase as $\langle S^x_{\mathbf{R}_i} \rangle = m \cos \mathbf{q}.\mathbf{R}_i$ and $\langle S^y_{\mathbf{R}_i} \rangle = \pm m \sin \mathbf{q}.\mathbf{R}_i$. Here the choice of the sign + or - corresponds to the sense of the rotation (i.e. a circular polarization in the clockwise rotation or counterclockwise

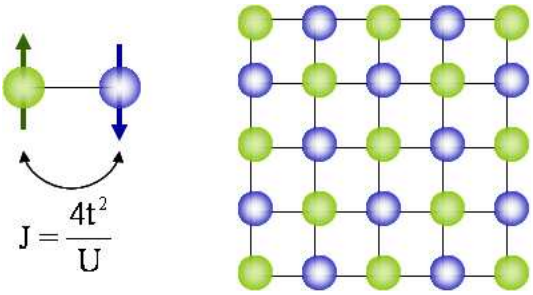


**Figure 3.4:** Commensurate spin density wave-Antiferromagnetic phase. Left panel shows the effective spin exchange coupling in the limit $U \gg t$. Right panel shows the possible SDW (AF) configuration stabilized by the effective exchange coupling $J = 4t^2/U$.

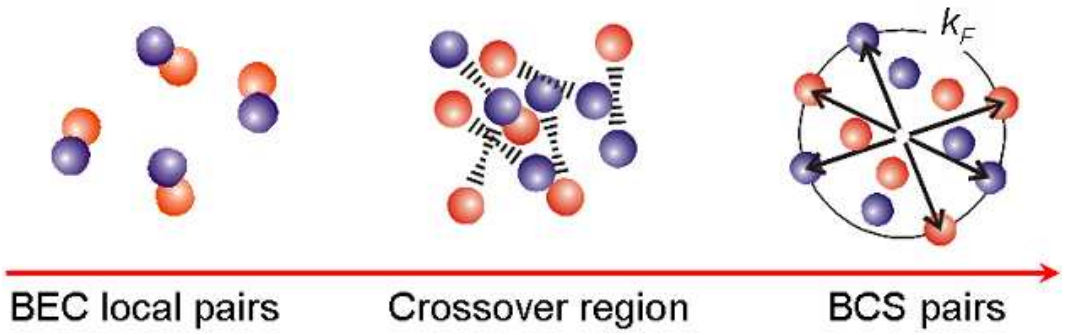


**Figure 3.5:** Superfluidity with zero total momentum pairing. This figure shows how the pairing changes across the BEC-BCS crossover. The left panel shows the BEC superfluid of the effective local bosons. The right panel shows the weak-coupling limit with the formation of the BCS superfluid with pairing at large distances. The middle panel shows the unitary regime with pairing at intermediate distances.

---

rotation). Within this thesis, we consider only the case of the commensurate spin density wave corresponding to $\mathbf{q} = (\pi/a, \ldots, \pi/a)$.

## 3.2 Hartree-Fock mean-field theory

As our objective is to study the model for mixtures of cold atoms with fixed atom numbers, we briefly recall the Legendre transform which is very useful for switching from a grand-canonical system with a fixed chemical potential to a canonical system with fixed number of atoms. We then give a general introduction on the strategy of static Hartree-Fock mean-field theory. We use this method to construct the framework for the mean-field study of the aforementioned phases.

### 3.2.1 Legendre transform

Let $g(x)$ be a convex function (i.e. $g"(x) > 0$). The Legendre transform $\bar{g}(p)$ of $g(x)$ is defined by

$$\bar{g}(p) = xp - g(x). \tag{3.4}$$

Here $x$ is a function of the variable $p$. $x(p)$ is defined by the root of the equation: $p = \partial g(x)/\partial x$. The condition of convexity is necessary for the existence of a unique solution x(p) for all $p \in [\min g'(x), \max g'(x)]$.

Another way to define the Legendre transform, which is the starting point of functional mean-field theory, is to define the two-variable function

$$\mathcal{G}(x, p) = xp - g(x), \tag{3.5}$$

where g(x) is still supposed to be convex. Then the Legendre transform is $\bar{g}(p) = \mathcal{G}(x(p), p)$, where $x(p)$ is the stationary point of $\mathcal{G}(x, p)$ when $p$ is fixed, i.e. $x(p)$ is solution of the equation

$$\frac{\partial \mathcal{G}(x, p)}{\partial x} = p - \frac{\partial g}{\partial x} = 0. \tag{3.6}$$

In thermodynamics, we define couples of conjugated variables such as $(P, V)$, $(T, S)$, $(h, m)$, $(\mu, n)$. In fact, in the thermodynamic limit, we can always determine one variable when the other is given. Here we denote this couple as $(x, p)$. Assuming that $F(T, x)$ is the free energy of the system when $x$ is fixed, then its Legendre transform is $G(T, p)$, the (Gibbs potential) energy of the system for fixed $p$

$$G(T, p) = F(T, x(p)) + x(p)p. \tag{3.7}$$

The reason for this transformation of the free energy is that we do not have the same Hamiltonian for the system when we fix different variables. For example, in the grand-canonical ensemble we fix the chemical potential $\mu$ and the Hamiltonian is $\hat{H} = \hat{H}_0 - \mu\hat{N}$, while the Hamiltonian for the canonical ensemble ($n$ is fixed) is simply $\hat{H}_0$.

Working directly with the canonical ensemble is very difficult, therefore the strategy is that we work in the grand canonical ensemble (we get the free energy $F(T, \mu)$) then we use the Legendre transform to determine the free energy in the canonical ensemble ($G(T, n)$). We must keep in mind the condition of validity, namely that the free energy is concave with respect to $\mu$

$$-\frac{\partial^2 F(T, \mu)}{\partial \mu^2} = \frac{\partial n(\mu)}{\partial \mu} > 0. \tag{3.8}$$

### 3.2.2 Mean-field theory strategy

As discussed above, all the phases except the normal phase break a symmetry that can be characterized by an order parameter. Let us assume that we have a system in the canonical ensemble (*i.e.* the number of particles is fixed) with an order parameter $\Delta$ which corresponds to the static average of the operator $\hat{\varphi}$. For example, we have $\hat{\varphi} = N^{-1}\sum_k c^\dagger_{k+Q\sigma}c_{k\sigma}$ for a charge-density-wave order or $\hat{\varphi} = N^{-1}\sum_k c^\dagger_{k\uparrow}c^\dagger_{-k\downarrow}$ for the BCS-superfluid order. Within a variational method, the ground state of the problem is found by fixing the mean value of the number of particle per site to $n$, and then by optimizing the energy with respect to the value of $\langle\hat{\varphi}\rangle = \Delta$.

### General mean-field approach

From the Legendre transform $\bar{g}(p)$ of a free energy $g(x)$, we can construct a free-energy functional $\mathcal{G}(x,p)$ of both variables $(x,p)$. The Legendre transform is then determined by is value at the stationary point. We do not need to impose any condition of convexity of $g(x)$, but the existence of the transformation depends on the invertibility of the stationary equation. We present here a method that allows to construct this functional of the energy with an initial Hamiltonian $\hat{H}$. We define a Hamiltonian $\hat{A}_{\mu,\psi}$ that realizes two conditions on the mean values of the density and the order parameter with two Lagrange multipliers $(\mu,\psi)$

$$\hat{A}_{\mu,\psi} = \hat{H} - N\mu(\hat{n}_i - n) - N\psi(\hat{\varphi} - \Delta). \tag{3.9}$$

Its energy is obtained as a function of two couples of variables $(\mu,n)$ and $(\psi,\Delta)$. This energy has exactly the same form as the function $\mathcal{G}(x,p)$ constructed above

$$\Omega[\Delta,n,\psi,\mu] = -\frac{1}{N\beta}\log \mathrm{Tr}(e^{-\beta\hat{A}_{\mu,\psi}}) = F[\psi,\mu] + \mu n + \psi\Delta. \tag{3.10}$$

Here, we have $\Omega[\Delta,n,\psi,\mu]$ playing the same role as the function $\mathcal{G}(x,p)$ in the Legendre transform. The stationary points of this function with respect to the two variables $\mu$ and $\psi$ will give the two constraints on the average values

$$\frac{\partial\Omega}{\partial\mu} = n - \langle\hat{n}\rangle_{\psi,\mu} = 0 \qquad \text{and} \qquad \frac{\partial\Omega}{\partial\psi} = \Delta - \langle\hat{\varphi}\rangle_{\psi,\mu} = 0. \tag{3.11}$$

These equations are reduced to two mean-field self-consistency equations $n(\psi,\mu) = n$ and $\varphi(\psi,\mu) = \Delta$. If these relations are invertible, we get the functions $\mu = \mu(\Delta,n)$ and $\psi = \psi(\Delta,n)$. Replacing these functions in the total energy, we get the energy of the system with fixed density $n$ and fixed order parameter $\Delta$. This energy $G(\Delta,n) = \Omega[\Delta,n,\psi(\Delta,n),\mu(\Delta,n)]$ is the Legendre transform of free energy $F[\psi,\mu]$

$$G(\Delta,n) = F[\psi(\Delta,n),\mu(\Delta,n)] + \mu(\Delta,n)n + \psi(\Delta,n)\Delta. \tag{3.12}$$

Until now, we have decided to compute the energy of a state whose particle number and order parameter are fixed. In order to find which order parameter is the optimal one in the canonical system, we have to minimize the energy $G(\Delta,n)$ with respect to $\Delta$. The gap equation for fixed $n$ reads $dG(\Delta,n)/d\Delta = 0$.

Note that for the case of a Hubbard Hamiltonian $\hat{H} = \hat{H}_0 + U\sum_i n_{i\uparrow}n_{i\downarrow}$, all the Lagrange multipliers are functions of the interaction $U$ because $\Omega[\Delta,\mu,\psi,\mu]$ depends on $U$. In addition, the calculation of the energy is not trivial because of the non-quadratic interaction term. Hence, in practice, we suppose that $U$ is small enough to do a perturbation development of all the functionals in powers of $U$ (for more detail, see [45]).

### Variational approach

Another strategy to do mean-field theory and which can help to overcome the difficulty of the non-quadratic Hamiltonian is to use a variational method. Assuming that $U$ is small enough for neglecting the fluctuations, we approximate the Hamiltonian by a quadratic Hamiltonian with a variational parameter $\Delta$. The initial $\hat{H}$ is now approximated to the class of mean-field Hamiltonians $\hat{H}_{MF}$, characterized by an order parameter $\Delta$. The choice of the variational parameter depends on the symmetry which we decide to break. This method is similar to the method in which we consider subspaces of variational wave functions characterized by an

order parameter. We apply the same construction of the general energy functional proposed above for the mean-field Hamiltonian

$$\hat{A}_\mu = \hat{H}_{MF} - N\mu(\hat{n} - n). \tag{3.13}$$

We now have a similar problem as above, but with only one Lagrange multiplier $\mu$ and the energy can be calculated easily for the quadratic Hamiltonian $\hat{H}_{MF}$. The total energy is

$$\Omega[\Delta, n, \mu] = -(N\beta)^{-1} \log \mathrm{Tr}(e^{-\beta \hat{A}_\mu}) = F_{MF}[\Delta, \mu] + \mu n, \tag{3.14}$$

where $F[\Delta, \mu]$ is the free energy of the grand canonical Hamiltonian $\hat{H}_{MF} - \mu\hat{n}$. The equation of the stationary point (saddle point) of $\Omega[\Delta, n, \mu]$ now reads

$$\frac{\partial \Omega}{\partial \mu} = n - \langle \hat{n} \rangle_{\Delta,\mu} = 0. \tag{3.15}$$

From this equation, we can extract the relation $n = n(\Delta, \mu)$. If this relation can be inverted we can then calculate the energy of the system with fixed number of particle $n$

$$G_{MF}(\Delta, n) = \Omega[\Delta, n, \mu(\Delta, n)] = F_{MF}[\Delta, \mu(\Delta, n)] + \mu(\Delta, n)n. \tag{3.16}$$

By comparing this energy to the one obtained with the initial Hamiltonian, $G(\Delta, n)$, we can demonstrate that $G_{MF}(\Delta, n)$ is the first-order approximation in $U$ of the true energy $G(\Delta, n)$ (this is demonstrated in [45])

$$G(\Delta, n) = G_{MF}(\Delta, n) + O(U^2). \tag{3.17}$$

In order to determine the phase diagram of the system, we need to minimize this mean-field energy with respect to $\Delta$ for $n$ fixed. This optimization leads to the gap equation

$$\frac{dG}{d\Delta} = \frac{\partial F}{\partial \Delta} + \frac{\partial F}{\partial \mu}\frac{\partial \mu}{\partial \Delta} + n\frac{\partial \mu}{\partial \Delta}. \tag{3.18}$$

Inserting the condition of stationarity for the chemical potential $\partial F/\partial \mu + n = 0$, we recover the usual form of the gap equation

$$\frac{\partial F[\Delta, \mu(\Delta, n)]}{\partial \Delta} = 0. \tag{3.19}$$

The ground state of a system with fixed number of particles and spontaneous broken symmetry is determined by the set of self-consistency equations

$$\frac{\partial F[\Delta, \mu]}{\partial \mu} + n = 0 \quad \text{and} \quad \frac{\partial F[\Delta, \mu]}{\partial \Delta} = 0. \tag{3.20}$$

This is exactly the same gap equation as for the grand canonical ensemble, but here we do not fix the chemical potential $\mu$. The Lagrange multiplier $\mu$ is a free parameter given by the equation $\mu = \mu(\Delta, n)$.

#### Second-order versus first-order transition

Let us suppose that we consider the grand-canonical system at temperature $T$, with a fixed chemical potential $\mu$. In general, the gap equation can have several solutions and in particular $\Delta(T) = 0$, which corresponds to the normal phase without any long-range order. A typical configuration of the free energy and of the gap for a second-order transition are shown in

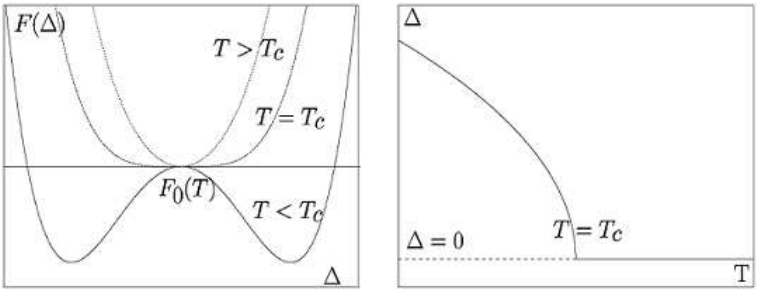


**Figure 3.6:** Typical energy and gap configurations in a second-order phase transition. Left panel: Free energy $F$ as a function of $\Delta$. Right panel: Gap $\Delta$ as a function of the temperature $T$. There is a second-order phase transition at $T = T_c$. Reprinted from Ref. [86]

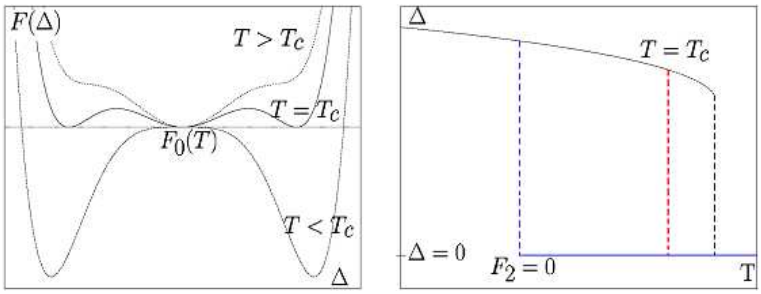


**Figure 3.7:** Typical energy and gap configurations for a first-order phase transition. Left panel: Free energy $F$ as a function of $\Delta$. Right panel: Gap $\Delta$ as a function of the temperature $T$. In a coexistence region around the critical temperature $T_c$ one can still stabilize solutions that are locally stable even if they do not have the lowest energy. Reprinted from Ref. [86]

---

Fig. 3.6. For large temperatures, $\Delta(T) = 0$ is the only solution of the gap equation. When $T$ is lowered below the critical temperature $T_c$, the gap equation starts to have several solutions and the ones with lowest energy have $\Delta \neq 0$. When the transition is second order, there is no jump in $\Delta$ at $T_c$.

The situation is different in a first-order transition, see Fig. 3.7. When the temperature reaches $T = T_c$, the gap equation has three solution but they are not degenerate as would be the case in a second-order transition. As a consequence, the optimal value for $\Delta$ jumps when $T$ is below $T_c$. Note that there can be a coexistence region around $T_c$ where some solutions that are not energetically most favorable are still locally stable.

### 3.2.3 Mean-field theory for the BCS phase

The BCS theory for conventional superconductors at low temperatures, shows that the Hubbard model with an attractive interaction ($U < 0$) has a stable BCS ground state [9, 116]. Here, we present this BCS mean-field theory extending it to the more general case in which there might be a density or a mass imbalance. The BCS ground state is characterized by the formation of pairs of electrons with opposite spin and momentum (Cooper pair). In the

variational approach, the ground state wave function has the form

$$|\phi\rangle = \prod_{\mathbf{k}} (u_{\mathbf{k}} + v_{\mathbf{k}} c^{\dagger}_{\mathbf{k}\uparrow} c^{\dagger}_{-\mathbf{k}\downarrow})|0\rangle, \tag{3.21}$$

where $u_{\mathbf{k}}$ and $v_{\mathbf{k}}$ are defined by the mean-field approximation. In the Hartree-Fock mean field for the BCS phase, one only keeps the Hartree term in the channel with $q = 0$: $(|U|/N)\sum_{\mathbf{k},\mathbf{k}'} c^{\dagger}_{\mathbf{k}\uparrow} c_{\mathbf{k}\uparrow} c^{\dagger}_{\mathbf{k}'\downarrow} c_{\mathbf{k}'\downarrow}$ and the term with $\mathbf{k} = -\mathbf{k}'$ in the "particle-particle" channel. Within this approach, we decouple the interaction in a quadratic form by introducing the order parameter $\Delta = (|U|/N)\sum_{\mathbf{k}} \langle c^{\dagger}_{\mathbf{k}\uparrow} c^{\dagger}_{\mathbf{k}\downarrow}\rangle$. The interaction can then be written in the following form which neglects the fluctuations

$$\frac{|U|}{N}\sum_{\mathbf{k},\mathbf{k}'} c^{\dagger}_{\mathbf{k}\uparrow} c_{\mathbf{k}'\uparrow} c^{\dagger}_{-\mathbf{k}\downarrow} c_{-\mathbf{k}'\downarrow} = \Delta \sum_{\mathbf{k}} (c^{\dagger}_{\mathbf{k}\uparrow} c^{\dagger}_{-\mathbf{k}\downarrow} + c_{-\mathbf{k}\downarrow} c_{\mathbf{k}\uparrow}) - \frac{N\Delta^2}{|U|}.$$

It is convenient to work with Nambu spinors $\psi^{\dagger}_{\mathbf{k}} = (c^{\dagger}_{\mathbf{k}\uparrow}, c_{\mathbf{k}\downarrow})$ to describe the superfluid phase. Inserting the decoupled interaction in the initial Hamiltonian, we obtain the following mean-field Hamiltonian for the BCS phase

$$H_{\mathrm{BCS}} = \sum_{\mathbf{k}} \psi^{\dagger}_{\mathbf{k}} \begin{bmatrix} \xi_{\mathbf{k}\uparrow} & -\Delta \\ -\Delta & -\xi_{\mathbf{k}\downarrow} \end{bmatrix} \psi_{\mathbf{k}} + E_0 + N(\mu_{\uparrow} n_{\uparrow} + \mu_{\downarrow} n_{\downarrow}) \tag{3.22}$$

Here, $\xi_{\mathbf{k}\sigma} = \varepsilon_{\mathbf{k}\sigma} - \tilde{\mu}_{\sigma}$, $\mu = (\mu_{\uparrow} + \mu_{\downarrow})/2$ and $\tilde{\mu}_{\sigma} \equiv \mu - U n_{-\sigma}$ is the renormalized chemical potential including the Hartree correction. The energy $E_0 = \sum_{\mathbf{k}} \xi_{\mathbf{k}\downarrow} + N|U| n_{\uparrow} n_{\downarrow} + N\Delta^2/|U|$. In this quadratic form, for a given value of the order parameter, we can easily diagonalize this mean-field Hamiltonian. The diagonalization of 3.22 yields the Bogoliubov modes with eigenvalues

$$E^{\pm}_{k} = \pm(\xi_{k\uparrow} - \xi_{k\downarrow})/2 + \sqrt{(\xi_{k\uparrow} + \xi_{k\downarrow})^2/4 + \Delta^2}.$$

The creation operators $a^{\dagger}_{\mathbf{k}}$ and $b^{\dagger}_{\mathbf{k}}$ corresponding to the two Bogoliubov branches $E^{\pm}_{\mathbf{k}}$ are related to the original basis by

$$\begin{aligned} a^{\dagger}_{\mathbf{k}} &= u_{\mathbf{k}} c^{\dagger}_{\mathbf{k}\uparrow} - v_{\mathbf{k}} c_{-\mathbf{k}\downarrow} \\ b^{\dagger}_{\mathbf{k}} &= u_{\mathbf{k}} c_{-\mathbf{k}\uparrow} + v_{\mathbf{k}} c^{\dagger}_{\mathbf{k}\downarrow} \end{aligned}$$

in which the normal and superfluid fractions are given by

$$u^2_{\mathbf{k}}, v^2_{\mathbf{k}} = \frac{1}{2}\left(1 \pm \frac{\xi_{\mathbf{k}\uparrow} + \xi_{\mathbf{k}\downarrow}}{\sqrt{(\xi_{\mathbf{k}\uparrow} + \xi_{\mathbf{k}\downarrow})^2 + 4\Delta^2}}\right).$$

Let us now rewrite the BCS mean-field Hamiltonian in the new diagonal basis of Bogoliubov modes

$$\hat{H}_{\mathrm{BCS}} = \sum_{\mathbf{k}} (E^{\dagger}_{\mathbf{k}} a^{\dagger}_{\mathbf{k}} a_{\mathbf{k}} + E^{-}_{\mathbf{k}} b^{\dagger}_{\mathbf{k}} b_{\mathbf{k}}) + E_G + N(\mu_{\uparrow} n_{\uparrow} + \mu_{\downarrow} n_{\downarrow}) \tag{3.23}$$

where $E_G = N\Delta^2/|U| + N|U| n_{\uparrow} n_{\downarrow} + \sum_k [(\xi_{k\uparrow} + \xi_{k\downarrow}) v^2_k - 2\Delta u_k v_k]$. In order to obtain the free energy as a function of the order parameter $\Delta$, we follow the MFT strategy discussed above and compute the partition function for the diagonalized Hamiltonian. This partition function reads

$$Z[\Delta, n_{\sigma}, \mu_{\sigma}] = \prod_{k} (1 + e^{-\beta E^{+}_{k}})(1 + e^{-\beta E^{-}_{k}}) e^{-\beta E_G - \beta N(\mu_{\uparrow} n_{\uparrow} + \mu_{\downarrow} n_{\downarrow})}. \tag{3.24}$$

The grand potential is $\Omega[\Delta, n_\sigma, \mu_\sigma] = -\beta^{-1}\log Z = F(\Delta, \mu_\sigma) + N(\mu_\uparrow n_\uparrow + \mu_\downarrow n_\downarrow)$ where $F(\Delta, \mu_\sigma)$ is the free energy. In order to determine the ground state of the Hamiltonian, we look for the extrema condition in the grand potential with respect to $\mu_{\sigma'}$ and $\Delta$. This optimization leads to a set of self-consistency equations $\partial F(\Delta, \mu_\sigma)/\partial\mu_{\sigma'} + n_{\sigma'} = 0$ and $\partial F(\Delta, \mu_\sigma)/\partial\Delta = 0$. These three equations yield the set of self-consistency equations for the filling, the density imbalance and the gap equation, respectively

$$\frac{1}{N}\sum_k \frac{(\xi_{k\uparrow} + \xi_{k\downarrow})[1 - f(E_k^+) - f(E_k^-)]}{\sqrt{(\xi_{k\uparrow} + \xi_{k\downarrow})^2 + 4\Delta^2}} + \delta = 0 \tag{3.25}$$

$$\frac{1}{N}\sum_k [f(E_k^+) - f(E_k^-)] - p = 0 \tag{3.26}$$

$$\frac{1}{N}\sum_k \frac{1 - f(E_k^+) - f(E_k^-)}{\sqrt{(\xi_{k\uparrow} + \xi_{k\downarrow})^2 + 4\Delta^2}} = \frac{1}{|U|}, \tag{3.27}$$

where $\delta = n_\uparrow + n_\downarrow - 1$ is the doping of the system away from half-filling and $p = n_\uparrow - n_\downarrow$ is the density imbalance. At zero temperature $T = 0$, the energy of the ground state in the canonical ensemble is simplified to

$$E_{BCS}[\Delta, n_\sigma, \mu_\sigma] = \sum_k [f(E_k^+)E_k^+ + f(E_k^-)E_k^-] + E_G + N\sum_\sigma \mu_\sigma n_\sigma, \tag{3.28}$$

where $(\mu, \Delta)$ is the solution of the self-consistency equations.

### 3.2.4 Mean-field theory for the CDW phase

As we have discussed above, a system with an attractive interaction might display a ground state with CDW order [54]. We will only consider the commensurate order here, but the incommensurate case could be addressed by an analysis of the linear response functions. Analogously to the BCS mean field, we can decouple the interaction in the CDW channel defined by the order parameter $\Delta_\sigma = (|U|/N)\sum_{\mathbf{k}}\langle c^\dagger_{\mathbf{k}+\mathbf{Q}\sigma} c_{\mathbf{k}\sigma}\rangle$ with $\mathbf{Q} = (\pi, \pi, \pi)$. The interaction term in the particle-hole channel can be rewritten by neglecting the fluctuations as

$$\frac{|U|}{N}\sum_{\mathbf{k},\mathbf{k}'} c^\dagger_{\mathbf{k}+\mathbf{Q}\uparrow} c_{\mathbf{k}\uparrow} c^\dagger_{\mathbf{k}'\downarrow} c_{\mathbf{k}'+\mathbf{Q}\downarrow} = \sum_{\mathbf{k}} (\Delta_\downarrow c^\dagger_{\mathbf{k}+\mathbf{Q}\uparrow} c_{\mathbf{k}\uparrow} + \Delta_\uparrow c^\dagger_{\mathbf{k}\downarrow} c_{\mathbf{k}+\mathbf{Q}\downarrow}) - \frac{N\Delta_\uparrow\Delta_\downarrow}{|U|}.$$

Introducing the spinor $\psi^\dagger_{\mathbf{k}\sigma} = (c^\dagger_{\mathbf{k}\sigma}, c^\dagger_{\mathbf{k}+\mathbf{Q}\sigma})$, and using the condition $\varepsilon_{\mathbf{k}+\mathbf{Q},\sigma} = -\varepsilon_{\mathbf{k},\sigma}$ to compute the sum in the reduced Brillouin zone (RBZ), the mean-field Hamiltonian reads

$$H_{\mathrm{CDW}} = \sum_{\mathbf{k}\in\mathrm{RBZ},\sigma} \psi^\dagger_{\mathbf{k}\sigma} \begin{bmatrix} \varepsilon_{\mathbf{k}\sigma} - \tilde{\mu}_\sigma & -\Delta_{\bar{\sigma}} \\ -\Delta_{\bar{\sigma}} & -\varepsilon_{\mathbf{k}\sigma} - \tilde{\mu}_\sigma \end{bmatrix} \psi_{\mathbf{k}\sigma} + E_0, \tag{3.29}$$

with $E_0 = N\Delta_\uparrow\Delta_\downarrow/|U| + N|U|n_\uparrow n_\downarrow$. It is readily diagonalized, with eigenvalues: $E^\pm_{\mathbf{k}\sigma} = \pm\sqrt{\varepsilon^2_{\mathbf{k}\sigma} + \Delta^2_{\bar{\sigma}}} - \tilde{\mu}_\sigma$. Hence, we obtain the diagonalized Hamiltonian

$$H_{\mathrm{CDW}} = E_0 + N(\mu_\uparrow n_\uparrow + \mu_\downarrow n_\downarrow) + \sum_{k\in\mathrm{RBZ},\sigma} (E^+_{k\sigma} a^\dagger_{k\sigma} a_{k\sigma} + E^-_{k\sigma} b^\dagger_{k\sigma} b_{k\sigma}). \tag{3.30}$$

The partition function is easily computed from the free modes in the diagonalized Hamiltonian

$$Z[\Delta_\sigma, n_\sigma, \mu_\sigma] = \prod_{k\in\mathrm{RBZ},\sigma} (1 + e^{-\beta E^+_{k\sigma}})(1 + e^{-\beta E^-_{k\sigma}})e^{-\beta E_0}. \tag{3.31}$$

As in the BCS case, the grand potential reads $\Omega[\Delta_\sigma, n_\sigma, \mu_\sigma] = -\frac{1}{\beta}\log Z = F(\Delta_\sigma, \mu_\sigma) + N(\mu_\uparrow n_\uparrow + \mu_\downarrow n_\downarrow)$, where $F(\Delta_\sigma, \mu_\sigma)$ is the free energy. The self-consistency equations are obtained by minimizing the energy with respect to $\mu_\uparrow$, $\mu_\downarrow$ and $\Delta$

$$\frac{1}{N}\sum_{\mathbf{k}\in \mathrm{RBZ}} [f(E^+_{\mathbf{k}\sigma}) + f(E^-_{\mathbf{k}\sigma})] = n_\sigma \tag{3.32}$$

$$\frac{\Delta_\sigma}{N}\sum_{\mathbf{k}\in \mathrm{RBZ}} \frac{f(E^-_{\mathbf{k}\bar{\sigma}}) - f(E^+_{\mathbf{k}\bar{\sigma}})}{\sqrt{\varepsilon^2_{\mathbf{k}\bar{\sigma}} + \Delta^2_\sigma}} = \frac{\Delta_{\bar{\sigma}}}{|U|}. \tag{3.33}$$

At zero temperature $T = 0$, the ground state energy for a system with a given number of atoms for each species and an imbalance of density is

$$E_{CDW}[\Delta_\sigma, n_\sigma, \mu_\sigma] = E_0 + \sum_{\sigma\mathbf{k}\in \mathrm{RBZ}} [f(E^+_{\mathbf{k}\sigma})E^+_{\mathbf{k}\sigma} + f(E^-_{\mathbf{k}\sigma})E^-_{\mathbf{k}\sigma}] + N\sum_\sigma \mu_\sigma n_\sigma, \tag{3.34}$$

in which $(\Delta_\sigma, \mu_\sigma)$ are solutions of the self-consistency equations.

We remind that in all the MFT of this section, both the densities and the order parameters are treated self-consistently. In the next chapters, we will explain why this treatment gives a more reliable physics and we will compare it with more sophisticated mean-field theories like the slave-boson mean field theory and dynamical mean-field theory.

### 3.2.5 The density of states

When the lattice is cubic, the non-interacting band dispersion is given by $\varepsilon_{\sigma\mathbf{k}} = -\sum_\mu 2t_\sigma \cos k_\mu$. In the mean-field theories introduced above, summations over the momenta ($\mathbf{k}$) of the Brillouin zone (BZ) frequently enter the self-consistency equations. In order simplify the calculations, we show here that it might be convenient to work with the density of the states (DOS), which is the distribution of states in an infinitesimal window of energy of the non-interacting system. The DOS is defined as

$$D(E) = \frac{1}{N}\sum_{\mathbf{k}\in \mathrm{BZ}} \delta(E - \varepsilon_{\mathbf{k}}) \approx \frac{1}{(2\pi)^d}\int_{\mathrm{BZ}} \delta(E - \varepsilon_{\mathbf{k}})\mathbf{dk}^d. \tag{3.35}$$

Using this quantity, the $\mathbf{k}$-sum are replaced by an integration over the energies, weighted by a density of states $N^{-1}\sum_{\mathbf{k}\in \mathrm{BZ}} \ldots \rightarrow \int D(E)dE \ldots$. In numerical calculations, using the DOS can strongly reduce the computational time. In addition, some limits offer a simple representation of the DOS. For example, in the limit of infinite dimensions, there is an analytical form for the DOS. We can thus obtain some analytical or asymptotic results. In some rough approximations, one can also treat the irrelevant part of the integral over the energy by a simplified form of the DOS, while the relevant part is treated more carefully. This can help to get a rapid guess for the physical properties without the loss of time due to a sophisticated numerical calculation.

Within this thesis, we study models of fermionic mixture with different DOS. For the 2D, 3D and infinite dimensional cases, numerical results will be presented. For an analytical understanding of problem, we propose to use the flat DOS

$$D_\sigma(\varepsilon) = \begin{cases} 1/W_\sigma & \text{if} \quad \varepsilon \in [-W_\sigma/2, W_\sigma/2] \\ 0 & \text{if} \quad \varepsilon \notin [-W_\sigma/2, W_\sigma/2] \end{cases}$$

In general, this simple DOS does not estimate exactly the values of physical quantities such as the gap, the critical temperature, the critical field, etc. However, it provides a qualitatively good physical description of the models such as the phase transitions, the phase diagram, etc.

## 3.3 Strong-coupling mean-field theory

The weak-coupling MFT is based on the decoupling of the interaction motivated by the condition $|U|/t \ll 1$, which allows to neglect fluctuations. In the opposite limit $|U|/t \gg 1$, a perturbation theory based on the development in powers of $t/|U|$ is also possible. In the following, we show that this degenerate perturbation theory can map the Hubbard model to some well-known models which were already treated by mean-field theory.

### 3.3.1 Positive coupling ($U > 0$)

**Limit of strong coupling at half-filling**

Let us first consider the large repulsive-$U$ limit at half-filling. In this limit ($|U| \gg t$), the Hubbard model with $t_\uparrow = t_\downarrow = t$ map onto a quantum Heisenberg spin model. Indeed, when the interaction strength is big enough, the atoms tend to stay on the same lattice site. They are distributed regularly over the lattice (one particle per site). In order to show the mapping, we propose to consider the problem of two atoms on two sites. There are only four possible configurations: i) one atom per site with two up-atoms, ii) one atom per site with two down-atoms, iii) one atom per site with one up and one down (2-fold degenerate), iv) two atoms (one up and one down) on one site and the other site empty (2-fold degenerate). If there is no hoping ($t = 0$) then the three states i, ii, iii are eigenstates of energy 0 and the last state is an eigenstate of energy $U$. When the hopping is small $t \ll U$, the tunneling term of the Hamiltonian couples the two states iii and iv with an amplitude $t$. In this case, up and down atoms can make a local move to the neighboring site and then hop back. This move makes the antiferromagnetic (AF) configuration iii lower in energy by a amount of the order of $2t^2/U$ when compared to the ferromagnetic (F) configurations i and ii. By introducing the spin-exchange coupling energy $J = 4t^2/U$ for the 1/2-spin model, we also find an energy difference between an AF configuration and an F configuration of the order of $2t^2/2$.

In the extended Hubbard model, this result is slightly modified by the fact that there is a mass imbalance. This mass imbalance induces an anisotropy of the AF spin coupling in different directions. The effective model is now an $XXZ$ model in an external field. This external field is used to fix the imbalance of density.

$$H = J \sum_{\langle i,j \rangle} \vec{S}_i . \vec{S}_j + \gamma J \sum_{\langle i,j \rangle} S_i^z S_j^z - 2h \sum_i (S_i^z - m), \tag{3.36}$$

where the spin operators and the couplings are defined by $\vec{S} = 1/2 c_\alpha^\dagger \vec{\sigma}_{\alpha\beta} c_\beta$, $J = 4t_\uparrow t_\downarrow / U$ and $\gamma = (t_\uparrow - t_\downarrow)^2 / 2t_\uparrow t_\downarrow$. Here, for the convenience of the spin model, we introduce the magnetization $m$ which measures the average value of the operator $S^z$. The magnetization is related to the polarization simply by $m = \langle S^z \rangle = (n_\uparrow - n_\downarrow)/2 = p/2$. In order to study the phase diagram of this model, we can use a classical spin mean-field approach. One can then go beyond MFT using the spin-wave theory [5, 101] (see also Appendix A.1 for detailed discussion).

The mean-field approach [101] amounts to treat the spin variables as classical. In order to study the commensurate spin density wave ordering, we break the translation invariance and consider a unit cell of two neighbor sites A and B. We define $\theta_A, \theta_B$ as the orientations of the spins on the two sites A and B, respectively (Fig. 3.8). The MFT strategy consists of minimizing the total energy over the angles $\theta_A, \theta_B$. The energy per site reads

$$E = \frac{N\zeta}{2} J S^2 \sin\theta_A \sin\theta_B + \frac{N\zeta}{2} J(1+\gamma) S^2 \cos\theta_A \cos\theta_B - \frac{Nh}{2} (S(\cos\theta_A + \cos\theta_B) - 2m). \tag{3.37}$$

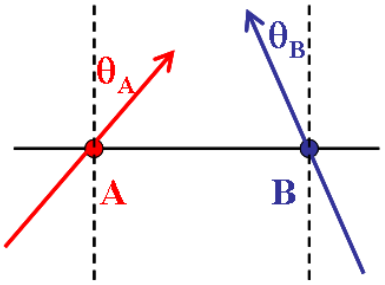


**Figure 3.8:** Spin configuration on the two neighbor sites which belong two sublattices A and B respectively. $\theta_A$ and $\theta_B$ are the orientation of spins on these sites.

---

Here, $\zeta$ is the number of nearest neighbors of a site in the lattice and $S = 1/2$ is the spin of the models. The spin configuration which minimizes the total energy with respect to $h, \theta_A, \theta_B$ must satisfy the mean-field equations $\partial E/\partial h = 0$, $\partial E/\partial \theta_A = 0$ and $\partial E/\partial \theta_B = 0$, or

$$\cos\theta_A + \cos\theta_B = \frac{2m}{S} \tag{3.38}$$

$$\frac{NzJS^2}{2}\cos\theta_A \sin\theta_B - \frac{NzJ(1+\gamma)S^2}{2}\sin\theta_A\cos\theta_B + \frac{NhS}{2}\sin\theta_A = 0 \tag{3.39}$$

$$\frac{NzJS^2}{2}\sin\theta_A \cos\theta_B - \frac{NzJ(1+\gamma)S^2}{2}\cos\theta_A\sin\theta_B + \frac{NhS}{2}\sin\theta_B = 0. \tag{3.40}$$

The solution of these equations gives the optimal value of the two angles $\theta_\alpha$ and $\theta_\beta$. We now define the two order parameters

$$\Delta_{AF} = \frac{1}{N}\sum_i (-1)^i S_i^z = \frac{S_A^z - S_B^z}{2} \tag{3.41}$$

$$\Delta_{XY} = \frac{1}{N}\sum_i (-1)^i S_i^x = \frac{S_A^x - S_B^x}{2}. \tag{3.42}$$

Here, $\Delta_{AF}$ is the order parameter of the antiferromagnetic phase, while $\Delta_{XY}$ is the order parameter of the in-plane $(XY)$ SDW. In the presence of a fixed external field, the self-consistency Eq. 3.39 and Eq. 3.40 become

$$\sin\frac{\theta_A+\theta_B}{2}\left[zJ\gamma S\cos\frac{\theta_A+\theta_B}{2} - h\cos\frac{\theta_A-\theta_B}{2}\right] = 0 \tag{3.43}$$

$$\sin\frac{\theta_B-\theta_A}{2}\left[zJ(2+\gamma)S\cos\frac{\theta_A-\theta_B}{2} - h\cos\frac{\theta_A+\theta_B}{2}\right] = 0. \tag{3.44}$$

### Limit of strong coupling away from half-filling

When the system is doped, the problem becomes more difficult. Even in the strong coupling limit, similar arguments lead to a complicated model. In this case, localized atoms still realize a spin-exchange interaction while the extra atoms (or holes) can move on this spin background. The extended Hubbard model away from half-filling maps to a $t-J$ model with a spin-anisotropic coupling

$$H = -\sum_{\langle i,j,\sigma\rangle}(t_\sigma \mathbf{P} c_{i\sigma}^\dagger c_{j\sigma}\mathbf{P} + H.c) + J\sum_{\langle i,j\rangle}\vec{S}_i.\vec{S}_j + \gamma J\sum_{\langle i,j\rangle} S_i^z S_j^z, \tag{3.45}$$

in which the definitions of $J$, $\gamma$ and $\vec{S}$ are the same as in the $XXZ$ model and $\mathbf{P}$ is the projector on the subspace with one particle per site. In this model, the first term describes the dynamics of the extra atoms, while the last terms are used for the spin interaction just as in the $XXZ$ model. The isotropic $t-J$ model has been studied with Schwinger-boson mean-field theory and slave-fermion methods by Auerbach [8].

### 3.3.2 Negative coupling ($U < 0$)

**Effective boson model for mixtures with the same density**

We now consider the negative-$U$ strong coupling MFT. As we have shown above, this model can be mapped to the positive-$U$ one via a particle-hole transformation. Here, when the attractive interaction between the two species of atoms becomes strong enough, the species form a bound state in order to gain potential energy. The model becomes an effective hard-core boson model (with bound states formed by a pair of local fermions) with bosons $b_i^+ = c_{i\uparrow}^+ c_{i\downarrow}$. When the mixture has the same density of both species, we obtain a effective model that only has hard-core bosons [22]. The hopping of the atoms in the initial model induces an effective hoping of the bosons $t_b = 4t^2/U$. The asymmetry of the hopping instead generates an effective interaction between nearest-neighbor bosons $V = 4\gamma t^2/U$. The resulting Hamiltonian is

$$H = -\sum_{\langle i,j\rangle} t_b b_i^+ b_j + V \sum_{\langle i,j\rangle} n_{bi} n_{bj} + \text{hard-core boson constraint.} \tag{3.46}$$

When there is no hopping imbalance, one obtains a gas of bosons in an optical lattice which can condense in high dimensions (D=3) to the ground state of a Bose-Einstein condensate.

**Effective boson-fermion mixture for the density imbalanced model**

When the mixture presents a density imbalance, we recover a model with a boson-fermion mixture. In this case, the available two species of atoms form hard-core bosons as above. The extra fermions still keep their fermionic statistics and contribute to the fermionic part for the total Hamiltonian

$$H = \sum_{\langle i,j\rangle} t_\sigma c_{i\sigma}^+ c_{j\sigma} - \sum_{\langle i,j\rangle} t_b b_i^+ b_j + V \sum_{\langle i,j\rangle} n_{bi} n_{bj} + \text{hard-core boson constraint.} \tag{3.47}$$

This model is relevant for a recent series of experiments on spin imbalanced mixtures realized in the MIT group and in the Rice group.

## 3.4 Slave-boson mean-field theory

The Hartree-Fock mean-field theory is formulated around the non-interacting limit and neglects all the quantum fluctuations. The validity of the theory is limited to the weak-coupling regime where $|U| \ll t_\sigma$. Here, we introduce another analytical approach, the slave-boson mean-field theory which allows to extend the domain of validity of the mean-field approach. A solid formalism of the slave-boson MFT has been recently given in [75]. For a matter of simplicity, we use here the basic formalism that has first been introduced in the work of Kotliar and Ruckenstein [71]. In order to further simplify the calculation, we only present the derivation of the mean-field equations for the model with no mass imbalance. The generalization for a mass imbalanced system is straightforward.

### 3.4.1 Formalism of the slave-boson mean-field theory

It is possible to develop the slave-boson mean-field theory directly for the negative-$U$ Hubbard model, see Bulka et al [17]. However, we choose a different route and prefer to construct the mean-field theory in the case of positive coupling and then apply the particle-hole transformation to map it to the negative-$U$ model [7, 108]. Let us recall that if, in the negative-$U$ case, the model has a polarization, then, in the positive coupling, it is doped with no external magnetic field.

The basic idea of the slave boson mean-field approach is that in strongly-correlated system, the process of hopping of particle is accompanied by a backflow of spin and charge excitations of the medium. This effect is equivalent to the renormalization of mass for the quasiparticles. This idea can be realized by representing the original Hamiltonian in a new basis of quasiparticles with slave bosons which describe the effect of mass renormalization. We define the for bosonic operators: $e^\dagger, d^\dagger, p_\uparrow^\dagger, p_\downarrow^\dagger$ which allow to compute the occupation numbers in each of for possible states available for hopping process: $|0\rangle$, $|\uparrow\downarrow\rangle$, $|\uparrow\rangle$, $|\downarrow\rangle$. In the new enlarged space with bosons and quasiparticles, the creation operator becomes

$$c_{i\sigma}^\dagger = z_{i\sigma}^\dagger f_{i\sigma}^\dagger \quad \text{with} \quad z_{i\sigma} = e_i^\dagger p_{i\sigma} + p_{i\bar{\sigma}}^\dagger d_i, \tag{3.48}$$

and the Hamiltonian reads

$$H_{SB} = -\sum_{\langle i,j\rangle\sigma} t_\sigma (f_{i\sigma}^\dagger f_{j\sigma} z_{i\sigma}^\dagger z_{j\sigma} + h.c) + U\sum_i d_i^\dagger d_i - \sum_{i,\sigma} \tilde{\mu}_\sigma (d_i^\dagger d_i + p_{i\sigma}^\dagger p_{i\sigma}). \tag{3.49}$$

Note that we are working in an enlarged space and therefore there is more than one way to express the Hamiltonian in this new basis. We chose here the simplest way, and write the local part of the Hamiltonian by in the boson basis. This simplifies the expression of the Hamiltonian and gives very good control in some limits of the mean-field approximation. It is always possible to write the Hamiltonian in a more complicated form. For instance, the part with the chemical potential could be written as $\sum_i \tilde{\mu}_\sigma f_{i\sigma}^\dagger f_{i\sigma} z_{i\sigma}^\dagger z_{i\sigma}$. Since we are working in an enlarged space, one must impose the following constraints in order to recover the physical subspace

$$p_{i\uparrow}^\dagger p_{i\uparrow} + p_{i\downarrow}^\dagger p_{i\downarrow} + e_i^\dagger e_i + d_i^\dagger d_i = 1 \tag{3.50}$$

$$p_{i\sigma}^\dagger p_{i\sigma} + d_i^\dagger d_i = f_{i\sigma}^\dagger f_{i\sigma}. \tag{3.51}$$

With this construction of the slave-boson MFT, one does not recover the correct non-interacting limit at the saddle-point approximation. As mentioned above, one has many ways to write the Hamiltonian in the new basis. In order to correct this problem, we introduce a unitary transformation on the boson $z_{i\sigma}$ which does not affect the construction of the enlarged space

$$\tilde{z}_{i\sigma} = (1 - d_i^\dagger d_i - p_{i\sigma}^\dagger p_{i\sigma})^{-1/2} z_{i\sigma} (1 - e_i^\dagger e_i - p_{i\bar{\sigma}}^\dagger p_{i\bar{\sigma}})^{-1/2}. \tag{3.52}$$

Finally, the correct Hamiltonian including the constraints with the corresponding Lagrangian multipliers $\lambda_0, \lambda_{i\sigma}$ is given by

$$\begin{aligned} H_{SB} = &-\sum_{\langle i,j\rangle\sigma} t_\sigma (f_{i\sigma}^\dagger f_{j\sigma} z_{i\sigma}^\dagger z_{j\sigma} + h.c) + U\sum_i d_i^\dagger d_i - \sum_{i,\sigma} \tilde{\mu}_\sigma (d_i^\dagger d_i + p_{i\sigma}^\dagger p_{i\sigma}) \\ &- \sum_i \lambda_{0i} (p_{i\uparrow}^\dagger p_{i\uparrow} + p_{i\downarrow}^\dagger p_{i\downarrow} + e_i^\dagger e_i + d_i^\dagger d_i - 1) - \sum_{i\sigma} \lambda_{\sigma i} (f_{i\sigma}^\dagger f_{i\sigma} - p_{i\sigma}^\dagger p_{i\sigma} - d_i^\dagger d_i). \end{aligned}$$

**Normal phase**

In the normal phase, we preserve the translational invariance. Therefore, the slave bosons are the same over the whole lattice: $e_i = e$, $d_i = d$, $p_{i\sigma} = p_\sigma$. In the system with spin symmetry SU(2), we have the additional condition $p_\sigma = p$.

**Phase with long-range order**

In the case of an isotropic hopping, the SU(2) spin symmetry is conserved. An $SDW_{xy}$ order is equivalent to an antiferromagnetic order ($SDW_z$). In order to be able to describe a situation with a broken symmetry as well, we will extend the formalism of the slave bosons on a bipartite lattice with two sublattices A (B). The four slave bosons and quasiparticles for each sublattice are $e_{A(B)}, d_{A(B)}, p_{\uparrow A(B)} p_{\downarrow A(B)}$, $f_{A(B)}$. We can restore the symmetry between these two sublattices with

$$e_A = e_B = e, \quad d_A = d_B = d, \quad p_\sigma = p_{\sigma A} = p_{\bar{\sigma} B}. \tag{3.53}$$

The AF order parameter (staggered magnetization) is defined by

$$\Delta_{AF} = p_{A\uparrow}^2 - p_{A\downarrow}^2 = p_\uparrow^2 - p_\downarrow^2. \tag{3.54}$$

### 3.4.2 Saddle-point approximation

The simplest approximation that we can envisage is the saddle-point approximation which consists in replacing the bosonic operators by their average value. We consider here the case without hopping imbalance ($z = 0$) as an example. The result for case with hopping imbalance case ($z \neq 0$) can be generalized straight forward. In addition, we suppose that the system is homogeneous over each sublattice[1]: $\langle \phi_{iA(B)} \rangle = \langle \phi_{A(B)} \rangle$ where $\phi_i = e_i, d_i, p_{\sigma i}$. We then define $q = \langle \tilde{z}_{i\sigma} \tilde{z}_{j\sigma} \rangle$, the quasiparticle weight

$$q = \frac{e^2 p_{A\sigma} p_{B\sigma} + d^2 p_{A\bar{\sigma}} p_{B\bar{\sigma}} + ed(e^2 p_{A\sigma} p_{B\bar{\sigma}} + e^2 p_{A\bar{\sigma}} p_{B\sigma})}{(1 - d^2 - p_{A\sigma}^2)^{-1/2} (1 - d^2 - p_{B\sigma}^2)^{-1/2} (1 - e^2 - p_{A\bar{\sigma}}^2)^{-1/2} (1 - e^2 - p_{B\bar{\sigma}}^2)^{-1/2}}. \tag{3.55}$$

Using the symmetry of the two sublattices A and B, we have $p_\sigma = p_{A\sigma} = p_{B\bar{\sigma}}$, $\lambda_\sigma = \lambda_{A\sigma} = \lambda_{B\bar{\sigma}}$. Performing the Fourier transform in the reduced Brillouin zone and defining the spinor $\psi_k^\dagger = (f_{Ak}^\dagger, f_{Bk}^\dagger)$, the Hamiltonian can be expressed in the following matrix form

$$H_{\mathrm{SB}} = \sum_{k \in RBZ, \sigma} \psi_k^\dagger \begin{bmatrix} -\lambda_\sigma & q\varepsilon_k \\ q\varepsilon_k & -\lambda_{\bar{\sigma}} \end{bmatrix} \psi_k + E_0, \tag{3.56}$$

with $E_0 = N(Ud^2 - \lambda_0(p_\uparrow^2 + p_\downarrow^2 + e^2 + d^2) + \lambda_\uparrow(p_\uparrow^2 + d^2) + \lambda_\downarrow(p_\downarrow^2 + d^2) - \tilde{\mu}(p_\uparrow^2 + p_\downarrow^2 + 2d^2 - 1))$. The sum is done over the half of the Brillouin zone. We define the new variables $\Lambda = (\lambda_\uparrow + \lambda_\downarrow)/2$, $\Delta = (\lambda_\uparrow - \lambda_\downarrow)/2$. In this quadratic form, we can now easily diagonalize the mean-field Hamiltonian and obtain the following eigenvalues $E_{k\sigma}^{\pm} = \pm\sqrt{q^2\varepsilon_k^2 + \Delta^2} - \Lambda$. The Hamiltonian in the diagonal basis now reads

$$H_{\mathrm{SB}} = \sum_{k \in RBZ, \sigma} (E_{k\sigma}^+ \alpha_{k\sigma}^\dagger \alpha_{k\sigma} + E_{k\sigma}^- \beta_{k\sigma}^\dagger \beta_{k\sigma}) + E_0. \tag{3.57}$$

[1] The translation invariance on each sublattice is preserved.

The partition function can be evaluated $Z = \prod_{k\in RBZ,\sigma}(1+e^{-\beta E^+_{k\sigma}})(1+e^{-\beta E^-_{k\sigma}})e^{-2\beta E_0}$. The free energy is given by $F = -\beta^{-1}\log Z$ and the self-consistency equations read

$$\frac{\partial F}{\partial \lambda} = 0, \quad \frac{\partial F}{\partial \phi} = 0 \tag{3.58}$$

where $\phi = e, d, p_\sigma$ and $\lambda = \lambda_0, \lambda_\sigma$. In order to simplify the calculation, we define the following variables

$$\Delta_{AF} = p^2_\uparrow - p^2_\downarrow, \quad \delta = d^2 - e^2, \quad \tilde{\Lambda} = \Lambda/q, \quad \tilde{\Delta} = \Delta/q. \tag{3.59}$$

With these new variables, we can simplify the expression of the energy $E_0$ and the quasiparticle weight

$$E_0/N = Ud^2 + \Lambda(1+\delta) - \tilde{\mu}\delta + \Delta\Delta_{AF}$$
$$q = \frac{2(2d^2-\delta)\sqrt{(1+\delta-2d^2)^2-\Delta^2_{AF}} + 4d\sqrt{d^2-\delta}(1+\delta-2d^2)}{\sqrt{(1+\delta)^2-\Delta^2_{AF}}\sqrt{(1-\delta)^2-\Delta^2_{AF}}}.$$

After some algebra, we obtain the set of self-consistency equations for the Slave Bosons mean-field theory

$$d^2 - e^2 = \delta \tag{3.60}$$
$$\frac{1}{N}\sum_{k\in RBZ,\sigma}[f(E^+_{k\sigma}) + f(E^-_{k\sigma})] = 1+\delta \tag{3.61}$$
$$\frac{1}{N}\sum_{k\in RBZ,\sigma}\frac{q\varepsilon^2_k[f(E^+_{k\sigma}) - f(E^-_{k\sigma})]}{\sqrt{q^2\varepsilon^2_k+\Delta^2}}\frac{\partial q^2}{\partial\delta} + \Lambda - \tilde{\mu} = 0 \tag{3.62}$$
$$\frac{1}{N}\sum_{k\in RBZ,\sigma}\frac{q\varepsilon^2_k[f(E^+_{k\sigma}) - f(E^-_{k\sigma})]}{\sqrt{q^2\varepsilon^2_k+\Delta^2}}\frac{\partial q^2}{\partial\Delta_{AF}} + \Delta = 0 \tag{3.63}$$
$$\frac{1}{N}\sum_{k\in RBZ,\sigma}\frac{\Delta[f(E^+_{k\sigma}) - f(E^-_{k\sigma})]}{\sqrt{q^2\varepsilon^2_k+\Delta^2}} + \Delta_{AF} = 0 \tag{3.64}$$
$$\frac{1}{N}\sum_{k\in RBZ,\sigma}\frac{q\varepsilon^2_k[f(E^+_{k\sigma}) - f(E^-_{k\sigma})]}{\sqrt{q^2\varepsilon^2_k+\Delta^2}}\frac{\partial q^2}{\partial d^2} + U = 0. \tag{3.65}$$

At zero temperature $T = 0$, the energy of the ground state of the canonical system is given by

$$E_G[\Delta_{AF},\Delta,\delta] = E_0 + \sum_{k\in RBZ,\sigma}[E^+_{k\sigma}f(E^+_{k\sigma}) + E^-_{k\sigma}f(E^-_{k\sigma})]. \tag{3.66}$$

in which the order parameter $\Delta_{AF}$ is the solution of the self-consistency equations. We remark that within this analysis the normal phase corresponds to the case where there is trivial solution $\Delta_{AF} = 0$. Therefore, the study on stability of the solutions of the self-consistency equations gives directly the condition for the phase transition from the normal phase to the phase AF phase.

## 3.5 Dynamical mean-field theory

Dynamical mean-filed theory (DMFT) is one of the most popular modern theoretical approaches designed to treat correlated fermions on a lattice [33, 43, 44]. The idea of the method

is to extend the classical mean-field strategy to quantum systems, replacing static mean-field averages by frequency-dependent (dynamical) objects. Just like classical mean-field theory, DMFT freezes spatial correlations, but allows for an unbiased treatment of the dynamics. A practical implementation of DMFT requires the self-consistent solution of a quantum impurity model, i.e., a model of a single interacting site coupled to a bath that allows for quantum fluctuations on the correlated site. In the mean-field spirit, a given site is representative of

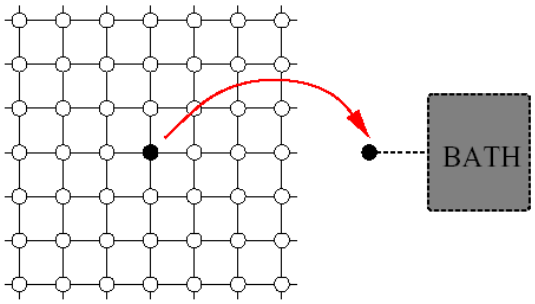


**Figure 3.9:** DMFT schema in which we replace a lattice model by a model with single site coupled to a self-consistent bath. Reprinted from Ref. [33]

any site of the original lattice. This correspondence is implemented via a self-consistency condition which contains the information about the original lattice through its non-interacting density of states. The self-consistency condition relates the frequency-dependent 'Weiss field' which describes the dynamics of the bath (analogous to the static Weiss field in the mean-field theory of magnetism) $\hat{\mathcal{G}}(i\omega)$ to the Green's function of the correlated site [44].

In the normal phase, DMFT is able to describe a Mott metal-insulator transition. The technique allows to address the strongly-correlated regime where the interaction is comparable to the kinetic energy of the system ($U \sim t$). For phases with long-range order, the advantage of this method is that it gives a very good description of the BEC-BCS crossover when both species have the same density [120]. It means that the off-diagonal order not only contains the BCS channel which is relevant for weak coupling but also the condensation of bosons formed by local fermionic pairs in the strong coupling limit. In addition, when the local fluctuations are frozen by replacing frequency-dependent objects by their average value, one recovers exactly the static mean-field description.

### 3.5.1 DMFT self-consistency equations

In order to keep the formalism easy, we will derive the self-consistency equations using the cavity method for the model defined on an infinite-dimensional Bethe lattice. In this part, we first discuss the DMFT of a normal phase without symmetry breaking. For the standard Hubbard model, the partition function reads

$$Z = \int \prod_i D c_{i\sigma}^\dagger D c_{i\sigma} e^{-S[c_{i\sigma}^\dagger, c_{i\sigma}]}, \tag{3.67}$$

where $S[c_{i\sigma}^\dagger, c_{i\sigma}]$ is the action of the Hubbard Hamiltonian defined by

$$S[c_{i\sigma}^\dagger, c_{i\sigma}] = \int_0^\beta d\tau \Big[ \sum_{i\sigma} c_{i\sigma}^\dagger (\partial_\tau - \mu_\sigma) c_{i\sigma} - \sum_{\langle i,j\rangle \sigma} t_{ij\sigma} c_{i\sigma}^\dagger c_{j\sigma} + U \sum_i n_{i\uparrow} n_{i\downarrow} \Big]. \tag{3.68}$$

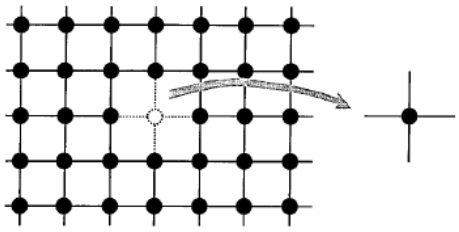

**Figure 3.10:** Illustration of the cavity method. The cavity is created in the full lattice by removing a given site and its adjacent bonds. Reprinted from Ref. [44]

.

---

We divide the system in two parts: the site "0" and "the lattice without site 0". We then integrate over all the degrees of freedom of the cavity in order to obtain the effective action

$$e^{-S_{eff}[c^\dagger_{i\sigma},c_{i\sigma}]} = \int \prod_{i\neq 0} Dc^\dagger_{i\sigma} Dc_{i\sigma} e^{-S[c^\dagger_{i\sigma},c_{i\sigma}]}. \tag{3.69}$$

Therefore, the partition function can now be written as

$$Z = \int Dc^\dagger_{0\sigma} Dc_{0\sigma} e^{-S_{eff}[c^\dagger_{i\sigma},c_{i\sigma}]}. \tag{3.70}$$

In order to evaluate this expression, we divide the total action in three parts: $S = S^{(0)} + \Delta S + S_0$. Here, $S^{(0)}$ is the action of the lattice with the cavity (this is the bath), $S_0$ is the action of the decoupled site "0" and $\Delta S$ is the action representing the hybridization of the decoupled site with the bath. We have

$$S_0 = \int_0^\beta d\tau \Big( \sum_\sigma c^\dagger_{0\sigma}(\partial_\tau - \mu_\sigma) c_{0\sigma} + U n_{0\uparrow} n_{0\downarrow} \Big)$$

$$\Delta S = -\int_0^\beta d\tau \sum_{\langle i,0\rangle\sigma} t_{i0\sigma}(c^\dagger_{i\sigma} c_{0\sigma} + h.c).$$

Here, we can define $\eta_{i\sigma} = t_{i0\sigma} c_{0\sigma}$ as a source which couples to $c^\dagger_{i\sigma}$. Using the gaussian integration, we obtain

$$S_{eff}[c^\dagger_{0\sigma}, c_{0\sigma}] = S_0 + \sum_{n=1}^{\infty} \sum_{i_1 \ldots j_n \sigma} \int \eta^\dagger_{i_1\sigma} \ldots \eta^\dagger_{i_n\sigma} G^{(0)}_{i_1 \ldots j_n \sigma}(\tau_{i_1} \ldots \tau_{j_n}) \eta_{j_1\sigma} \ldots \eta_{j_n\sigma} + \text{const.} \tag{3.71}$$

When we take the infinite-dimension limit ($d \to \infty$) and the Fourier transform, all terms of order higher than 1 vanish and we get a very simple relation

$$S_{eff}[c^\dagger_{0\sigma}, c_{0\sigma}] = S_0 + \sum_\sigma c^\dagger_{0\sigma} \mathcal{G}^{-1}_{0\sigma}(i\omega_n) c_{0\sigma} + U n_{0\uparrow} n_{0\downarrow}, \tag{3.72}$$

where

$$\mathcal{G}^{-1}_{0\sigma}(i\omega_n) = i\omega_n + \mu_\sigma - \sum_{\langle i,j\rangle\sigma} t_{0i\sigma} t_{0j\sigma} G^{(0)}_{ij\sigma}(i\omega_n). \tag{3.73}$$

In the Bethe lattice, the hopping $t_{0i\sigma} \to t_{0i\sigma}/\sqrt{d}$ is renormalized in order to have a non-trivial physical limit when $d \to \infty$. When the site "0" is removed, then $G^{(0)}_{ij} = 0$ with

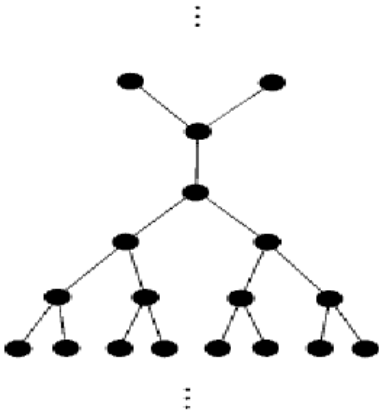

**Figure 3.11:** Bethe lattice (depicted here with connectivity $z = 3$). Reprinted from Ref. [44]

$i \neq j$ and $G_{ii\sigma} = G_\sigma$ because of the translational invariance. Finally, we have the following self-consistency equation

$$\mathcal{G}_0^{-1}(i\omega_n) = i\omega_n + \mu_\sigma - t_\sigma^2 G_\sigma(i\omega_n). \tag{3.74}$$

So far, we have discussed the main ideas of DMFT and established the self-consistency equations. Although this theory turns the many-body problem into a much simpler version, it still remains a complicated quantum problem to solve. An analytical solution within this mean-field theory can only be obtained in some specific limits such as the atomic limit or the Falicov-Kimball limit. Fortunately, the reduced problem with less degrees of freedom can be solved using various numerical methods. The schema of the procedure to solve a one-band Hubbard model within DMFT is shown in Fig. 3.12. We start with a guess for the non-

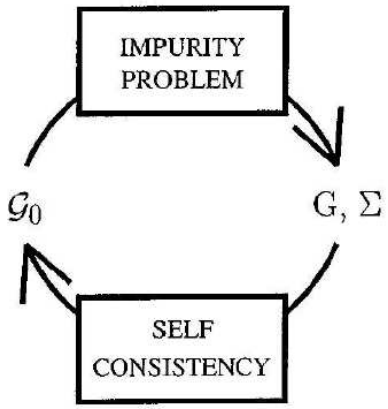


**Figure 3.12:** Schema of the DMFT iteration loop.

interacting Green's function $\mathcal{G}_0(i\omega_n)$ which is enough to define the effective action of the local impurity problem. Next, we solve this effective problem to get the local Green's function $\mathcal{G}_{imp}(i\omega_n)$. The local self-energy is then obtained by $\Sigma(i\omega_n) = \mathcal{G}_0^{-1}(i\omega_n - \mathcal{G}_{imp}(i\omega_n$. Inserting this local Green's function and its self-energy in the DMFT self-consistency equations, we obtain a new guess Green's function $\mathcal{G}_0(i\omega_n)$ for the next iteration. The solution is achieved when these iterations converge. Finally, the different physical quantities are computed from

the Green's functions. As we are working on the imaginary Matsubara frequency axis, in order to obtain the spectral function we need then to do an analytical continuation to the real axis [117].

### 3.5.2 DMFT for phases with a broken symmetry

We now discuss the possibility to study phases with broken symmetries within DMFT [44]. We propose to divide our model into two classes: (i) the model with positive coupling and (ii) the model with negative coupling. As discussed above, in the positive coupling limit we will establish the framework to study the stability of the antiferromagnetic ground state, while in the negative coupling regime, we will include both the CDW and SF order.

#### DMFT for the positive-$U$ Hubbard model

Let us consider this model on a bipartite lattice with two sublattices A and B. In order to study the phases with symmetry breaking, we introduce an external field to break the translational invariance. The external magnetic field has a modulation over the lattice such as to form an antiferromagnetic phase (AF)

$$h = h_s \sum_{i\sigma} e^{iQ.R_i} c^\dagger_{i\sigma} c_{i\sigma} \quad \text{with} \quad Q = (\pi, \dots \pi).$$

This way, we break the translation invariance of the lattice but we can restore it for an elementary cell with two sites (A,B). The external field added in the Hamiltonian just changes the chemical potential on the two sublattices, therefore we can apply the DMFT self-consistency equations obtained in the last section

$$\mathcal{G}^{-1}_{0A(B)}(i\omega_n) = i\omega_n + \mu_\sigma \mp \sigma h_s - t^2 G_{B(A)\sigma}(i\omega_n). \tag{3.75}$$

We introduced the field $h$ in order to break the translational symmetry, but we will set it to zero in the actual calculation and obtain

$$\mathcal{G}^{-1}_{A(B)0}(i\omega_n) = i\omega_n + \mu_\sigma - t^2 G_{B(A)\sigma}(i\omega_n). \tag{3.76}$$

When the hopping is the same for both species and there is no external magnetic field, we have an SU(2) spin rotational invariance. This symmetry is reduced when the field is non-zero (when the translational symmetry is broken) and we have $c_{A\uparrow} \to c_{B\downarrow}$ or $i \in A, \sigma \to i \in B, -\sigma$, which induces an additional relation on the Green's function on the two sublattices $G_{A\sigma}(i\omega_n) = G_{B-\sigma}(\omega_n)$. Finally, the self-consistency equation is simplified to

$$\mathcal{G}^{-1}_0(i\omega_n) = i\omega_n + \mu_\sigma - t^2 G_{-\sigma}(i\omega_n). \tag{3.77}$$

#### DMFT for the negative-$U$ Hubbard model

Instead of studying the Hubbard model in the positive coupling limit for the half-filled model, we can also study directly the phases in the attractive model. In this case, the Hamiltonian reads

$$H = -\sum_{\langle i,j\rangle} t_\sigma (c^\dagger_{i\sigma} c_{j\sigma} + h.c) - |U| \sum_i n_{i\uparrow} n_{i\downarrow} - \sum_i \mu_\sigma c^\dagger_{i\sigma} c_{i\sigma}. \tag{3.78}$$

We define the Nambu spinor $\psi^\dagger_i = (c^\dagger_{i\uparrow}, c_{i\downarrow})$, and the Hamiltonian becomes

$$H = -\sum_{\langle i,j\rangle} (\psi^\dagger_i T \psi_j + h.c) - |U| \sum_i n_{i\uparrow} n_{i\downarrow} - \sum_i \psi^\dagger_i \mu \psi_i + \text{const}, \tag{3.79}$$

where $T$ and $\mu$ are diagonal matrices of the hopping and of the chemical potential for the Nambu spinors. They are defined as

$$T = \begin{bmatrix} t_\uparrow & 0 \\ 0 & -t_\downarrow \end{bmatrix}, \qquad \mu = \begin{bmatrix} \mu_\uparrow & 0 \\ 0 & -\mu_\downarrow \end{bmatrix} \tag{3.80}$$

In this representation, the action of the Hamiltonian reads

$$S = -\int_0^\beta d\tau \sum_{\langle i,o\rangle} (\psi_i^\dagger T \psi_o + h.c) + \int_0^\beta d\tau \psi_o^\dagger (\partial_\tau - \mu)\psi_o + |U| n_{o\uparrow} n_{o\downarrow} + S^{(o)}, \tag{3.81}$$

where $S^{(o)}$ is the action of the lattice without site "$o$". We define the Green's function for these Nambu spinors by

$$\mathbf{G}(k,\tau) = \langle \mathrm{T}_\tau \psi_{k,\tau} \psi_{k,0}^\dagger \rangle = \begin{bmatrix} \langle T_\tau c_{k\uparrow}(\tau) c_{k\uparrow}^\dagger(0)\rangle & \langle T_\tau c_{k\uparrow}(\tau) c_{-k\downarrow}(0)\rangle \\ \langle T_\tau c_{-k\downarrow}^\dagger(\tau) c_{k\uparrow}(0)\rangle & \langle T_\tau c_{-k\downarrow}^\dagger(\tau) c_{-k\downarrow}(0)\rangle \end{bmatrix} \tag{3.82}$$

The Fourier transform yields

$$\mathbf{G}(k, i\omega_n) = \begin{bmatrix} G_\uparrow(k, i\omega_n) & F(k, i\omega_n) \\ F(k, i\omega_n) & -G_\downarrow(-k, -i\omega_n) \end{bmatrix} \tag{3.83}$$

As in the first part of DMFT, we calculate the effective action in the $d \to \infty$ limit and we have

$$S_{eff}^o = \int_0^\beta d\tau \psi_o^\dagger (\partial_\tau - \mu)\psi_o + \sum_{\langle ij,o\rangle} \psi_o^\dagger T^+ G_{ij}^{(o)} T \psi_o - |U| n_{o\uparrow} n_{o\downarrow} + \text{const.} \tag{3.84}$$

Again, we consider the Bethe lattice for simplicity and get the final result

$$S_{eff}^o = -\sum_{i\omega_n} \psi_o^\dagger [i\omega_n + \mu - T^+ \mathbf{G}(i\omega_n) T] \psi_o - |U| n_{o\uparrow} n_{o\downarrow}. \tag{3.85}$$

Here $G(i\omega_n)$ is the Green's function of the neighboring site. The self-consistency finally reads

$$\mathcal{G}_A^{-1}(i\omega_n) = i\omega_n + \mu - T \mathbf{G}_B(i\omega_n) T. \tag{3.86}$$

The most difficult part in solving the DMFT equations comes from the quantum impurity problem. Fortunately, many different techniques have been developed in order to treat the physics of impurities embedded in a bath. In the context of this thesis, we will consider the exact diagonalization (ED) solver that uses the Lanczos algorithm (see Appendix B.2) and the continuous-time quantum Monte Carlo (CTQMC, see Ref. [122]) algorithm. The exact diagonalization solver is geared at the zero-temperature problem, while the CTQMC algorithm is able to address a wide range of temperatures (from high down to very low temperatures).

# Chapter 4

# Mass-imbalanced mixtures in optical lattices

*In this chapter, we consider two-component fermionic mixtures confined in an optical lattice. The two species have different masses and are subject to an attractive on-site coupling. Using dynamical mean-field theory, we first establish the phase diagram as a function of the coupling strength and mass imbalance. In order to have more insight into the weak-coupling regime, we use a Hartree-Fock mean-field theory. We also address the strong-coupling limit with a static mean-field theory and describe the ground state and its stability. Finally, we consider the experimentally-relevant effect of a trapping potential. We include the trap by using the local density approximation (LDA) and verify its validity by a Monte Carlo simulation in a finite inhomogeneous system. The two methods show a very good agreement and reveal the presence of a phase with spatial segregation between a superfluid and a charge density wave phase.*

## 4.1 Introduction

The remarkable advances in handling ultracold atomic gases have given birth to the new field of "condensed matter physics with light and atoms". Cold atoms in optical lattices, with tunable and controllable parameters, have been studied in many different contexts (for reviews, see [12, 58, 123]). Mixtures of two-component atoms with different masses (e.g $^6$Li, $^{40}$K) introduce an additional parameter, namely the difference between the hopping amplitudes associated with each species in the optical lattice. This may affect the stability of the possible quantum phases or even induce new ones. Recently, a phase diagram has been worked out in the one-dimensional (1D) case [22] and in continuum models [78].

As discussed in Section 1.1.1, the mixture of two fermionic components in optical lattices can be described by an extended Hubbard model. In this chapter we consider this model to describe a mixture with mass imbalance. Under the conditions discussed in [31, 58, 121], the mixture with mass imbalance is described by

$$H = -\sum_{\langle i,j\rangle,\sigma} \mathrm{t}_\sigma(\mathrm{c}^+_{\mathrm{i}\sigma}\mathrm{c}_{\mathrm{j}\sigma} + \mathrm{h.c.}) \; - \; |\mathrm{U}| \sum_{\mathrm{i}} \mathrm{n}_{\mathrm{i}\uparrow}\mathrm{n}_{\mathrm{i}\downarrow}. \tag{4.1}$$

Here, the (pseudo-) spin index $\sigma$ refers to the two different species. Feshbach resonances between $^6$Li and $^{40}$K have been investigated in the Innsbruck group (see Ref. [124]), and can generate an attractive interaction (i.e. $U < 0$) with a tunable strength. To parametrize the hopping imbalance we define the parameter $z = (t_\uparrow - t_\downarrow)/(t_\uparrow + t_\downarrow)$. In the following, we consider a bipartite optical lattice made of two interpenetrating $(A, B)$ sublattices arranged such that the neighbors of $A$ sites are all of the $B$ type and *viceversa* (this happens for instance in the cubic lattice). In order to simplify the numerical calculation, we use a semi-circular density of states (corresponding to the Bethe lattice) in order to approximate the 3D lattice [44].

We study the phase diagram of this model at zero temperature as a function of the interaction strength and the hopping imbalance parameter $(|U|, z)$. The number of atoms for each species is well controlled in ultracold atom experiments. Here, we consider the case with equal number of atoms for each species ($n_\uparrow = n_\downarrow$) both at half-filling and away from half-filling. In the following, the doping will be denoted by $\delta$. We will establish a complete phase diagram at zero temperature using the dynamical mean-field theory (DMFT). Then for some special limits, we will use static mean-field theory to reach a better analytical understanding of the physical properties. We also consider the experimentally relevant effect of the trap potential, which is shown to induce a spatial segregation between a superfluid (SF) and a charge density wave (CDW) phase. The effect of the trapping potential will be treated within local-density approximation and compared to the result of Monte Carlo simulations.

## 4.2 Generic phase diagram obtained by dynamical mean-field theory

Let us begin by presenting the DMFT phase diagram of the uniform system, displayed in Fig. 4.1. When the fermions have the same mass (i.e. $z = 0$), the ground state is a superfluid for all $|U|$ (with a crossover from BCS to BEC as $|U|$ is increased). In the weak-coupling regime, the system is in a superfluid phase of Cooper pairs while in the strong coupling regime, we have the condensation of hard-core local bosons. A competing ordering exists, namely a charge density wave, considered here in the simplest (commensurate) case in which the charge is modulated with an alternating pattern on the $A$ and $B$ sublattices. At half-filling, i.e., when the number of fermions is equal to the number of lattice sites ($\langle n_\uparrow + n_\downarrow\rangle = 1$), the SF and the CDW states are degenerate.

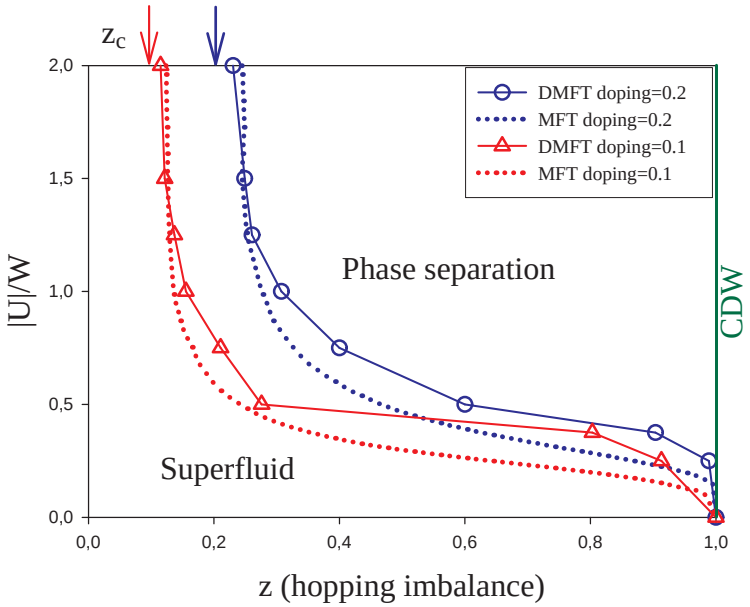


**Figure 4.1:** Phase diagram of the uniform system in the $(z, |U|)$ plane, obtained from DMFT. Below the curves (displayed here for two doping levels $\delta \equiv n - 1 = 0.1, 0.2$), the SF is stable. Above the curves, the system is phase-separated into a half-filled charge density wave and a SF. The arrows indicate the analytical strong-coupling values. The dotted lines are the weak-coupling mean-field approximation (see text). $|U|$ is normalized to the bandwidth $W$ of $(\varepsilon_{\mathbf{k}\uparrow} + \varepsilon_{\mathbf{k}\downarrow})/2$ [29].

This no longer applies in the 'doped' system, in which the number of fermionic atoms no longer coincides with the number of sites in the optical lattice: for equal masses, the SF phase is stabilized by doping for all $|U|$, but a large mass imbalance may favor the CDW phase over a SF state in which the Cooper pairs must be formed by fermions with different mobilities [22]. Hence the SF/CDW competition becomes more interesting in the presence of mass imbalance. As displayed in Fig. 4.1, we find that the uniform system has a SF ground-state for all values of $|U|$ as long as the mass imbalance $z \equiv (\mathrm{t}_\uparrow - \mathrm{t}_\downarrow)/(\mathrm{t}_\uparrow + \mathrm{t}_\downarrow)$ is smaller than a limiting value $z_c$ (which depends on the average density). For $z > z_c$, a (first-order) phase boundary is crossed as $|U|$ is increased, beyond which the uniform system undergoes a phase separation (PS) between a doped SF and a half-filled CDW phase.

### 4.2.1 Determination of the phase diagram

This diagram has been obtained by comparing the energies of the different possible states described above (see Section 3.1.3): normal, SF, CDW and phase separation in a canonical ensemble (i.e. the total number of particles is fixed).

A normal ground state is never stable towards a superfluid phase at zero temperature when there is equal number of particle for each species. For a weak attractive interaction between the fermionic species, the Fermi surface becomes unstable. A Bardeen-Cooper-Schrieffer (BCS) ground state is stabilized with a pairing between species of opposite momentum near their common Fermi surface. When the correlations are stronger, the species bind into localized pairs and form a Bose-Einstein condensate (BEC) [119, 120].

At half-filling, the nesting of the Fermi surface favors the stabilization of the commensurate

CDW phase. When the hoppings of both species are the same, this CDW phase has the same energy as the SF phase. As soon as the hopping imbalance increases (i.e. one species becomes less mobile), it is more difficult to form the superfluid phase with pairing and the CDW becomes more favorable in energy. In the Falicov-Kimball limit ($z = 1$), the heavy species is completely frozen on the lattice and therefore it is no longer possible to form a SF phase, while the CDW phase is more stable because of the periodic charge distribution [40]. Therefore, at half-filling a CDW is always more stable than a SF phase when $z \neq 0$.

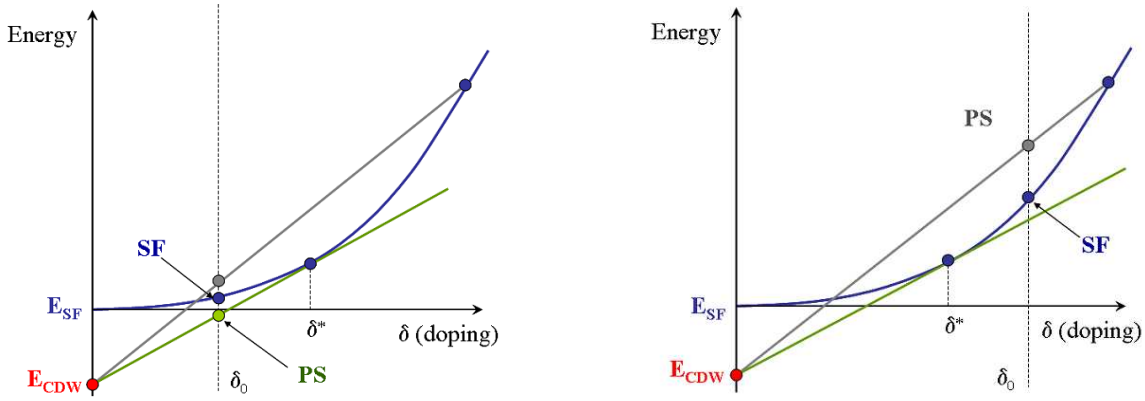


**Figure 4.2:** Construction of the phase separation (PS) between CDW and SF. Left panel: the PS has a lower energy than the SF. Right panel: the SF phase has a lower energy. In both panels, the gray line corresponds to the construction of the PS phase with a fixed average doping $\delta_0$ as a function of the doping $\delta$ of the SF phase. The point of tangency $\delta^*$ corresponds to the critical doping at which the phase transition between SF and PS occurs.

For a system away from half-filling, a configuration with a phase separation between the CDW and the SF might have a lower energy than a pure SF state. This means that it is more convenient to separate the system into a fraction $1 - x$ with CDW order (at half-filling) and a fraction $x$ with a doped SF order (its doping is $\delta$). The total average doping of the phase separation is determined by $\delta_0 = x\delta$. The optimal configuration is reached by minimizing over $x$ the expression $E_{\rm PS}(x)(\delta_0) = (1 - x)E_{\rm CDW} + xE_{SF}(\delta)$. These two conditions lead to the determination of the PS by minimizing over the doping $\delta$

$$E_{\rm PS}(\delta_0) = \min_{\delta} \left[(1 - \frac{\delta_0}{\delta})E_{\rm CDW} + \frac{\delta_0}{\delta}E_{SF}(\delta)\right]. \tag{4.2}$$

In practice, we will determine the energy of the superfluid phase for different doping $E_{SF}(\delta)$. The energy of the phase separation can be obtained by the construction shown in the Fig. 4.2. In this figure, the gray line shows how to construct a PS with average doping $\delta_0$ (gray point) from a CDW phase (red point) and a SF phase at fixed doping $\delta$ (blue point on the gray line). The optimization of this energy over the doping variable $\delta$ defines a critical doping $\delta^*$ corresponding to the point of contact of the tangent starting from $E_{CDW}$ to the curve $E_{SF}(\delta)$. For $\delta_0 < \delta^*$, the optimal configuration of PS obtained by CDW and SF at critical doping $\delta^*$ has a lower energy than the SF phase (Fig. 4.2 left panel). When $\delta_0 \geq \delta^*$, the energy of the optimal PS has zero volume of CDW, therefore the SF has a lower energy and it is the stable ground state (Fig. 4.2 right panel). For each value of the interaction and the hopping imbalance, we will obtain a value $\delta^*(U, z)$ which determines the phase transition from SF to PS.

### 4.2.2 Dynamical mean-field theory

We briefly recall the main result obtained in Chapter 3 for the DMFT method [20, 65, 73]. In order to describe the superconducting phase, we work with Nambu spinors $\psi^+ = (c_\uparrow^+, c_\downarrow)$. The key quantity in DMFT is the local (on-site) Green's function at finite temperature: $\hat{G}(\tau) = \langle \mathrm{T}_\tau \psi_i(\tau)\psi_i^+(0)\rangle$[1]. Here, $\tau$ is defined as the imaginary time and the Green's function $\hat{G}(\tau)$ is antiperiodic of period $2\beta = 2/k_B T$ because of the anticommutation for fermions. Its Fourier transform for imaginary frequencies reads

$$\hat{G}(i\omega) = \begin{bmatrix} G_\uparrow(i\omega) & F(i\omega) \\ F(i\omega) & -G_\downarrow(-i\omega) \end{bmatrix}, \tag{4.3}$$

where $G(\tau) = -\langle \mathrm{T}_\tau c(\tau)c^\dagger(0)\rangle$ is the normal Green's function on a given site, and $F(\tau) = -\langle \mathrm{T}_\tau c_\uparrow(\tau)c_\downarrow(0)\rangle$ is the anomalous Green's function associated to superfluid order. The superfluid order parameter is indeed given by $\Delta_{SF} = \langle c_{i\uparrow}c_{i\downarrow}\rangle = F(\tau = 0) = \sum_\omega F(i\omega)$. In the case of a CDW state the local Green's function takes different values ($\hat{G}_A$ and $\hat{G}_B$) on the two alternating sublattices A and B. The CDW order parameter is the difference of densities on the two sublattices $\Delta_{\mathrm{CDW}} = \langle n_A - n_B\rangle$. The self-consistency equations in DMFT for a Bethe lattice reads

$$\hat{\mathcal{G}}^{-1}_{A(B)}(i\omega) \;=\; i\omega\,\hat{1} + \hat{\mu} - \hat{T}\,\hat{\mathbf{G}}_{B(A)}(i\omega)\,\hat{T}, \tag{4.4}$$

where $\hat{1}$ is the identity matrix, while $\hat{T} = \mathrm{diag}[\mathrm{t}_\uparrow, -\mathrm{t}_\downarrow]$ and $\hat{\mu} = \mathrm{diag}[\mu_\uparrow, -\mu_\downarrow]$ are diagonal matrices, whose elements are the half-bandwidths and the chemical potentials of the two species.

Since we are able to study all the different broken-symmetry phases, the $T = 0$ phase diagram is easily determined by comparing the energies of the different solutions [119, 120]. The energy is evaluated as

$$\langle H\rangle = \langle K\rangle - |U| \sum_i \langle n_{i\uparrow}n_{i\downarrow}\rangle, \tag{4.5}$$

where $\langle K\rangle$ is the kinetic part of the Hamiltonian. The expectation value of the interaction term is easily computed through the calculation of the expectation value of $\sum_i n_{i\uparrow}n_{i\downarrow}$, while the the kinetic energy in the SF and the CDW phases reads respectively

$$\langle K\rangle_{SF} = \beta^{-1} \sum_{\omega,\sigma} \mathrm{t}_\sigma^2 [\mathrm{G}_\sigma^2(\sigma \mathrm{i}\omega) - \mathrm{F}^2(\mathrm{i}\omega)]$$

$$\langle K\rangle_{\mathrm{CDW}} = \beta^{-1} \sum_{\omega,\sigma} \mathrm{t}_\sigma^2 \mathrm{G}_{\mathrm{A}\sigma}(\mathrm{i}\omega)\mathrm{G}_{\mathrm{B}\sigma}(\mathrm{i}\omega).$$

Finally, the energy of the PS phase is computed by the Maxwell construction presented in the last section. The ground state will be obtained by the comparison of energy between these phases.

### 4.2.3 Superfluid phase

We perform the DMFT calculation at zero temperature $T = 0$ employing the exact diagonalization solver (see Appendix B.2) for the phase with superfluid ordering. For a mixture with hopping imbalance, we always find a converged solution for the superfluid phase with a non-zero paring parameter determined from the off-diagonal Green's function $\Delta_{SF} = \sum_n F(i\omega_n)$. In order to determine the critical line of the phase transition as displayed in Fig. 4.1 (see

[1] $\mathrm{T}_\tau$ is the time order product and defined as $\mathrm{T}_\tau c(\tau)c^\dagger(\tau') \equiv \theta(\tau - \tau')c(\tau)c^\dagger(\tau') - \theta(\tau' - \tau)c^\dagger(\tau')c(\tau)$.

also [29]) for a fixed set of parameter $(|U|, z)$ we compute the energy of the of the SF phase for different doping $E_{SF}^{U,z}(\delta)$ (see Fig. 4.3). It can be very well fitted by the relation

$$E_{SF}^{U,z}(\delta) \approx E_{SF}^{U,z}(0) + c(z)\delta^2. \tag{4.6}$$

As an example, in Fig. 4.3, we compute the energy curve $E_{SF}^{U,z}(\delta)$ versus $\delta$ for $|U| = 1.5W$ and $z = 0.3$. We obtained $c(z) = 2.937W$ and $E_{SF}^{U,z}(0) = -0.827W$.

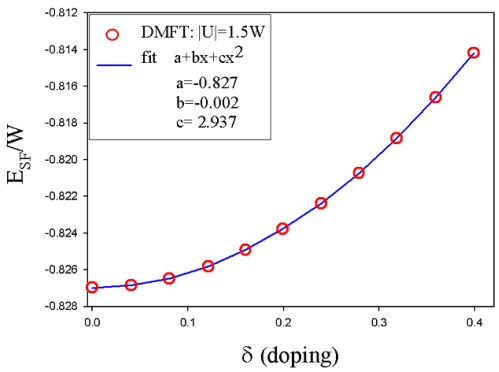


**Figure 4.3:** Energy of the superfluid phase versus doping $\delta$ within DMFT for $z = 0.3, |U|/W = 1.5$.

In order to understand the physics of the SF phase, we look at the Green's functions $G_\sigma(i\omega_n)$ and $F(i\omega_n)$ (Fig. 4.4). From these quantities, we can compute the superfluid order parameter and the doping for a given chemical potential. In Matsubara frequencies, we find that the imaginary part of the Green's function tends to zero when $\omega_n \to 0$ (Fig. 4.4 left panel) which is the signature of the gap in the spectral function. In order to measure the gap

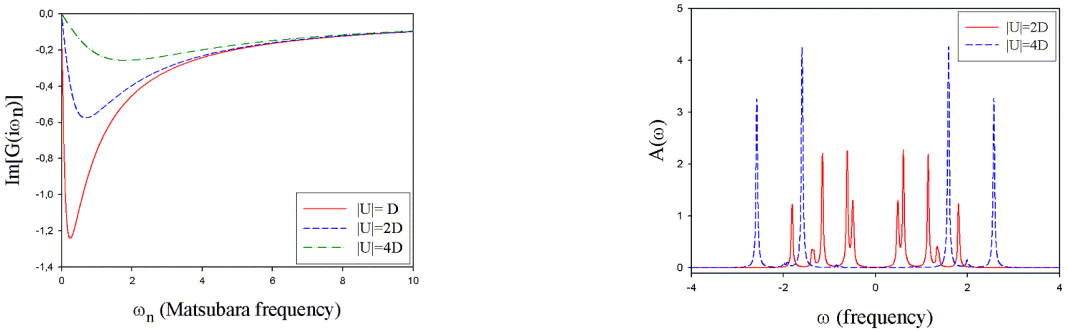


**Figure 4.4:** Left panel: The imaginary part of the Green's function in the imaginary axes of Matsubara frequency. Right panel: The spectral function obtained in DMFT with the exact diagonalization solver

of the SF phase, we compute the Green's function in real frequency, then take the analytical continuation to obtain the spectral function (Fig. 4.4 right panel). As the discrete Anderson impurity model is truncated with a finite number of sites in the bath ($n_s \sim 6-10$), the spectral function is represented by a set of discrete peaks. However, from this spectral function we can directly measure the superfluid gap $\Delta_G$. Notice that in DMFT the gap in the spectral function is not the same as the order parameter $\Delta_{SF}$, while these two quantities are imposed to be the same in a static MFT treatment. In varying the doping parameter $\delta$, we remark that for very different interaction coupling, even in the strongly-correlated regime ($|U| = 4D$),

the order parameter still respects the asymptotic behavior for small doping obtained in MFT (Fig. 4.5 left panel)

$$\Delta_{SF} = \Delta_0(1 - \frac{\delta^2}{2}) + o(\delta^4). \tag{4.7}$$

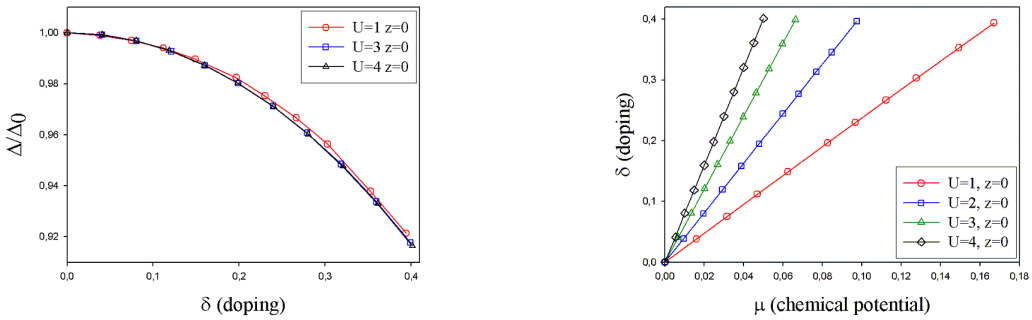


**Figure 4.5:** Left panel: Relation between the order parameter $\Delta/\Delta_0$ and the doping $\delta$. It shows a good agreement with the fitting function $1-\delta^2/2$ obtained in static MFT. Right panel: Relation between the doping $\delta$ and the chemical potential $\mu$. It shows a good agreement with the renormalization of the quasiparticle mass obtained in improved MFT by including the Fermi liquid effects.

We now compute the dependence of the doping on the external chemical potential. In plotting this relation (Fig. 4.5 right panel), we see that the slope of these curves changes when we vary the value of the interaction strength. This observation shows the effect of the interaction on the effective mass of the quasiparticles.

### 4.2.4 Charge density wave phase

For the charge density wave, we set the pairing parameters of the bath in the ED solver to zero $\Delta_k = 0$ (see discussion in the Appendix B.2), then iterate the DMFT procedure on two neighboring sites belonging to two sublattices A and B. In contrast to the superfluid solution which exists for any doping, a converged CDW solution is obtained only at half-filling. We compute the energy of this phase as a function of the interaction and the hopping

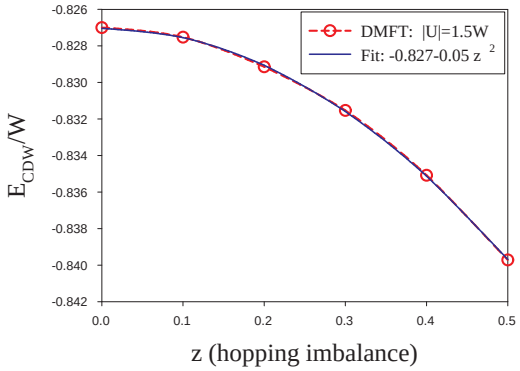


**Figure 4.6:** Energy of the CDW phase obtained within DMFT for |U|=1.5W

imbalance. For a fixed interaction strength, this phase becomes energetically more favorable

as the hopping imbalance increases (see Fig. 4.6). The reason for this energy gain is that when the hopping imbalance is increased, the heavy species becomes less mobile and has a larger CDW order parameter. This value goes to 0.5 when the heavy species is completely frozen in the lattice (Fig. 4.7).

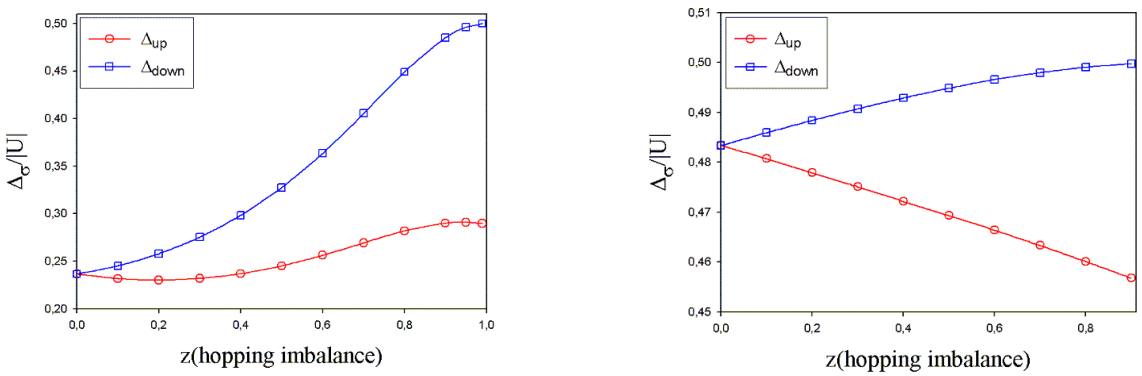


**Figure 4.7:** Order parameters of the up and down species in the CDW phase obtained within DMFT. A different behavior is found for weak interactions (left figure with $|U|/W = 0.5$) and at strong coupling (right figure $|U|/W = 2$).

### Phase separation and critical line of phase transition

Solving DMFT with exact diagonalization, we only find a stable CDW solution at half-filling. Away from half-filling we do not find a stable CDW phase. Later, in the analytical discussion of the MFT solution, we will demonstrate that a stable CDW phase away from half-filling can be found only very close to the Falicov-Kimball limit with small couplings. In this region, the ED algorithm is not able to resolve low energy scales because of the discretized bath, making it very difficult to capture this phase. For small and intermediate couplings, we can construct the phase separation between the half-filled CDW and a doped SF. For instance, taking $|U| = 1.5W$, we determine the critical line of the phase transition $\delta^*(z) \approx \sqrt{(E^{U,z}_{SF}(0) - E^{U,z}_{CDW})/c(z)}$ as shown in Fig. 4.8. Repeating this calculation for different $z$, we then establish the relation $z_c(\delta)$.

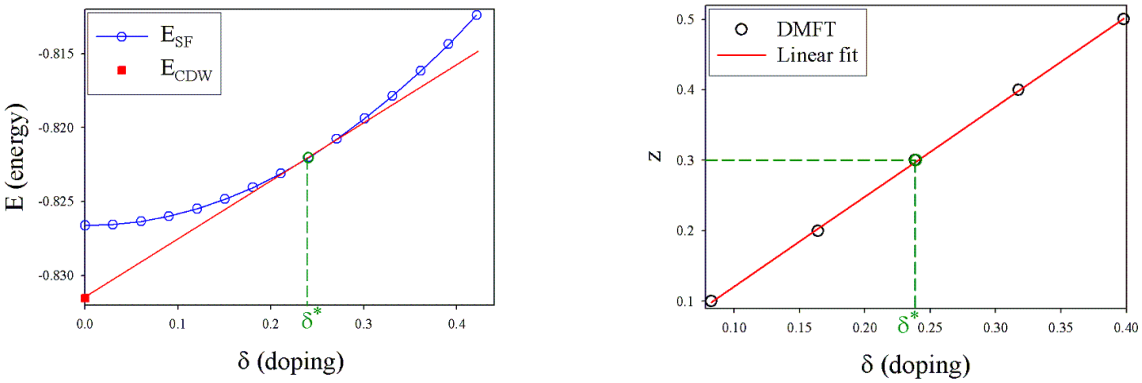


**Figure 4.8:** Determination the critical point $z(\delta)$ for $|U| = 1.5W$. Left panel: Critical value of the doping for $z = 0.3$ obtained by DMFT. Right panel: Relation $z(\delta)$.

Fig. 4.1 shows the phase diagram obtained within DMFT. For a better understanding,

we can address different limits using analytical methods. For example, in the strong-coupling regime, we can map our initial model to an effective $XXZ$ spin model and apply various methods designed for Heisenberg-like models (MFT, Spin-wave theory etc). The weak-coupling limit can be understood by the Hartree-Fock mean-field theory, neglecting the fluctuations. Note that the limit which $z = 1$ is mapped to a Falicov-Kimball model, which has an analytical solution within DMFT [40].

## 4.3 Strong-coupling regime, mapping on a spin model

In this section, we describe analytical mean-field calculations for the strong coupling which help understanding the DMFT phase diagram established numerically. This strong-coupling analysis holds for $|U| \gg \mathrm{t}_\uparrow, \mathrm{t}_\downarrow$. In order to analyze this limit, we find it useful to resort to a particle-hole transformation that maps our negative-$U$ model onto the positive-$U$ Hubbard model and work in the repulsive interaction framework. We emphasize that we are not switching to truly repulsive interactions, but we simply exploit a mathematical property to gain information on the physical system of interest. As shown in Chapter 3, under the particle-hole mapping, our model is transformed, at large $|U| \gg \mathrm{t}_\uparrow, \mathrm{t}_\downarrow$, into an $XXZ$ quantum spin-1/2 model [22, 31]

$$H = J \sum_{\langle i,j \rangle} \vec{S}_i . \vec{S}_j + \gamma J \sum_{\langle i,j \rangle} S_i^z S_j^z - 2h \sum_i S_i^z, \tag{4.8}$$

where $\vec{S} \equiv \frac{1}{2} d_\alpha^+ \vec{\sigma}_{\alpha\beta} d_\beta$, $J = 4t_\uparrow t_\downarrow / |U|$ and $\gamma = (t_\uparrow - t_\downarrow)^2 / 2t_\uparrow t_\downarrow = 2z^2/(1-z^2)$. Hence, the mass imbalance turns into a spin exchange anisotropy. The effective magnetic field $h$ and the polarization $p$ correspond respectively to the chemical potential $\mu - |U|/2$ and the doping $\delta$ in the original model. For convenience, we introduce the magnetization $m = \langle S^z \rangle = (n_\uparrow - n_\downarrow)/2 = p/2$. Therefore a magnetization $m = p/2$ in this model corresponds to half the doping in the attractive model.

We use the results presented in Chapter 3 for the $XXZ$ spin model to establish the phase diagram in the strong positive-$U$ limit and then switch to the negative coupling limit via the particle-hole transformation. We remind the self-consistency equation of the mean-field theory for the spin model

$$\sin \frac{\theta_A + \theta_B}{2} \left[ zJ\gamma S \cos \frac{\theta_A + \theta_B}{2} - h \cos \frac{\theta_A - \theta_B}{2} \right] = 0 \tag{4.9}$$

$$\sin \frac{\theta_B - \theta_A}{2} \left[ zJ(2+\gamma) S \cos \frac{\theta_A - \theta_B}{2} - h \cos \frac{\theta_A + \theta_B}{2} \right] = 0. \tag{4.10}$$

We first consider the different solutions of the mean-field equations in an ensemble with fixed magnetic field, then turn to the canonical ensemble with fixed polarization by the Legendre transformation (see Chapter 3). The solution of these equations are the local extrema of the free energy, therefore in order to obtain the true ground state (with lowest energy) we need to compare the energy of the different solutions.

### Ferromagnetic phase

A trivial solution of the equations is $\theta_A$, $\theta_\beta$ satisfying $\sin[(\theta_A \pm \theta_B)/2] = 0$. These equations give $\theta_A = \theta_B = 0$ (or $\pi$) which is simply a ferromagnetic phase. This phase becomes a stable solution only in the limit where the external field is strong enough to polarize all the spins. The energy of this state simply reads $F_{FM} = N\zeta J(1+\gamma)S^2/2 - NhS$.

**Spin density wave in the $XY$ plane (SDW$_{XY}$)**

This solution corresponds to the case where $\theta_A$ and $\theta_B$ satisfy the following equations

$$\sin\frac{\theta_A+\theta_B}{2}=0 \tag{4.11}$$

$$zJ(2+\gamma)S\cos\frac{\theta_A-\theta_B}{2}-h\cos\frac{\theta_A+\theta_B}{2}=0. \tag{4.12}$$

Therefore, we obtain $\theta_A=-\theta_B$ and $\cos\theta_A=h/zJ(2+\gamma)S$. The order parameters which are defined in Section 3.3.1 can be estimated

$$m=\frac{\cos\theta_A+\cos\theta_B}{2}S=\frac{h}{zJ(2+\gamma)}$$

$$\Delta_{AF}=\frac{S}{2}(\cos\theta_A-\cos\theta_B)=0$$

$$\Delta_{XY}=\frac{S}{2}(\sin\theta_A-\sin\theta_B)=\sqrt{S^2-\frac{h^2}{z^2J^2(2+\gamma)^2}}.$$

This phase has a non-zero total magnetization with a spin density wave order in the $x-y$ plane. The free energy of this local minimum reads

$$F_{XY}=-\frac{N\zeta JS^2}{2}-\frac{Nh^2}{2\zeta J(2+\gamma)}. \tag{4.13}$$

**Normal phase**

The third solution is the one satisfying the following equations

$$\sin\frac{\theta_A-\theta_B}{2}=0$$

$$zJ\gamma S\cos\frac{\theta_A+\theta_B}{2}-h\cos\frac{\theta_A-\theta_B}{2}=0.$$

Thus, we obtain $\theta_A=\theta_B$ and $\cos\theta_A=h/\zeta J\gamma S$. Again, we compute the order parameters in this case and obtain

$$m=\frac{\cos\theta_A+\cos\theta_B}{2}S=\frac{h}{zJ\gamma}$$

$$\Delta_{AF}=\frac{S}{2}(\cos\theta_A-\cos\theta_B)=0$$

$$\Delta_{XY}=\frac{S}{2}(\sin\theta_A-\sin\theta_B)=0.$$

In this case, the solution is a normal phase without any long rang order parameter. The free energy of this phase reads: $F_N=N\zeta JS^2/2-Nh^2/2\zeta J\gamma$.

**Antiferromagnetic phase (AF)**

The fourth solution of the self-consistency equations is the one satisfying

$$h\cos\frac{\theta_A-\theta_B}{2}=JSz\gamma\cos\frac{\theta_A+\theta_B}{2}$$

$$h\cos\frac{\theta_A+\theta_B}{2}=JSz(2+\gamma)\cos\frac{\theta_A-\theta_B}{2}.$$

There is a unique solution to these equations: $\theta_A = 0$ and $\theta_B = \pi$. This solution does not depend on the magnitude of the external magnetic field. We can estimate the order parameters in this case

$$m = \frac{\cos\theta_A + \cos\theta_B}{2} S = 0$$
$$\Delta_{AF} = \frac{S}{2}(\cos\theta_A - \cos\theta_B) = S$$
$$\Delta_{XY} = \frac{S}{2}(\sin\theta_A - \sin\theta_B) = 0.$$

This solution describes an antiferromagnetic phase with modulation of the density in the $z$ direction. The free energy of this AF phase is: $F_{AF} = -N\zeta J(1+\gamma)S^2/2$

**Phase diagram**

Here, we study the spin model at zero temperature with an external magnetic field. In order to determine the ground state of the system, we compare the energy of the four states above. Let us first start with the energy comparison of the AF state and a SDW$_{XY}$ state

$$F_{AF} - F_{XY} = -\frac{N\zeta J(1+\gamma)S^2}{2} + \frac{N\zeta JS^2}{2} + \frac{Nh^2}{2\zeta J(2+\gamma)}. \tag{4.14}$$

This equation gives a critical value for the external field $h_c = \zeta JS\sqrt{\gamma(\gamma+2)}$. When $h < h_c$ the stable state is one with AF order while $h > h_c$ the stable state is one with $SDW_{XY}$ order. The relation between the magnetization and the external field is $m = 0$ for $h < h_c$ and $m = h/\zeta J(2+\gamma)$ for $h > h_c$, see Fig. **??**.

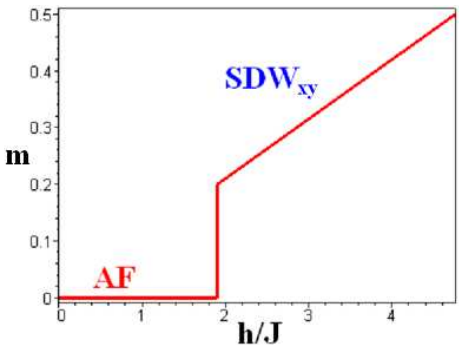


**Figure 4.9:** Curve of magnetization versus the magnetic field.

As discussed above, there is also a locally stable normal phase with magnetization $m = h/\zeta J\gamma$. Within this normal phase, there is a critical field $h^* = \zeta JS\gamma < h_c$ such that for $h < h^*$ we obtain a polarized normal phase with $m < S = 1/2$ while for $h > h^*$ the system becomes ferromagnetic with $m = 1/2$. Let us note that the energetic competition between SDW$_{xy}$ and the ferromagnetic phase shows that the ferromagnetic phase is always unstable except for strong enough external magnetic fields $h > 2\zeta JS(2+\gamma)$. Moreover, for any $h < h_c$ the AF phase is always the most stable phase and therefore the normal phase is never stable.

We now consider the problem with fixed magnetization. The relation between the magnetization and the external field shows that, when $h > h_c$ or $m > m_c = S\gamma/(\gamma+2)$, we can use the Legendre transform from the grand canonical system to the canonical system. So

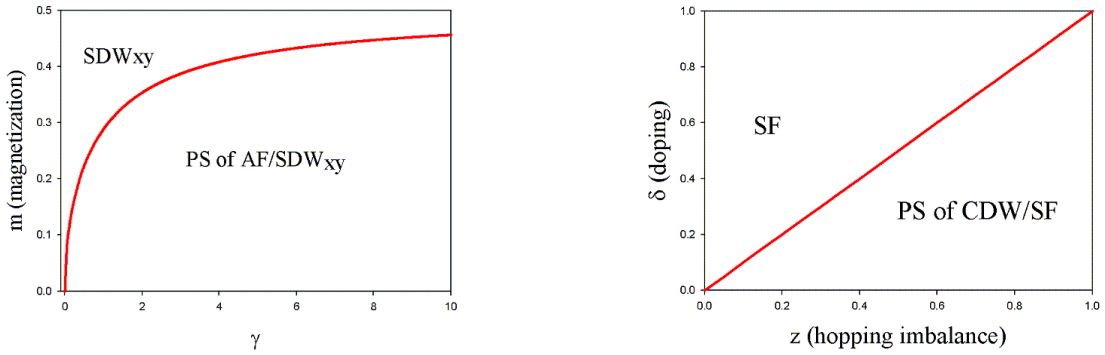


**Figure 4.10:** Left panel: phase diagram of the positive coupling model on the plane (m,$\gamma$). Right panel: phase diagram of the negative coupling model on the plane ($\delta$,z).

for $m > m_c$ we have the $SDW_{XY}$ phase in the canonical system. When $m < m_c$ we can only form a solution with phase separation. In this solution part of the system has AF order without magnetization, and part has $SDW_{XY}$ order with magnetization. The phase diagram of the $XXZ$ model (see Fig. 4.10 left panel) can be summarized as follows

- $p = 0 \rightarrow$ AF phase.
- $0 < p < 2S\sqrt{\gamma/(\gamma+2)} \rightarrow$ phase separation between the AF order and the $SDW_{XY}$ order.
- $2S\sqrt{\gamma/(\gamma+2)} < p < 2S \rightarrow SDW_{XY}$ phase.
- $p = 2S \rightarrow$ ferromagnetic phase.

Let us come back to the original model in the negative limit via the particle-hole transformation. The phase diagram consists of the competition between the superfluid phase and the phase separation of CDW and SF. We have a first order transition between SF and PS (see Fig. 4.10 right panel). Within this classical mean-field treatment, we have shown that there is a phase transition at zero temperature when the hopping imbalance parameter varies. The critical value of the mass imbalance is $z_c = \delta$ which is consistent with the value obtained in the DMFT in the strong interaction regime. In order to further understand the low-energy excitations, we can use the spin-wave approximation (see Appendix A.1).

## 4.4 Weak-coupling regime, Hartree-Fock mean-field theory

We now consider the problem of mass-imbalanced mixtures in the weak-coupling regime ($|U|/t_\sigma \ll 1$). In this limit, as shown in Chapter 3, we can ignore the quantum fluctuations and solve the problem by Hartree-Fock mean-field theory. We will study the energetic competition of the four potential candidates for the ground state which are the normal phase, the BCS phase with Cooper pairs, the charge density wave phase and the phase separation between the CDW phase and the BCS superfluid.

### 4.4.1 BCS superfluid

First, we study the MFT equations for the conventional superfluid phase (BCS). As shown in Chapter 3, the set of self-consistency equations read

$$\delta = -\frac{1}{N}\sum_{\mathbf{k}} \frac{\xi_{\mathbf{k}}[1 - f(E^+_{\mathbf{k}}) - f(E^-_{\mathbf{k}})]}{\sqrt{\xi^2_{\mathbf{k}} + \Delta^2}} \tag{4.15}$$

$$p = \frac{1}{N}\sum_{\mathbf{k}} [f(E^+_{\mathbf{k}}) - f(E^-_{\mathbf{k}})] \tag{4.16}$$

$$\frac{2\Delta}{|U|} = \frac{1}{N}\sum_{\mathbf{k}} \frac{[1 - f(E^+_{\mathbf{k}}) - f(E^-_{\mathbf{k}})]\Delta}{\sqrt{\xi^2_{\mathbf{k}} + \Delta^2}}, \tag{4.17}$$

where $\delta = n - 1$ is the doping of the system away from half-filling, $p$ is the polarization of the system and the last self-consistency equation (Eq. 4.17) defines the superfluid order parameter $\Delta$. Here $f(E)$ is the Fermi-Dirac statistic distribution and $N$ is the number of lattice sites. $E^{\pm}_{\mathbf{k}} = \pm(z\varepsilon_{\mathbf{k}} - \tilde{h}) + \sqrt{(\varepsilon_{\mathbf{k}} - \tilde{\mu})^2 + \Delta^2}$ are the eigenvalues of the BCS Hamiltonian defined in the Section 3.2.3 (the Bogoliubov excitation modes). Within this MFT description, we have included the Hartree corrections in the renormalized chemical potential $\tilde{\mu} = \mu - U(1+\delta)/4$ and in the renormalized magnetic field $\tilde{h} = h - Up/4$. We remind that $\mu = (\mu_\uparrow + \mu_\downarrow)/2$, $h = (\mu_\uparrow - \mu_\downarrow)/2$ are defined as the chemical potential and effective magnetic field.

We will prove that for the system with no polarization $p = 0$, the excitation spectrum of the Bogoliubov modes must be gapped: $E^{\pm}(\varepsilon_{\mathbf{k}}) > 0$. From Eq. 4.16 the condition of equal density induces that $\sum_{\mathbf{k}} f(E^+_{\mathbf{k}}) = \sum_{\mathbf{k}} f(E^-_{\mathbf{k}})$. Let us solve the self-consistency equations assuming that $\tilde{h} > 0$ and, *ad absurdum*, that these two sums have non-zero values. At zero temperature $T = 0$, we have $f[E^{\pm}(\varepsilon)] = 0$ whenever $E^{\pm}(\varepsilon) > 0$ and $f[E^{\pm}(\varepsilon)] = 1$ whenever $E^{\pm}(\varepsilon) < 0$. Therefore, there is a domain of $\varepsilon$ in which $E^{\pm}(\varepsilon) < 0$. In fact, the inequality $E^+(\varepsilon) < 0$ gives the solution $E_1 < \varepsilon < \min(E_0, E_2)$ while $E^-(\varepsilon) < 0$ gives the solution $\max(E_0, E_1) < \varepsilon < E_2$. Here, $E_0 = \tilde{h}/z$ while $E_{1,2}$ is obtained by the condition $E^{\pm}(\varepsilon) = 0$

$$E_{1,2} = \frac{\tilde{\mu} - \tilde{h}z \mp \sqrt{(\tilde{h} - \tilde{\mu}z)^2 - (1 - z^2)\Delta^2}}{1 - z^2}. \tag{4.18}$$

When $E_0 > E_1, E_2$, we deduce that $f(E^-_{\mathbf{k}}) > 0$ for all $\varepsilon_{\mathbf{k}}$, thus $\sum_{\mathbf{k}} f(E^-_{\mathbf{k}}) = 0$ and $f(E^+_{\mathbf{k}}) = 1$ for $E_1 < \varepsilon_{\mathbf{k}} < E_2$, thus $\sum_{\mathbf{k}} f(E^-_{\mathbf{k}}) > 0$. Therefore, this case induces an imbalanced population $p > 0$. By a similar argument, the other case $E_0 < E_1, E_2$ induces a polarization $p < 0$. In order to have a non-zero value for both sums $\sum_{\mathbf{k}} f(E^{\pm}_{\mathbf{k}})$, we need to have $E_1 < E_0 < E_2$. This condition induces the following inequality: $|\tilde{h} - \tilde{\mu}z| < z\sqrt{(\tilde{h} - \tilde{\mu}z)^2 - (1 - z^2)\Delta^2}$ which is impossible. Therefore, for the mixture without polarization at zero temperature, we have $E^{\pm}_{\mathbf{k}} > 0$ for every $\varepsilon_{\mathbf{k}}$. From this condition, we can write the constraint on the external field

$$\Delta > |\tilde{h} - z\tilde{\mu}|/\sqrt{1 - z^2}. \tag{4.19}$$

In the case without mass imbalance ($z = 0$), this condition simply requires that the external field has to be smaller than the superfluid gap. In the general case, in order to be sure that we always obtain a unpolarized system for any solution $\Delta$ of the gap equation, we need to impose the condition $\tilde{h} - z\tilde{\mu} = 0$ which is equivalent to a system with equal hoppings and no

external field. The self-consistency set of equations is simplified now and reads

$$\delta = -\int_{-\infty}^{\infty} \frac{(\varepsilon - \tilde{\mu})D(\varepsilon)}{\sqrt{(\varepsilon - \tilde{\mu})^2 + \Delta^2}} d\varepsilon \tag{4.20}$$

$$\frac{2\Delta}{|U|} = \int_{-\infty}^{\infty} \frac{\Delta D(\varepsilon) d\varepsilon}{\sqrt{(\varepsilon - \tilde{\mu})^2 + \Delta^2}}., \tag{4.21}$$

where $D(\varepsilon)$ is the density of states. At zero temperature, we can compute the energy of the ground state in the canonical ensemble by applying the Legendre transform on the free energy. The energy of the BCS ground state reads

$$E[\Delta, \delta] = -\frac{N|U|}{4}(1+\delta)^2 - \frac{N\Delta^2}{|U|} - N\int_{-\infty}^{\infty} \frac{E(E-\tilde{\mu})D(E)dE}{\sqrt{(E-\tilde{\mu})^2 + \Delta^2}}. \tag{4.22}$$

Let us consider now two possible cases when the system is at half-filling and away from half-filling.

**a. At half-filling,** $n_\uparrow = n_\downarrow = 1/2$

At half-filling, the different sites are equally populated with one particle per site and $\delta = 0$. The trivial solution of the Eq. 4.20 is $\tilde{\mu} = 0$. The verification is very simple: the function under the integration is odd when $\tilde{\mu} = 0$ and the DOS is symmetric with respect to zero. Therefore, the real chemical potential at half-filling is $\mu = U/4$. Inserting this result into the gap equation (Eq. 4.21) and using a flat DOS, we obtain an analytical expression for the order parameter

$$\Delta_0 = \frac{W}{2\sinh(W/|U|)}. \tag{4.23}$$

The energy difference between the BCS and the normal phase reads

$$E_{BCS} - E_n \equiv E[\Delta_0, \delta = 0] - E[\Delta = 0, \delta = 0] = -\Delta_0^2/2W. \tag{4.24}$$

One can clearly see that, at weak coupling, the normal phase is unstable towards the BCS superfluid phase for any attractive interaction.

**b. Away from half-filling,** $n_\uparrow = n_\downarrow \neq 1/2$

For a flat DOS, the Eq. 4.20 can still be solved analytically and it gives the dependence of the renormalized chemical potential on the doping

$$W\delta = \sqrt{(W/2 + \tilde{\mu})^2 + \Delta^2} - \sqrt{(W/2 - \tilde{\mu})^2 + \Delta^2}. \tag{4.25}$$

In the low doping limit, $\delta \ll 1$ the above expression can be simplified to $\tilde{\mu} = W\delta/2 = \mu - U(1+\delta)/4$. Therefore, the doping reads

$$\delta \approx (2\mu - U/2)/(W - U/2). \tag{4.26}$$

We note that this result is in very good agreement with the mass renormalization effect obtained within the DMFT calculation, see Fig. 4.5. Substituting this chemical potential into the gap equation (Eq. 4.21), we obtain

$$\frac{2}{|U|} = \frac{1}{W}\text{arcsinh}\frac{W(1+\delta)}{2\Delta} + \frac{1}{W}\text{arcsinh}\frac{W(1-\delta)}{2\Delta}. \tag{4.27}$$

Taking the Taylor development of Eq. 4.27 in the limit $\delta \ll 1$, we derive a simple expression for the order parameter[2]: $\Delta = \Delta_0(1-\delta^2/2) + O(\delta^4)$. The energy per site of the BCS state compared to the initial normal state reads

$$E_{BCS} - E_n \equiv E[\Delta, \delta] - E[\Delta = 0, \delta] = -\Delta^2/2W. \tag{4.28}$$

Here, $E_n = U(1+\delta)^2/4 - W(1-\delta^2)/4$ and $\Delta$ is the solution of the gap equation. This BCS mean-field analysis shows that for a negative coupling, a superfluid phase with Cooper pairing is always more stable than a normal phase.

### 4.4.2 Charge density wave

We now discuss the possibility to realize a phase with commensurate density modulation using a flat density of states at zero temperature. The MFT study for this phase is more complicated than the BCS phase considered in the previous discussion where we have found a second-order transition from the normal state to the BCS phase (at $U = 0$). Here, even for the mixture with the same mass ($z = 0$), we will show that there is a first-order phase transition from the CDW phase to the normal phase. As soon as we tune the mass imbalance parameter away from zero ($z \neq 0$), a richer physics appears within MFT, so that the phase transition between the CDW phase and the normal phase becomes second order whenever $z$ is bigger than some critical value. Let us study the solutions of the self-consistency equations and their stability.

We remind the filling equation and the gap equation obtained by MFT for the CDW phase in Chapter 3

$$n_\sigma = \frac{1}{N}\sum_{\mathbf{k}\in \mathrm{RBZ}} [f(E^+_{\mathbf{k}\sigma}) + f(E^-_{\mathbf{k}\sigma})] \tag{4.29}$$

$$\frac{\Delta_\sigma}{|U|} = \frac{\Delta_{\bar\sigma}}{N}\sum_{\mathbf{k}\in \mathrm{RBZ}} \frac{f(E^-_{\mathbf{k}\sigma}) - f(E^+_{\mathbf{k}\sigma})}{\sqrt{\varepsilon^2_{\mathbf{k}\sigma} + \Delta^2_{\bar\sigma}}}, \tag{4.30}$$

where $n_\sigma$ and $\Delta_\sigma$ are the populations and gaps for the different atomic species. $E^\pm_{\mathbf{k}\sigma} = \pm\sqrt{\varepsilon^2_{\mathbf{k}\sigma} + \Delta^2_{\bar\sigma}} - \tilde\mu_\sigma$ are the eigenvalues of the CDW mean-field Hamiltonian (see Section 3.2.4). $\Delta_\sigma$ is the order parameter for the commensurate CDW[3] for the species $\sigma$, while $\tilde\mu_\sigma = \mu_\sigma - |U|(1+\delta)/4$ is the renormalized chemical potential (due to the Fermi liquid effects). At zero temperature, the Fermi-Dirac statistic distribution $f(E)$ becomes a step function. We recall that the system has the same filling for both species of atoms $n_\sigma = (1+\delta)/2$.

Let us consider the particle-doped case with $\delta \geq 0$. In fact, when $|\tilde\mu_\sigma| < \Delta_{\bar\sigma}$, we have $E^+(\varepsilon) > 0$ and $E^-(\varepsilon) < 0$. Therefore, the system is at half-filling because $n_\sigma = N^{-1}\sum_{\mathrm{RBZ}} f(E^-_{\mathbf{k}\sigma}) = 1/2$. In contrast, when $\tilde\mu_\sigma > \Delta_{\bar\sigma}$, the system is doped ($n_\sigma > 1/2$) because the lower band $E^-_{\mathbf{k}} < 0$ is completely filled (i.e $f(E^-_{\mathbf{k}\sigma}) = 1$ for every $\mathbf{k} \in$ RBZ) while the upper band $E^+_{\mathbf{k}\sigma}$ must be partially filled. We have $E^+_{\mathbf{k}\sigma} < 0$ when $\varepsilon_{\mathbf{k}\sigma}$ satisfies $-\sqrt{\tilde\mu^2_\sigma - \Delta^2_{\bar\sigma}} < \varepsilon_{\mathbf{k}\sigma} < 0$. We set $\xi_\sigma = \sqrt{\tilde\mu^2_\sigma - \Delta^2_{\bar\sigma}}$ and rewrite the set of self-consistency equations (with a DOS) as

$$\frac{\delta}{2} = \int_{-\xi_\sigma}^{0} D_\sigma(\varepsilon)d\varepsilon \tag{4.31}$$

$$\frac{\Delta_\sigma}{|U|} = \int_{-\infty}^{-\xi_\sigma} \frac{\Delta_{\bar\sigma} D_\sigma(\varepsilon)d\varepsilon}{\sqrt{\varepsilon^2 + \Delta^2_{\bar\sigma}}}. \tag{4.32}$$

[2] In MFT, the order parameter is the same to the gap in spectral function.
[3] The charge density is modulated with wave vector $\mathbf{q} = (\pi, ..\pi)$.

The energy of the CDW phase for the canonical system can be computed using the Legendre transform. This energy reads

$$E_{CDW}[\Delta_\sigma, \delta] = \frac{N\Delta_\uparrow\Delta_\downarrow}{|U|} - \frac{N|U|(1+\delta)^2}{4} - N\sum_\sigma \int_{-\infty}^{-\xi_\sigma} \sqrt{\varepsilon^2 + \Delta_{\bar{\sigma}}^2} D_\sigma(\varepsilon) d\varepsilon. \tag{4.33}$$

Without loss of generality, we use a flat DOS to simplify the self-consistency equations. In order to study the number of solutions of this equation, we propose to calculate the instability of the normal state by imposing $\Delta_\sigma = 0$ in the gap equation. Hence, for a given value of the doping $\delta$, the renormalized chemical potential $\tilde{\mu}_\sigma$ is simply $\tilde{\mu}_\sigma = \delta W_\sigma/2 = (1+\sigma z)\delta W/2$. We obtain a condition on the interaction strength $|U|$. When the interaction strength $|U| < |U_c|$, the normal phase is more stable than any CDW phase while when $|U| > |U_c|$, we start to have CDW order in the mixture. The critical value $U_c$ for the flat DOS is given by

$$\frac{1}{U_0^2} = \frac{1}{W^2(1-z^2)} \ln\frac{2\tilde{\mu}_\uparrow}{W(1+z)} \ln\frac{2\tilde{\mu}_\downarrow}{W(1-z)}. \tag{4.34}$$

**a. Limit with mass balance $z = 0$**

As an example, let us consider the case with $z = 0$, thus we recover the symmetry between up and down species which leads to $\tilde{\mu}_\uparrow = \tilde{\mu}_\downarrow = \tilde{\mu}$ and $\Delta_\uparrow = \Delta_\downarrow = \Delta$. Using the flat DOS, the gap equation now becomes

$$\frac{\Delta}{|U|} = \frac{\Delta}{W}\text{arcsinh}\frac{W}{2\Delta} \qquad \text{for} \quad \Delta > \tilde{\mu} \tag{4.35}$$

$$\frac{\Delta}{|U|} = \frac{\Delta}{W}\left[\text{arcsinh}\frac{W}{2\Delta} - \text{arcsinh}\frac{\sqrt{\tilde{\mu}^2 - \Delta^2}}{\Delta}\right] \qquad \text{for} \quad \Delta < \tilde{\mu}. \tag{4.36}$$

The critical value for the interaction strength in this case simply reads $U_c = W/\ln(2\tilde{\mu}/W)$.

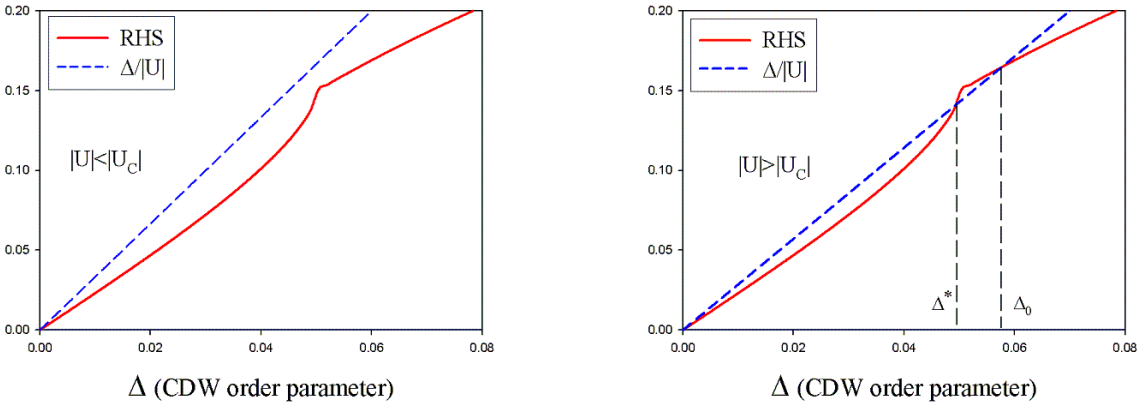


**Figure 4.11:** The solution of the gap equation for the mass-balanced mixture ($z = 0$) is obtained by finding the intersection between the curve $\Delta/|U|$ (the blue dashed line) with the right-hand side (RHS) of the gap equation (the red continuous line). Left panel: When $|U| < |U_c|$, there is only one solution $\Delta = 0$ corresponding to the normal phase. Right panel: When $|U| > |U_c|$, there are three solutions $\Delta = 0, \Delta^*, \Delta_0$. The solution in the middle corresponds to a local maximum.

In order to study the solution of the gap equation, we plot the left-hand side (LHS) and the right-hand side (RHS) of the gap equation and look for the intersection points. When the

interaction is small $|U| < |U_c|$, the gap equation has only one solution $\Delta = 0$ (see Fig. 4.11, left panel). In contrast, when $|U| > |U_c|$, we find in the right panel of Fig. 4.11 three points of intersection corresponding to $\Delta = 0$ (the normal phase), $\Delta = \Delta^*$ (a doped CDW) and $\Delta = \Delta_0$ (the CDW at half-filling). In fact, only $\Delta = 0, \Delta_0$ are local minima for the energy. The solution in the middle $\Delta = \Delta^*$ corresponds to a local maximum of the energy and is unstable. So the phase transition is obtained by comparing the energy of the normal state and the half-filled CDW.

Let us now turn to the general case with mass imbalance ($z \neq 0$). As shown in the gap equation above, whenever the gap (the CDW order parameter) is greater than the renormalized chemical potential, the chemical potential is included in the gap and there is no way to dope the system. Thus, we always obtain a solution of CDW at half-filling. However, when the chemical potential is greater than the gap we can expect a doped CDW. The question is whether such a solution is stable[4]. In order to understand the effect of the additional hopping imbalance parameter $z$ on the stability of this solution, we consider two cases:

### b. At half-filling, $\bar{n}_\uparrow = \bar{n}_\downarrow = 1/2$ ($z \neq 0$)

At half-filling, the renormalized chemical potential $\tilde{\mu}_\sigma$ is located inside the two dispersions $E^{\pm}_{\mathbf{k}\sigma}$ thus $f(E^{+}_{\mathbf{k}\sigma}) = 0$, $f(E^{-}_{\mathbf{k}\sigma}) = 1$ which means that the lower band is completely filled while the upper band is empty. The gap equations for a flat DOS have a solution $\Delta_{0\sigma}$ which satisfies

$$\frac{\Delta_{0\sigma}}{|U|} = \frac{\Delta_{0\bar{\sigma}}}{W_\sigma} \operatorname{arcsinh} \frac{W_\sigma}{2\Delta_{0\bar{\sigma}}}. \tag{4.37}$$

In Fig. 4.12, we show the behavior of the CDW order parameter for both species at weak

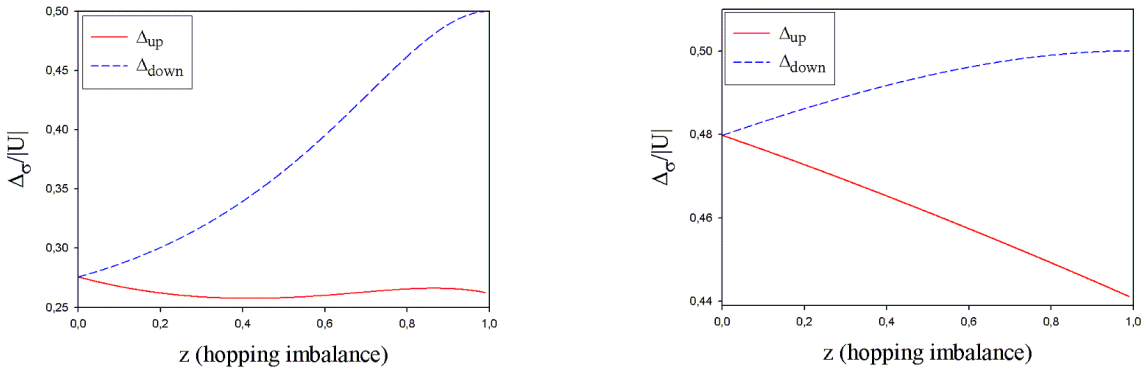


**Figure 4.12:** Order parameters of the up and down species in the CDW phase obtained within MFT. A different behavior is found for weak interactions (left figure with $|U|/W = 0.5$) and at strong coupling (right figure $|U|/W = 2$)

coupling ($|U| = 0.5W$) and at intermediate coupling ($|U| = 2W$). We find that in both limits the order parameter of the down atom (the heavy one) is monotonously increased when $z$ increases. When $z$ goes to 1, $\Delta_{0\downarrow}/|U|$ goes to 1/2. In this limit, the atoms of the heavy species are frozen on the lattice and distributed in a checkerboard pattern. The order parameter of the light species is not the same for $|U| = 0.5W$ and $|U| = 2W$. This result is in very good agreement with the DMFT calculations (see Fig. 4.7) which indicates that the gaps $\Delta_\sigma$ are quite well estimated within MFT even at relatively strong coupling.

[4] In the case without mass imbalance, this doped CDW is always a local maximum and hence unstable.

The energy of commensurate CDW at half-filling reads[5]

$$E^0_{CDW} - E^0_n \equiv E[\Delta_{0\sigma}, \delta = 0] - E[\Delta_\sigma = 0, \delta = 0] = -\frac{1}{4}\Big(\frac{\Delta^2_{0\uparrow}}{W_\uparrow} + \frac{\Delta^2_{0\downarrow}}{W_\downarrow}\Big). \tag{4.38}$$

We clearly see that at zero temperature, for the system at half-filling, the normal phase is always unstable towards the CDW phase.

### c. Away from half-filling, $\bar{n}_\uparrow = \bar{n}_\downarrow \neq 1/2$ $(z \neq 0)$

Again without loss of generality, in order to study the analytical properties of the solution, we use the integrable square DOS. The Eq. 4.31 reads

$$\sqrt{\tilde{\mu}^2_\sigma - \Delta^2_{\bar{\sigma}}} = \delta W_\sigma/2, \tag{4.39}$$

Substituting the relation 4.39 into the gap equations 4.32 and using the definition $W_\sigma = (1+\sigma z)W$, we obtain

$$\frac{\Delta_\sigma}{(1-\sigma z)} = \frac{|U|\Delta_{\bar{\sigma}}}{(1-z^2)W}\Big(\text{arcsh}\frac{(1+\sigma z)W}{2\Delta_{\bar{\sigma}}} - \text{arcsh}\frac{(1+\sigma z)\delta W}{2\Delta_{\bar{\sigma}}}\Big). \tag{4.40}$$

Fig. 4.13 shows the solution of the gap equation for a strong hopping imbalance $z = 0.9$ and

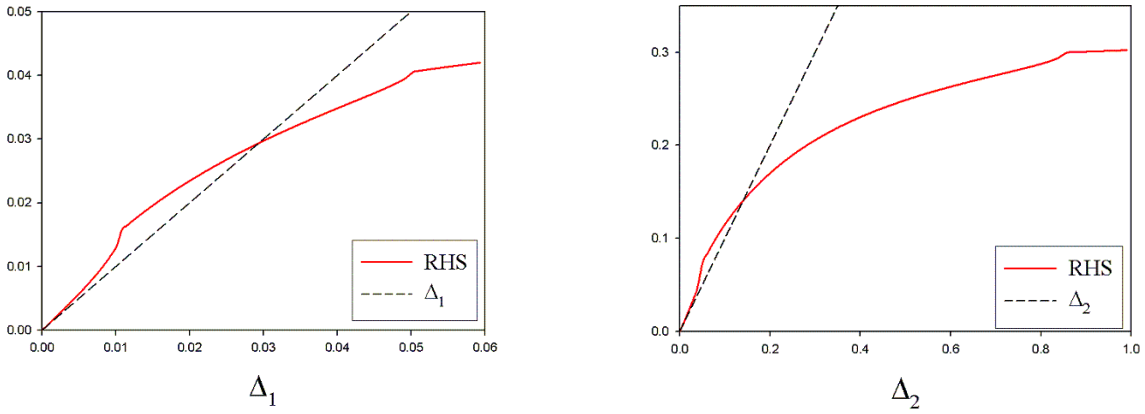


**Figure 4.13:** Solution of the gap equation for the mass-imbalanced mixture $z = 0.9$ and $|U| = 0.2W$. Left panel: The solution for the CDW order parameter for the up atoms $\Delta_1 = \Delta_\uparrow/(1-z)$. Right panel: The solution for CDW order for the down-atom $\Delta_2 = \Delta_\downarrow/(1+z)$.

a small interaction $|U| = 0.2W$. In this case, we have $\Delta_\uparrow \ll \Delta_\downarrow$. We define new variables in order to scale the order parameter of both species to a comparable order of magnitude: $\Delta_1 = \Delta_\uparrow/(1-z)$ and $\Delta_2 = \Delta_\downarrow/(1+z)$. In the figure, the solution is determined by the intersection of the line $\Delta_{1(2)}$ with the right-hand side of Eq. 4.40. In this case, the gap equation has a stable doped-CDW solution and an unstable solution $\Delta_\sigma = 0$ corresponding to the normal phase. The difference in energy per site between the doped-CDW phase and the normal phase reads

$$E_{CDW} - E_n \equiv E[\Delta_\sigma, \delta] - E[\Delta_\sigma = 0, \delta] = -\sum_\sigma \frac{1-\sigma z}{4W}\Big[\sqrt{\frac{\Delta^2_\sigma}{(1-\sigma z)^2} + \frac{W^2\delta^2}{4}} - \frac{W\delta}{2}\Big]^2. \tag{4.41}$$

[5] We used the following formula to get the integral: $\int \frac{E^2 dE}{\sqrt{E^2+\Delta^2}} = \frac{E}{2}\sqrt{E^2+\Delta^2} - \frac{\Delta^2}{2}\text{arcsh}(\frac{E}{\Delta})$.

Here, $E_n = U(1+\delta)^2/4 - W(1-\delta^2)/4$ is the energy of the normal phase with doping $\delta$. This energy comparison between the normal phase and the doped-CDW phase shows that the normal phase is always an unstable state at zero temperature.

### 4.4.3 Phase separation, Maxwell construction

In the previous discussion on the doped CDW, we saw that structure of the solution of the gap equation is very rich. Depending on the choice of the imbalance of hopping, we can stabilize a phase with a doped-CDW order or not.

For small hopping imbalance, we saw that the gap equation does not have a stable doped-CDW solution. In the grand canonical system, there are only two competing phases: the superfluid phase and the CDW at half-filling. Indeed, we have shown that the normal phase is always unstable towards a BCS superfluid phase within the MFT analysis for the BCS phase. For ultracold atom system, the number of atoms is fixed and it may be more convenient to separate the system into a fraction of CDW at half-filling and a doped-BCS phase. The stable phase separated configuration is found by minimizing the total energy of the phase over the volume ratio of these two parts (with a constraint on the total number of atoms in the system).

On the contrary, in the strong hopping imbalance limit ($z \to 1$), a doped-CDW solution can be stabilized within MFT. In order to understand the phase transition from the PS at small $z \ll 1$ to the stable doped CDW at strong hopping imbalance, we compute the energy of these two states in both limits and compare them.

We suppose that the PS state is composed by a BCS part of volume $xV$ and a half-filled CDW part of volume $(1-x)V$. Then, the total energy of this phase reads

$$E_{PS}(\delta) = xE_{BCS}(\delta) + (1-x)E^0_{CDW}, \tag{4.42}$$

where $\delta$ is the doping of the BCS part and $\delta_0$ is the expected doping of our mixture. The mixture must respect the condition of fixed number of atoms or the fixed doping $x\delta = \delta_0$. We can then minimize this total energy over the variable $\delta$ instead of $x$

$$E_{PS}(\delta) = \frac{\delta_0}{\delta}\Big[E_n(\delta) - \frac{\Delta^2_{BCS}}{2W}\Big] + (1-\frac{\delta_0}{\delta})\Big[E_n(0) - \frac{1}{4W}(\frac{\Delta^2_{0\uparrow}}{1-z} + \frac{\Delta^2_{0\downarrow}}{1+z})\Big]. \tag{4.43}$$

The quantities $\Delta_{BCS}, \Delta_{0\sigma}$ are the solutions of the gap equations for the BCS phase (Eq. 4.27) and the half-filled CDW phase (Eq. 4.37). $E_n(\delta) = -|U|(1+\delta)^2/4 - W(1-\delta^2)/4$ is the energy of the normal state with doping $\delta$. In fact, in the limit $\delta \ll 1$, we can take the Taylor expansion of the BCS gap equation around $\delta = 0$, and get the solution for the gap

$$\Delta_{BCS} = \Delta_0(1 - \frac{\delta^2}{2}) + O(\delta^4), \tag{4.44}$$

where $\Delta_0$ is the solution of the BCS gap equation for $\delta = 0$. The optimal value of doping which minimizes the above energy is

$$\delta = \frac{1}{W}\Big[\frac{\Delta^2_{0\uparrow}}{1-z} + \frac{0\Delta^2_{\downarrow}}{1+z} - 2\Delta^2_0\Big]^{1/2},$$

and the optimal energy difference between the normal and the PS state reads

$$E_{PS} - E_n(\delta_0) = -\frac{\Delta^2_{BCS}}{2W} - \frac{1}{4W}\Big[\sqrt{\frac{\Delta^2_{0\uparrow}}{1-z} + \frac{\Delta^2_{0\downarrow}}{1+z} - 2\Delta^2_0} - \delta_0 W\Big]^2. \tag{4.45}$$

### 4.4.4 Hartree-Fock mean-field phase diagram

Before figuring out the phase diagram by making an energy comparison, we would like to discuss the validity condition for the Hartree-Fock mean-field theory. The decoupling of the local Hubbard interaction is correct if we can ignore the quantum fluctuations around the mean value of the order parameter. This condition is valid only for small coupling strengths $|U| \ll W_\uparrow, W_\downarrow$ (see [45]). In our notation, the unit of energy is $(t_\uparrow + t_\downarrow)/2$ and we have

$$|U|/W_\downarrow = |U|/(1-z) \ll 1 \quad \Rightarrow \quad |U| \ll (1-z) \tag{4.46}$$

In the MFT phase diagram discussed below, we will extend the result to the strongly-correlated regime, far from the validity of this theory.

#### Phase diagram at half-filling

At half-filling, in a mixture with the same mass for both species, it is well-known that there is a degeneracy between the BCS and the CDW phase [54]. Under the effect of a mass imbalance, we clearly see that the gap equation (Eq. 4.23) and the energy for the BCS phase (Eq. 4.24) have no dependence on $z$, while the energy for the CDW phase (Eq. 4.38) is decreasing when the asymmetry of the hopping gets bigger. Thus, we expect to have a CDW phase which is more stable in energy whenever the hoppings of the two species are different. Comparing the energies $E_{BCS}$ and $E_{CDW}$ we obtain

$$E_{CDW} - E_{BCS} = -\frac{1}{4W}\left[\frac{\Delta_{0\uparrow}^2}{1-z} + \frac{\Delta_{0\downarrow}^2}{1+z}\right] + \frac{\Delta_{BCS}^2}{2W}. \tag{4.47}$$

In Appendix A.3, we demonstrate the inequality $E_{CDW} - E_{BCS} \leq 0$ for any $\Delta_{BCS}$ and $\Delta_{0\sigma}$ that are solutions of the gap equations for the BCS phase (Eq. 4.23) and the CDW phase (Eq. 4.37). In conclusion, the CDW phase is the dominating phase when $U$ is negative (by particle-hole symmetry, we have that the SDW in the $z$ direction is also the dominating phase when $U$ is positive).

#### Phase diagram away from half-filling

Away from half-filling, there are three competing phases for the ground state: the BCS state, the doped CDW and the phase separation between a doped-BCS superfluid and a half-filled CDW phase. We compare the energy of these three states and figure out the phase diagram as a function of the interaction strength $|U|/W$ and the hopping imbalance $z$.

*Competition between BCS and phase separation:* Using the above calculation of the energy of a phase separated state between a CDW and a BCS state, it is possible to find the transition line between the BCS state and the PS state, by analyzing when the ratio of the BCS part in the PS state goes from 1 to $x < 1$. Therefore, the transition line is given by $\delta = \delta_0$ or

$$\delta_0 W = \sqrt{\frac{\Delta_{0\uparrow}^2}{1-z} + \frac{\Delta_{0\downarrow}^2}{1+z} - 2\Delta_{0BCS}^2}. \tag{4.48}$$

Here, $\Delta_{0\sigma}$ is the solution of gap equation for the half-filled CDW phase (Eq. 4.37) and $\Delta_{0BCS} = W/2\sinh(W/|U|)$. This condition yields the transition line (the red line with triangular symbols in Fig. 4.14) between the BCS superfluid phase and the PS between the half-filled CDW and the superfluid. Below this line, the superfluid phase is energetically more stable than the PS.

*Competition between doped CDW and BCS:* The transition line between these two phases is determined by the energetic comparison $\Delta E = E_{CDW} - E_{BCS} = 0$. For a fixed doping $\delta$, we substitute the expressions of $E_{CDW}$ and $E_{BCS}$ obtained above and obtain

$$\Delta_{BCS}^2 - \frac{\delta^2}{2} - \frac{1}{2}\left(\frac{\Delta_\uparrow^2}{1+z} + \frac{\Delta_\downarrow^2}{1-z}\right) + \sum_\sigma \frac{\delta}{2}\sqrt{\frac{\delta^2(1+\sigma z)^2}{4} + \Delta_\sigma^2} = 0. \tag{4.49}$$

Here, $\Delta_{BCS}$ is the solution of the gap equation for the BCS phase (Eq. 4.27) and $\Delta_\sigma$ is the solution of the gap equation for the doped-CDW phase (Eq. 4.40). The numerical result of energy competition between these two phases is represented by the black curve with circles in Fig. 4.14 for $\delta = 0.05$. Below the back curve the BCS superfluid phase is stable, while above this curve the doped CDW has a lower energy.

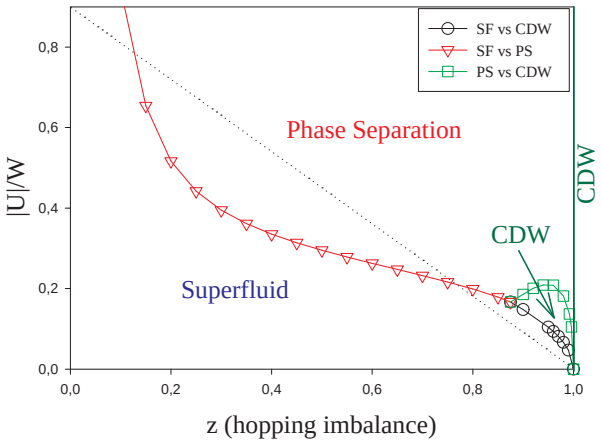


**Figure 4.14:** Phase diagram for $\delta = 0.05$ obtained by weak-coupling mean field theory (its validity is questionable above the dotted line). For simplicity, a square density of states was used here.

*Competition between doped CDW and phase separation:* Here, we consider the difference in energy between the PS and the CDW phase: $\Delta E = E_{PS} - E_{CDW}$. Substituting the two expressions for the energy calculated above, we derive the transition line between the PS and the doped-CDW phase

$$\Delta E = -\frac{\Delta_{BCS}^2}{2W} - \frac{1}{4W}\left[\sqrt{\frac{\Delta_{0\uparrow}^2}{1-z} + \frac{\Delta_{0\downarrow}^2}{1+z} - 2\Delta_0^2} - \delta_0 W\right]^2 + \sum_\sigma \frac{1-\sigma z}{4W}\left[\sqrt{\frac{\Delta_\sigma^2}{(1-\sigma z)^2} + \frac{W^2\delta^2}{4}} - \frac{W\delta}{2}\right]^2.$$

In this expression, the order parameter $\Delta_{0\sigma}$ is obtained from the gap equation for the half-filled CDW phase (Eq. 4.37), $\Delta_\sigma$ is obtained from the gap equation for the doped-CDW phase (Eq. 4.40) and $\Delta_{BCS}$ is the solution of Eq. 4.27. The transition line between these two phases is represented by the green curve in Fig. 4.14.

We recall that the weak-coupling mean-field is justified only when $|U| \lesssim t_\uparrow, t_\downarrow$, i.e., $|U|/W \lesssim (1-z)$. An indicative line (the dotted line in Fig. 4.14) defines a region below which the weak-coupling static mean-field is reliable. In order to obtain the phase diagram,

we performed a detailed comparison of the ground-state energies of three mean-field solutions: the homogeneous SF, the phase separated SF/CDW phase, and the homogeneous CDW with $\delta \neq 0$ (when it exists). We first compared the ground-state energies of two mean-field solutions: the homogeneous SF, and the SF/half-filled CDW phase-separated solution obtained from a Maxwell construction. The resulting phase boundary (Fig. 4.1) is seen to be qualitatively reasonable, and even quantitatively accurate (in comparison to the numerical DMFT result) for some intermediate range of $z$. For a strong hopping imbalance, the comparison of the energy between these three phases yields a small region of parameters, for large $z$, in which a doped CDW is stable.

Here, we obtained the phase diagram by looking at the state with lowest energy in a certain range of parameters $(|U|, z)$. Therefore, we do not know the nature of the phase transition between the SF phase and the doped CDW. The nature of this phase transition could be better understood by a more sophisticate mean-field approach allowing simultaneously for both CDW and BCS orders (see Appendix A.2). Within this approach a different scenario from a first-order transition could be realized. Namely CDW and BCS orders can coexist in the same solution for some range of parameters, giving rise to a supersolid phase, which here becomes favored by the presence of the underlying optical lattice.

## 4.5 Ultracold atoms in the presence of a harmonic potential

So far, we discussed the phase diagram of mass-imbalanced ultracold atoms in a homogeneous system. In this section, we consider the effect produced by the harmonic potential due to the magneto-optical trap (MOT) or due to the gaussian profile of the laser beam. This potential can be understood as an added chemical potential which varies in real space. By particle-hole transformation, we turn the attractive Hubbard model into an $XXZ$ spin model with strong positive coupling, where the external magnetic field varies in real space. In order to understand the influence of the trap on the density profile and on the ground state, we propose to apply a local-density approximation which is, in general, valid for smooth variations of the trapping potential (see also Section 1.1.2). A full numerical minimization of the energy on a finite system is finally computed using a Monte Carlo algorithm.

### 4.5.1 Local density approximation for the trapping potential

Above, we have seen that the phase diagram that one obtains in the strong-coupling limit is actually quite generic at a qualitative level. This motivates us to consider this specific limit in the following in order to simplify the calculations. Our aim is then to discuss the density profile of the two species using the spin model obtain after particle-hole transformation. The presence of the harmonic trap potential can be modeled by a magnetic field which favors the spin down orientation, and has the form

$$h(r) = h - \frac{1}{2} m \omega_{\mathrm{ho}}^2 r^2,$$

where $\omega_{\mathrm{ho}}$ is the frequency of the harmonic trap. Let $R_0$ be the radius of the trap, we define $h_0 = m\omega_{\mathrm{ho}}^2 R_0^2/2$. Therefore, the local magnetic field now reads $h(r) = h - h_0 r^2/R_0^2$. From the MFT for the homogeneous system, we see that when the magnetic field $|h(r)| < h_c = JS\zeta\sqrt{\gamma(\gamma+2)}$, we obtain a $\mathrm{SDW}_z$ phase, otherwise we have a $\mathrm{SDW}_{xy}$ phase. When the average magnetization per site is $m$, the external magnetic field satisfies the condition $m = \int m(r) dr^2/V$. According to the polarization in the system, we have the following phases:

### Antiferromagnetism (CDW in the attractive model)

We can realize an antiferromagnetic phase (CDW in the attractive model) in the trap when the system is at half-filling without polarization and the local magnetic field satisfies $|h(r)| < h_c$.

### Spin density wave XY (SF in the attractive model)

We consider now the case where the local magnetic field satisfies $|h(r)| > h_c$ for any position in the trap. We have the two following situations:

- If we have $h < -h_c$ then $h(r) < -h_c$ for any $r < R_0$. We obtain a configuration with only the SDW$_{xy}$ phase (SF phase in the negative-coupling limit). The profile of the magnetic field reads $m(r) = h/2J\zeta(\gamma+2)$. The condition on $h$ is equivalent to a condition on the average polarization $m$ for which we obtain a SDW$_{xy}$ (SF): $m < -(h_0+2h_c)/2J\zeta(\gamma+2)$
- If $h - h_0 > h_c$ then $h(r) > h_c$ for any $r < R_0$. In this case, there is also a SDW$_{xy}$ phase everywhere with the polarization profile $m(r) = h/2J\zeta(\gamma+2)$. In this phase, the average value of the polarization satisfies $m > (h_0 + 2h_c)/2J\zeta(\gamma+2)$.

### Phase separation

Let us now consider the situation where the variation of the local magnetic field in the trap induces a phase separation in real space. Depending on the total spin imbalance, we obtain different situations of phase separation. We note that in the trap $0 < r < R_0$, the local magnetic field $h(r) = h - h_0 r^2/R_0^2$ satisfies $h > h(\mathbf{r}) > h - h_0$.

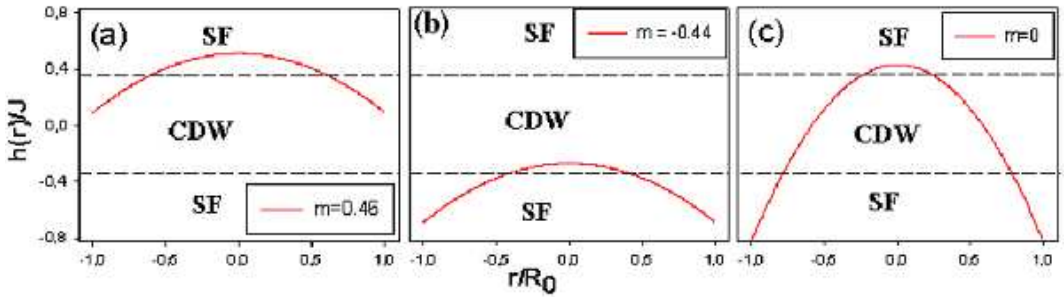


**Figure 4.15:** LDA calculation for the spatial phase separation configuration. (a) The PS with SDW$_z$ in the center. (b) The PS with SDW$_{xy}$ in the center. (c) The three shell structures.

- *Phase separation with a SDW$_{xy}$ in the center:* If we have $h > h_0$ and $|h - h_0| < |h_c|$ (see Fig. 4.15, left panel), then there is a zero $R_1 = R_0\sqrt{(h-h_c)/h_0}$ for the equation $h(r) = h_c$. Therefore, the region in the center of the trap ($r < R_1$) will be a SDW$_{xy}$ phase, while in the exterior ring we obtain a SDW$_z$. This case corresponds to the polarization
$$\max\{0, -\frac{h_0 - 2h_c}{2J\zeta(\gamma+2)}\} < m < \frac{h_0 + 2h_c}{2J\zeta(\gamma+2)}.$$
- *Phase separation with a SDW$_z$ in the center:* If we have $|h| < h_c$ and $h - h_0 < -h_c$ (see Fig. 4.15, middle panel) then there is a solution $R_2 = R_0\sqrt{(h+h_c)/h_0}$ for $h(r) = -h_c$. The region in the center of the trap $r < R_2$ has a local magnetic field $h(r) < -h_c$. Therefore, a SDW$_z$ phase is present in the center of the trap while the exterior ring will

be occupied by a $\mathrm{SDW}_{xy}$ phase. This case corresponds to the condition on the average polarization

$$-\frac{h_0+2h_c}{2J\zeta(\gamma+2)} < m < \min\{0, -\frac{h_0-2h_c}{2J\zeta(\gamma+2)}\}.$$

- *Phase separation with three shells structure:* If we have $h_0 > 2h_c$ (see Fig. 4.15, right panel), there is a solution $R_1$ for the equation $h(r) = h_c$ and a solution $R_2$ for the equation $h(r) = -h_c$. In this case, we can obtain a more exotic phase with $\mathrm{SDW}_z$ in the region $R_1 < r < R_2$ and a $\mathrm{SDW}_{xy}$ in the region $r < R_1$ and $r > R_2$. The condition for the magnetization in this case reads

$$-\frac{h_0-2h_c}{2J\zeta(\gamma+2)} < m < \frac{h_0-2h_c}{2J\zeta(\gamma+2)}.$$

### 4.5.2 Monte Carlo simulation for the Heisenberg model

We note that within the LDA approach, we obtained a sharp jump in the profile of the polarization for the phase separated configurations, which means that there is sharp jump in the density in the initial problem with negative coupling. The jump of the polarization (resp. density) occurs at the frontier between the AF and $\mathrm{SDW}_{xy}$. In order to justify the LDA calculation, we perform a Mont Carlo simulation for the classical Heisenberg model on a finite size system. We concentrate here on the comparison between these two methods in the case with a phase separation both in the 1D spin chain and in a 2D system.

In both cases, the numerical calculation shows a good agreement with the LDA approximation. In the one-dimensional spin chain (Fig. 4.16), the comparison gives a very good agreement despite the finite size of the Mont Carlo system. As shown in the DMFT phase diagram, the phase transition between a $\mathrm{SDW}_z$ and the phase separation is generic for any coupling (only the critical value of the hopping imbalance is changed). Therefore, the density profile of the PS phase at intermediate coupling in the presence of the harmonic trap will be similar to the physics at strong coupling. For the system in two dimensions, we also obtain

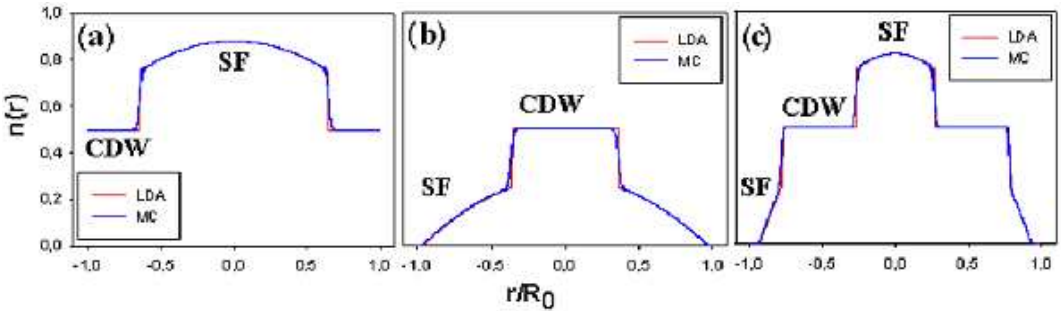


**Figure 4.16:** Density profile obtained both by Monte Carlo and within the LDA approximation for the 1D $XXZ$ model.

three different configurations for the profile of the phases in the harmonic trap.

## 4.6 Conclusion

In this chapter, we have studied the phase diagram of mixtures of fermionic atoms with different masses confined in an optical lattice with an attractive interaction. In the case of equal masses ($z = 0$), the system forms a stable superfluid state. As soon as the mass imbalance is

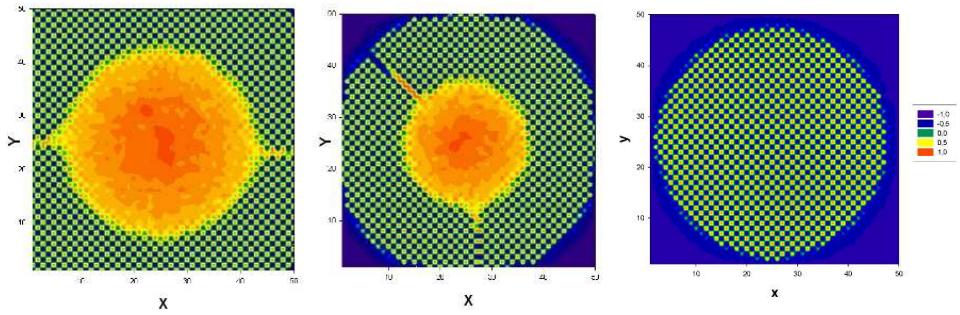


**Figure 4.17:** Density profile obtained by Monte Carlo in the 2D $XXZ$ model.

non-zero but still close to this limit, the system remains in a homogeneous superfluid phase. When the anisotropy exceeds a given critical value, which depends on the density of fermions, the system is a pure superfluid at weak-coupling, while increasing the coupling induces a phase separation between a doped superfluid state and a commensurate charge density wave. We note that, within the static mean-field including the Hartree correction, we find a small window of parameters, close to the Falicov-Kimball limit, where the doped CDW becomes stable.

When the harmonic trap potential is taken into account, the phase separation is actually realized in different regions of the trap (for example the superfluid can be present in the central region, while the charge density wave is confined to the outer part of the trap), with rapid variations of the local density at the phase boundaries. We finally note that, in the case of an $^6$Li/$^{40}$K mixture, a simple estimate shows that the mass imbalance $z$ can be varied over a large range by changing the lattice depth $V_0/E_R$ ($z \ll 1$ at small $V_0/E_R$ and $z \simeq 0.9$ for $V_0/E_R \simeq 15$), so that the effects discussed in this work can actually be observed.

**Second article:**

Competing superfluid and density-wave ground-states of fermionic mixtures with mass imbalance in optical lattices

*Physical Review B* 76, 104517 (2007)

Eprint: cond-mat/0704.2660

# Competing superfluid and density-wave ground-states of fermionic mixtures with mass imbalance in optical lattices

Tung-Lam Dao,[1] Antoine Georges,[1] and Massimo Capone[2]
[1]*Centre de Physique Théorique, École Polytechnique, CNRS, 91128 Palaiseau Cedex, France*
[2]*SMC, CNR-INFM and Dipartimento di Fisica, "Sapienza" Universitá di Roma, Piazzale Aldo Moro 2, I-00185 Roma, Italy and ISC-CNR, Via dei Taurini 19, I-00185 Roma, Italy*

(Received 2 July 2007; revised manuscript received 27 August 2007; published 24 September 2007)

We study the effect of mass imbalance on the phase diagram of a two-component fermionic mixture with attractive interactions in optical lattices. Using static and dynamical mean-field theories, we show that the pure superfluid phase is stable for all couplings when the mass imbalance is smaller than a limiting value. For larger imbalance, phase separation between a superfluid and a charge-density wave takes place when the coupling exceeds a critical strength. The harmonic trap induces a spatial segregation of the two phases, with a rapid variation of the density at the boundary.

DOI: 10.1103/PhysRevB.76.104517 PACS number(s): 67.20.+k, 05.30.Fk, 03.75.Lm, 71.10.Fd

## I. INTRODUCTION

The remarkable advances in handling ultracold atomic gases have given birth to the new field of "condensed matter physics with light and atoms." Cold atoms in optical lattices, with tunable and controllable parameters, have been studied in many different contexts (for reviews, see Ref. 1). Mixtures of two-component atoms with different masses (e.g., $^6$Li and $^{40}$K) introduce an additional parameter, namely, the difference between the hopping amplitudes associated with each species in the optical lattice. This may affect the stability of the possible quantum phases or even induce new ones. Recently, a phase diagram has been worked out in the one-dimensional (1D) case[2] and in continuum models.[3]

In this paper, we consider such fermionic mixtures in three dimensions, with an attractive on-site coupling. Using analytical and numerical techniques, we establish a ground-state phase diagram as a function of coupling strength and mass imbalance, in all regimes of couplings. We also consider the experimentally relevant effect of the trap potential, which is shown to induce a spatial segregation between superfluid and density-wave phases.

Under conditions discussed, e.g., in Refs. 1, 4, and 5, fermionic mixtures are described by a Hubbard model,

$$H = -\sum_{\langle i,j\rangle,\sigma} t_\sigma (c_{i\sigma}^\dagger c_{j\sigma} + \text{H.c.}) - |U| \sum_i n_{i\uparrow} n_{i\downarrow}. \qquad (1)$$

The (pseudo)spin index $\sigma$ refers to the two different species. Feshbach resonances between $^6$Li and $^{40}$K are currently under investigation,[6] and it would allow for an attractive interaction with a tunable strength, as assumed in Eq. (1). For an example of heteroatomic resonances in the boson-fermion case, see e.g., Ref. 7. In the following, we consider a bipartite optical lattice made of two interpenetrating $(A,B)$ sublattices arranged such that the neighbors of $A$ sites are all of $B$ type and vice versa (this happens, for instance, in the cubic lattice). For simplicity, we consider an equal number of atoms for each species, leaving for future work the study of imbalanced populations.

The paper is organized as follows: in Sec. II, we anticipate the phase diagram obtained by means of dynamical mean field theory (DMFT), and we introduce the DMFT method itself; in Sec. III, we discuss the results of weak- and strong-coupling static mean-field methods; in Sec. IV, we consider the effect of the trapping potential within local density approximation; while Sec. V is dedicated to concluding remarks.

## II. GENERIC PHASE DIAGRAM AND DYNAMICAL MEAN-FIELD THEORY

In order to study the zero temperature ground-state phase diagram of model (1), we use DMFT,[8] together with analytical mean-field theory calculations for both weak and strong couplings. Let us anticipate the DMFT phase diagram of the uniform system, displayed in Fig. 1. When the fermions have the same mass, the ground state is a superfluid (SF) for all $|U|$. A competing ordering exists, namely, a charge-density wave (CDW), considered here in the simplest (commensurate) case in which the charge is modulated with an alternating pattern on $A$ and $B$ sublattices. At half-filling, i.e., when the number of fermions is equal to the number of lattice sites ($\langle n_\uparrow + n_\downarrow \rangle = 1$), it is well known that the SF and CDW states are degenerate. This no longer applies in the "doped" system, in which the number of fermionic atoms no longer coincides with the number of sites in the optical lattice; for equal masses, the SF phase is stabilized by doping for all $|U|$, but a large mass imbalance favors the CDW phase over a SF state in which the Cooper pairs must be formed by fermions with different mobilities.[2] Hence, the SF/CDW competition becomes more interesting in the presence of mass imbalance. As displayed in Fig. 1, we find that the uniform system has a SF ground state for all values of $|U|$ as long as the mass imbalance $z \equiv (t_\uparrow - t_\downarrow)/(t_\uparrow + t_\downarrow)$ is smaller than a limiting value $z_c$ (which depends on the average density). For $z > z_c$, a (first-order) phase boundary is crossed as $|U|$ is increased, beyond which the uniform system undergoes a phase separation (PS) between a SF and a CDW phase. As discussed later in this paper, this implies that, in the presence of a harmonic trap, the CDW and SF phases may both exist in different regions of the trap.

 

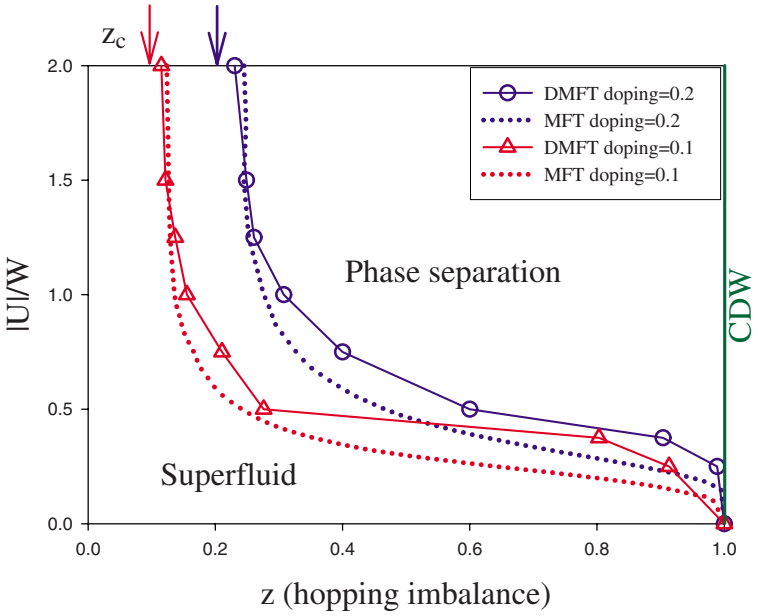


FIG. 1. (Color online) Phase diagram of the uniform system in the $(z,|U|)$ plane obtained from DMFT. Below the curves (displayed here for two "doping" levels $\delta \equiv n-1=0.1,0.2$), the SF is stable. Above the curves, the system is phase separated into a half-filled CDW and a SF. The arrows indicate the analytical strong-coupling values. The dotted lines are the weak-coupling mean-field approximation (see text). $|U|$ is normalized to the bandwidth $W$ of $(\varepsilon_{\mathbf{k}\uparrow}+\varepsilon_{\mathbf{k}\downarrow})/2$.

DMFT is one of the most popular modern theoretical approaches designed to treat correlated fermions on a lattice. The idea of the method is to extend to the quantum domain the mean-field strategy by replacing the static mean-field averages with frequency-dependent (dynamical) objects. Just like classical mean-field theory, the method freezes the spatial correlations, but the DMFT allows for an unbiased treatment of the dynamics. A practical implementation of DMFT requires the self-consistent solution of a quantum impurity model, i.e., a model of a single interacting site coupled to a bath that allows for quantum fluctuations on the correlated site. In the mean-field spirit, the site is representative of any site of the original lattice. This correspondence is implemented via a self-consistency condition which contains information about the original lattice through the noninteracting density of states. The self-consistency condition relates the frequency-dependent "Weiss field" which describes the dynamics of the bath (analogous to the static Weiss field in mean-field theory of magnetism) $\hat{\mathcal{G}}(i\omega)$ entering the effective "impurity model" to the Green's function.

The general form of the self-consistency equation (we write it for simplicity for the normal metallic phase, but the generalization to the broken-symmetry phases is straightforward) is

$$G(i\omega)=\int d\varepsilon \frac{D(\varepsilon)}{i\omega+\mu-\varepsilon-\Sigma(i\omega)}, \tag{2}$$

where $\Sigma(i\omega)=\mathcal{G}^{-1}(i\omega)-G^{-1}(i\omega)$ is the local self-energy and $D(\varepsilon)$ is the noninteracting density of states. For the case of a semicircular density of states $D(\varepsilon)=2/\sqrt{(\pi D)}\sqrt{4t^2-\varepsilon^2}$ with bandwidth $W=4t$, this equation is greatly simplified, and it becomes

$$\mathcal{G}(i\omega)=i\omega+\mu-t^2G(i\omega). \tag{3}$$

In this work, we use this density of states, which has been shown to satisfactorily reproduce results in $d=3$ in the context of solid state physics. For more details on DMFT, we refer to Ref. 8.

A crucial property of DMFT is that it does not require any assumption on the values of the coupling terms appearing in the Hamiltonian, and it indeed becomes exact both in the small interaction limit and in the strong interaction one. This has been explicitly shown in DMFT studies of the attractive Hubbard model with equal masses, where the crossover from Bardeen-Cooper-Schrieffer superconductivity to Bose-Einstein condensation of preformed pairs has been studied both in the normal[9] and the superconducting,[10] and both the limiting regimes are basically exactly reproduced.

To describe the superconducting phase, it is convenient to work with Nambu's spinors $\psi^+=(c_\uparrow^+,c_\downarrow)$. The key quantity in DMFT is the local (on-site) Green's function, $\hat{G}(\tau)=\langle \mathrm{T}_\tau \psi_i(\tau)\psi_i^+(0)\rangle$, and its Fourier transform for imaginary frequencies is

$$\hat{G}(i\omega)=\begin{bmatrix} G_\uparrow(i\omega) & F(i\omega) \\ F^*(i\omega) & -G_\downarrow(-i\omega) \end{bmatrix}, \tag{4}$$

where $G(\tau)=-\langle Tc(\tau)c^\dagger(0)\rangle$ is the normal Green's function on a given site, and $F(\tau)=-\langle Tc_\uparrow(\tau)c_\downarrow(0)\rangle$ is the anomalous Green's function associated with superfluid ordering. The superfluid order parameter is indeed given by $\Delta_{SF}=\langle c_{i\uparrow}c_{i\downarrow}\rangle=F(\tau=0)=\Sigma_\omega F(i\omega)$.

In this work, we also consider the possibility of a CDW state which establishes on our bipartite lattice. In this case, the local Green's function takes different values ($\hat{G}_A$ and $\hat{G}_B$) on the two alternating sublattices. The CDW order parameter is the difference of densities on the two sublattices: $\Delta_{\mathrm{CDW}}=\langle n_A-n_B\rangle$.

We can generalize the self-consistency of Eq. (3) to the case where both SF and CDW are possible. The result is $\hat{\mathcal{G}}_{A(B)}^{-1}(i\omega)=i\omega\hat{1}+\hat{\mu}-\hat{T}\hat{\mathbf{G}}_{B(A)}(i\omega)\hat{T}$, in which $\hat{T}=\mathrm{diag}[t_\uparrow,-t_\downarrow]$

and $\hat{\mu}=\mathrm{diag}[\mu_\uparrow,-\mu_\downarrow]$ are diagonal matrices, whose elements are the half-bandwidths and the chemical potentials of the two species.

Since we are able to study all the different broken-symmetry phases, the $T=0$ phase diagram is easily determined by comparing the energies of the different solutions. The energy is evaluated as $\langle H\rangle=\langle K\rangle-|U|\Sigma_i\langle n_{i\uparrow}n_{i\downarrow}\rangle$. The expectation value of the interaction term is easily computed through the calculation of the expectation value of $\Sigma_i n_{i\uparrow}n_{i\downarrow}$, while the kinetic energies $\langle K\rangle$ in the SF and CDW phases read $\langle K\rangle_{SF}=\beta^{-1}\Sigma_{\omega,\sigma}t_\sigma^2[G_\sigma^2(\sigma i\omega)-F^2(i\omega)]$ and $\langle K\rangle_{\mathrm{CDW}}=\beta^{-1}\Sigma_{\omega,\sigma}t_\sigma^2 G_{A\sigma}(i\omega)G_{B\sigma}(i\omega)$, respectively.

We performed DMFT calculations[14] exploiting the nonperturbative nature of DMFT to span the whole range of coupling $|U|$ and imbalance $z$. We focused on the vicinity of half-filling and found the phase diagram of the uniform system (Fig. 1) to be qualitatively independent on the "doping level," i.e., the relative difference between the number of atoms and optical lattice sites, $\delta=\langle n_\uparrow+n_\downarrow-1\rangle$. For small enough values $z<z_c(\delta)$ of the mass imbalance, a pure SF solution is stable for all $|U|$. In contrast, for $z>z_c$, the pure SF phase is stable only for small interactions (below the line drawn in Fig. 1). Above this line (which depends on $\delta$), the pure SF solution becomes unstable toward phase separation between a SF and a CDW phase. (Note that we did not find a homogeneous CDW solution out of half-filling, except at $z=1$). This means that it is more convenient to separate the system into a fraction $1-x$ with CDW order and $\delta=0$ and a fraction $x$ with SF order accommodating the rest of the particles. This conclusion is reached by minimizing over $x$ the expression $E_{\mathrm{PS}}(x)=(1-x)E_{\mathrm{CDW}}+xE_{SF}$. We note that the SF phase is more stable than in the 1D case[2] (in which nesting favors a CDW with $\mathbf{Q}=2k_F$). We underline that this diagram has been obtained by comparing the energies of the different possible states (normal, SF, and CDW), and that a normal ground state is never stable, either as a pure state or as one of the phases in the case of phase separation. No solution with coexistence of SF and CDW in the same homogeneous state has, instead, been found.

## III. MEAN FIELD THEORY ANALYSIS

### A. Strong-coupling mean-field theory

In this section, we describe analytical mean-field calculations for both weak and strong couplings which help in understanding the DMFT phase diagram established numerically. We first present a *strong-coupling* analysis, which holds for $|U|\gg t_\uparrow,t_\downarrow$. In order to analyze this limit, we find it useful to resort to a particle-hole transformation (Table I) that maps our negative-$U$ model onto the positive-$U$ Hubbard model and work in the repulsive-$U$ framework. We emphasize that we are not switching to truly repulsive interactions, but we simply exploit a mathematical property to gain information on the physical system of our interest. Under this mapping, our model is transformed, at large $|U|\gg t_\uparrow,t_\downarrow$, into an $XXZ$ quantum spin-1/2 model:[2,5]

$$H=J\sum_{\langle i,j\rangle}\vec{S}_i\cdot\vec{S}_j+\gamma J\sum_{\langle i,j\rangle}S_i^zS_j^z-h\sum_i(2S_i^z-m), \qquad (5)$$

TABLE I. Particle-hole transformation mapping the $U<0$ model with $\langle n_\uparrow\rangle=\langle n_\downarrow\rangle$ onto a half-filled $U>0$ model with a magnetic field.

| $-\|U\|<0$ | $\|U\|>0$ |
|---|---|
| $c_{i\uparrow}^+$, $c_{i\downarrow}^+$ | $d_{i\uparrow}^+$, $(-1)^i d_{i\downarrow}$ |
| $n_{c\uparrow}$, $n_{c\downarrow}$ | $n_{d\uparrow}$, $1-n_{d\downarrow}$ |
| $\delta\equiv n_c-1=\langle n_{c\uparrow}+n_{c\downarrow}\rangle-1$ | $m_d=\langle n_{d\uparrow}-n_{d\downarrow}\rangle$ |
| Chemical potential $\mu_c$ | Field $h_d=\mu_c-\|U\|/2$ |
| $h_c$ | $\mu_d=h_c+\|U\|/2$ |
| SF: $\langle c_{i\uparrow}^+c_{i\downarrow}^+\rangle$ | $\mathrm{SDW}_{xy}$: $(-1)^i\langle d_{i\uparrow}^+d_{i\downarrow}\rangle$ |
| CDW: $(-1)^i\langle\hat{n}_{ci}\rangle$ | $\mathrm{SDW}_z$: $(-1)^i\langle S_{di}^z\rangle$ |

in which $\vec{S}\equiv\frac{1}{2}d_\alpha^+\vec{\sigma}_{\alpha\beta}d_\beta$, $J=4t_\uparrow t_\downarrow/|U|$, and $\gamma=(t_\uparrow-t_\downarrow)^2/2t_\uparrow t_\downarrow=2z^2/(1-z^2)$. Hence, the mass imbalance turns into a spin exchange anisotropy. The uniform magnetic field $h$ corresponds to the original chemical potential $\mu-|U|/2$ and the magnetization to the doping $\delta$ (Table. I). The mean-field approach[11] amounts for treating the spin variables as classical and minimizes the energy over the angles $\theta_A$, $\theta_B$ describing the orientation of the spins in the two sublattices. The energy per site reads (with $\zeta$ the lattice connectivity and $c_{A,B}\equiv\cos\theta_{A,B}$ and $s_{A,B}\equiv\sin\theta_{A,B}$)

$$\frac{E}{N}=\frac{\zeta}{8}Js_As_B+\frac{\zeta}{8}J(1+\gamma)c_Ac_B-\frac{h}{2}[c_A+c_B-2m]. \qquad (6)$$

The phase diagram is characterized by the competition between the $xy$ spin-density wave ($\mathrm{SDW}_{xy}$) with order parameter $\Delta_{xy}=\langle(-1)^iS_i^x\rangle$ (corresponding to SF ordering for $U<0$), and Néel order ($\mathrm{SDW}_z$) $\Delta_z=\langle(-1)^iS_i^z\rangle$ (corresponding to CDW). The solution changes according to the magnetization $m$ of the system (i.e., the doping of our physical model). The $m$ vs $h$ curve has a discontinuity of amplitude $m_c=\sqrt{\gamma/(\gamma+2)}=z$. For $m=0$ (half-filling $\delta=0$), a $\mathrm{SDW}_z$ (CDW) state is obtained. For $m\in[m_c,1]$, the homogeneous SDW $\mathrm{SDW}_{xy}$ (SF) state is stable, while for $0<m<m_c$ phase separation takes place between the two types of ordering. Thus, when working at fixed magnetization (corresponding to fixed doping $\delta$), one finds a SF for $z<z_c=m=\delta$ and phase separation for $z>z_c=\delta$. This strong-coupling value (indicated by arrows in Fig. 1) agrees very well with our DMFT results.

### B. Weak-coupling mean-field theory

We now turn to the opposite weak-coupling limit. We decouple the interaction term in the SF and the CDW channels and determine the regions of stability of each phase. We first consider the BCS decoupling of the interaction, introducing the order parameter $\Delta_{\mathrm{BCS}}=(|U|/N)\Sigma_{\mathbf{k}}\langle c_{\mathbf{k}\uparrow}^\dagger c_{\mathbf{k}\downarrow}^\dagger\rangle$ to make the Hamiltonian quadratic. In Nambu formalism, it reads

$$H_{\mathrm{BCS}}=\sum_{\mathbf{k}}\psi_{\mathbf{k}}^\dagger\begin{bmatrix}\xi_{\mathbf{k}\uparrow} & -\Delta_{\mathrm{BCS}}\\ -\Delta_{\mathrm{BCS}} & -\xi_{\mathbf{k}\downarrow}\end{bmatrix}\psi_{\mathbf{k}}+E_G. \qquad (7)$$

Here, $\tilde{\mu}_\sigma\equiv\mu-Un_{-\sigma}$, $\xi_{\mathbf{k}\sigma}=\varepsilon_{\mathbf{k}\sigma}-\tilde{\mu}_\sigma$, and $E_G=\Sigma_{\mathbf{k}}\xi_{\mathbf{k}\downarrow}+N|U|n_\uparrow n_\downarrow+N\Delta_{\mathrm{BCS}}^2/|U|$. The diagonalization of Eq. (7)

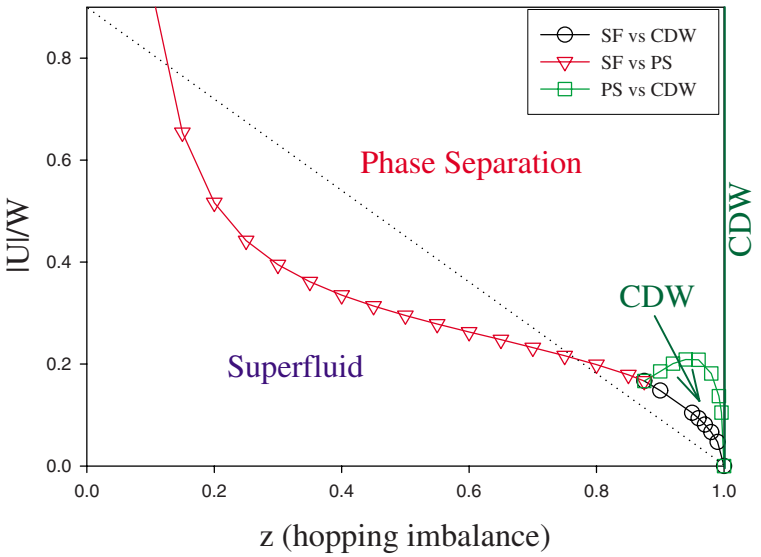


FIG. 2. (Color online) Phase diagram for $\delta=0.05$ from weak-coupling mean field (whose validity is questionable above the dotted line) (see text). For simplicity, a square density of states was used here.

yields the Bogoliubov modes with eigenvalues $E^{\pm}_{\mathbf{k}}=\pm(\xi_{\mathbf{k}\uparrow}-\xi_{\mathbf{k}\downarrow})/2+\sqrt{(\xi_{\mathbf{k}\uparrow}+\xi_{\mathbf{k}\downarrow})^2/4+\Delta^2_{\mathrm{BCS}}}$. Defining new variables $\xi_{\mathbf{k}}=(\xi_{\mathbf{k}\uparrow}+\xi_{\mathbf{k}\downarrow})/2$ and $\tilde{\mu}=(\tilde{\mu}_{\uparrow}+\tilde{\mu}_{\downarrow})/2$, the usual form of the BCS gap equation is recovered. We can readily compute the energy of BCS phase, obtaining $E_{\mathrm{BCS}}-E_n=-\Delta^2_{\mathrm{BCS}}/2W$, which tells us that the normal state is always unstable toward SF ordering.

Analogously, we can decouple the interaction in the CDW channel defined by the order parameter $\Delta_{\sigma}=(|U|/N)\Sigma_{\mathbf{k}}\langle c^{\dagger}_{\mathbf{k}+\mathbf{Q}\sigma}c_{\mathbf{k}\sigma}\rangle$ with $\mathbf{Q}=(\pi,\pi,\pi)$. Introducing the spinor $\psi^{\dagger}_{\mathbf{k}\sigma}=(c^{\dagger}_{\mathbf{k}\sigma},c^{\dagger}_{\mathbf{k}\dagger\mathbf{Q}\sigma})$, the mean-field Hamiltonian reads

$$H_{\mathrm{CDW}}=\sum_{\mathbf{k}\in\mathrm{RBZ},\sigma}\psi^{\dagger}_{\mathbf{k}\sigma}\begin{bmatrix}\varepsilon_{\mathbf{k}\sigma}-\tilde{\mu}_{\sigma} & -\Delta_{\sigma}\\ -\Delta_{\sigma} & -\varepsilon_{\mathbf{k}\sigma}-\tilde{\mu}_{\sigma}\end{bmatrix}\psi_{\mathbf{k}\sigma}+E_0, \tag{8}$$

with $E_0=N\Delta_{\uparrow}\Delta_{\downarrow}/|U|+N|U|n_{\uparrow}n_{\downarrow}$. It is readily diagonalized, with eigenvalues, $E^{\pm}_{\mathbf{k}\sigma}=\pm\sqrt{\varepsilon^2_{\mathbf{k}\sigma}+\Delta^2_{\sigma}}-\tilde{\mu}_{\sigma}$. This yields the following two self-consistent conditions:

$$\frac{1}{N}\sum_{\mathbf{k}\in\mathrm{RBZ}}[f(E^{+}_{\mathbf{k}\sigma})+f(E^{-}_{\mathbf{k}\sigma})]=n_{\sigma},$$

$$\frac{\Delta_{\sigma}}{N}\sum_{\mathbf{k}\in\mathrm{RBZ}}\frac{f(E^{-}_{\mathbf{k}})-f(E^{+}_{\mathbf{k}})}{\sqrt{\varepsilon^2_{\mathbf{k}\sigma}+\Delta^2_{\sigma}}}=\frac{\Delta_{-\sigma}}{|U|}. \tag{9}$$

At a fixed value of the chemical potential, these CDW equations have the following solutions: (i) for all $|U|$ and $z$, a normal solution with $\Delta_{\mathrm{CDW}}=0$, which is unstable toward SF; (ii) for large enough $|U|$, a half-filled (commensurate) CDW; and (iii) for large values of $z$ close to 1, a homogeneous CDW solution is also found with a density different from unity ($\delta\neq 0$).

We first compare the ground-state energies of the two mean-field solutions: the homogeneous SF and the SF/half-filled CDW phase-separated solution obtained from a Maxwell construction. The resulting phase boundary (Fig. 1) is seen to be qualitatively reasonable and even quantitatively accurate (in comparison to the numerical DMFT result) for some intermediate range of $z$. Indeed, the weak-coupling mean field is justified only when $|U|\lesssim t_{\uparrow},t_{\downarrow}$, i.e., $|U|/W\lesssim(1-z)$.[12] An indicative line below which weak-coupling static mean field is reliable is shown in panel (b) of Fig. 3

In Fig. 2, we perform a more detailed comparison of the ground-state energies of three mean-field solutions: the homogeneous SF, the phase-separated SF/CDW, and the homogeneous CDW with $\delta\neq 0$ (when it exists). This comparison yields a small region of parameters, for large $z$, in which a homogeneous CDW with a density different from one atom per site is stable. The phase transition between SF and CDW could be studied by a more sophisticate mean-field approach allowing simultaneously for both CDW and BCS orders. Within this approach, a different scenario from a first-order transition can be realized. Namely, CDW and BCS orders can coexist in the same solution for some range of parameters, giving rise to a supersolid phase, which here becomes favored by the presence of the underlying optical lattice. In light of the absence of a supersolid state in DMFT, we did not consider this possibility in the weak-coupling mean-field theory.

## IV. LOCAL DENSITY APPROXIMATION FOR THE HARMONIC TRAP POTENTIAL

We finally discuss the effect of the trap potential. For simplicity, we perform an explicit calculation only in the strong-coupling limit, using again the particle-hole transformation (Table I) and considering the effective spin model [Eq. (5)]. A harmonic trap potential yields a position-dependent chemical potential which corresponds under the particle-hole transformation to a spatially varying magnetic field $h(r)=h-h_0r^2/R_0^2$. Here, $R_0$ is the radius of the circular trap, $h_0=m\omega_0^2R_0^2/2$, and $h=\mu-|U|/2$ is related to the chemical potential at the center of the trap, which must be adjusted so that the local density $n(r)$ integrates to the total number of atoms. We start from a local density approximation (LDA) and also compare with a Monte Carlo solution of the strong-

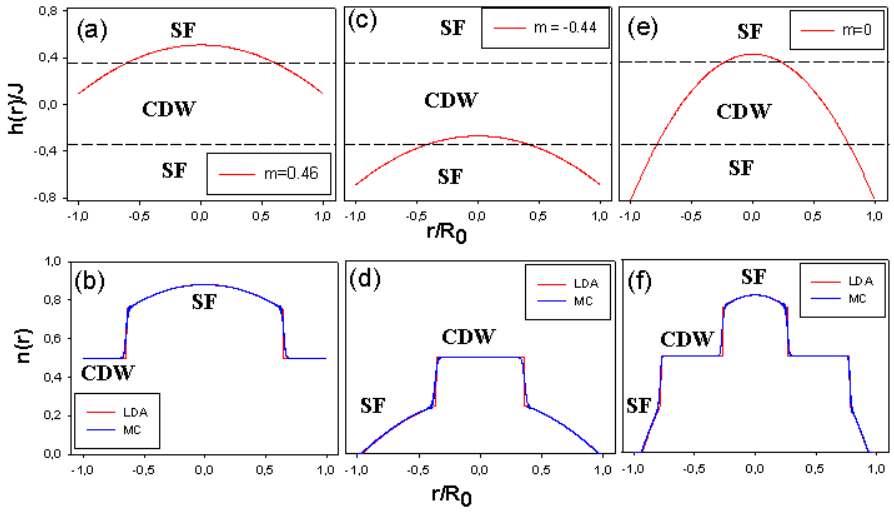


FIG. 3. (Color online) Density profiles and domains with different orderings inside the trap (bottom panels), as discussed in text. The top panels show how the trap potential intersects the characteristic values of the chemical potential in each case.

coupling model in the presence of $h(r)$. As described above, the strong-coupling analysis of the uniform system yields a critical magnetic field (chemical potential) at which $m(h)$ is discontinuous. For $|h|<h_c=J\zeta\sqrt{\gamma(\gamma+2)}=\frac{8z\zeta}{1-z^2}\frac{t_\uparrow t_\downarrow}{|U|}$, we have a $\mathrm{SDW}_z$ (CDW) phase; otherwise we have a $\mathrm{SDW}_{xy}$ (SF) phase. Within the LDA approximation, this implies that in a region where $|h(r)|$ is smaller (larger) than $h_c$, we locally observe $\mathrm{SDW}_z$/CDW ordering ($\mathrm{SDW}_{xy}$/SF). According to the values of the parameters $h$ and $h_0$, and noting that $h-h_0<h(r)<h$, one finds several different regimes:

(i) $h-h_0>h_c$ or $h<-h_c$. The trap potential is always larger than $h_c$, or smaller than $-h_c$, so that the system is in a $\mathrm{SDW}_{xy}$ (SF) phase everywhere inside the trap, and the density profile varies smoothly.

(ii) $h>h_c$ and $|h-h_0|<h_c$. In this case, $h(r)>h_c$ inside a circle of radius $R_1=R_0\sqrt{(h-h_c)/h_0}$ centered at $r=0$. Hence, one has phase separation into two distinct regions: $\mathrm{SDW}_{xy}$(SF) ordering within this circle and $\mathrm{SDW}_z$(CDW) in the outer ring (Fig. 3, left panel).

(iii) $h-h_0<-h_c$ and $|h|<h_c$. We find again phase separation with the opposite spatial arrangement. The $\mathrm{SDW}_{xy}$(SF) part is stable out or a circle of radius $R_2=R_0\sqrt{(h+h_c)/h_0}$, inside which there is a $\mathrm{SDW}_z$(CDW) phase (Fig. 3, middle panel).

(iv) $h>h_c$ and $h-h_0<-h_c$. Then, the magnetic field profile crosses both $h_c$ and $-h_c$, so that there are three spatial regions: $R<R_1$ where we find $\mathrm{SDW}_{xy}$(SF), then the ring $R_1<r<R_2$ where $\mathrm{SDW}_z$(CDW) establishes, and finally an outer ring $r>R_2$ with $\mathrm{SDW}_{xy}$(SF) ordering (Fig. 3, right panel).

In the three last cases [(ii)–(iv)], in which phase separation occurs, the LDA approximation predicts a jump of the magnetization at the phase boundaries $R_1$ and $R_2$, corresponding to a jump of the density in the original $U<0$ model (see also Refs. 13). In order to test this prediction and assess the validity of LDA, we performed a classical Monte Carlo simulation of model [Eq. (5)] in the presence of a spatially dependent field $h(r)$. For simplicity, this test was performed in a one-dimensional geometry. We find a remarkable agreement between the LDA density profiles and the Monte Carlo solution, which confirms that very sharp variations of the local density indeed takes place at the boundary between domains in cases [(ii)–(iv)].

## V. CONCLUSION

In this paper, we have studied the phase diagram of mixtures of fermionic atoms with different masses in a cubic optical lattice in the case in which the interaction is attractive. For small values of the unbalance, the system remains in a homogeneous superfluid phase, exactly as in the case of equal masses. When the anisotropy exceeds a given critical value, which depends on the density of fermions, the system is a pure superfluid only in weak coupling, and increasing the coupling determines a phase separation between a superfluid state and a commensurate charge density wave, in which an alternated pattern of atoms is observed. Once the harmonic trap potential is taken into account, the phase separation is actually realized in different regions of the trap (for example, the superfluid can be present in the central region, while the density wave is confined to the outer part of the trap), with rapid variations of the local density at the phase boundaries. We note finally that, in the case of the $^6\mathrm{Li}/^{40}\mathrm{K}$ mixture, a simple estimate shows that the mass imbalance $z$ can be varied over a large range by changing the lattice depth $V_0/E_R$ ($z\ll 1$ at small $V_0/E_R$ and $z\simeq 0.9$ for $V_0/E_R\simeq 15$), so that the effects discussed in this work can indeed be actually observable in these systems.

## ACKNOWLEDGMENTS

We are grateful to I. Carusotto, F. Chevy, P. S. Cornaglia, T. Giamarchi, D. Rohe, C. Salomon, and F. Schreck for useful discussions. Support was provided by the ANR under "GASCOR," and by CNRS, Ecole Polytechnique and MIUR-PRIN under Project No. 200522492.

[1] D. Jaksch and P. Zoller, Ann. Phys. **315**, 52 (2005); W. Zwerger, J. Opt. B: Quantum Semiclassical Opt. **5**, 9 (2003); I. Bloch, Nat. Phys. **1**, 24 (2005); A. Georges, arXiv:cond-mat/0702122 (unpublished).

[2] M. A. Cazalilla, A. F. Ho, and T. Giamarchi, Phys. Rev. Lett. **95**, 226402 (2005).

[3] W. V. Liu and F. Wilczek, Phys. Rev. Lett. **90**, 047002 (2003); M. Iskin and C. A. R. Sa de Melo, *ibid.* **97**, 100404 (2006).

[4] F. Werner, O. Parcollet, A. Georges, and S. R. Hassan, Phys. Rev. Lett. **95**, 056401 (2005).

[5] L.-M. Duan, Phys. Rev. Lett. **95**, 243202 (2005).

[6] Innsbruck group (private communication).

[7] C. A. Stan, M. W. Zwierlein, C. H. Schunck, S. M. F. Raupach, and W. Ketterle, Phys. Rev. Lett. **93**, 143001 (2004).

[8] A. Georges, G. Kotliar, W. Krauth, and M. J. Rozenberg, Rev. Mod. Phys. **68**, 13 (1996).

[9] M. Keller, W. Metzner, and U. Schollwöck, Phys. Rev. Lett. **86**, 4612 (2001); M. Capone, C. Castellani, and M. Grilli, *ibid.* **88**, 126403 (2002); B. Kyung, A. Georges, and A.-M. S. Tremblay, Phys. Rev. B **74**, 024501 (2006).

[10] A. Toschi, P. Barone, M. Capone, and C. Castellani, New J. Phys. **7**, 7 (2005); A. Toschi, M. Capone, and C. Castellani, Phys. Rev. B **72**, 235118 (2005).

[11] R. T. Scalettar, G. G. Batrouni, A. P. Kampf, and G. T. Zimanyi, Phys. Rev. B **51**, 8467 (1995).

[12] J. K. Freericks and V. Zlatic, Rev. Mod. Phys. **75**, 1333 (2003).

[13] G.-D. Lin, W. Yi, and L.-M. Duan, Phys. Rev. A **74**, 031604(R) (2006).

[14] The DMFT equations were solved using exact diagonalization (Ref. 8), with eight energy levels in the effective bath.

# Chapter 5

# Density-imbalanced mixtures in optical lattices

*In this chapter, we consider a two-component fermionic mixture confined in a three dimensional optical lattice. The mixtures interact via an on-site attractive coupling and have the same mass but different densities. Using both static and dynamical mean-field theory, we establish the phase diagram as a function of temperature and density imbalance for weak- and intermediate-coupling strengths. We focus mainly on the stability of the polarized superfluid phase, a uniform phase where both superfluidity and a finite polarization coexist. We show that at weak coupling both techniques yield very similar results and that at low temperatures, the polarized superfluid phase is unstable against a phase separation between a superfluid and a polarized normal fluid formed by the excess fermions of the majority species. Instead, the intermediate-coupling regime is not addressed properly by static mean-field theory and our analysis shows that in that case, contrary to its predictions, the polarized superfluid phase can be stabilized down to extremely low temperatures. We trace back the stabilization of the phase to the reduced polarizability of the underlying normal phase due to the formation of preformed local pairs.*

## 5.1 Introduction

Mixtures of two-component atoms with different densities have attracted a lot of interest. Indeed, a fundamental challenge for both theorists and experimentalists is to clarify the phase diagram when a difference in the densities is introduced. Until now, there is no clear answer to this problem. However, progresses in experiments on ultracold atoms offer new clues. Recently, the Rice and the MIT group have observed superfluidity in spin imbalanced mixtures, in the strongly-correlated regime. Although the physics of such mixtures has intensively been addressed by static mean-field and variational studies for the gases in continuum ( see Ref. [79, 93, 104, 109]), much less studies treating correctly the correlation in the strong coupling regime has been done on the lattice.

### 5.1.1 Experiments on polarized Fermi gases

The possibility to tune experimental parameters in ultracold atomic system allows to enter regimes that are forbidden in other solid state physics systems. The spin-polarized mixture with two hyperfine states in Lithium 6 was used in the experiments of both the MIT and the Rice group. In the following, we briefly describe the setups of these experiments and their main results.

#### Experiment in the MIT group

The observation of superfluidity in the MIT group has been realized via the imaging of the vortices present in a rotating gas [107, 126, 127]. The degenerate gases were initially prepared

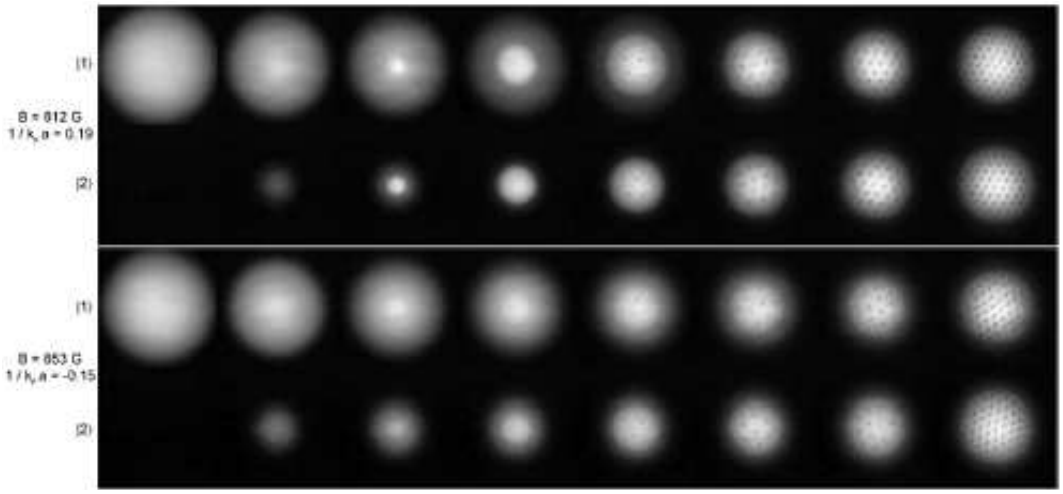


**Figure 5.1:** Superfluidity in a strongly-interacting Fermi gas with imbalanced populations. The upper (lower) pair of rows shows clouds prepared at 812 G (853 G), where $1/k_F a = 0.2$ ($1/k_F a = -0.15$). In each pair of rows, the upper picture shows state $|1\rangle$, the lower one state $|2\rangle$. For the 812 G data, from left to right the value of $p$ was consequently 100%, 90%, 80%, 62%, 28%, 18%, 10% and 0%. For the 853 G data, the mismatch was 100%, 74%, 58%, 48%, 32%, 16%, 7% and 0%. Reprinted from Ref. [126].

by using the usual methods of cooling, such as the laser cooling, the sympathetic cooling by sodium atoms and optical trapping. A radio-frequency sweep created a variable spin mixture with two lowest spin states $|1\rangle$, $|2\rangle$. The interaction between atoms in these internal states

is controlled by a 300G-wide Feshbach resonance located at $B_0 = 834G$. In this continuum limit, the interaction strength is described by the parameter $1/a_s k_F$, where $a_s$ is the s-wave scattering length and $k_F$ is the Fermi momentum for the non-interacting system. In order to observe the presence of superfluidity in the mixture around the Feshbach resonance (in both BEC and BCS sides), the optical trap is rotated symmetrically around the cloud. In this experiment, it is possible to control both the interaction and the spin imbalance. To image the fermion pair condensate, the optical trap is released and binding energy of the pairs is increased by switching the magnetic field deep in the BEC side (far from the resonance). The TOF image shows the presence of vortices which is the proof of the superfluidity.

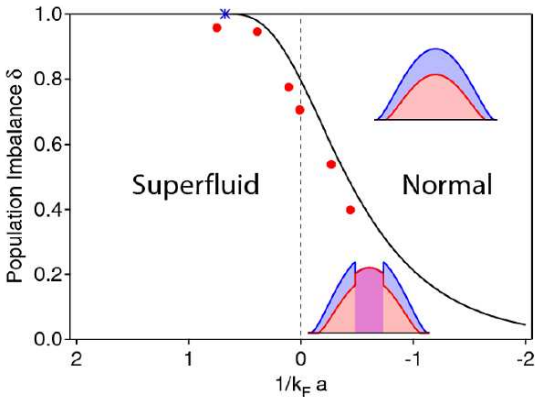


**Figure 5.2:** Observation of the superfluid-to-normal phase transition in the experiment of the MIT group. The profiles indicate the distribution of the gas in the harmonic trap. Reprinted from [125].

The experimental results are presented in Fig. 5.1. Two series of images of the rotating mixtures were taken in presence of a magnetic field $B = 812G$ ($1/k_F a = 0.2$ BEC-side) and $B = 853G$ ($1/k_F a = -0.15$ BCS-side). The population imbalance is defined by $p = (N2 - N1)/(N1 + N2)$, where $N1$ is the number of atoms in state $|1\rangle$ and $N2$ the number of atoms in state $|2\rangle$. For different $p$, the total number of atoms varied only within 20% around $N = 7 \times 10^6$, with the exception of the fully polarized cases $p = 100\%$ ($N = 1 \times 10^7$) and $p = 0\%$ ($N = 1.2 \times 10^7$). The evidence of the superfluidity can be observed by the the emergence of vortices in the polarized gas both in the BEC side and BCS side when the polarization $p$ is greater than some critical value $p_c$. We observe that this value is of the order $p_c \sim 80\%$ for $1/k_F a = 0.2$ and $p_c \sim 48\%$ for $1/k_F a = -0.15$. However, near the phase boundary, it is quite difficult to create and observe the vortices. In order to obtain the phase diagram shown in Fig. 5.2, the pair condensation was used as an indicator for superfluidity.

### Experiment in the Rice group

At the same time, another evidence of the normal-superfluid transition was realized in the group of Rice University. Using the same mixture of two hyperfine states of Lithium atoms ($F = 1/2, m_F = \pm 1/2$), the spin imbalance is controlled by adjusting the radio-frequency. The mixture has approximately $N \sim 10^5$ atoms per spin state. The temperature must be inferior to $0.1T_F$. The BEC-BCS crossover is realized by tuning the interaction strength via a Feshbach resonance. The real-space distribution of atoms in the trap are obtained by in-situ absorbing imaging where each spin state is sequentially and independently imaged. The resulting column density distribution are fit to model distributions in order to obtain estimates for $N_1$, $N_2$ as well as the temperature $T$.

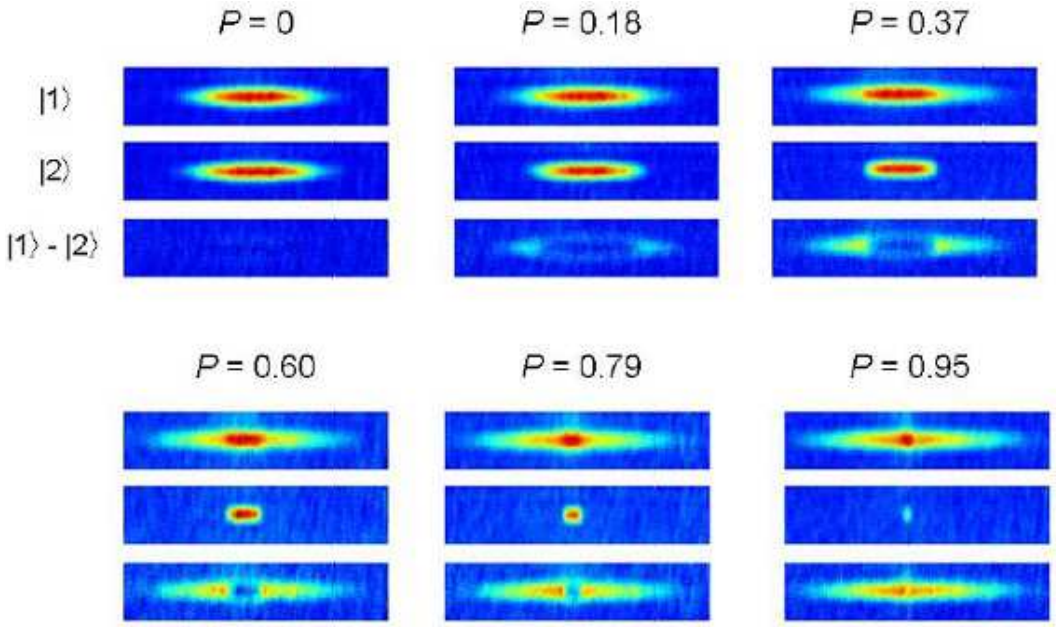


**Figure 5.3:** Experiment of the Rice group on the evidence of superfluidity in the polarized gas. Absorption images of trapped atoms were taken selectively for atoms in different hyperfine states. The field of view for these images is 1654$\mu$m by 81$\mu$m. Reprinted from [77]

The Fig. 5.3 shows the experimental images of the density distributions for the atoms in the trap. The difference of density distributions between atoms in state $|1\rangle$ and atoms in state $|2\rangle$ shows that paring of an equal number of atoms occurs in the center of the trap up to very high polarization.

### 5.1.2 Standard BCS-BEC crossover

Let us first consider simple mixtures without spin imbalance. At low temperature, they exhibit superfluidity which has the form of a BCS state at weak coupling or of a BEC state at strong coupling. The physics of the crossover between these two limits is a fascinating topic which has attracted a lot of interest. Here, we will discuss some important results about this BCS-BEC crossover.

For the problem in the continuum, this crossover is quite well understood both in experiments on ultracold Fermi gases (see Refs. [14, 61, 82, 128]) and theoretically by both analytical approaches and Monte Carlo simulations (see Refs. [13, 18, 55, 76, 85, 91]). In the analytical approaches, two main directions have been followed. The first approach consists in using a one-channel model [76, 85, 91] with a contact potential defined by a bare coupling constant $g$. The divergence of the energy at first order in perturbation is eliminated by absorbing the divergent term into the definition of the s-wave scattering length $a_s$

$$\frac{m}{4\pi a_s} = \frac{1}{g} + \sum_k \frac{1}{2\varepsilon_k}. \tag{5.1}$$

Therefore, the only control parameter in this theory is the scattering length $a_s$. The sign of the scattering length is changed from negative to positive whenever one crosses the unitary limit from the BCS to the BEC side. The second theoretical approach is based on a two-channel

model [55] in which the open channel describes the fermion gas while the closed channel describes the formation of the bound state. This model is described by the Hamiltonian

$$H = \sum_{\mathbf{k},\sigma}(\varepsilon_{\mathbf{k}\sigma} - \mu_\sigma)a^\dagger_{\mathbf{k}\sigma}a_{\mathbf{k}\sigma} + \sum_{\mathbf{q}}(\frac{\varepsilon_{\mathbf{q}}}{2} + \delta_0 - 2\mu)b^\dagger_{\mathbf{q}}b_{\mathbf{q}} + g\sum_{\mathbf{k},\mathbf{q}}(b^\dagger_{\mathbf{q}}a_{\mathbf{k}+\frac{\mathbf{q}}{2}\downarrow}a_{-\mathbf{k}+\frac{\mathbf{q}}{2}\uparrow} + \text{h.c}). \quad (5.2)$$

The s-wave scattering length can be related to the detuning of the bound state to the energy level of two free fermions. The sign of the scattering length depends on the sign of the detuning. In fact, both approaches give a qualitative picture of the BEC-BCS crossover which is comparable to numerical simulation [13]. As the main physical properties of this crossover is very similar to the one occurring in the lattice model. Therefore, we will concentrate more on the explanation of this phenomenal for the lattice model.

Let us now switch to the situation where the atoms are confined in an optical lattice. Also in this case, there is a BCS-BEC crossover as a function of the interaction strength, which can be described in a Hubbard model with an on-site attractive coupling (see Refs. [65, 119, 120]). In the weak-coupling regime the superfluidity is due to the instability of the Fermi surface towards the the formation of BCS-pairs, while in the strong-coupling regime, the system prefers to form local bosonic pairs which condense at low temperature. These two regimes can be addressed using static mean-field theory both in the weak- and the strong-coupling limit (see Fig. 5.4). In the weak-coupling limit, as predicted by the MFT analysis of the

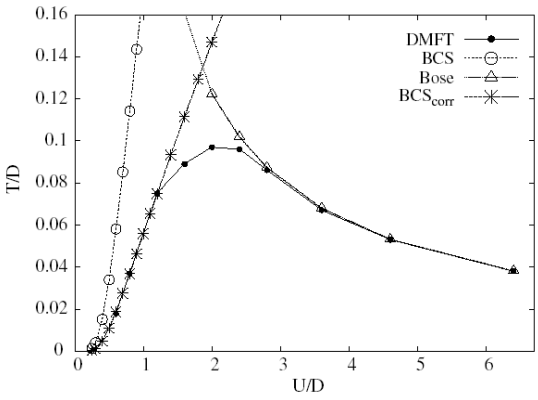


**Figure 5.4:** Critical temperature as a function of $|U|$ at $n = 0.75$: the DMFT data (dot) are compared with the BCS both the bare (circle) and the rescaled one (asterisk)and the BE mean-field predictions (triangle) for a hard-core boson system. Reprinted from Ref. [119]

superfluid phase, the critical temperature is proportional to the gap opened at Fermi surface $T_c \propto \Delta_{\text{BCS}} \propto e^{-W/|U|}$ (red curve). The strong-coupling regime with $|U| \gg W$ is characterized by the formation of local bosons and can be described by effective bosonic model in which the tunneling is proportional to $t^2/|U|$. The critical temperature for the condensation is of the same order as this hopping (blue curve). The intermediate-coupling regime cannot be described by these static MFT. We therefore need to go beyond the MFT to explain the crossover from the BCS (with Cooper pairs of long healing length) to the BEC (with local bosonic pairs of short healing length). In the next sections, we will demonstrate that by taking local fluctuations into account, it is possible to connect these two limits (black curve in Fig. 5.4). At high temperatures, the fermions which are uncorrelated at weak coupling start to couple as the interaction is increased. They produce a pseudogapped normal state characterized by preformed pairs (using the particle-hole transformation, this corresponds to

a Mott insulator in the repulsive Hubbard model). As a function of the interaction strength there is therefore a transition between a Fermi liquid and a pseudogapped normal phase. When we cool down the system, in the weak-coupling regime, there is a phase transition from the normal Fermi liquid to the BCS phase. Instead, in the strong-coupling regime, the transition is from the phase with preformed pairs to the BEC condensate.

### 5.1.3 Mixture with spin imbalance, novel physics?

When a spin imbalance is introduced in the system, the question of the nature of the ground state in the mixture is a very non-trivial issue. Indeed, in spin imbalanced mixtures, either superfluidity disappears in favor of a polarized normal fluid or more exotic forms of pairing might occur. One candidate that has been proposed is the Fulde-Ferrell-Larkin-Ovchinnikov state (FFLO) [41, 74] in which Cooper pairs appear at a non-zero total momentum. Another possible kind of pairing is the polarized superfluid namely Sarma phase (or breached-pair phase at zero temperature) [79, 100], which is a non-BCS polarized superfluid state with gapless fermionic excitations.

The FFLO phase has first been studied in [41, 74] and is described as a phase with a superfluid order parameter varying in real space. The formation of Cooper pairs produces a gain in condensation energy but it is difficult to enter a polarized phase with these pairs. A solution, which maintains the superfluidity and allows for a polarization, is to have a superfluid order parameter varying in space. In the node of this variation $\Delta(r) = 0$, there are no Cooper pairs and a polarization can occur. More detailed studies on the critical behaviors of the FFLO phase were presented in the works done by C. Mora and R. Combescot [25, 106].

At zero temperature, two other possible phases that exhibit both a non-zero superfluid order parameter and a finite polarization have been proposed: the Sarma (or breached-pair BP2) phase [79, 100] and the BP1 phase [93, 104, 109]. At weak-coupling, the Sarma phase is unstable unless specific types of interactions are considered [39]. The BP1 has been proposed as a stable ground state deep in the BEC regime of trapped fermionic gases, where the system is described by a Bose-Fermi mixture. While both of these phases are polarized superfluids with gapless excitations, their nature is different: the Sarma phase has two Fermi surfaces while the BP1 phase has a single Fermi surface for the unpaired fermions. These non-standard phases are in general unstable at weak coupling, resulting in phase separation between an unpolarized superfluid and a polarized normal fluid formed by the excess fermions, an effect which has been observed experimentally [92, 126, 127]. At zero temperature $T = 0$, the Sarma and BP1 phases are signaled by a non-zero superfluid order parameter together with a finite polarization. When $T > 0$, this criterion is no longer valid because a standard BCS or BEC state also acquires a small polarization coming from thermally excited quasiparticles.

Finally, a possibility to see both superfluidity and a finite polarization is to have a phase separation between a superfluid state and a polarized normal liquid. As we will see, at weak coupling at low temperature, this phase has been shown to be the most stable in energy within a static MFT of the Hubbard model. However, when we enter into the strong-coupling regime, the picture described by the BCS-MFT is no longer valid and we expect that the phase separation competes with other phases described above.

### 5.1.4 Polarized mixture in the continuum

The phase diagram for the spin-imbalanced system has been studied intensively in the continuum after the great debate on the interpretation of the experimental results obtained by the Rice and the MIT groups. Until now, there is no final conclusion on the phase diagram as a function of all the experimental parameters: temperature, polarization and interaction

strength. At zero temperature, the most convincing results have been discussed in an analytical approach by Daniel E. Sheehy et al. for the two-channel model (Ref. [104]) and in a numerical approach by the Trento group for the one-channel model (Ref. [93]). Both works show very similar phase diagrams.

Let us first discuss the analytical results obtained in the two-channel model. The control parameter is the detuning $\delta_0$ which can be related to the s-wave scattering length $a_s$. The phase diagram is shown in Fig. 5.5). It is constituted by the competition of the following

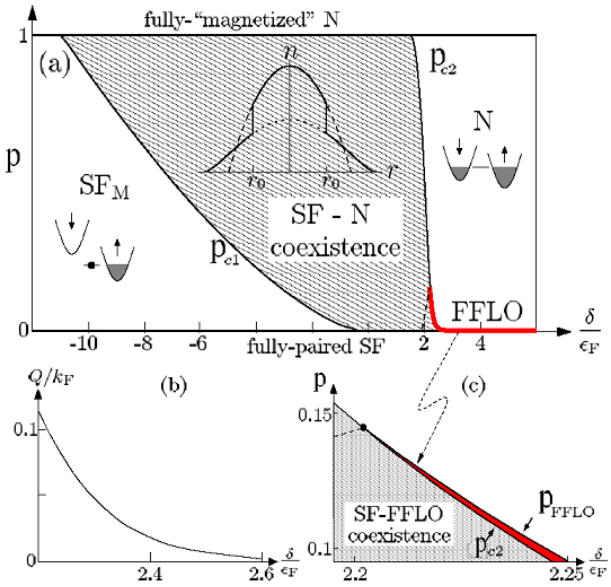


**Figure 5.5:** Detuning, $\delta$-population difference, $p = (n_\uparrow - n_\downarrow)/(n_\uparrow + n_\downarrow)$ phase diagram (for coupling $\gamma$=0.1) in (a) displaying "normal" (N), magnetized superfluid ($SF_M$), FFLO (thick red line) and SF-N coexistence states, (b) showing the FFLO wave-vector $Q(\delta)$ along the FFLO-N phase boundary, and (c) zoom-in on the FFLO state, stable only for $\delta > \delta^* \simeq 2.2E_F$.

phases: (i) the normal state (the phase without any long-range ordering); (ii) an unpolarized superfluid (the BCS superfluid or BEC condensate of molecules); (iii) a phase separation (PS) between the normal state and the unpolarized SF; (iv) the FFLO state (with pairing at non-zero momentum); (v) a polarized superfluid (pSF). The phase diagram is as follows. In the negative weak-coupling limit (the BCS limit), the phase competition can be understood by the BCS theory. The four phases in competition are the normal phase, the BCS, the FFLO and the PS. At $p = 0$ and zero temperature, we obtain a BCS superfluid. When the polarization is close to 0 ($p < p_{c1}$) the stable phase is the phase separation. For $p_{c1} < p < p_{c12}$, the FFLO phase is the most stable phase (see Ref. [86]). Finally, when the polarization is high, a normal fluid is stabilized. In the opposite limit, deep in the BEC side, the phase diagram is characterized by the competition of three phases: the BEC superfluid, the polarized superfluid and the phase separation. When we are in molecular regime, the phase transition is smooth from the BEC to the polarized superfluid and then to the fully polarized normal state. By contrast, close to the unitary limit, this phase transition changes and is first-order between the polarized superfluid and the normal state. The first-order transition induces a phase separation when the total atom number and the polarization are fixed.

The numerical results for the one-channel model were obtained using a fixed node Monte Carlo. They are shown in Fig. 5.6. The phase diagram at zero temperature is qualitatively

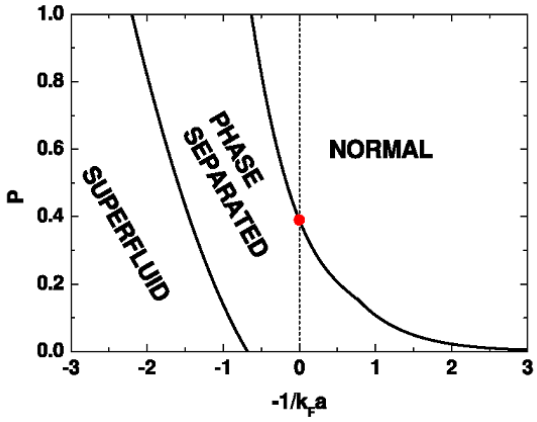


**Figure 5.6:** Qualitative phase diagram as a function of the interaction strength -1/kF a and of the polarization P. The circle at unitarity corresponds to the critical value Pc = 0.39 discussed in Sec. IXB. The Fermi wave vector corresponds here to the total average density: $k_F = [3\pi^2(n_\uparrow + n_\downarrow)]1/3$. Notice that the possible occurrence of the FFLO phase is not considered on this diagram.

comparable to the analytical result discussed above. However, the QMC simulation displays a normal phase which is much more larger than in the analytical model. In the unitary limit ($1/a_s k_F = 0$ or $\delta = 0$), the normal phase in QMC is obtained for $p > p_c = 0.4$ while in the two-channel model, the phase separation is stable up to full polarization $p = 1$. This is also the main point in the debate between the two experiments described in the first section. In our view, the mean-field theory approach in the two-channel model is not able to fully take into account the strong correlation effects in the Fermi gas. In fact, the Fermi gas in this model is described as a free Fermi gas where the superfluid order parameter is zero. Therefore, all the effects of strong interactions, which could make the normal state energetically more stable, are neglected. Indeed as we shall see, the effect of preformed pairs can make the energy of the normal state become favorable in a larger domain. Instead, the fixed-node QMC approach can include the strong correlation effects in the normal state and, as a consequence, the normal state solution appears earlier.

## 5.2 Polarized mixture in an optical lattice

In this chapter, we want to focus on mixtures that are confined in an three-dimensional optical lattice and we will address the stability of the polarized superfluid phase at weak and intermediate coupling. Note that we will not consider the FFLO phase in the following. Our goal is to study the competition between the polarized normal fluid, the unpolarized superfluid and the polarized superfluid by treating the effect of correlations beyond static mean-field theory. For intermediate coupling, we show that the pSF phase can be stabilized down to very low temperatures due to the reduction of the polarizability of the normal fluid. The pSF phase turns out to be profoundly different from the unpolarized BEC superfluid which holds at the same coupling strength in the absence of imbalance. Indeed, the unpolarized BEC phase is stabilized by a kinetic energy gain in comparison to the normal fluid, while the pSF phase has a higher kinetic energy with respect to the normal state, and is stabilized by a potential energy gain, as in BCS.

We start with some energetic considerations, which clarify the general conditions under which a pSF phase can be stable at $T = 0$. In order to control the imbalance between

the populations of the two species, we introduce a chemical potential difference (or effective 'magnetic field') $h \equiv (\mu_\uparrow - \mu_\downarrow)/2$ between them. In Fig. 5.7, we show two typical behaviors of the energy in different phases as a function of the magnetic field. In both cases, a small

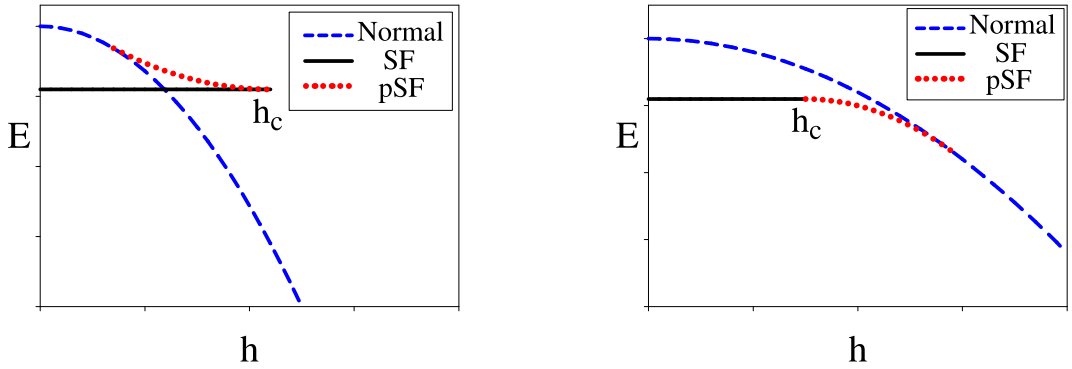


**Figure 5.7:** (Color online) Sketches of the energy $E$ vs $h$, for the normal state, the unpolarized superfluid (SF) and the pSF phase. Two situations can appear as function of the external parameters (*e.g.* the interaction strength). Left panel (a): the pSF branch is unstable and the system undergoes a phase separation. Right panel (b): the pSF branch is stable.

magnetic field $h$ is expelled from the unpolarized superfluid, and the energy is independent of $h$. This unpolarized superfluid is locally stable up to a critical value $h_c$. For $h > h_c$ the magnetic field breaks the pairs, leading to the disappearance of this solution. On the other hand, the energy of the polarized normal state is a decreasing function of $h$: its derivative $p \equiv -\partial E/\partial h > 0$ is the polarization (population imbalance) and its curvature $\chi \equiv -\partial^2 E/\partial h^2 = \partial p/\partial h$ defines the polarizability of the normal fluid.

In general the pSF phase can bridge between these two solutions. The way in which this connection occurs depends on the two key parameters $h_c$ and $\chi$. When $h_c$ and $\chi$ are large, we anticipate the situation in Fig. 5.7a. In this case, the pSF branch is expected not to be stable, and the system undergoes a first-order transition as a function of $h$ which results in a phase separation if we try to prepare the system with a polarization corresponding to the unstable branch. In contrast, if $h_c$ and $\chi$ are small enough, the energies of the unpolarized superfluid and polarized normal solutions do not cross, and the pSF phase can be stable in a region bridging these two states, as shown in Fig. 5.7b. Therefore, a stable pSF phase is likely to form when $\chi$ or $h_c$ are small. Interestingly, this suggests that an increasing attractive coupling may help stabilizing the pSF phase. Indeed, in the BEC regime, the normal state presents preformed pairs in a singlet state that strongly reduce $\chi$, hence stabilizing a pSF phase.

## 5.3 Model and methods

Here, we present the analytical and numerical techniques that we use in order to establish the phase diagram as a function of temperature and density imbalance.

### 5.3.1 Model for mixtures in an optical lattice

Let us first describe the model for fermionic mixtures in an optical lattice under the conditions discussed in Refs. [31, 58, 121]. In this work, we consider the half-filled, three-dimensional

attractive Hubbard model in order to describe unbalanced fermionic fluids in an optical lattice

$$H = -t \sum_{\langle i,j \rangle} c^{\dagger}_{i\sigma} c_{j\sigma} - U \sum_{i} n_{i\uparrow} n_{i\downarrow} - \mu \sum_{i} (n_{i\uparrow} + n_{i\downarrow}) - h \sum_{i} (n_{i\uparrow} - n_{i\downarrow}).$$

The (pseudo-) spin index $\sigma$ refers to the two different species. In experiments, Feshbach resonances between two hyperfine states of $^6$Li or $^{40}$ K are very well controlled and allow to change the interaction strength. Here, the coupling is controlled by the local attraction $U$. The hopping amplitude $t$ gives rise to a band of width $W = 12t$. We fix the chemical potential $\mu$ in order to set the right number of fermions. Finally, $h$ is a magnetic field that controls the polarization of the fluid, i.e., the unbalance between the two fermionic species. In the following, all energies will be expressed in units of the half-bandwidth $D = 6t = 1$. The relation between the model parameters and the properties of the optical lattice has been discussed in Chapter 1.

### 5.3.2 Dynamical mean-field theory

In order to address all interaction regimes we use the dynamical mean-field theory (DMFT) This method is able to give a good description of the BCS-BEC crossover when both species have the same density. It means that the off-diagonal order contains not only the BCS channel which is relevant for weak-coupling but also the condensation of bosons formed by local fermion pairs in the strong-coupling limit.

The main idea of DMFT has been presented in Section 3.5 for the Bethe lattice within the cavity method. In this chapter, we use the set of DMFT self-consistency equations established for a three-dimensional lattice (see Appendix B.1 for a more detailed discussion). Within this framework, we can obtain the local Green's function in a matrix form and the off-diagonal elements correspond to the particle-particle channel. The average value of physical observables can be obtained from the Green's function.

Our goal is to study the energetic competition between different phases in the context of a lattice model. Our strategy is to compute the energy of the system in these different phases and to study its evolution when the external magnetic field is increased. The internal energy per site can be computed by

$$\langle H \rangle = \langle K \rangle + U \langle n_{\uparrow} n_{\downarrow} \rangle. \tag{5.3}$$

Here, the kinetic energy and the interaction term are obtained using Eq. 26.10 and Eq. 26.11 in Ref. [62]

$$\langle K \rangle = - \sum_{\langle i,j \rangle, \sigma} t_{\sigma} \langle c^{+}_{i} c_{j} \rangle = \beta^{-1} \sum_{k,\sigma,n} \varepsilon_{k\sigma} G_{\sigma}(i\omega_n, k) \tag{5.4}$$

$$\langle H_{int} \rangle = U \langle n_{\uparrow} n_{\downarrow} \rangle = \sum_{n} \mathrm{Tr}[\mathbf{\Sigma}(\mathbf{i\omega_n}) \mathbf{G}(i\omega_n)]. \tag{5.5}$$

### 5.3.3 BCS-Stoner mean-field theory

We will also treat the weak-coupling regime using the static mean-field theory described in Chapter 3. We will suppose that $h > 0$ and use the density of states $D(\varepsilon) = (2\pi)^{-d} \int d^d\mathbf{k}\, \delta(\varepsilon_{\mathbf{k}} - \varepsilon)$. For a mixture of atoms with equal mass and density imbalance, the self-consistency equa-

tions read

$$p = \int [f(E^+) - f(E^-)] D(\varepsilon) d\varepsilon \tag{5.6}$$

$$\delta = -\int \frac{(\varepsilon - \tilde{\mu})[1 - f(E^+) - f(E^-)]}{\sqrt{(\varepsilon - \tilde{\mu})^2 + \Delta^2}} D(\varepsilon) d\varepsilon \tag{5.7}$$

$$\frac{2\Delta}{|U|} = \int \frac{\Delta[1 - f(E^+) - f(E^-)]}{\sqrt{(\varepsilon - \tilde{\mu})^2 + \Delta^2}} D(\varepsilon) d\varepsilon, \tag{5.8}$$

where $E^{\pm} = \mp(h - |U|p/4) + \sqrt{(\varepsilon - \tilde{\mu})^2 + \Delta^2}$ and $f(E) = 1/(1 + e^{-\beta E})$ is the Fermi-Dirac distribution. In these self-consistency equations, all the variables $\Delta, p, \delta$ are treated self-consistently. As we will see, this is quite different from the standard BCS mean-field analysis which treats only one variational parameter $\Delta$.

### 5.3.4 Mean-field theory for the strong-coupling regime

We can also address the strong-coupling limit in this half-filled model using a static mean-field theory. The strong-coupling regime, $|U| \gg W$, is situated on the BEC side. In this limit, for a system without polarization, we can obtain an effective model of free bosons (see Chapter 3). In order to gain the kinetic energy, the composite bosons condense around the zero-momentum state and form a BEC of molecules. When a small polarization is introduced, we can modify this model into an effective model of fermions and hard-core bosons. At low polarization (small density of fermions), the hare-core bosons can move easily in the lattice with an effective hopping $t_b = 4t^2/|U|$. We obtain a two-fluid model: the fluid of extra fermions and the fluid of hard-core bosons. At low temperature, the bosons can condense to form a superfluid while the extra fermions form a normal fluid. These two fluids stabilize a homogeneous polarized superfluid. As the polarization increases, the density of fermions in this mixture increases while that of the bosons decreases. When one reaches the limit $p \simeq 1$, the density of the up-atoms is almost 1 and the density of the down-atoms is very small. In this case, the up-atoms will be distributed over every site of the lattice. The description by effective bosons is still valid, however, it becomes very difficult for a boson to hop in this lattice and the gain in kinetic energy of the condensate is very small. Because of the Pauli principle, the atoms will be distributed regularly over the lattice except for some unfilled sites. Therefore, the density fluctuations for both up- and down- particles is small. If the interaction energy satisfies $|U|\langle n_\uparrow\rangle\langle n_\downarrow\rangle = |U|(1+p)(1-p)/4 \ll W$, we can treat the interaction by MFT.

## 5.4 Weak-coupling regime

We start our study in the weak-coupling regime using the BCS-Stoner mean-field theory. In order to fix the density of both species, we consider a grand-canonical ensemble where the number of atoms for each species is controlled by the external chemical potentials $\mu_\sigma$. Using the Legendre transform, we can go back to the mixture with fixed number of particles and its total energy. We also solve the problem using the standard BCS mean-field which is used in many other works (Ref. [31, 70, 100]). We then compare these results to those obtained by the improved BCS-Stoner MFT [69, 86]), which takes the Fermi liquid effects into account.

### 5.4.1 Phase diagram in temperature and polarization

The $(T, p)$-phase diagram at weak coupling is shown in Fig. 5.8 for the BCS-Stoner and the standard BCS approaches. In both approaches, we find the same generic phase diagram with

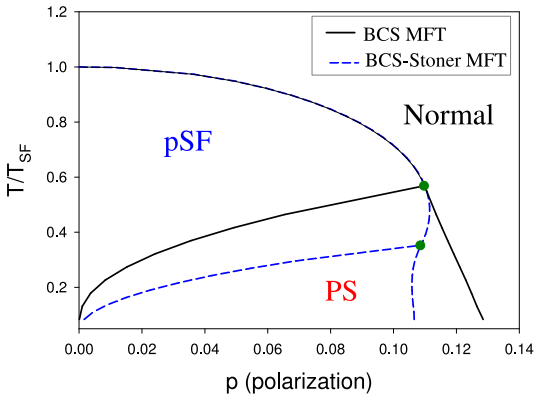


**Figure 5.8:** Comparison of the phase diagrams obtained by the standard BCS and the BCS-Stoner approaches for the weak-coupling regime $|U| = 0.5D$. The polarized-superfluid phase is shown to be more stable within the BCS-Stoner MFT. This is because the polarizability is calculated more accurately in the improved mean-field theory.

---

three competing phases: the normal phase, the polarized superfluid phase (Sarma phase) and the phase separation between an unpolarized superfluid and the normal fluid. The normal phase is more favorable at high temperatures and strong polarization, while a polarized superfluid phase can be stabilized in a region of low polarization for temperatures $T < T_{SF}$. At lower temperatures, a phase separation configuration is shown to be the most stable state. In this phase diagram, we do not discuss the stability of the FFLO phase. The main difference between the results obtained by the two static mean-field methods is that the pSF phase is more stable in the BCS-Stoner approach. For $U = 0.5D$, the tricritical temperature obtained by the BCS-Stoner MFT is almost half that predicted by the standard BCS theory.

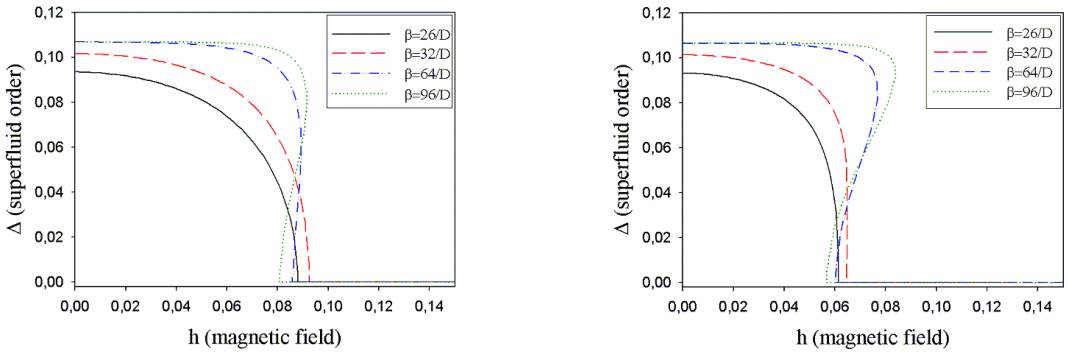


**Figure 5.9:** Relation between the superfluid order parameter and the magnetic field $h$ for a weak interaction $|U| = 0.5D$. The left panel shows the SF order parameter $\Delta_{SF}(h)$ obtained by the BCS-Stoner mean-field theory. The right panel shows $\Delta_{SF}(h)$ obtained by the standard BCS mean-field theory. The region where one can find a coexistence of solution is reduced in the BCS-Stoner approach.

Next, we compare the superfluid order parameter $\Delta(h)$ and the polarization $p(h)$ obtained as a function of the external magnetic field $h$. In Figs. 5.9 and 5.10, we see that both calculations give a similar picture for the weak-coupling regime: (i) the superfluid order

parameter (which is the same as the gap in the excitation spectrum[1]) $\Delta_0$ for an unpolarized mixture at $T = 0$ is the same. In addition, the critical polarization $p_c$ at which the normal phase becomes unstable towards the superfluid phase is again the same $p_c$; (ii) Above a critical temperature $T^c$, the phase transition from the SF to the normal phase is second-order, while below $T_c$ the phase transition is first-order; (iii) For $T > T_c$ the polarized superfluid is a stable phase. However, the fact that we treat the polarization as a variational parameter in

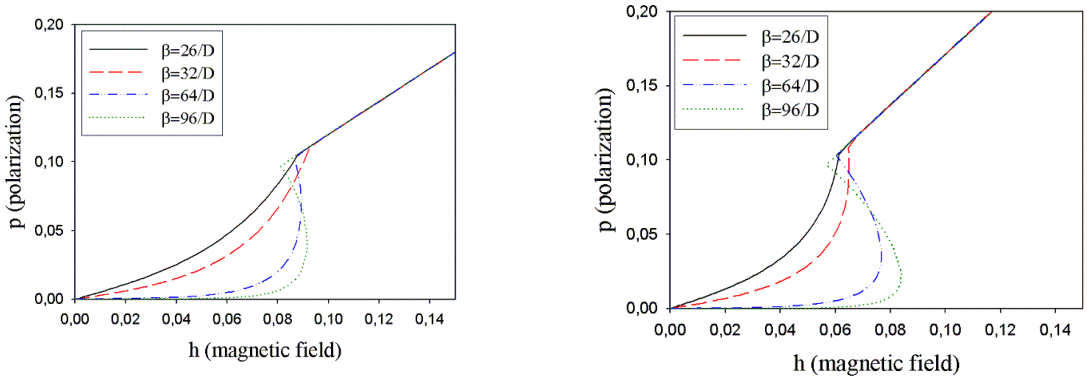


**Figure 5.10:** Relation between the polarization and the magnetic field $p(h)$ for weak interaction $|U| = 0.25W = 0.5D$. The left panel shows the polarization versus the external field within the BCS-Stoner approach. The right panel shows the relation $p(h)$ obtained by standard BCS approach.

the Stoner-BCS gives a renormalization effect to the susceptibility. In including the Hartree correction term, the system becomes more resistant to the external magnetic field. Therefore we obtain two different behaviors in these calculations: (i) when $T > T_c$ we see that $\chi = \partial p/\partial h$ in the Stoner-BCS is smaller than the standard one for both the superfluid and the normal phases. That is also the reason why we have a lower critical temperature $T_c$ in the Stoner-BCS. (ii) Given that $\chi$ is smaller in the improved MFT, the critical magnetic field $h_c$ corresponding to $p_c$ is greater, while the critical value for the stability of the superfluid phase is always $h_0 = \Delta_{bcs} < \Delta_0$. Therefore, the region with coexistence of a normal and a superfluid solutions is reduced.

### 5.4.2 Nature of the polarized-superfluid phases

Let us now discuss the nature of these polarized-superfluid phases. The BCS-Stoner mean-field calculation shows that in the phase-separated region, with $T < T_c$, the free-energy as a function of $h$ has three branches (Fig. 5.11a) as in the scenario of Fig. 5.7a. If $T$ is small, the properties of the three branches are directly linked to their $T = 0$ counterparts. One branch corresponds to the BCS superfluid with thermal excitations. It has a small polarization that comes from thermally excited Bogoliubov quasiparticles in a small momentum-range around the Fermi momentum $k_F$ of the unpolarized state. As a consequence, the density $n(k)$ deviates from the standard BCS distribution around $k_F$ over a range of order $T/v_F$ (see A in Fig. 5.11c). This branch is connected to the unstable thermally excited Sarma phase. In contrast to the BCS state, the Sarma phase has two Fermi surfaces at $T = 0$, which are individually broadened when $T > 0$. This is clearly visible in $n(k)$ (see B in Fig. 5.11d) which displays two humps associated with each Fermi momentum, with a separation set by the polarization instead of the thermal broadening.

[1] This is very particular result of the static MFT. In general, the superfluid order parameter $\langle c_\uparrow c_\downarrow \rangle = \sum_n F(i\omega_n)$ is different from the gap in the excitation spectrum $\Delta_{\rm bcs}$.

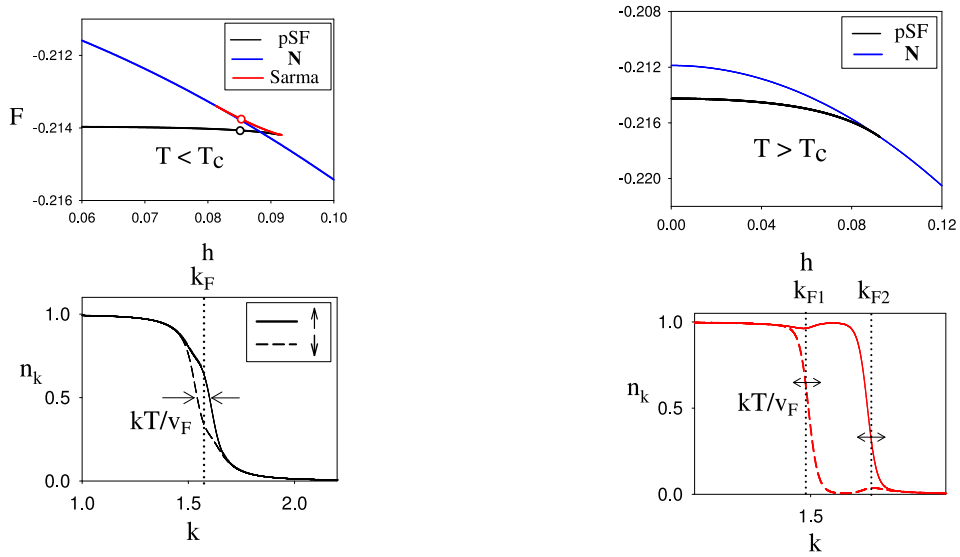


**Figure 5.11:** Upper panels (a-b): free-energy *vs.* $h$ below and above the critical temperature $T_c$. Lower panels (c-d): momentum distribution $n(k)$ at the black and the red point indicated on the free-energy curves of panel (a).

As the temperature $T$ is increased, the unstable branch becomes smaller and eventually disappears at $T = T_c$. For $T > T_c$, the pSF phase is stable and the free-energy has the behavior shown in Fig. 5.11b with only two solutions. Because $T_c$ is rather large, there is no clear distinction between the thermally excited BCS and the Sarma phases: as $h$ is increased along the superfluid branch a crossover takes place between the BCS regime and the Sarma regime. However, because $T$ is large, no particular structure appears in the density $n(k)$, even close to the normal phase. Therefore, at weak coupling, the stable pSF phase has essentially a thermal nature and its properties cannot be linked to the physics of the Sarma phase.

### 5.4.3 Extrapolation of the MFT to intermediate coupling

We now extend our mean-field results to intermediate couplings. Although this extrapolation violates the condition of validity of the mean-field theory, we can expect to see more difference between the two mean-field calculations and extract the major effect of the correlations. The extrapolation of the mean-field calculation to the intermediate coupling limit (see Fig. 5.12) gives us a similar picture as in the weak-coupling limit. However, we note that within the BCS-Stoner approach, the polarized superfluid becomes more robust and the region occupied by the phase separation in the temperature-polarization phase diagram is strongly reduced. Both the critical temperature $T_c$ and the critical polarization $p_c$ in this case are smaller than in the usual MFT result.

The region of the phase separation is characterized by the negative value of the slopes of the $\Delta(h)$ and $p(h)$ curves at low temperature, i.e. $d\Delta/dh < 0$, $dp/dh < 0$ (see Fig. 5.13). In the improved MFT calculation, there is a tendency to reduce the width of the coexistence region when the interaction strength increases. In the limit $|U|/W \to \infty$ the width of this region goes to zero and a vertical jump occurs in both curves $\Delta(h), p(h)$ at the critical value $h_c$ of the unpolarized superfluid to normal state transition.

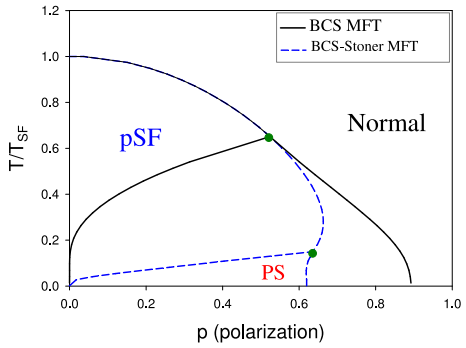


**Figure 5.12:** Comparison of the phase diagrams obtained by the standard BCS and the BCS-Stoner approaches for an intermediate coupling $|U| = 2.5D$. The polarized superfluid is much more stable in the BCS-Stoner MFT. The the tricritical temperature in BCS-Stoner approach is one order of magnitude smaller than in the standard BCS approach.

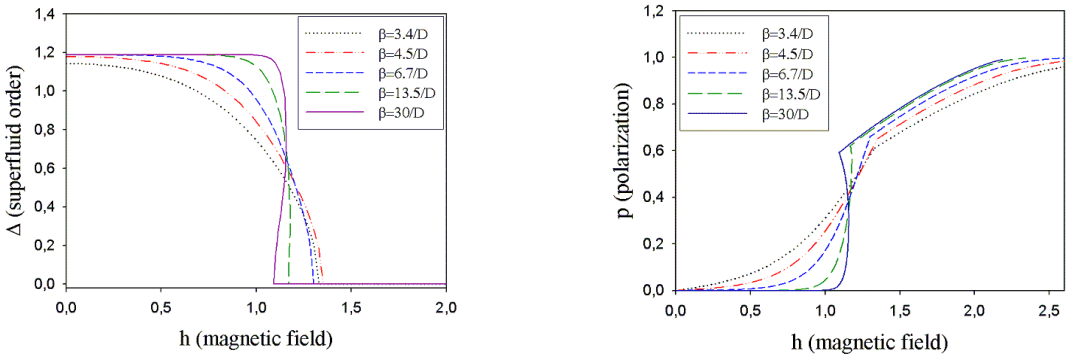


**Figure 5.13:** The superfluid order parameter and the polarization versus the effective magnetic field for an intermediate interaction $|U| = 2.5D$ obtained by the BCS-Stoner mean-field theory. The left panel shows the SF order parameter $\Delta_{SF}(h)$, while the right panel shows $p(h)$. The region where we can find a coexistence of solution is reduced in the BCS-Stoner approach.

## 5.5 Strong-coupling limit and high polarization

We now consider the limit of a very strong coupling and a high polarization. We demonstrate by a simple MFT calculation that the normal phase is the most stable in this limit.

Let us consider first the normal phase at strong polarization (Fig. 5.14, left panel). At strong polarization, we have a very low density of down-atoms $n_\downarrow = (1-p)/2$ which are very mobile. For the up-atoms, the density is close to one particle per site $n_\uparrow = (1+p)/2$ and they are mostly distributed over all the lattice except for some unfilled sites (the up-holes). The up-atom are essentially frozen on the lattice and do not contribute to the kinetic energy except for the up-hole. The density of up-holes is $(1-p)/2$. Given that the up-atoms are distributed over all the lattice, the mean value of the interaction energy is $-|U|\langle n_\uparrow\rangle\langle n_\downarrow\rangle = -|U|(1-p^2)/4$. The total energy of the normal state for a simple square DOS reads

$$E_N = -\frac{W}{8}(1-p^2) - \frac{W}{8}(1-p^2) - \frac{|U|}{4}(1-p^2). \tag{5.9}$$

The superfluid phase is described by a mixture of localized fermion pairs (hare-core bosons)

**Figure 5.14:** Left panel: Normal state with one mobile down-atom and one mobile up-hole. Right panel: Superfluid state with a bound molecule and one mobile up-hole.

with density $(1-p)/2$ and extra up-atoms. In the limit of strong interactions, the formation of bosons yields an energy gain $(1-p)|U|/2$. The hard-core bosons can only hop to the empty sites with a hopping amplitude $4t^2/|U|$. Given that the lattice is almost filled by the up-atoms, it is very difficult for bosons to hop and they are trapped in a bath of up atoms. The gain in condensation energy is now negligible. There are always some up-holes with very low density $(1-p)/2$, and therefore this phase gains kinetic energy through these holes. The total energy of the polarized superfluid phase reads

$$E_{SF} = -\frac{W}{8}(1-p^2) - \frac{|U|}{2}(1-p) \tag{5.10}$$

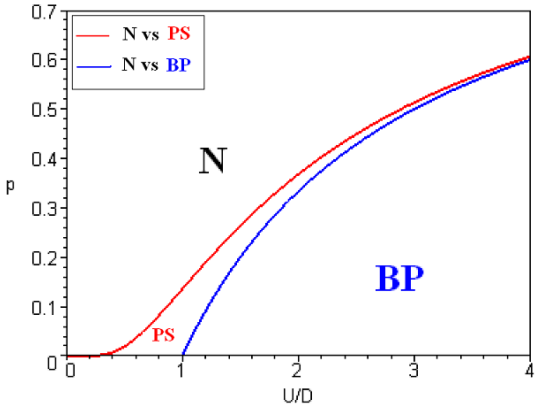


**Figure 5.15:** The phase diagram obtained in static MFT at zero temperature $T = 0$. In the limit of weak interactions, we have a competition between the normal phase (N) and the phase separation (PS) (red curve). In the strong polarization limit, the competition between the normal phase and the polarized superfluid phase is presented by the blue curve. The extrapolation of these two results to strong coupling gives a qualitative phase diagram. Here, we did not study the phase transition from PS to pSF.

We now study the energetic competition between these two phases by computing the difference in their energies

$$\Delta E = E_N - E_{SF} = -W(1-p^2)/8 + |U|(1-p^2)/4.$$

For $2|U|/W < (1+p)/(1-p)$ or $p > (2|U|/W-1)/(2|U|/W+1)$, we have $\Delta E < 0$ and the normal phase is more stable. Otherwise, the polarized superfluid phase is more stable. This result leads to the phase diagram presented in Fig. 5.15. In the limit of strong polarization $p \approx 1$, the most stable phase is the normal phase. This result is derived from the fact that we are at half-filling (one particle per site). Indeed, the half-filling restricts the appearance of composite bosons and reduces the gain in kinetic energy when the bosons condense. In contrast, for a dilute gas of fermions (in the continuum or in the lattice), the hard-core bosons can move more easily. They have a bigger effective mass (for example $M = 2m$ in the continuum). The condensation of these bosons at low temperature makes an important gain in kinetic energy and that is the reason why the polarized superfluid is more stable (see Figs. 5.5 and 5.6).

## 5.6 Intermediate-coupling regime

### 5.6.1 Phase diagram

We recall that in the weak-coupling BCS theory the phase separation scenario is realized at low temperatures. Increasing the temperature the critical field decreases and stabilizing the pSF phase. While the behavior at weak coupling is now quite clear, much less is known about stronger couplings, where the superfluid state is evolving towards a BEC state. On a qualitative level, we expect that, as $|U|$ is increased, an increasing number of bosons (local pairs) in a spin-singlet state are formed. Spin degrees of freedom are therefore blocked (this leads to the opening of a pseudogap above $T_c$ ). Hence, the polarizability $\chi$ of the normal fluid is expected to decrease dramatically, leading to a situation closer to the right panel of Fig. 5.7, hence favoring the pSF phase.

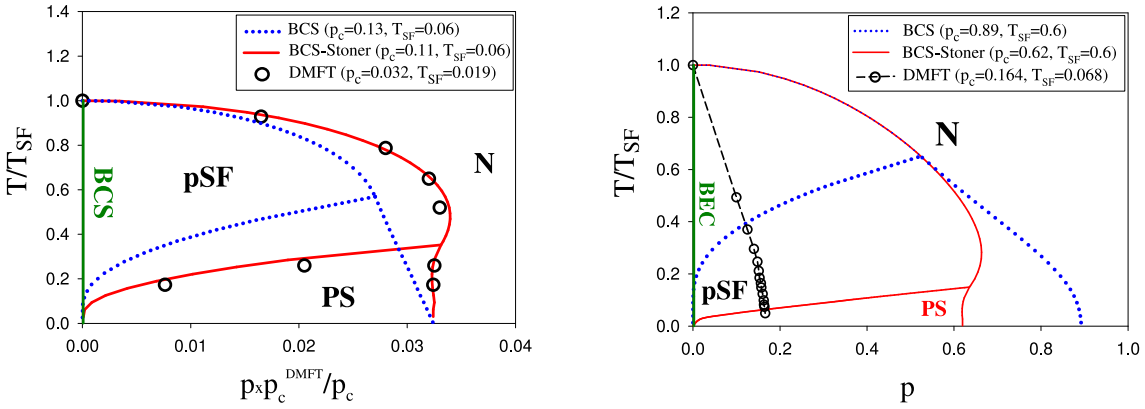


**Figure 5.16:** Phase diagram in the (T-p) temperature-polarization plane at weak coupling $U = 0.5$ (upper panel) and $U = 2.5$ (lower panel), obtained using DMFT, BCS and BCS-Stoner mean-field. $T_{SF}$ and $p_c$ are defined in the text. pSF, PS and N label polarized superfluid, phase separation and normal phase, resp. For $U = 0.5$, the results are plotted against $p/(p_c/p_c^{DMFT})$ to allow both a comparison in relative units between the three approaches at small $U$ and a direct comparison between the DMFT results of the two panels. Note that in the lower panel the PS phase is only found using the BCS and BCS-Stoner mean-field approaches.

We now analyze the model within dynamical mean-field theory (DMFT) [44], which as we have shown above, realizes a quantum (dynamical) mean field of the lattice model in terms of

a single correlated site embedded in a self-consistent bath. We solve this correlated problem using continuous-time quantum Monte Carlo (CTQMC) [122]. Contrary to static mean-field approximations, whose validity is expected to be limited to weak interactions, DMFT allows to study all the interaction regimes. We will compare the DMFT results with the simpler static mean-field calculations shown above, namely a standard BCS mean field [70, 100] and the more accurate BCS-Stoner mean field [69, 86].

The phase diagram obtained by using the BCS, BCS-Stoner and DMFT approaches is presented in Fig. 5.16. First, we consider a rather weak coupling $U = 0.5$ (upper panel). For large $p$ or at high $T$ the stable phase is the polarized normal fluid. As $T$ is decreased the system enters the pSF phase which exhibits both a non-zero superfluid order parameter $\Delta = |U|\langle\sum_i c^\dagger_{i\uparrow} c^\dagger_{i\downarrow}\rangle$ and a finite polarization, as we shall see in more details below. When $T$ is further lowered, the pSF phase becomes unstable towards a phase separation between a BCS superfluid and a polarized normal fluid. While the overall phase diagram is the same in all approaches, the BCS mean-field underestimates the extent of the pSF phase with respects to DMFT, mainly because it overestimates $\chi$ in the normal state. As we have discussed above, this effect is substantially reduced by the BCS-Stoner mean-field, in which the population imbalance is determined self-consistently. This leads to a lower $\chi$, which extends the stability of the pSF phase and improves the agreement with DMFT. Note that, for each approach, the temperature is normalized by $T_{SF}$, the superfluid critical temperature at $h = 0$. In the upper panel, the polarization is normalized by $p_c/p_c^{DMFT}$, where $p_c$ is the polarization of the normal phase at $T = 0, h = h_c$ and $p_c^{DMFT}$ is value of $p_c$ obtained by DMFT. The values of $T_{SF}$ and $p_c$ are indeed different in the three approaches (see the insets of Fig. 5.16) and they are overestimated in static mean-field approximations, making a comparison in relative units more appropriate. The BCS-Stoner phase diagram is seen to be in good agreement with the DMFT result in this weak-coupling regime.

We now turn to an intermediate coupling $U = 2.5$ (lower panel), where for identical populations the superfluid state is on the BEC side of the BCS/BEC crossover [73, 119, 120]. The DMFT results clearly show that the interaction strongly increases the stability region of the pSF phase compared to the small $U$ case: it exists for a larger range of polarization (up to $p \lesssim 16$ % instead of $p \lesssim 3\%$ for $U = 0.5$) and is stable down to the lowest temperature we could investigate by DMFT ($T/T_{SF} = 0.049$). From our present CTQMC solutions of DMFT, we can not determine whether a phase separation eventually appears at lower temperatures, as in the mean-field approaches. In this intermediate coupling region, the static mean-field approximations are not expected to be accurate, and indeed the agreement with DMFT results is quite poor. In particular, the BCS mean-field approximation misses the stabilization of the pSF state, and gives rise to a wide range of phase separation. The effect is partially corrected in the BCS-Stoner approximation, which reduces the phase separation region, but largely overestimates the stability region of the pSF phase as a function of $p$.

### 5.6.2 Stability of the polarized superfluid phase

The CTQMC solver can reach very small temperatures ($\sim T = D/300$) and therefore allows to account for the complicated structure of the local Green's function at low energy. This low-energy structures are relevant to describe the stability of the polarized superfluid.

We now analyze the properties of this phase focusing on the polarization as a function of the chemical potential difference $h$ both in the weak- and intermediate-coupling limits. The behavior of the polarization $p(h)$ is displayed in Fig. 5.17 for $U = 0.5D$ in the left panel and for $U = 2.5D$ in the right panel.

In Fig. 5.17 we plot the superfluid order parameter $\Delta$ and the polarization as a function of $h$ for different temperatures. At high temperatures, the polarization gradually increases

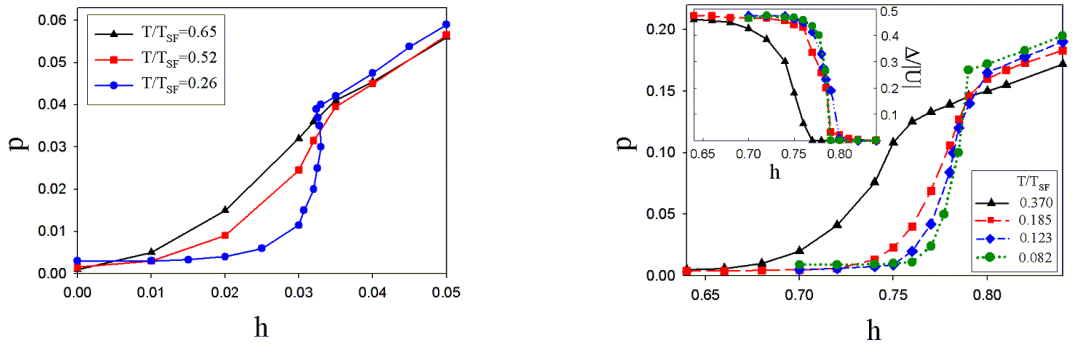


**Figure 5.17:** Polarization as a function of the external magnetic field $h$ for different temperatures $T$. Left panel: the coupling is $U = 2.5$ and $T_{\rm SF}$is the critical temperature below which the BCS superfluid is stable. Right panel: the coupling is $U = 2.5$ and $T_{\rm SF}$ is the critical temperature below which the superfluid BEC phase is stable in the absence of a magnetic field. Inset: superfluid order parameter over the same range of magnetic fields.

with $h$ and the pSF phase smoothly connects to the normal phase. As the temperature is decreased, two regimes appear in the pSF phase, even though there is no phase transition between them. At small $h \lesssim 0.75$, the polarization is very small and can be traced back to thermal excitations in the BEC state. Around $h \sim 0.75$ a *stable branch* connects to the normal phase. The polarization in this branch is too large to originate from thermal fluctuations and it has a different nature.

Indeed, the density $n(k)$ in this region (see Fig. 5.18) displays two humps, just like in the weak-coupling Sarma phase (Fig. 5.11d). This is very different from what is expected at low temperature in a standard thermally excited superfluid where $n(k)$ is broadened around $k_F$ over a small range $\sim T/v_F$. The two humps also indicate that the underlying $T = 0$ phase has two Fermi surfaces, unlike the BP1 phase proposed deep in the BEC regime of trapped fermionic gases. This shows that at intermediate couplings on a lattice, it is not possible to reduce the problem to a simple Bose-Fermi mixture.

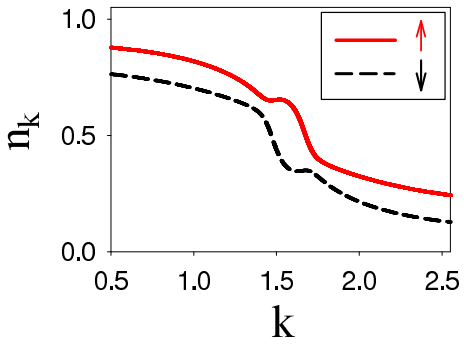


**Figure 5.18:** Density distribution $n_{\mathbf{k}}$ in the diagonal direction for both species. The red curve is for the "up" species while the black curve is for the "down" species.

### 5.6.3 Energy behavior across the phase transition

Finally, we study quantitatively the energetic balance underlying the stabilization of the pSF phase, in connection with the qualitative arguments presented above. The total internal energy and the kinetic energy of each phase are displayed in Fig. 5.19 as a function of $h$, for $U = 2.5$ and $T = 0.148\ T_{SF}$. The total energy curve follows nicely the second scenario

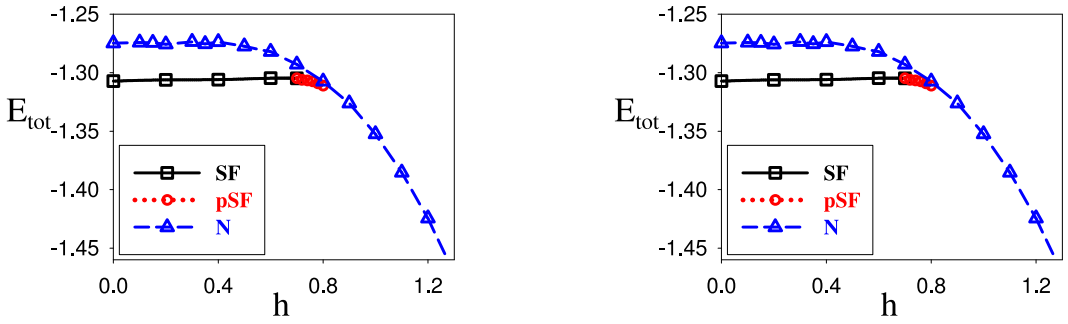


**Figure 5.19:** Energetic balance in strong coupling $U = 1.25W$. In the left panel we plot the kinetic energy for the three phases (SF: solid line with open squares, pSF red dashed line and open circles, Normal blue dashed line with triangles), and in the right panel the internal total energy for the same solutions.

described above (we are at low-$T$, so we neglect the entropy term and replace the free energy by the energy in this discussion). A stable pSF phase bridges between the flat energy of the superfluid and the energy curve of the polarized normal fluid. We have checked that the total energy branch corresponding to the normal phase has a reduced curvature compared to weaker couplings, indicating a small $\chi$ of the normal fluid. Moreover, this branch is shifted towards higher magnetic fields because the normal phase is gapped up to a critical field $h \sim 0.4$. These combined effects strongly favor the stability of the pSF phase.

A very important point is apparent from the kinetic energy plot in Fig. 5.19. For small $h$, the superfluid state has a lower kinetic energy than the normal state. Indeed, in contrast to the weak-coupling BCS regime, the BEC superfluid is stabilized by a gain of kinetic energy [73, 120]. Instead, we see that the pSF phase has a higher kinetic energy and a smaller potential energy than the normal state. Therefore, the pSF phase is stabilized by a gain in the potential energy, as in the BCS regime, even though we are not in the weak-coupling regime. As a function of the imbalance of populations, the system will turn from a regular BEC system which gains kinetic energy in the superfluid state to a pSF phase which loses kinetic energy. Measurements of energies are experimentally possible in cold atomic systems [113] and it would be of great interest to investigate these energetic considerations for polarized gases.

## 5.7 Conclusion

In conclusion, we have studied in this chapter the problem of fermionic mixtures with imbalanced populations. General arguments based on energy considerations suggest that a polarized gapless superfluid phase can be stabilized by the formation of preformed pairs with a reduced polarizability, on the BEC side of the BCS-BEC crossover.

For the model in the continuum, via the analysis of some recent works, we have shown that the physics of the BCS-BEC crossover is fundamental for the stability of novel phases when the polarization increases. We also argued that the non-trivial physics of the normal phase at the unitary limit induces the critical polarization.

We have also substantiated these arguments with a DMFT solution of the half-filled Hubbard model on the cubic lattice, which demonstrates the stabilization of the pSF phase down to very low temperatures for an intermediate coupling $U/(6t) = 2.5$. The nature of this phase is closely connected to the physics of the Sarma (BP2) phase that has been previously discussed at weak coupling by static mean-field theory, but is usually unstable in this regime. We have shown that the stabilized pSF phase is clearly distinct from a BP1 phase and from a standard thermally excited superfluid state. While the BEC superfluid (in contrast to the weak-coupling BCS one) is stabilized by the kinetic energy, the pSF-phase condensation energy corresponds to a potential energy gain in comparison to the polarized normal fluid.

Finally, at high polarizations deep inside the BEC limit, we have shown that, in the lattice model at half-filling, a polarized normal fluid is always stable against a polarized gapless superfluid which is different from the continuum limit. This is simply because the effective molecules (the bound states) have more mobility in the continuum than in the lattice model at half-filling.

**Third article:**

Gapless superfluidity in the attractive Hubbard model with population imbalance

accepted to *Physical Review Letters*

Eprint: cond-mat/0807.2923

# Polarized superfluidity in the attractive Hubbard model with population imbalance

Tung-Lam Dao,[1] Michel Ferrero,[1] Antoine Georges,[1] Massimo Capone,[2] and Olivier Parcollet[3]

[1] *Centre de Physique Théorique, CNRS, Ecole Polytechnique, F-91128 Palaiseau Cedex, France.*
[2] *SMC, CNR-INFM and Università di Roma "La Sapienza", Piazzale Aldo Moro 2, I-00185 Roma, Italy*
[3] *Institut de Physique Théorique, CEA, IPhT, CNRS, URA 2306, F-91191 Gif-sur-Yvette, France*

(Dated: October 18, 2008)

We study a two-component Fermi system with attractive interactions and different populations of the two species in a cubic lattice. For an intermediate coupling we find a uniformly polarized superfluid which is stable down to very low temperatures. The momentum distribution of this phase closely resembles that of the Sarma phase, characterized by two Fermi surfaces. This phase is shown to be stabilized by a potential energy gain, as in a BCS superfluid, in contrast to the unpolarized BEC which is stabilized by kinetic energy. We present general arguments suggesting that preformed pairs in the unpolarized superfluid favor the stabilization of a polarized superfluid phase.

PACS numbers: 71.10.Fd, 37.10.Jk, 71.10.-w, 71.30.+h, 03.75.Lm, 05.30.Fk

The study of superfluid phases is a fundamental issue in condensed matter physics. It has received a revived interest with the experimental realization of cold atomic systems that allow to probe such phases with a remarkable controllability [1–3]. It is for instance possible to address a large range of interaction strengths or to control the population imbalance between atoms in different hyperfine states. For fermionic fluids composed of two species, the latter parameter, which introduces a mismatch in the Fermi surfaces, raises exciting questions about the stability of the conventional superfluid phase and the possible generation of more exotic ones. Indeed, in the absence of imbalance, a weak attractive interaction between the fermionic species stabilizes a Bardeen-Cooper-Schrieffer (BCS) ground state, with a pairing between species of opposite momentum near their common Fermi surface. When the interaction is strong, the fermions pair in real space, and superfluidity is associated with the Bose-Einstein condensation (BEC) of pairs. The BEC-BCS crossover has been studied intensively both experimentally [4–6] and theoretically [7–10].

The situation is far less clear when a population imbalance introduces a mismatch between the Fermi surfaces. At small imbalance, the species are expected to still form a standard BCS or BEC state. At larger imbalance, either superfluidity disappears in favor of a polarized normal fluid or more exotic forms of pairing occur. One candidate is the Fulde-Ferrell-Larkin-Ovchinnikov state [11–14] in which Cooper pairs appear at a non-zero total momentum. At zero temperature, two other possible phases that exhibit both a non-zero superfluid order parameter and a finite polarization have been proposed: the Sarma (or breached-pair BP2) phase [15, 16] and the BP1 phase [17–19]. At weak-coupling, the Sarma phase is unstable unless specific types of interactions are considered [20]. The BP1 has been proposed as a stable ground state deep in the BEC regime of trapped fermionic gases, where the system is described by a Bose-Fermi mixture. While both of these phases are polarized superfluids with gapless excitations, their nature is different: the Sarma phase has two Fermi surfaces while the BP1 phase has a single Fermi surface for the unpaired fermions. These non-standard phases are in general unstable at weak coupling, resulting in phase separation between an unpolarized superfluid and a polarized normal fluid formed by the excess fermions, an effect which has been observed experimentally [21–23]. At zero temperature $T = 0$, the Sarma and BP1 phases are signaled by a non-zero superfluid order parameter together with a finite polarization. When $T > 0$, this criterion is no longer valid because a standard BCS or BEC state also acquires a small polarization coming from thermally excited quasiparticles.

In this paper, we focus on polarized superfluid phases (pSF) in a three-dimensional cubic lattice. We study their nature at weak and intermediate coupling as a function of the temperature, treating the effect of correlations beyond static mean field. Our main result is that, at intermediate coupling, a pSF phase can be stabilized down to very low temperatures, with properties which are clearly associated with the Sarma phase. The mechanism responsible for this stabilization is the reduction of the polarizability of the normal fluid due to the existence of preformed pairs. We will show that this phase is profoundly different from the unpolarized BEC superfluid which holds at the same coupling strength in the absence of imbalance.

We start with some energetic considerations, which clarify the general conditions under which a pSF phase can be stable at $T = 0$. In order to control the imbalance between the populations of the two species, we introduce a chemical potential difference (or effective 'magnetic field') $h \equiv (\mu_\uparrow - \mu_\downarrow)/2$ between them. In Fig. 1, we show two typical behaviors of the energy in different phases as a function of the magnetic field. In both cases, a small magnetic field $h$ is expelled from the unpolarized superfluid, and the energy is independent of $h$. This unpolarized superfluid is locally stable up to a critical value $h_c$. For $h > h_c$ the magnetic field breaks the pairs, lead-

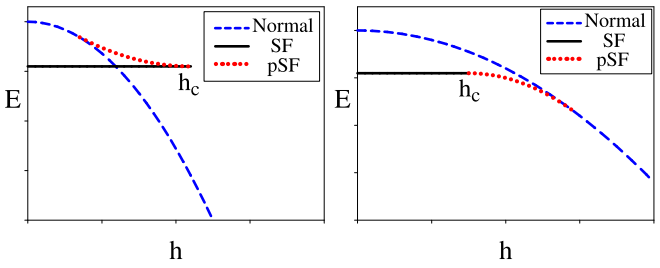


FIG. 1: (Color online) Sketches of the energy $E$ vs $h$, for the normal state, the unpolarized superfluid (SF) and the pSF phase. Two situations can appear as function of the external parameters (*e.g.* the interaction strength). Left panel (a): the pSF branch is unstable and the system undergoes a phase separation. Right panel (b): the pSF branch is stable.

ing to the disappearance of this solution. On the other hand, the energy of the polarized normal state is a decreasing function of $h$: its derivative $p \equiv -\partial E/\partial h > 0$ is the polarization (population imbalance) and its curvature $\chi \equiv -\partial^2 E/\partial h^2 = \partial p/\partial h$ defines the polarizability of the normal fluid.

In general the pSF phase can bridge between these two solutions. The way in which this connection occurs depends on the two key parameters $h_c$ and $\chi$. When $h_c$ and $\chi$ are large, we anticipate the situation in Fig. 1a. In this case, the pSF branch is expected not to be stable, and the system undergoes a first-order transition as a function of $h$ which results in a phase separation if we try to prepare the system with a polarization corresponding to the unstable branch. In contrast, if $h_c$ and $\chi$ are small enough, the energies of the unpolarized superfluid and polarized normal solutions do not cross, and the pSF phase can be stable in a region bridging these two states, as shown in Fig. 1b. Therefore, a stable pSF phase is likely to form when $\chi$ or $h_c$ are small. Interestingly, this suggests that an increasing attractive coupling may help stabilizing the pSF phase. Indeed, in the BEC regime, the normal state presents preformed pairs in a singlet state that strongly reduce $\chi$, hence stabilizing a pSF phase.

In order to explore the validity of these qualitative arguments we study an attractive Hubbard model at half-filling, on a three-dimensional cubic lattice with nearest-neighbor hopping:

$$\mathcal{H} = -t \sum_{<ij>\sigma} (c^\dagger_{i\sigma} c_{j\sigma} + \text{h.c.}) - U \sum_i n_{i\uparrow} n_{i\downarrow} - \sum_i \mu_\sigma n_{i\sigma}$$

where $c^\dagger_{i\sigma}$ ($c_{i\sigma}$) creates (destroys) a fermion of species $\sigma$ on the site $i$, $n_{i\sigma} = c^\dagger_{i\sigma} c_{i\sigma}$ is the number operator, $t$ is the hopping amplitude and $U > 0$ is the Hubbard on-site attraction. When the total number of fermions is identical to the number of lattice sites (half-filling) $\mu_\uparrow = -U/2 + h$ and $\mu_\downarrow = -U/2 - h$. In the following, all energies will be expressed in units of the half-bandwidth $D = 6t = 1$.

We analyze the model within dynamical mean-field theory (DMFT) [24], which realizes a quantum (dynamical) mean field of the lattice model in terms of a single correlated site embedded in a self-consistent bath. This correlated local problem is then solved using continuous-time quantum Monte Carlo (CTQMC) [25]. Contrary to static mean-field approximations, whose validity is expected to be limited to weak interactions, DMFT allows to study all the interaction regimes [24]. We compare the DMFT results with simpler static mean-field calculations, namely with a standard BCS mean field and a more accurate 'BCS-Stoner' mean field [13, 26], which introduces a mean-field decoupling of the interaction both in the particle-particle channel (as in BCS) and in the particle-hole channel (as in Stoner theory) in order to compute both the superfluid order parameter and the polarization self-consistently.

We first consider a rather weak coupling $U = 0.5$. The phase diagram obtained by using the BCS, BCS-Stoner and DMFT approaches is presented in Fig. 2e. For large $p$ or at high $T$ the stable phase is the polar-

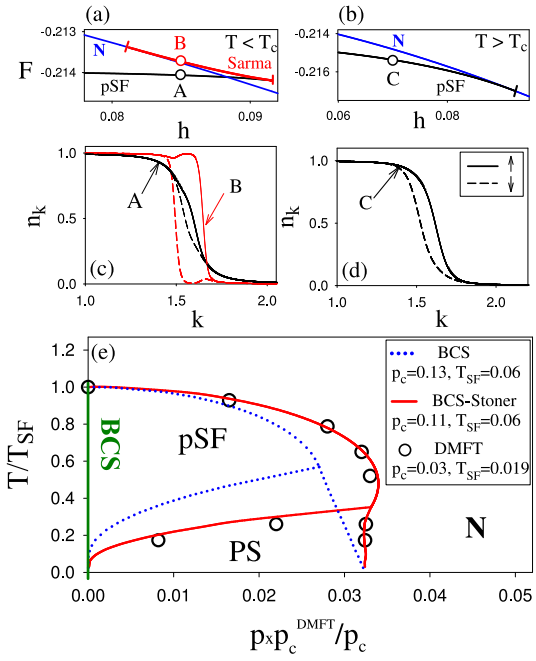


FIG. 2: (Color online) Lower panel (e): Phase diagram in the $T - p$ plane at weak coupling $U = 0.5$ (lower panel) obtained using DMFT, BCS and BCS-Stoner mean-field. $T_{SF}$ and $p_c$ are defined in the text. pSF, PS and N label polarized superfluid, phase separation and normal phase, resp. The results are plotted against $p/(p_c/p_c^{DMFT})$ to allow for a comparison in relative units. Upper panels (a-b): free-energy *vs.* $h$ below and above the critical temperature $T_c$. Middle panels (c-d): momentum distribution $n(k)$ at three points (A), (B), (C) indicated on the free-energy curves of panel (a).

ized normal fluid. As $T$ is decreased the system enters a pSF phase which exhibits both a non-zero superfluid

order parameter $\Delta = (U/N)\langle\sum_i c^\dagger_{i\uparrow} c^\dagger_{i\downarrow}\rangle$ and a finite polarization. When $T$ is further lowered, the pSF phase becomes unstable towards a phase separation between a thermally excited BCS superfluid and a polarized normal fluid. While the overall phase diagram is the same in all approaches in relative units (defined below), the BCS mean-field underestimates the extent of the pSF phase with respects to DMFT, mainly because it overestimates $\chi$ in the normal state. This effect is substantially reduced by the BCS-Stoner mean-field, in which the population imbalance is determined self-consistently. This leads to a lower $\chi$, which extends the stability of the pSF phase and improves the agreement with DMFT. Note that, for each approach, the temperature is normalized by $T_{\rm SF}$, the superfluid critical temperature at $h = 0$. The polarization is normalized by $p_c/p_c^{\rm DMFT}$, where $p_c$ is the polarization of the normal phase at $T = 0, h = h_c$ and $p_c^{\rm DMFT}$ is the value of $p_c$ obtained with DMFT. The values of $T_{\rm SF}$ and $p_c$ are overestimated in static mean-field approximations, making a comparison in relative units more appropriate. In these units, the BCS-Stoner phase diagram is seen to be in good agreement with the DMFT result in this weak-coupling regime.

Let us now discuss the nature of these phases. The BCS-Stoner mean-field calculation shows that in the phase-separated region, with $T < T_c$, the free-energy as a function of $h$ has three branches (Fig. 2a) as in the scenario of Fig. 1a. If $T$ is small, the properties of the three branches are directly linked to their $T = 0$ counterparts. One branch corresponds to the BCS superfluid with thermal excitations. It has a small polarization that comes from thermally excited Bogoliubov quasiparticles in a small momentum-range around the Fermi momentum $k_F$ of the unpolarized state. As a consequence, the density $n(k)$ deviates from the standard BCS distribution around $k_F$ over a range of order $T/v_F$ (see A in Fig. 2c). This branch is connected to the unstable thermally excited Sarma phase. In contrast to the BCS state, the Sarma phase has two Fermi surfaces at $T = 0$, which are individually broadened when $T > 0$. This is clearly visible in $n(k)$ (see B in Fig. 2c) which displays two humps associated with each Fermi momentum, with a separation set by the polarization instead of the thermal broadening.

As the temperature $T$ is increased, the unstable branch becomes smaller and eventually disappears at $T = T_c$. For $T > T_c$, the pSF phase is stable and the free-energy has the behavior shown in Fig. 2b with only two solutions. Because $T_c$ is rather large, there is no clear distinction between the thermally excited BCS and the Sarma phases: as $h$ is increased along the superfluid branch a crossover takes place between the BCS regime and the Sarma regime. However, because $T$ is large, no particular structure appears in the density $n(k)$, even close to the normal phase (see C in Fig. 2d). Therefore, at weak coupling, the stable pSF phase has essentially a thermal nature and its properties cannot be linked to the physics of the Sarma phase.

We now turn to an intermediate coupling $U = 2.5$, where for identical populations the superfluid state is on the BEC side of the BCS/BEC crossover [27–29]. In this regime, the static mean-field approximations are not expected to be accurate and we only describe our DMFT results. As is clear from Fig. 3e, the interaction strongly

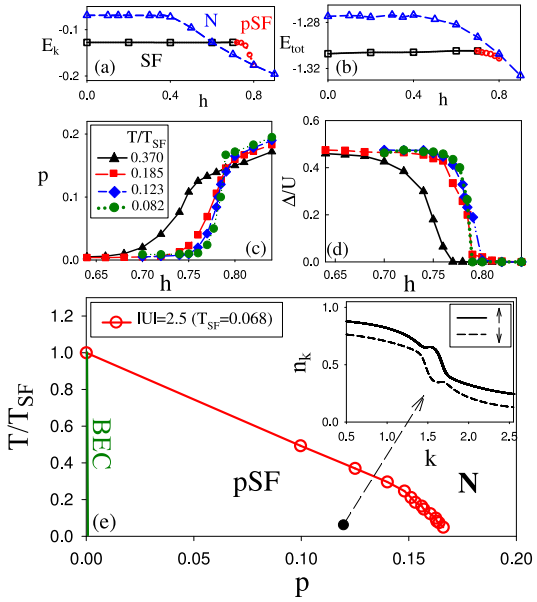


FIG. 3: (Color online) Lower panel (e): Phase diagram in the $T - p$ plane at intermediate coupling $U = 2.5$ obtained using DMFT. Inset of (e): momentum distribtion $n(k)$ for $p = 0.12$ at the lowest temperature $T/T_{\rm SF} = 0.049$. Upper panels: kinetic energy $E_k$ (a) and total internal energy $E_{tot}$ (b) as a function of $h$ for $T = 0.148\ T_{\rm SF}$. Middle panels: polarization (c) and superfluid order parameter (d) as a function of $h$.

increases the stability region of the pSF phase compared to the small $U$ case: it exists for a larger range of polarization (up to $p \lesssim 16$ % instead of $p \lesssim 3\%$ for $U = 0.5$) and is stable down to the lowest temperature we could investigate with DMFT ($T/T_{\rm SF} = 0.049$). From our present CTQMC solutions of DMFT, we cannot determine whether a phase separation eventually appears at lower temperatures, as in the weak coupling regime, but extrapolations of our numerical data are consistent with a stable pSF phase down to $T = 0$.

In Fig. 3c-d we plot the superfluid order parameter $\Delta$ and the polarization as a function of $h$ for different temperatures. At high temperatures, the polarization gradually increases with $h$ and the pSF phase smoothly connects to the normal phase. As the temperature is decreased, two regimes appear in the pSF phase, even though there is no phase transition between them. At small $h \lesssim 0.75$, the polarization is very small and can be traced back to thermal excitations in the BEC state. Around $h \sim 0.75$ a *stable branch* connects to the normal

phase. The polarization in this branch is too large to originate from thermal fluctuations and it has a different nature. Indeed, the density $n(k)$ in this region (Inset in Fig. 3e) displays two humps, just like in the weak-coupling Sarma phase (Fig. 2). This is very different from what is expected at low temperature in a standard thermally excited superfluid where $n(k)$ is broadened around $k_F$ over a small range $\sim T/v_F$. The two humps also indicate that the underlying $T = 0$ phase has two Fermi surfaces, unlike the BP1 phase proposed deep in the BEC regime of trapped fermionic gases. This shows that at intermediate couplings on a lattice, it is not possible to reduce the problem to a simple Bose-Fermi mixture.

Hence, our results show that a larger coupling stabilizes a region which displays properties very similar to the Sarma phase discussed at weak coupling, in agreement with the qualitative energetic arguments that a reduced polarizability and preformed pairs help stabilizing the pSF phase at low temperatures. This is actually confirmed by a direct computation of the energetic balance underlying this stabilization. The total internal energy and the kinetic energy of each phase are displayed in Fig. 3a-b as a function of $h$, for $U = 2.5$ and $T = 0.148\ T_{\rm SF}$. For this very low temperature, the entropy term can be neglected and we consider the energy instead of the free-energy. The total energy curve nicely follows the second scenario described above (Fig. 1b). A stable pSF phase bridges between the flat energy of the unpolarized superfluid and the energy curve of the polarized normal fluid. The total energy branch corresponding to the normal phase is seen to have a reduced curvature in comparison to weaker couplings, indicating a small $\chi$ of the normal fluid (within DMFT, this branch has actually vanishing polarization up to to a field $h \sim 0.4$). These effects strongly favor the stability of the pSF phase.

The energetic balance of the transition to the pSF state is particularly interesting. In the absence of imbalance it has been shown that for $U = 2.5$ the system is in the BEC regime and the superfluid state is stabilized by a gain of kinetic energy [27–29], in contrast with the BCS state which gains potential energy. Here we find, as shown in Fig. 3a, that the pSF has instead higher kinetic energy than the normal state and it is therefore stabilized by potential energy, even though we are not in the BCS regime. Therefore, as a function of the imbalance of populations, the system will turn from a regular BEC system which gains kinetic energy in the superfluid state to a pSF phase which loses kinetic energy. Measurements of energies are experimentally possible in cold atomic systems [30] and it would be of great interest to investigate these energetic considerations for polarized gases.

In conclusion, general arguments based on energy considerations suggest that a polarized superfluid phase can be stabilized by the formation of preformed pairs with a reduced polarizability on the BEC side of the BCS-BEC crossover. We have substantiated these arguments with a DMFT solution of the half-filled attractive Hubbard model on the cubic lattice, which demonstrates the stabilization of a pSF phase down to very low temperatures for an intermediate coupling $U/(6t) = 2.5$. The nature of this phase is closely connected to the physics of the Sarma (BP2) phase that has been previously discussed at weak coupling by static mean-field theory, but is usually unstable in this regime. We have shown that the stabilized pSF phase is clearly distinct from a BP1 phase and from a standard thermally excited superfluid state. Finally, while the BEC superfluid (in contrast to the weak-coupling BCS one) is stabilized by a gain in kinetic energy, the pSF-phase condensation energy corresponds to a potential energy gain in comparison to the polarized normal fluid.

We thank P. S. Cornaglia, C. Mora, T.-S. Dam and W. V. Liu for useful discussions, and the Aspen Center for Physics for hospitality. We acknowledge the support of the Agence Nationale de la Recherche (ANR) under contracts GASCOR and FABIOLA, the DARPA-OLE program and Italian MIUR PRIN 2007.

[1] M. Greiner, O. Mandel, T. Esslinger, T. Hänsch, and I. Bloch, Nature **415**, 39 (2002).
[2] I. Bloch, Nat. Phys. **1**, 23 (2005).
[3] D. Jaksch and P. Zoller, Ann. Phys. **315**, 52 (2005).
[4] S. Jochim, M. Bartenstein, A. Altmeyer, G. Hendl, S. Ried, C. Chin, J. H. Denschlag, and R. Grimm, Science **302**, 2101 (2002).
[5] M. W. Zwierlein, C. A. Stan, C. H. Schunck, S. M. F. Raupach, S. Gupta, Z. Hadzibabic, and W. Ketterle, Phys. Rev. Lett. **91**, 250401 (2003).
[6] T. Bourdel, L. Khaykovich, J. Cubizolles, J. Zhang, F. Chevy, M. Teichmann, L. Tarruell, S. J. J. M. F. Kokkelmans, and C. Salomon, Phys. Rev. Lett. **93**, 050401 (2004).
[7] A. Leggett, *Modern Trends in the Theory of Condensed Matter* (Springer-Verlag, Berlin, 1980).
[8] P. Nozières and S. Schmitt-Rink, J. Low Temp. Phys **59**, 195 (1985).
[9] C. A. R. Sá de Melo, M. Randeria, and J. R. Engelbrecht, Phys. Rev. Lett. **71**, 3202 (1993).
[10] M. Keller, W. Metzner, and U. Schollwöck, Phys. Rev. Lett. **86**, 4612 (2001).
[11] P. Fulde and R. A. Ferrell, Phys. Rev. **135**, A550 (1964).
[12] A. I. Larkin and Y. N. Ovchinnikov, Sov. Phys. JETP **20**, 762 (1965).
[13] T. K. Koponen, T. Paananen, J.-P. Martikainen, M. R. Bakhtiari, and P. Törmä, New J. Phys. **10**, 045014 (2008).
[14] N. Yoshida and S.-K. Yip, Phys. Rev. A **75**, 063601 (pages 6) (2007).
[15] G. Sarma, J. Phys. Chem. Solids **24**, 1029 (1963).
[16] W. V. Liu and F. Wilczek, Phys. Rev. Lett. **90**, 047002 (2003).
[17] D. E. Sheehy and L. Radzihovsky, Phys. Rev. Lett. **96**, 060401 (2006).

[18] D. T. Son and M. A. Stephanov, Phys. Rev. A **74**, 013614 (2006).
[19] S. Pilati and S. Giorgini, Phys. Rev. Lett. **100**, 030401 (2008).
[20] M. M. Forbes, E. Gubankova, W. V. Liu, and F. Wilczek, Phys. Rev. Lett. **94**, 017001 (2005).
[21] G. B. Partridge, W. Lia, R. I. Kamar, Y. an Liao, and R. G. Hulet, Science **311**, 503 (2006).
[22] M. W. Zwierlein, A. Schirotzek, C. H. Schunck, and W. Ketterle, Science **311**, 492 (2006).
[23] M. W. Zwierlein, C. H. Schunck, A. Schirotzek, and W. Ketterle, Nature **442**, 54 (2006).
[24] A. Georges, G. Kotliar, W. Krauth, and M. J. Rozenberg, Rev. Mod. Phys. **68**, 13 (1996).
[25] P. Werner, A. Comanac, L. de' Medici, M. Troyer, and A. J. Millis, Phys. Rev. Lett. **97**, 076405 (2006).
[26] C. Mora, Ph.D. thesis, ENS de Paris (2004).
[27] A. Toschi, P. Barone, C. Castellani, and M. Capone, New J. Phys. **7**, 7 (2005).
[28] A. Toschi, M. Capone, and C. Castellani, Phys. Rev. B **72**, 235118 (2005).
[29] B. Kyung, A. Georges, and A.-M. S. Tremblay, Phys. Rev. B **74**, 024501 (2006).
[30] J. T. Stewart, J. P. Gaebler, C. A. Regal, and D. S. Jin, Phys. Rev. Lett. **97**, 220406 (2006).

# Conclusion

This thesis is concerned with the theoretical study of strongly correlated quantum states of ultra-cold fermionic atoms trapped in optical lattices. This field has grown considerably in recent years, following the experimental progress made in cooling and controlling atomic gases, which has led to the observation of the first Bose-Einstein condensation (in 1995 [4]). The trapping of these gases in optical lattices has opened a new field of research at the interface between atomic physics and condensed matter physics. The observation of the transition from a superfluid to a Mott insulator for bosonic atoms [46] paved the way for the study of strongly correlated phases and quantum phase transitions in these systems. Very recently, the investigation of the Mott insulator state of fermionic atoms [63] provides additional motivation to conduct such theoretical studies. This thesis can be divided broadly into two types of work:

- On the one hand, we have proposed a new type of spectroscopy to measure single-particle correlators and associated physical observables in these strongly correlated states.
- On the other hand, we have studied the ground state of the fermionic Hubbard model under different conditions (mass imbalance, population imbalance) by using analytical techniques and numerical simulations.

In a collaboration with J. Dalibard and C. Salomon (LKB at the ENS Paris) and I. Carusotto (Trento, Italy), we have proposed and studied a novel spectroscopic method for the measurement and characterization of single particle excitations (in particular, the low energy excitations, namely the quasiparticles) in systems of cold fermionic atoms, with energy and momentum resolution. This type of spectroscopy is an analogue of angular-resolved photoemission in solid state physics (ARPES). We have shown, via simple models, that this method of measurement can characterize quasiparticles not only in the "conventional" phases such as the weakly interacting gas in the lattice or in Fermi liquids, but also in unusual phases such as the normal state of high-temperature superconductivity with a pseudogap (leading to a differentiation between nodes and anti-nodes) observed in condensed mater physics. The first experiment implementing a type of spectroscopy (RF spectroscopy) very closely related to our proposal has been recently realized at Boulder in D. S. Jin's group, just as this thesis was being written up.

In the second part of this thesis, we have performed theoretical studies of several phases of strongly correlated fermions in optical lattices in the framework of theoretical models such as the Hubbard model. We have implemented and developed analytical methods (Hartree-Fock mean field theory at weak coupling, mapping on a effective spin model at strong coupling) and numerical methods (the dynamic mean field theory approach). This work has led to two particular types of studies. The first one studies the competition between a superfluid phase and a density wave (or phase separation) for fermions with mass imbalance and attractive interaction. We have shown that the superfluid phase is unstable beyond a certain value of the mass ratio, which depends on the interaction. The second study treats a gas with imbalanced populations (polarized gas) with an attractive interaction in a three dimensional

optical lattice. The main result is a phase diagram showing the stability of a uniform superfluid phase with polarization (Sarma phase or breached pair phase) in a certain parameter regime. Via an energetic argument, we concluded that the stability of the polarized superfluid phase is due to the reduction of the polarizability and the critical field of the non-polarized superfluid phase. In the strong coupling regime of the Hubbard model, within the DMFT method, we have shown that the formation of the preformed pair in the normal state reduces the polarizability and favors the stability of the breached pair phase.

Although some aspects have been addressed in this thesis, many interesting questions still remain open for future work. In the first part, the framework of the novel spectroscopy method established in chapter 2 can allow for different concrete studies of the nature of strongly correlated states. For example, it should be very interesting to understand the spectra of single particle excitation in non trivial phases such as the Mott insulator, the preformed-pairs or phases with long range order. In the second part, the construction of the improved (BCS-Slater) mean field theory including the Hartree correction allows for a better comparison to modern methods (DMFT and Slave Bosons). For the system with the same population for both species, the region close to the Falicov-Kimball model is not yet well understood in our DMFT analysis because of problems in numerical convergence within the exact-diagonalization method. However, within the mean field theory analysis, we see that a novel uniform phase of charge density wave (doped-CDW) can be stabilized thanks to the high asymmetry of hopping. In order to clarify this question, a study by Slave Boson mean-field theory could be very useful. This method has two advantages: First, it contains the strongly correlated physics (including quantum fluctuations); second, in some simple cases we can extract the analytical behavior of the solution. In addition, a full treatment within MFT for both order parameters, the superfluid and the CDW, should be useful for understanding the nature of the phase transition in this limit. Another perspective of this thesis is the understanding of the nature of the polarized superfluid phase. The mismatch of the Fermi surfaces considered in this thesis is due to the population imbalance. We can always control this mismatch by introducing furthermore a mass imbalance. In the region with high mass imbalance, it is likely that the stability of the polarized uniform superfluid phase may be further enhanced.

Within this thesis, the effects of the confining potential have been included via the local density approximation. For a weak and smooth potential, this approximation is expected to be accurate. However, for stronger confinement, it may become more questionable. Indeed, this issue has been recently debated in the literature, in the context of the interpretation of experiments with population imbalance [92, 126]. Dynamical Mean-Field Theory can be implemented in an inhomogeneous framework, beyond LDA [53, 95, 102] and this could be used to assess the validity of the LDA approximation for problems such as those studied in this thesis. This could be relevant in particular to the current debate on the phases of the fermionic systems with population imbalance.

# Appendix A

# Appendix on mean-field theory

## A.1 Spin-wave study

We study here by spin-wave theory for this $XXZ$ model to determine the spectrum of excitations at low energy. In fact, it must be a semi-classical calculation because the spin-wave study is performed around the classical fundamental state which is found in the last section. This study is very similar to the work of R. T. Scalettar [101]. Considering a rotation of angle

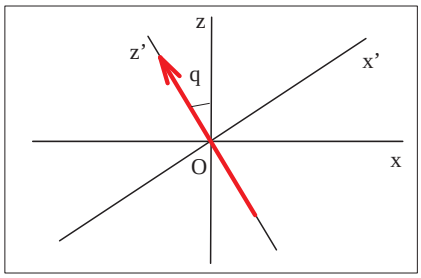


**Figure A.1:** Rotation of the spin vector

$\theta_{A(B)}$ in the plane $(x-y)$, in the classical representation, the spin vector $\vec{S}$ is transformed to

$$\begin{aligned} S_z &= \cos\theta_A S'_z - \sin\theta_A S'_x \\ S_x &= \cos\theta_A S'_x + \sin\theta_A S'_z \\ S_y &= S'_y. \end{aligned}$$

We propose to study the small fluctuations characterized by creation operators $a^\dagger, b^\dagger$ around the direction $Oz'$ on the two different sites A and B.

$$\begin{aligned} S'^{z}_{A} &= S - a^\dagger a & \qquad S'^{z}_{B} &= S - b^\dagger b \\ S'^{+}_{A} &= a^\dagger & \qquad S'^{+}_{B} &= b^\dagger \\ S'^{-}_{A} &= a & \qquad S'^{-}_{B} &= b \end{aligned}$$

Including these fluctuations in the spin vector $\vec{S}$ obtained by the rotation from Oz' axis to the Oz axis, we have the following expression

$$\begin{aligned} S_{zA} &= \cos\theta_A(\frac{1}{2} - a^\dagger a) - \sin\theta_A \frac{a^\dagger + a}{2} \\ S_{xA} &= \cos\theta_A \frac{a^\dagger + a}{2} + \sin\theta_A \frac{a^\dagger + a}{2}(\frac{1}{2} - a^\dagger a) \\ S_{yA} &= \frac{a^\dagger - a}{2}. \end{aligned}$$

The Hamiltonian of our model in the strong interaction limit reads

$$H = J\sum_{\langle i,j\rangle} \vec{S}_i.\vec{S}_j + \gamma J \sum_{\langle i,j\rangle} S_i^z S_j^z - h\sum_i (S_i^z - m) \tag{A.1}$$

Let us calculate the different terms in this Hamiltonian in the semi-classical representation

$$\begin{aligned} J\sum_{\langle i,j\rangle} \vec{S}_i\vec{S}_j &= J\sum_{\langle i,j\rangle} \Big[ \cos(\theta_A - \theta_B)(\frac{1}{2} - a_i^\dagger a_i)(\frac{1}{2} - b_j^\dagger b_j) + \cos(\theta_A - \theta_B)\frac{(a_i^\dagger + a_i)(b_j^\dagger + b_j)}{4} \\ &+ \sin(\theta_B - \theta_A)\frac{a_i^\dagger + a_i}{2}(\frac{1}{2} - b_j^\dagger b_j) + \sin(\theta_A - \theta_B)\frac{b_j^\dagger + b_j}{2}(\frac{1}{2} - a_i^\dagger a_i) - \frac{(a_i^\dagger - a_i)(b_j^\dagger - b_j)}{4}\Big] \\ \gamma J\sum_{\langle i,j\rangle} S_i^z S_j^z &= \gamma J\sum_{\langle i,j\rangle} \Big[ \cos\theta_A\cos\theta_B(\frac{1}{2} - a_i^\dagger a_i)(\frac{1}{2} - b_j^\dagger b_j) + \sin\theta_A\sin\theta_B\frac{(a_i^\dagger + a_i)(b_j^\dagger + b_j)}{4} \\ &- \sin\theta_A\cos\theta_B\frac{a_i^\dagger + a_i}{2}(\frac{1}{2} - b_j^\dagger b_j) - \sin\theta_B\cos\theta_A\frac{b_j^\dagger + b_j}{2}(\frac{1}{2} - a_i^\dagger a_i)\Big] \\ h\sum_i S_i^z &= h\sum_{i\in A}\Big[\cos\theta_A(\frac{1}{2} - a_i^\dagger a_i) - \sin\theta_A\frac{a_i^\dagger + a_i}{2}\Big] - h\sum_{i\in B}\Big[\cos\theta_B(\frac{1}{2} - b_i^\dagger b_i) - \sin\theta_B\frac{b_i^\dagger + b_i}{2}\Big]. \end{aligned}$$

Let us assume two hypothesis in this spin-wave approximation:

- We suppose that $\langle a_i^\dagger a_i\rangle$ and $\langle b_j^\dagger b_j\rangle$ are small, so we neglect all the terms with order more than 2
- The coefficients of the first order terms are zero because we evaluate this Hamiltonian around the classical fundamental state

If we impose the coefficients of the first order term to zero, we get also mean field equations in the last section

$$\begin{cases} (2h/z)\sin\theta_A = & J\sin(\theta_A - \theta_B) + \gamma J\sin\theta_A\cos\theta_B \\ (2h/z)\sin\theta_B = & J\sin(\theta_B - \theta_A) + \gamma J\sin\theta_B\cos\theta_A \end{cases}$$

Therefore the Hamiltonian can be written as follow

$$\begin{aligned}H = E_0 &+ \sum_{i\in A}\Big[h\cos\theta_A - \frac{Jz}{4}\cos(\theta_A-\theta_B) - \frac{J\gamma z}{2}\cos\theta_A\cos\theta_B\Big]a_i^\dagger a_i \\ &+ \sum_{j\in B}\Big[h\cos\theta_B - \frac{Jz}{4}\cos(\theta_A-\theta_B) - \frac{J\gamma z}{2}\cos\theta_A\cos\theta_B\Big]b_j^\dagger b_j \\ &+ \sum_{\langle i,j\rangle}\frac{J}{4}\Big[\cos(\theta_A-\theta_B) + \gamma\sin\theta_A\sin\theta_B - 1\Big](a_i^\dagger b_j^\dagger + a_i b_j) \\ &+ \sum_{\langle i,j\rangle}\frac{J}{4}\Big[\cos(\theta_A-\theta_B) + \gamma\sin\theta_A\sin\theta_B + 1\Big](a_i^\dagger b_j + b_j^\dagger a_i),\end{aligned}$$

in which $E_0 = \frac{NJz}{8}\cos(\theta_A-\theta_B) - \frac{Nh}{4}(\cos\theta_A+\cos\theta_B) + Nhm$. We define a set of parameters

$$H_1 = h\cos\theta_A - \frac{Jz}{4}\cos(\theta_A-\theta_B) - \frac{J\gamma z}{2}\cos\theta_A\cos\theta_B \tag{A.2}$$

$$H_2 = h\cos\theta_B - \frac{Jz}{4}\cos(\theta_A-\theta_B) - \frac{J\gamma z}{2}\cos\theta_A\cos\theta_B \tag{A.3}$$

$$H_3 = \frac{J}{4}\Big[\cos(\theta_A-\theta_B) + \gamma\sin\theta_A\sin\theta_B - 1\Big] \tag{A.4}$$

$$H_4 = \frac{J}{4}\Big[\cos(\theta_A-\theta_B) + \gamma\sin\theta_A\sin\theta_B + 1\Big], \tag{A.5}$$

Finally we obtain a quadratic spin-wave Hamiltonian

$$\mathbf{H} = E_0 + \sum_{i\in A}H_1 a_i^\dagger a_i + \sum_{j\in B}H_2 b_j^\dagger b_j + \sum_{\langle i,j\rangle}H_3(a_i^\dagger b_j^\dagger + a_i b_j) + \sum_{\langle i,j\rangle}H_4(a_i^\dagger b_j + b_j^\dagger a_i). \tag{A.6}$$

The diagonalization this Hamiltonian gives us the whole picture of the excitation spectrum at low energy. The detailed calculation of the spectrum for this model were performed by R.T.Scalettar in Ref. [101].

## A.2 Coexistence of CDW and BCS orders

In order to better understand the nature of the phase transition between the CDW and the superfluid phase, we propose to study the possibility of the coexistence of a phase with both CDW order and superfluid BCS order. In mean field theory, we keep three relevant terms of the interaction: the Hartree term (renormalization effect on the normal liquid), the particle-hole channel (CDW ordering) and the particle-particle channel (BCS superfluid ordering).

$$\begin{aligned}H =& N(\mu_\uparrow\bar{n}_\uparrow + \mu_\downarrow\bar{n}_\downarrow) + \sum_{k,\sigma}(\varepsilon_{k\sigma}-\mu_\sigma)c_{k\sigma}^\dagger c_{k\sigma} - \frac{|U|}{N}\sum_{k,k'}c_{k\uparrow}^\dagger c_{k\uparrow}c_{k'\downarrow}^\dagger c_{k'\downarrow} \\ &- \frac{|U|}{N}\sum_{k,k'}c_{k\uparrow}^\dagger c_{k'\uparrow}c_{-k\downarrow}^\dagger c_{-k'\downarrow} - \frac{|U|}{N}\sum_{k,k'}c_{k+Q\uparrow}^\dagger c_{k\uparrow}c_{k'\downarrow}^\dagger c_{k'+Q\downarrow}\end{aligned}$$

As done in the last sections, we define the order parameter for the BCS superfluid ordering as $\Delta_b = |U|N^{-1}\sum_k\langle c_{k\uparrow}^\dagger c_{-k\downarrow}^\dagger\rangle$ and the CDW ordering as $\Delta_{c\sigma} = |U|N^{-1}\sum_k\langle c_{k+Q\sigma}^\dagger c_{k\sigma}\rangle$. Then using the Hartree-Fock approximation, we have

$$H_{MF} = E_0 + \sum_{k,\sigma}\xi_{k\sigma}c_{k\sigma}^\dagger c_{k\sigma} - \Delta_b\sum_k(c_{k\uparrow}^\dagger c_{-k\downarrow}^\dagger + c_{-k\downarrow}c_{k\uparrow}) - \sum_{k,\sigma}\Delta_{c\sigma}c_{k+Q\sigma}^\dagger c_{k\sigma}, \tag{A.7}$$

in which $E_0/N = (\mu_\uparrow \bar{n}_\uparrow + \mu_\downarrow \bar{n}_\downarrow) + |U|\bar{n}_\uparrow \bar{n}_\downarrow + \Delta_b^2/|U| + \Delta_{c\uparrow}\Delta_{c\downarrow}/|U|$ and $\xi_{k\sigma} = \varepsilon_{k\sigma} - \mu_\sigma - |U| n_{\bar{\sigma}} = \varepsilon_{k\sigma} - \tilde{\mu}_\sigma$. Defining the spinor $\psi_k^\dagger = (c_{k\uparrow}^\dagger, c_{-k\downarrow}, c_{k+Q\uparrow}^\dagger, c_{-k-Q\downarrow})$ we can rewrite the Hamiltonian as

$$H_{MF} = E_0 - N\tilde{\mu}_\downarrow + \sum_{k \in \mathrm{RBZ}} \psi_k^\dagger M_k \psi_k, \tag{A.8}$$

where the matrix $M_{\mathbf{k}}$ has the form

$$M_{\mathbf{k}} = \begin{pmatrix} \varepsilon_{k\uparrow} - \tilde{\mu}_\uparrow & -\Delta_b & -\Delta_{c\uparrow} & 0 \\ -\Delta_b & -\varepsilon_{k\downarrow} + \tilde{\mu}_\downarrow & 0 & -\Delta_{c\downarrow} \\ -\Delta_{c\uparrow} & 0 & -\varepsilon_{k\uparrow} - \tilde{\mu}_\uparrow & -\Delta_b \\ 0 & -\Delta_{c\downarrow} & -\Delta_b & \varepsilon_{k\downarrow} + \tilde{\mu}_\downarrow \end{pmatrix} \tag{A.9}$$

We suppose that the matrix 4×4 can be diagonalized, and the eigenvalues: $E_{1,k}, -E_{2,k}, E_{3,k}, -E_{4,k}$ and eigenvectors are: $\varphi^\dagger = (a_{1,k}^\dagger, a_{2,k}, a_{3,k}^\dagger, a_{4,k})$. Therefore we obtain the diagonal Hamiltonian

$$H_{MF} = E_0 - N\tilde{\mu}_\downarrow - \sum_{k \in \mathrm{RBZ}} (E_{2,k} + E_{4,k}) + \sum_{k \in \mathrm{RBZ}, \nu} E_{\nu k} a_{\nu k}^\dagger a_{\nu k}. \tag{A.10}$$

In fact, we can not obtain an analytical expression of the eigenvalues, so we can not minimize the free energy to get the self-consistency equations. We will try to solve this problem in the following by numerical method. We suppose a lattice with a finite number of sites, then for each wave vector $k$ we diagonalize the matrix $M_k$, and calculate the functional of free energy

$$F[\Delta_b, \Delta_{c\uparrow}, \Delta_{c\downarrow}] = E_0 - N\tilde{\mu_\downarrow} - \sum_{k \in \mathrm{RBZ}} (E_{2,k} + E_{4,k}) - \beta^{-1} \sum_{\nu, k \in \mathrm{RBZ}} \log(1 + e^{-\beta E_{\nu k}}). \tag{A.11}$$

When $T = 0$ the functional of energy of the ground state is

$$\mathbf{E}[\Delta_b, \Delta_{c\uparrow}, \Delta_{c\downarrow}] = E_0 - N\tilde{\mu_\downarrow} - \sum_{k \in \mathrm{RBZ}} (E_{2,k} + E_{4,k}) + \sum_{\nu, k \in \mathrm{RBZ}} E_{\nu k} f(E_{\nu k}). \tag{A.12}$$

For each couple $(U, z)$, we plot the energy of the ground state, and determine all the local minima. The global minimum gives the order parameters of the ground state. In this general approach, there is no explicit form of the self-consistency equations. We proposed to use a numerical scheme to solve the problem. The self-consistency condition relates the static average value of the observable to a parameter. Therefore, we can start with a certain guess for the order parameter, compute the static average value of the observable then reenter it into the mean-field Hamiltonian as a new guess of order parameter. The iteration finishes whenever a converged solution is reached.

## A.3 Energy competition at half-filling

In the CDW phase, at half-filling the energy and the gap equations read

$$E_{CDW} - E_n = -\frac{1}{4}\left(\frac{\Delta_\uparrow^2}{W_\uparrow} + \frac{\Delta_\downarrow^2}{W_\downarrow}\right) \tag{A.13}$$

$$\frac{1}{N} \sum_{k \in \mathrm{RBZ}} \frac{\Delta_\sigma}{\sqrt{\varepsilon_{k\sigma}^2 + \Delta_\sigma^2}} = \frac{\Delta_{-\sigma}}{|U|}. \tag{A.14}$$

In the BCS phase, we have the energy and the gap equations

$$E_{BCS} - E_n = -\frac{\Delta_{BCS}^2}{W_\uparrow + W_\downarrow} \tag{A.15}$$

$$\frac{1}{N}\sum_k \frac{1}{\sqrt{\varepsilon_k^2+\Delta_{BCS}^2}} = \frac{2}{|U|}. \tag{A.16}$$

where $\varepsilon_k$ is defined as $(\varepsilon_\uparrow + \varepsilon_\downarrow)/2$. The energy difference between $E_{BCS}$ and $E_{CDW}$ reads

$$E_{CDW} - E_{BCS} = -\frac{1}{4}\left(\frac{\Delta_\uparrow^2}{W_\uparrow} + \frac{\Delta_\downarrow^2}{W_\downarrow}\right) + \frac{\Delta_{BCS}^2}{W_\uparrow + W_\downarrow}. \tag{A.17}$$

In the mean-field strategy, the energy of the CDW phase is obtained by minimizing over two parameters $\Delta_\uparrow$ and $\Delta_\downarrow$

$$E_{CDW} = \min_{(\Delta_\uparrow,\Delta_\downarrow)} E_{CDW}[\Delta_\uparrow, \Delta_\downarrow].$$

Let us now consider the energy $E_{CDW}^*$ defined as

$$E_{CDW}^* = \min_{\Delta} E_{CDW}[\Delta,\Delta] = -\frac{\Delta_{CDW}^2}{4}\left(\frac{1}{W_\uparrow} + \frac{1}{W_\downarrow}\right) \geq E_{CDW}.$$

The minimization over the parameter $\Delta$ induces that $\Delta_{CDW}$ is solution of the following gap equation:

$$\frac{2}{|U|} = \sum_{k,\sigma} \frac{1}{\sqrt{\varepsilon_{k\sigma}^2 + \Delta_{CDW}^2}}. \tag{A.18}$$

We will compare this energy $E_{CDW}^*$ to the energy of the BCS phase $E_{BCS}$. As the function $g(x) = 1/\sqrt{x^2+\Delta^2}$ is convex, therefore

$$\frac{1}{\sqrt{\varepsilon_{k\uparrow}^2+\Delta^2}} + \frac{1}{\sqrt{\varepsilon_{k\downarrow}^2+\Delta^2}} \geq \frac{2}{\sqrt{\varepsilon_k^2+\Delta^2}}$$

$$\Rightarrow \quad \frac{1}{N}\sum_{k\in \mathrm{RBZ},\sigma} \frac{1}{\sqrt{\varepsilon_{k\sigma}^2+\Delta_{CDW}^2}} \geq \frac{1}{N}\sum_k \frac{1}{\sqrt{\varepsilon_k^2+\Delta_{CDW}^2}}$$

$\Delta_{BCS}$ and $\Delta_{CDW}$ are satisfied the gap equations Eq.A.16 and Eq.A.18, respectively. Thus we obtain:

$$\frac{1}{N}\sum_k \frac{1}{\sqrt{\varepsilon_k^2+\Delta_{CDW}^2}} \leq \frac{2}{|U|} = \frac{1}{N}\sum_k \frac{1}{\sqrt{\varepsilon_k^2+\Delta_{BCS}^2}}. \tag{A.19}$$

The function $1/\sqrt{x^2+\Delta^2}$ is positive and monotonously decreased in variable $\Delta$, therefore we have: $\Delta_{CDW} \geq \Delta_{BCS}$. In addition, we have the following inequality for all $W = W_\uparrow + W_\downarrow$:

$$\frac{1}{W_\uparrow} + \frac{1}{W_\downarrow} \geq \frac{4}{W_\uparrow + W_\downarrow}$$

We conclude that

$$E_{CDW}^* - E_{BCS} = -\frac{\Delta_{CDW}^2}{4}\left(\frac{1}{W_\uparrow} + \frac{1}{W_\downarrow}\right) + \frac{\Delta_{BCS}^2}{W_\uparrow + W_\downarrow} \leq 0, \tag{A.20}$$

which means that $E_{CDW} - E_{BCS} \leq 0$ for all $z = (W_\uparrow - W_\downarrow)/(W_\uparrow + W_\downarrow)$.

# Appendix B

# Appendix on dynamical mean-field theory

## B.1 DMFT for the phase with long range order

Here, we use the DMFT description for the study of the super-fluid phase with off-diagonal long rang order in presence of an external field.

$$H = -\sum_{\langle i,j\rangle} t_\sigma (c^\dagger_{i\sigma} c_{j\sigma} + h.c) - |U| \sum_i n_{i\uparrow} n_{i\downarrow} - \sum_i \mu_\sigma c^\dagger_{i\sigma} c_{i\sigma} \tag{B.1}$$

We define the Nambu spinor: $\psi^\dagger_i = (c^\dagger_{i\uparrow}, c_{i\downarrow})$, then the Hamiltonian is

$$H = -\sum_{\langle i,j\rangle} (\psi^\dagger_i T \psi_j + h.c) - |U| \sum_i n_{i\uparrow} n_{i\downarrow} - \sum_i \psi^\dagger_i \mu \psi_i + \mathrm{C}, \tag{B.2}$$

where C is a constant and $T = \mathrm{diag}[t_\uparrow, -t_\downarrow]$, $\mu = \mathrm{diag}[\mu_\uparrow, -\mu_\downarrow]$. We define the Green function for these Nambu spinors: $\mathbf{G}(k,\tau) = \langle \mathrm{T}_\tau \psi_{k,\tau} \psi^\dagger_{k,0} \rangle$. Its Fourier transformation is

$$\mathbf{G}(k, i\omega_n) = \begin{bmatrix} G_\uparrow(k, i\omega_n) & F(k, i\omega_n) \\ F(k, i\omega_n) & -G_\downarrow(-k, -i\omega_n) \end{bmatrix}. \tag{B.3}$$

The effective impurity action reads

$$\begin{aligned} S^o_{eff} = &\int_0^\beta d\tau \int_0^\beta d\tau' \psi^\dagger_o(\tau) G_0^{-1}(\tau - \tau') \psi_o(\tau') \\ &- |U| \int_0^\beta d\tau n_{o\uparrow}(\tau) n_{o\downarrow}(\tau). \end{aligned}$$

We define the on-site self-energy as following

$$\mathbf{\Sigma_{imp}}(i\omega) = \mathbf{G}_0^{-1}(i\omega) - \mathbf{G}^{-1}(i\omega), \tag{B.4}$$

this local self-energy in this case has the matrix form

$$\mathbf{\Sigma_{imp}}(i\omega_n) = \begin{bmatrix} \Sigma_\uparrow(i\omega_n) & S(i\omega_n) \\ S(i\omega_n) & \Sigma_\downarrow(i\omega_n) \end{bmatrix}. \tag{B.5}$$

The DMFT consists to approximate the lattice self-energy to the impurity self-energy. In the real space, this means that we neglect the non-local component of $\mathbf{\Sigma_{ij}}$ and approximate the on-site one by $\mathbf{\Sigma_{imp}}$

$$\mathbf{\Sigma_{ii}} \simeq \mathbf{\Sigma_{imp}}, \quad \mathbf{\Sigma_{i\neq j}} \simeq 0.$$

Hence, it yields the mean field self-consistency equation

$$\mathbf{G_{imp}}(i\omega) = \sum_k \begin{bmatrix} \zeta_\uparrow(i\omega_n) - \varepsilon_{k\uparrow} & -S(i\omega_n) \\ -S(i\omega_n) & \zeta_\downarrow(i\omega_n) + \varepsilon_{k\downarrow} \end{bmatrix}^{-1}, \tag{B.6}$$

where $\zeta_\sigma(i\omega_n) = i\omega_n + \sigma\mu_\sigma - \Sigma_\sigma(i\omega_n)$. In the limit $d \to \infty$ for the Bethe lattice, this relation can be simplified to

$$\mathcal{G}^{-1}(i\omega_n) = i\omega_n + \mu\sigma_z - T\mathbf{G}(i\omega_n)T. \tag{B.7}$$

## B.2 Exact diagonalization solver, Lanczos method

In order to study the ground state at zero temperature, we propose to use the exact diagonalization by the Lanczos method to solve the Anderson's impurity model.

### B.2.1 Anderson impurity model

We consider an effective Anderson local impurity model in which the local site (note "d") is in contact with a bath with $n_s$ (<10) sites via the hopping parameters $\mathrm{t_{k\sigma}}$ ($k = 1, 2\ldots$). The bath has the energy distribution $\varepsilon_{k\sigma}$ without interaction. In the impurity site, the interaction is $Un_{d\uparrow}n_{d\downarrow}$. In order to study the paring state in the impurity site, we introduce the paring coupling on the bath $\Delta_k c_{k\uparrow}c_{k\downarrow}$ + h.c. The Anderson's impurity model reads

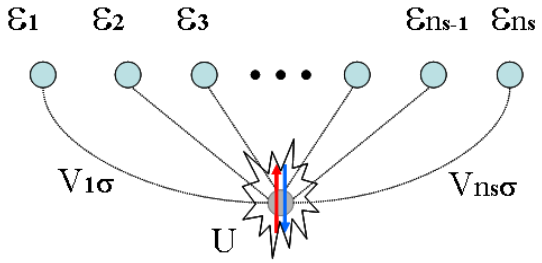


**Figure B.1:** Discrete Anderson's impurity model where the impurity site "d" (gray site) is connected with all the sites in the conduction bath (blue sites) via the hopping $V_{k\sigma}$.

$$H_{\mathrm{AIM}} = \sum_{k,\sigma} \varepsilon_{k\sigma} c^\dagger_{k\sigma} c_{k\sigma} + \sum_{k,\sigma} \Delta_k (c_{k\uparrow}c_{k\downarrow} + \mathrm{h.c}) + \sum_{k,\sigma} t_{k\sigma}(c^\dagger_{k\sigma} d_\sigma + \mathrm{h.c}) - \sum_\sigma \mu_\sigma n_{d\sigma} + U n_{d\uparrow} n_{d\downarrow}, \tag{B.8}$$

where $n_{d\sigma} = d^\dagger_\sigma d_\sigma$ and the creation operator of a particle in conduction band is noted by $c^\dagger_{k\sigma}$. Again, in the Nambu representation, the Hamiltonian can be rewritten

$$H_{\mathrm{AIM}} = \sum_k (\psi^\dagger_k \begin{bmatrix} V_{k\uparrow} & 0 \\ 0 & -V_{k\downarrow} \end{bmatrix} \psi_d + \mathrm{h.c}) + \sum_k \psi^\dagger_k \begin{bmatrix} \varepsilon_{k\uparrow} & \Delta_k \\ \Delta_k & -\varepsilon_{k\downarrow} \end{bmatrix} \psi_k - \psi^\dagger_d \hat{\mu} \psi_d + U n_{d\uparrow} n_{d\downarrow}. \tag{B.9}$$

The starting Green's function (non-interaction Green's function) for DMFT iteration can be computed from the Anderson's parameters of this impurity model $\varepsilon_{k\sigma}, Delta_k, V_{k\sigma}$

$$\mathcal{G}^{-1}_{0AIM}(i\omega_n) = i\omega_n - \sum_k \hat{V}_k G^{\mathrm{bath}}_k(i\omega_n)\hat{V}_k, \tag{B.10}$$

where $\hat{V}_k = \mathrm{diag}[V_{k\uparrow}, V_{k\downarrow}]$, and $G_k^{\mathrm{bath}}$ is the Green's function of the conduction bath

$$G_k^{\mathrm{bath}}(i\omega_n) = \begin{bmatrix} i\omega_n - \varepsilon_{k\uparrow} & -\Delta_k \\ -\Delta_k & i\omega_n + \varepsilon_{k\downarrow} \end{bmatrix}^{-1}. \tag{B.11}$$

Thus we have finally the guessed Green's function for the effective model

$$[\mathcal{G}_{0AIM}^{-1}]_{\sigma\sigma} = -\sum_k \frac{V_{k\sigma}^2(i\omega_n - \bar{\sigma}\varepsilon_{k\bar{\sigma}})}{(i\omega_n - \sigma\varepsilon_{k\sigma})(i\omega_n - \bar{\sigma}\varepsilon_{k\bar{\sigma}}) - \Delta_k^2} + i\omega_n + \sigma\mu_\sigma$$

$$[\mathcal{G}_{0AIM}^{-1}]_{\sigma\bar{\sigma}} = \sum_k \frac{V_{k\sigma}V_{k\bar{\sigma}}\Delta_k}{(i\omega_n - \sigma\varepsilon_{k\sigma})(i\omega_n - \bar{\sigma}\varepsilon_{k\bar{\sigma}}) - \Delta_k^2}.$$

### B.2.2 Lanczos algorithm

The idea of the Lanczos method is to construct a basis in which the Hamiltonian has the form of a tridiagonal matrix [26]. The procedure consists of iterating the basis from an initial state $|\phi_0\rangle$. In order to obtain the ground state, the guessed state must have a non-zero overlap with the ground state. If we do not known any thing about the ground state, it should be the random summation of all the states in the Hilbert space. Otherwise, if we know some information about the symmetry (quantum number), the spin, charge or paring of the ground state, then we can start from a specific sector (subspace). We start with the initial state $|\phi_0\rangle$, then the new vector is defined by the vector $H|\phi_0\rangle$ subtracted by its projection on the initial state

$$|\phi_1\rangle = H|\phi_0\rangle - \frac{\langle\phi_0|H|\phi_0\rangle}{\langle\phi_0|\phi_0\rangle}|\phi_0\rangle. \tag{B.12}$$

This state is orthogonal with the initial state: $\langle\phi_1|\phi_0\rangle = 0$. We construct the new one which is orthogonal with both states $|\phi_0\rangle$, $|\phi_1\rangle$

$$|\phi_2\rangle = H|\phi_1\rangle - \frac{\langle\phi_1|H|\phi_1\rangle}{\langle\phi_1|\phi_1\rangle}|\phi_1\rangle - \frac{\langle\phi_1|\phi_1\rangle}{\langle\phi_0|\phi_0\rangle}|\phi_0\rangle. \tag{B.13}$$

The orthogonality $\langle\phi_2|\phi_1\rangle = 0$ comes directly the definition and the orthogonality of $|\phi_1\rangle$ and $|\phi_0\rangle$ while the one $\langle\phi_2|\phi_0\rangle$ comes from the hermitian property of the Hamiltonian: $\langle\phi_0|H|\phi_1\rangle = \langle\phi_1|H|\phi_0\rangle$. By recurrence, we can define the vector $|\phi_{n+1}\rangle$ from the couple $|\phi_n\rangle$ and $|\phi_{n-1}\rangle$

$$|\phi_{n+1}\rangle = H|\phi_n\rangle - a_n|\phi_1\rangle - b_n^2|\phi_{n-1}\rangle, \tag{B.14}$$

where $n = 0, 1, 2\ldots$ and the coefficients are

$$a_n = \frac{\langle\phi_n|H|\phi_n\rangle}{\langle\phi_n|\phi_n\rangle}, \quad b_n^2 = \frac{\langle\phi_n|\phi_n\rangle}{\langle\phi_{n-1}|\phi_{n-1}\rangle}. \tag{B.15}$$

In this basis the Hamiltonian has the tridiagonal matrix form

$$H = \begin{bmatrix} a_0 & b_1 & 0 & 0 & \ldots \\ b_1^* & a_1 & b_2 & 0 & \ldots \\ 0 & b_2^* & a_2 & b_3 & \ldots \\ 0 & 0 & b_3^* & a_3 & \ldots \\ \vdots & \vdots & \vdots & \vdots & \ddots \end{bmatrix}. \tag{B.16}$$

The diagonalization of this tridiagonal matrix can be done by using some standard library. In fact, the convergence of the ground state (the lowest energy state) is quite rapid. Within this algorithm, we do not need to construct the whole basis of the Hilbert space in order to find the ground state and the low energy excitations state. As shown in [26], when the number of iteration is around 100, the ground state is already accurate enough. Thus this method is convenient to study the low-temperature physics.

# Bibliography


[1] A. A. Abrikosov, e., 1963, *Methods of Quantum Field Theory in Statistical Physics* (Dover, New York). 20, 27

[2] van Abeelen, F. A., B. J. Verhaar, and A. J. Moerdijk, 1997, Phys. Rev. A **55**(6), 4377. 45, 46

[3] Altman, E., E. Demler, and M. D. Lukin, 2004, Phys. Rev. A **70**(1), 013603. 17

[4] Anderson, M. H., J. R. Ensher, M. R. Matthews, C. E. Wieman, and E. A. Cornell, 1995, Science **269**, 198. 13, 153

[5] Anderson, P. W., 1952, Phys. Rev. **86**(5), 694. 78

[6] Antoine Georges, and Thierry Giamarchi, 2002, *Introduciton au problème à N corps et à la Physique des fermions fortement corrélés* (Cours de DEA de physique théotique). 20

[7] Arrigoni, E., and G. C. Strinati, 1991, Phys. Rev. B **44**(14), 7455. 81

[8] Auerbach, A., 1998, *Interacting Electrons and Quantum Magnetism* (Springer). 80

[9] Bardeen, J., L. N. Cooper, and J. R. Schrieffer, 1957, Phys. Rev. **108**(5), 1175. 74

[10] Batrouni, G. G., V. Rousseau, R. T. Scalettar, M. Rigol, A. Muramatsu, P. J. H. Denteneer, and M. Troyer, 2002, Phys. Rev. Lett. **89**(11), 117203. 10

[11] Blakie, P. B., 2006, New J. Phys. **8**, 157. 26

[12] Bloch, I., 2005, Nature Physics **1**, 23. 2, 13, 90

[13] Bloch, I., J. Dalibard, and W. Zwerger, 2007, ArXiv e-prints **704**. 6, 7, 8, 15, 126, 127

[14] Bourdel, T., L. Khaykovich, J. Cubizolles, J. Zhang, F. Chevy, M. Teichmann, L. Tarruell, S. J. J. M. F. Kokkelmans, and C. Salomon, 2004, Phys. Rev. Lett. **93**(5), 050401. 126

[15] Brown, R. H., 1956, Nature **177**, 27. 17

[16] Bruun, G. M., and G. Baym, 2006, Physical Review A (Atomic, Molecular, and Optical Physics) **74**(3), 033623 (pages 8). 15

[17] Bul/ka, B. R., and S. Robaszkiewicz, 1996, Phys. Rev. B **54**(18), 13138. 81

[18] Burovski, E., N. Prokof'ev, B. Svistunov, and M. Troyer, 2006, Physical Review Letters **96**(16), 160402 (pages 4). 126

[19] C. J. Pethick, and H. Smith, 2001, *Bose-Einstein Condensation in Dilute Gases* (Cambridge University Press). 5, 6, 7

[20] Capone, M., C. Castellani, and M. Grilli, 2002, Phys. Rev. Lett. **88**(12), 126403. 93

[21] Carusotto, I., 2006, Journal of Physics B Atomic Molecular Physics **39**, 211. 15

[22] Cazalilla, M. A., A. F. Ho, and T. Giamarchi, 2005, Phys. Rev. Lett. **95**(22), 226402 (pages 4). 80, 90, 91, 97

[23] Chin, C., M. Bartenstein, A. Altmeyer, S. Riedl, S. Jochim, J. H. Denschlag, and R. Grimm, 2004, Science **305**, 1128. 15

[24] Civelli, M., M. Capone, S. S. Kancharla, O. Parcollet, and G. Kotliar, 2005, Physical Review Letters **95**(10), 106402 (pages 4). 37

[25] Combescot, R., and C. Mora, 2002, Eur. J. P. B **28**, 397. 128

[26] Dagotto, E., 1994, Rev. Mod. Phys. **66**(3), 763. 163

[27] Damascelli, A., 2004, Physica Scripta **T 109**, 61. 22, 23, 24

[28] Damascelli, A., Z. Hussain, and Z.-X. Shen, 2003, Rev. Mod. Phys. **75**(2), 473. 22

[29] Dao, T.-L., A. Georges, and M. Capone, 2007, Phys. Rev. B **76**(10), 104517 (pages 6). 91, 94

[30] Dao, T.-L., A. Georges, J. Dalibard, C. Salomon, and I. Carusotto, 2007, Phys. Rev. Lett. **98**(24), 240402 (pages 4). 24

[31] Duan, L.-M., 2005, Phys. Rev. Lett. **95**(24), 243202 (pages 4). 25, 90, 97, 131, 133

[32] Engelbrecht, J. R., M. Randeria, and C. A. R. Sáde Melo, 1997, Phys. Rev. B **55**(22), 15153. 56

[33] Ferdinando Mancini, U. d. S. d. S., Università degli Studi di Salerno Adolfo Avella (ed.), 2003, *Strongly Correlated Electron Materials: Dynamical Mean-Field Theory and Electronic Structure*, volume 715 of *AIP Conference Proceedings*. 83, 84

[34] Ferrero, M., P. S. Cornaglia, L. De Leo, O. Parcollet, G. Kotliar, and A. Georges, 2008, ArXiv e-prints **806**. 37

[35] Feshbach, H., 1958, Annals of Physics **5**, 357. 6

[36] Fisher, M. P. A., P. B. Weichman, G. Grinstein, and D. S. Fisher, 1989, Phys. Rev. B **40**(1), 546. 9

[37] Fölling, S., F. Gerbier, A. Widera, O. Mandel, T. Gericke, and I. Bloch, 2005, Nature **434**, 481. 17

[38] Folling, S., A. Widera, T. Muller, F. Gerbier, and I. Bloch, 2006, Physical Review Letters **97**(6), 060403 (pages 4). 10

[39] Forbes, M. M., E. Gubankova, W. V. Liu, and F. Wilczek, 2005, Physical Review Letters **94**(1), 017001 (pages 4). 128

[40] Freericks, J. K., and V. Zlatić, 2003, Rev. Mod. Phys. **75**(4), 1333. 92, 97

[41] Fulde, P., and R. A. Ferrell, 1964, Phys. Rev. **135**(3A), A550. 128

[42] Georges, A., 2007, Proceedings of the international school of physics "Enrico Fermi" **CLXYV**, 477. 2, 9, 69

[43] Georges, A., and G. Kotliar, 1992, Phys. Rev. B **45**(12), 6479. 83

[44] Georges, A., G. Kotliar, W. Krauth, and M. J. Rozenberg, 1996, Rev. Mod. Phys. **68**(1), 13. 83, 84, 85, 86, 87, 90, 139

[45] Georges, A., and J. S. Yedidia, 1991, Phys. Rev. B **43**(4), 3475. 72, 73, 108

[46] Greiner, M., O. Mandel, T. Esslinger, T. Hänsch, and I. Bloch, 2002, Nature **415**, 39. 1, 9, 153

[47] Greiner, M., C. A. Regal, J. T. Stewart, and D. S. Jin, 2005, Phys. Rev. Lett. **94**(11), 110401 (pages 4). 17

[48] Grimm, R., 2007, Proceedings of the international school of physics "Enrico Fermi" **CLXYV**, 413. 14, 15

[49] Gupta, S., Z. Hadzibabic, M. W. Zwierlein, C. A. Stan, K. Dieckmann, C. H. Schunck, E. G. M. van Kempen, B. J. Verhaar, and W. Ketterle, 2003, Science **300**, 1723. 14

[50] Hadzibabic, Z., S. Gupta, C. A. Stan, C. H. Schunck, M. W. Zwierlein, K. Dieckmann, and W. Ketterle, 2003, Phys. Rev. Lett. **91**(16), 160401. 46

[51] Hagley, E. W., L. Deng, M. Kozuma, J. Wen, K. Helmerson, S. L. Rolston, and W. D. Phillips, 1999, Science **283**(5408), 1706. 25

[52] He, Y., Q. Chen, and K. Levin, 2005, Physical Review A (Atomic, Molecular, and Optical Physics) **72**(1), 011602 (pages 4). 15

[53] Helmes, R. W., T. A. Costi, and A. Rosch, 2008, Physical Review Letters **100**(5), 056403 (pages 4). 154

[54] Héritier, M., 2004, *Electrons corrélés et supraconductivité* (Cours du DEA de Physique de solide). 69, 76, 108

[55] Holland, M., S. J. J. M. F. Kokkelmans, M. L. Chiofalo, and R. Walser, 2001, Phys. Rev. Lett. **87**(12), 120406. 126, 127

[56] Honerkamp, C., M. Salmhofer, N. Furukawa, and T. M. Rice, 2001, Phys. Rev. B **63**(3), 035109. 37

[57] Jaksch, D., C. Bruder, J. I. Cirac, C. W. Gardiner, and P. Zoller, 1998, Phys. Rev. Lett. **81**(15), 3108. 8

[58] Jaksch, D., and P. Zoller, 2005, Annals of Physics **315**, 52. 2, 90, 131

[59] Japha, Y., S. Choi, K. Burnett, and Y. B. Band, 1999, Phys. Rev. Lett. **82**(6), 1079. 25, 26

[60] Jeltes, T., J. M. McNamara, W. Hogervorst, W. Vassen, V. Krachmalnicoff, M. Schellekens, A. Perrin, H. Chang, D. Boiron, A. Aspect, and C. I. Westbrook, 2007, Nature **445**, 402. 17

[61] Jochim, S., M. Bartenstein, A. Altmeyer, G. Hendl, S. Ried, C. Chin, J. H. Denschlag, and R. Grimm1, 2002, Science **302**(5653), 2101. 126

[62] Alexander L. Fetterand John Dirk Walecka, 2003, *Quantum Theory of Many-Particle Systems* (Dover Publications). 132

[63] Jördens, R., N. Strohmaier1, K. Günter, H. Moritz, and T. Esslinger, 2008, ArXiv e-prints 0804.4009. 1, 10, 153

[64] Katanin, A. A., and A. P. Kampf, 2004, Phys. Rev. Lett. **93**(10), 106406. 37

[65] Keller, M., W. Metzner, and U. Schollwöck, 2001, Phys. Rev. Lett. **86**(20), 4612. 93, 127

[66] Kinnunen, J., M. Rodríguez, and P. Törmä, 2004, Science **305**, 1131. 15

[67] Kohl, M., H. Moritz, T. Stoferle, K. Gunter, and T. Esslinger, 2005, Phys. Rev. Lett. **94**(8), 080403 (pages 4). 13, 14

[68] Kohler, T., K. Goral, and P. S. Julienne, 2006, Reviews of Modern Physics **78**(4), 1311 (pages 51). 6

[69] Koponen, T. K., T. Paananen, J.-P. Martikainen, M. R. Bakhtiari, and P. Törmä, 2008, New J. Phys. **10**(4), 045014. 133, 140

[70] Koponen, T. K., T. Paananen, J.-P. Martikainen, and P. Törmä, 2007, Phys. Rev. Lett. **99**(12), 120403. 133, 140

[71] Kotliar, G., and A. E. Ruckenstein, 1986, Phys. Rev. Lett. **57**(11), 1362. 80

[72] Kyle M. Shen, e., 2005, Science **307**, 901. 37

[73] Kyung, B., A. Georges, and A.-M. S. Tremblay, 2006, Phys. Rev. B **74**(2), 024501 (pages 5). 93, 140, 142

[74] Larkin, A. I., and Y. N. Ovchinnikov, 1965, Sov. Phys. JETP **20**, 762. 128

[75] Lechermann, F., A. Georges, G. Kotliar, and O. Parcollet, 2007, Physical Review B (Condensed Matter and Materials Physics) **76**(15), 155102 (pages 20). 80

[76] Leggett, A., 1980, *Modern Trends in the Theory of Condensed Matter* (Springer-Verlag, Berlin). 126

[77] Li, W., G. B. Partridge, Y. A. Liao, and R. G. Hulet, 2007, Nuclear Physics A **790**, 88. 126

[78] Liu, W. V., and F. Wilczek, 2003, Phys. Rev. Lett. **90**(4), 047002. 90

[79] Liu, W. V., and F. Wilczek, 2003, Phys. Rev. Lett. **90**(4), 047002. 124, 128

[80] Lorenzo De Leo, Corinna Kollath, Antoine Georges, Michel Ferrero, and Olivier Parcollet, 2008, ArXiv e-prints 0807.0790. 6

[81] Luxat, D. L., and A. Griffin, 2002, Phys. Rev. A **65**(4), 043618. 25, 26

[82] M. Greiner, C. R., and D. Jin, 2003, Nature **426**, 537. 47, 126

[83] Mahan, G. D., 1981, *Many Particle Physics* (Plenum, New York). 20, 27

[84] Mazets, I. E., G. Kurizki, N. Katz, and N. Davidson, 2005, Phys. Rev. Lett. **94**(19), 190403 (pages 4). 25

[85] Sá de Melo, C. A. R., M. Randeria, and J. R. Engelbrecht, 1993, Phys. Rev. Lett. **71**(19), 3202. 126

[86] Mora, C., 2004, *Gaz de bosons et de fermions condensés: phases de Fulde-Ferrell-Larkin-Ochinnikov et quasicondensats*, Ph.D. thesis, ENS de Paris. 74, 129, 133, 140

[87] Morsch, O., and M. Oberthaler, 2006, Reviews of Modern Physics **78**(1), 179 (pages 37). 3

[88] N. W. Ashcroft and N. D. Mermin, 1999, *Solid State Physics* (Cengage Learning). 4

[89] Niu, Q., I. Carusotto, and A. B. Kuklov, 2006, Phys. Rev. A. **73**(5), 053604 (pages 9). 12

[90] Norman, M. R., M. Randeria, H. Ding, and J. C. Campuzano, 1998, Phys. Rev. B **57**(18), R11093. 37

[91] Nozières, P., and S. Schmitt-Rink, 1985, J. Low Temp. Phys **59**(3–4), 195. 126

[92] Partridge, G. B., W. Li, R. I. Kamar, Y.-A. Liao, and R. G. Hulet, 2006, Science **311**(5760), 503. 128, 154

[93] Pilati, S., and S. Giorgini, 2008, Physical Review Letters **100**(3), 030401 (pages 4). 124, 128, 129

[94] Polkovnikov, A., E. Altman, and E. Demler, 2006, Proceedings of the National Academy of Science **103**, 6125. 12

[95] Potthoff, M., and W. Nolting, 1999, Phys. Rev. B **59**(4), 2549. 154

[96] Regal, C. A., M. Greiner, and D. S. Jin, 2004, Phys. Rev. Lett. **92**(4), 040403. 47

[97] Regal, C. A., and D. S. Jin, 2003, Phys. Rev. Lett. **90**(23), 230404. 14

[98] Rigol, M., A. Muramatsu, G. G. Batrouni, and R. T. Scalettar, 2003, Phys. Rev. Lett. **91**(13), 130403. 6

[99] Santos, L., M. A. Baranov, J. I. Cirac, H.-U. Everts, H. Fehrmann, and M. Lewenstein, 2004, Phys. Rev. Lett. **93**(3), 030601. 3

[100] Sarma, G., 1963, J. Phys. Chem. Solids **24**, 1029. 128, 133, 140

[101] Scalettar, R. T., G. G. Batrouni, A. P. Kampf, and G. T. Zimanyi, 1995, Phys. Rev. B **51**(13), 8467. 78, 155, 157

[102] Schwieger, S., M. Potthoff, and W. Nolting, 2003, Phys. Rev. B **67**(16), 165408. 154

[103] Sénéchal, D., and A.-M. S. Tremblay, 2004, Phys. Rev. Lett. **92**(12), 126401. 37

[104] Sheehy, D. E., and L. Radzihovsky, 2006, Physical Review Letters **96**(6), 060401 (pages 4). 124, 128, 129

[105] Sheshadri, K., H. R. Krishnamurthy, R. Pandit, and T. V. Ramakrishnan, 1993, Europhysics Letters **22**, 257. 9

[106] Shimahara, H., 1994, Phys. Rev. B **50**(17), 12760. 128

[107] Shin, Y., M. W. Zwierlein, C. H. Schunck, A. Schirotzek, and W. Ketterle, 2006, Phys. Rev. Lett. **97**(3), 030401 (pages 4). 124

[108] Sofo, J. O., and C. A. Balseiro, 1992, Phys. Rev. B **45**(1), 377. 81

[109] Son, D. T., and M. A. Stephanov, 2006, Physical Review A (Atomic, Molecular, and Optical Physics) **74**(1), 013614 (pages 6). 124, 128

[110] Stamper-Kurn, D. M., A. P. Chikkatur, A. Görlitz, S. Inouye, S. Gupta, D. E. Pritchard, and W. Ketterle, 1999, Phys. Rev. Lett. **83**(15), 2876. 15, 16

[111] Stenger, J., S. Inouye, A. P. Chikkatur, D. M. Stamper-Kurn, D. E. Pritchard, and W. Ketterle, 1999, Phys. Rev. Lett. **82**(23), 4569. 15

[112] Stewart, J. T., J. P. Gaebler, and D. S. Jin, 2008, ArXiv e-prints `0805.0026v1`. 14, 48, 49, 51

[113] Stewart, J. T., J. P. Gaebler, C. A. Regal, and D. S. Jin, 2006, Physical Review Letters **97**(22), 220406 (pages 4). 47, 142

[114] Stoof, H. T. C., M. Houbiers, C. A. Sackett, and R. G. Hulet, 1996, Phys. Rev. Lett. **76**(1), 10. 45, 46

[115] Tiesinga, E., B. J. Verhaar, and H. T. C. Stoof, 1993, Phys. Rev. A **47**(5), 4114. 6

[116] Tinkham, M., 2004, *Introduction to Superconductivity* (Dover Publications). 74

[117] Tomczak, J. M., 2007, *Spectral and Optical Properties of Correlatted Materials*, Ph.D. thesis, Ecole Polytechnique. 87

[118] Törmä, P., and P. Zoller, 2000, Phys. Rev. Lett. **85**(3), 487. 25

[119] Toschi, A., P. Barone, M. Capone, and C. Castellani, 2005, New Journal of Physics **7**, 7. 91, 93, 127, 140

[120] Toschi, A., M. Capone, and C. Castellani, 2005, Phys. Rev. B **72**(23), 235118 (pages 10). 84, 91, 93, 127, 140, 142

[121] Werner, F., O. Parcollet, A. Georges, and S. R. Hassan, 2005, Phys. Rev. Lett. **95**(5), 056401 (pages 4). 2, 4, 5, 90, 131

[122] Werner, P., A. Comanac, L. de' Medici, M. Troyer, and A. J. Millis, 2006, Physical Review Letters **97**(7), 076405 (pages 4). 88, 140

[123] Wilhelm Zwerger, 2003, Journal of Optics B: Quantum and Semiclassical Optics **5**(2), S9. 2, 5, 90

[124] Wille, E., F. M. Spiegelhalder, G. Kerner, D. Naik, A. Trenkwalder, G. Hendl, F. Schreck, R. Grimm, T. G. Tiecke, J. T. M. Walraven, S. J. J. M. F. Kokkelmans, E. Tiesinga, *et al.*, 2008, Physical Review Letters **100**(5), 053201 (pages 4). 90

[125] Wolfgang Ketterle, and Martin W. Zwierlein, 2007, Proceedings of the international school of physics "Enrico Fermi" **CLXYV**, 95. 15, 47, 125

[126] Zwierlein, M. W., A. Schirotzek, C. H. Schunck, and W. Ketterle, 2006, Science **311**(5760), 492. 124, 128, 154

[127] Zwierlein, M. W., C. H. Schunck, A. Schirotzek, and W. Ketterle, 2006, Nature **442**, 54. 124, 128

[128] Zwierlein, M. W., C. A. Stan, C. H. Schunck, S. M. F. Raupach, S. Gupta, Z. Hadzibabic, and W. Ketterle, 2003, Phys. Rev. Lett. **91**(25), 250401. 126